Layer-by-Layer assembly of nanocellulose composite films with bio-inspired helicoidal superstructures

Randy Mujica

UNIVERSITÉ DE STRASBOURG

ÉCOLE DOCTORALE DE PHYSIQUE ET CHIMIE-PHYSIQUE

INSTITUT CHARLES SADRON (UPR22-CNRS)

THÈSE présentée par :

Randy MUJICA

soutenue le : **15 septembre 2020**

pour obtenir le grade de : **Docteur de l'université de Strasbourg**
Discipline/ Spécialité : Chimie – Physique

Layer-by-Layer assembly of nanocellulose composite films with bio-inspired helicoidal superstructures

THÈSE dirigée par :

M. FELIX Olivier	Chargé de recherche, Université de Strasbourg
M. LE HOUEROU Vincent	Professeur, Université de Strasbourg

RAPPORTEURS :

M. WÅGBERG Lars	Professeur, KTH Royal Institute of Technology
M. ROTH Stephan	Professeur, Deutsches Elektronen-Synchrotron (DESY)

AUTRES MEMBRES DU JURY :

Mme. BÉGIN-COLIN Sylvie	Professeur, Université de Strasbourg
M. PARDOEN Thomas	Professeur, Université Catholique de Louvain

MEMBRES INVITÉS :

M. DECHER Gero	Professeur, Université de Strasbourg
M. BATTIE Yann	Maître de conférences, Université de Lorraine

To my family and my wife

Acknowledgments

I would like to express my sincere gratitude to all people who contributed, in different ways, to the completion of this thesis. First of all, I am very thankful to my Ph.D. advisors, Dr. Olivier Félix and Prof. Vincent Le Houerou, for their guidance and optimism during the whole duration of my thesis. I also thank the members of the jury committee: Professors Lars Wågberg, Stephan Roth, Sylvie Bégin-Colin, Thomas Pardoen, Gero Decher, and Dr. Yann Battie for having accepted to evaluate my thesis work.

I would also like to thank all members of Prof. Decher's group with whom I worked for the last 3+ years, including my former and current lab mates. Particularly, I thank Anusree Augustine for her enthusiastic contribution to the preparation of relevant samples for this manuscript and for having brought her joy to the lab.

Further, this dissertation would not be accomplished without the help, support, and advice of many others: I thank Mircea Rastei for granting me access to the AFM platform at the IPCMS, without which it would not have been possible to complete my work on time; I am very grateful to Leandro Jacomine for his invaluable support, advice, and discussions about nanoindentation and other matters, as well as his willingness to help me; I appreciate the very important contribution of Yann Battie to the characterization of the optical properties of my samples by Mueller matrix ellipsometry, and I thank Matthias Pauly for his revision and discussions of the chapter on optical properties.

I am also very grateful to the rest of colleagues at the ICS who contributed to obtaining and analyzing many of the data, particularly to Damien Favier for his diligent support for the mechanical characterization of the films, to Alain Carvalho for the SEM imaging, and to Christophe Contal for many AFM imaging and discussions.

I would like to thank the French Ministry of Higher Education and Research (Ministère de l'Enseignement Supérieur et de la Recherche) for the financial support to my thesis and to Bruno Jean for kindly providing cellulose nanocrystals for some of the experiments.

Last but not least, I thank everyone at the ICS whose everyday chit-chat and companionship made the long research workdays more pleasant.

Preface

Through millions of years of evolution, a plethora of structural materials has been developed by nature with various adapted mechanical properties based on the complex hierarchical organization of limited and relatively weak structural units such as small molecules, polymers, proteins, and biominerals. Moreover, this hierarchical organization provides most biological materials with multifunctionality (e.g., structural coloring, self-repairing, water barrier, etc.). On the contrary, synthetic materials are produced from a larger variety of elements and compounds but they lack the hierarchical organization in terms of composition and structure at the nano-, micro-, and mesolevels exhibited by their natural counterparts.

Approaches for synthesizing materials inspired by biological systems are a young field with high potential for technological breakthroughs in material sciences. However, the development of fabrication methods allowing good structuring control at the nano- and microscale remains the bottleneck for the replication of the complex architectures (and their associated properties) encountered in biological systems.

The present research work explores the utilization of the Layer-by-Layer (LbL) assembly methodology combined with the so-called Grazing Incidence Spraying (GIS) as an additive manufacturing process in which the direction of in-plane alignment of individual layers of cellulose nanofibrils (CNFs) is rationally selected to achieve thin composite films possessing a complex internal structuring of the reinforcing phase. We rely on this directed assembly approach to fabricate multilayer films of CNF/polyelectrolyte possessing either unidirectional, cross-ply, or helicoidal arrangements of the reinforcing nanofibrils, the latter being inspired by the interesting damage tolerance and chiral optical properties induced by this architecture in biological systems.

The results described herein encompass (a) the systematic investigation of the processing conditions required to obtain a high degree of alignment of the individual nanocellulose layers, (b) the fabrication of complex nanostructured cellulose-based thin films, (c) the optical characterization of unidirectionally and helicoidally structured films, and (d) the use of different nanoindentation methodologies to characterize the mechanical behavior of the resulting films.

Table of contents

List of abbreviations

AC	Alternating current
AFM	Atomic force microscopy
AGU	Anhydroglucose unit
ANOVA	Analysis of variance
BNC	Bacterial nanocellulose
CAD	Computer-aided design
CB	Circular birefringence
CD	Circular dichroism
CERMAV	Centre de recherches sur les macromolécules végétales
CHI	Chitosan
CNC	Cellulose nanocrystals
CNF	Cellulose nanofibers
CNRS	Centre national de la recherche scientifique
CPL	Circularly polarized light
CSM	Continuous stiffness measurement
DOE	Design of experiments
DPPC	L-α-dipalmitoylphosphatidylcholine
EBL	Electron beam lithography
EISA	Evaporation induced self-assembly

EIT	Indentation elastic modulus
FEG-SEM	Field emission gun scanning electron microscopy
FEP	Fluorinated ethylene-propylene
FIB	Focused ion beam
GA	Glutaraldehyde
GIS	Grazing incidence spraying
HIT	Indentation hardness
HPC	Hydroxypropyl-cellulose
IIT	Instrumented indentation technique
IQR	Interquartile range
LB	Linear birefringence
L-B	Langmuir-Blodgett
LbL	Layer-by-layer
L-CPL	Left-handed circularly polarized light
LD	Linear dichroism
MFC	Microfibrillated cellulose
MMSE	Mueller matrix spectroscopic ellipsometry
MTM	Montmorillonite
NFC	Nanofibrillated cellulose
NIL	Nanoimprint lithography
NP	Nanoparticle
OVAT	One-variable-at-a-time

PAH	Poly(allylamine hydrochloride)
PDDA	Poly(diallyldimethylammonium chloride)
PDMS	Poly(dimethylsiloxane)
PEC	Polyelectrolyte complex
PEG	Poly(ethylene glycol)
PEI	Poly(ethylene imine)
PEM	Polyelectrolyte multilayer
PSS	Poly(styrene sulfonate)
PVAm	Poly(vinylamine)
PVDF	Poly(vinylidene fluoride)
QCM	Quartz crystal microbalance
QCM-D	Quartz crystal microbalance with dissipation monitoring
R2R	Roll-to-roll
R-CPL	Right-handed circularly polarized light
RH	Relative humidity
RIE	Reactive ion etching
RMS	Root mean square
RMSE	Root mean square error
SAM	Self-assembled monolayer
SDEMT	Shape distributed effective medium theory
SEM	Scanning electron microscopy
STM	Scanning tunneling microscopy

SWCNT	Single-wall carbon nanotubes
TEM	Transmission electron microscopy
TEMPO	2,2,6,6-tetramethylpiperidine-1-oxyl
UV-Vis-NIR	Ultraviolet-visible-near infrared

Chapter 1. Introduction

Composite materials combine two or more synergistic components to maximize the resulting physical or chemical properties. For instance, hardness, toughness, stiffness, strength, damage tolerance, and lightweight are properties commonly optimized by the conscious selection of different compositions and architectures of the material constituents.[1]

Mankind has created composite materials for thousands of years, being mudbrick one of the most ancient examples: it combines the compression resistance of dried mud with the tensile strength of straw. More recently, the use of nanosized building blocks to create materials with unprecedented improvements in their physical properties has dragged the attention of materials scientists and engineers around the world. This growing interest is mainly encouraged by the examples of naturally occurring composite materials such as bone, nacre, crustacean shells, wood, among others, whose mechanical properties are outstanding given the weak properties of their building blocks (e.g. proteins, polysaccharides, and biominerals).[2]

The restricted strength of the natural building blocks is the result of the limited availability of elements (C, N, O, H, P, Si, Ca, among others) and the mild processing conditions at which biological materials are produced (ambient temperature, atmospheric pressure, and aqueous environments). Through millions of years of evolution, though, nature has overcome this weakness by developing sophisticated hierarchically organized structures of the building blocks at the nano-, micro-, and meso-levels. Moreover, this hierarchical organization provides most

biological materials with multifunctional characteristics, i.e., they combine specialized functions such as structural, optical, barrier, adhesion, self-repairing, water repulsion, etc.

Certainly, human beings have copied biological models since ancient times, sometimes unintentionally, however, it took a long time until mankind got the awareness of the incredible source of inspiration that nature represents when seeking solutions to problems often encountered in science and technology. The systematic research of biological systems for technical applications, termed bionics, only emerged after 1960, becoming worldwide disciplines with high potential for innovation only with the new millennium.[3]

In the present chapter, we first discuss the reinforcing mechanisms of biological materials associated with the hierarchical organization of fibrillar structures, which serve as inspiration for the development of the next generation of high-performance composite materials. Then, we introduce the advantageous characteristics of cellulose for its use as a sustainable building block for the fabrication of nanocomposite materials, and finally, we discuss different approaches that might be used to prepare nanostructured thin films. At the end of the chapter, we define the purpose of the present work and the organization of this manuscript.

1.1. Natural nanofibrillar materials

Natural materials are generally more complex than synthetic ones. Independently of their chemical composition, they often form hierarchical structures of features such as nanofibrils, laminar multilayer stacking, mesoporous structures, among others.[4] One of the most common structural features of biological materials that fulfill structural functions is the nanofibril, ubiquitous in many materials at any of the organizational multilevel. For instance, cellulose nanofibrils constitute the elementary structural component of the primary cell wall of green plants and algae; chitin nanofibrils are the primary component present in the exoskeletons of arthropods, mollusks, the scales of fish, and fungi; keratin nanofibrils are present in animal hairs, nails, feathers, horns, and claws, while collagen nanofibrils are found in fibrous tissues such as tendons, ligaments, and skin.[2] All these nanofibrils are made up of biopolymers such as polysaccharides

or polypeptides that self-assemble into highly oriented semicrystalline structures stabilized by hydrogen bonds and van der Waals forces.[5,6] The reinforcing mechanism of the nanofibrillar structure can be illustrated by the spider dragline silk fibers, one of the toughest materials known. Silk fibers exhibit a unique combination of high-tensile strength (1 – 2 GPa) and extensibility (50 – 60% strain at failure)[7] that enables the material to absorb amounts of energy before breaking which are higher than that of many engineering materials such as steel or Kevlar.[7–9]

However, the semi-amorphous and nanocrystalline b-sheet protein domains that constitute the silk fibers are formed by hydrogen bonds, i.e. one of the weakest chemical bonds, and moreover, it has been found that silk fibers contain many defects such as voids reaching several hundred nanometers in size that – according to Griffith's theory – may act as stress concentrators.[10–12] Therefore, the superior mechanical properties of spider silk can only be explained by structural effects. Nova et al.[13] developed the first spider-silk mesoscale model that demonstrates how the geometrical confinement of the silk fibrils to few nanometers is responsible for the enhanced resistance to failure of this natural material, which can be reasonably extrapolated to other fibrillar structures. Figure 1.1 shows the stress-strain response observed in silk fibrils under tensile loading, which is divided into four regimes. Initially, an elastic regime is ascribed to the homogeneous stretching of semi-amorphous regions rich in hydrogen bonding. The rupture of these hydrogen bonds marks the beginning of a yielding process in regime II, characterized by the gradual unfolding of the semi-amorphous protein chains in the pulling direction. At around 50% strain, when the semi-amorphous phase is completely stretched out, a stiffening regime develops in which the strain is sustained by the crystalline phase. Finally, a stick-slip failure mechanism of the b-sheet nanocrystals is responsible for a softening of the fibers right before failure.

Giesa et al.[14] further scaled up this ideal model to the microscale by including the effect of structural inhomogeneities acting as stress concentrators and found that there exists a critical fiber diameter (estimated to be ~50 nm) above which molecular unfolding (regime II) is significantly localized around the edge of the crack and thus a very small fraction of less than 1% of the entire

material contributes to the overall mechanical resistance of the fiber. Under these conditions, catastrophic failure of the fiber is obtained at significantly low strains (15%). On the contrary, for fiber diameters below the critical value, all the material in the fiber contributes synergistically to resist the deformation and to reach all four regimes of deformation homogeneously in spite of the presence of very large defects. This nanoconfinement of weak but regenerative hydrogen bonds illustrates how nature developed efficient strategies to turn a weakness into a strength. Most engineering materials, on the other hand, rely on strong bonds (for example, covalent) that can lead to catastrophic failure once they break.

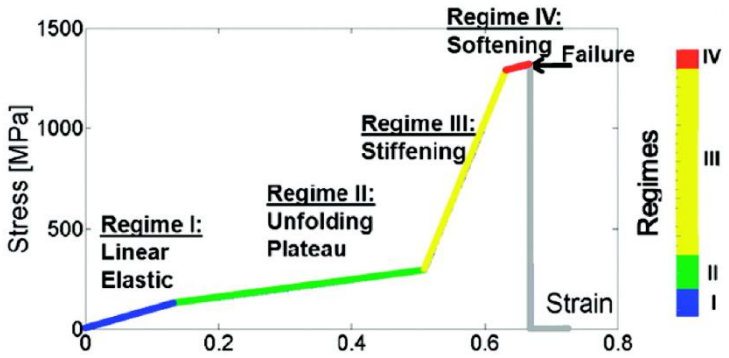

Figure 1.1: Different regimes of the stress-strain behavior of defect-free silk fibers.[14]

Another important aspect of biocomposites is the increased contribution of the interfaces to the resulting reinforced properties. Biological materials are strong and tough (two properties that are typically mutually exclusive in engineering materials), in part because they include organic-rich interfaces that can glide and slide. These interfaces provide nonlinear deformation mechanisms, redistribute stresses around defects, and deflect cracks into configurations in which their propagation is hindered or arrested.[15] In the particular case of nanofibrillar components, the interfaces can favor crack propagation in the longitudinal direction over the lateral direction, avoiding the complete cleavage of the fibril, as demonstrated by Zhang et al. for *Antheraea yamamai* silk fibers.[16] They observed that notched silk fibers exhibited the same strain-curves as the un-notched fibers, unlike for fibers of Nylon-66. The difference was ascribed to microfibril splitting and crack shifting around 90° during the tensile experiment in the case of the natural fiber instead of the linear crack propagation observed for the synthetic one (Figure 1.2).

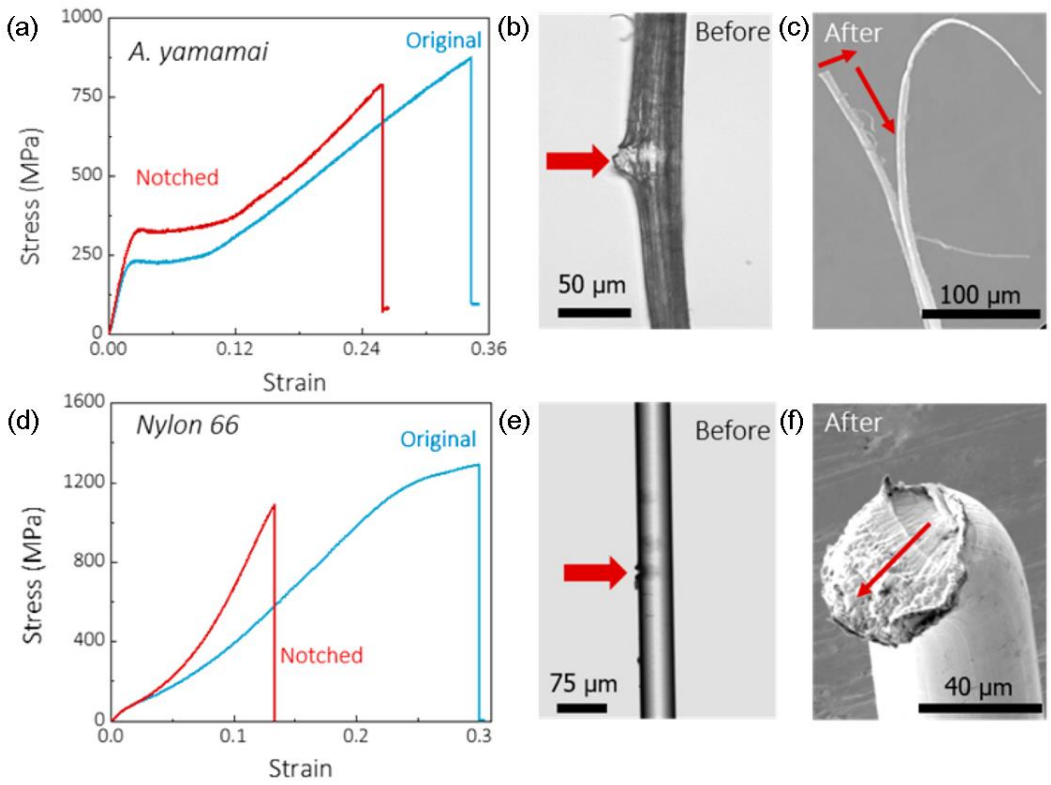

Figure 1.2: Comparison of the mechanical performance of *A. yamamai* silk and Nylon-66 fibers. (a, d) Stress-strain curves of original and notched silk fibers and Nylon fibers, respectively. (b, e) Optical micrographs of notched silk and Nylon fibers, respectively, before the tensile loading. (c, f) SEM images of the notched silk and Nylon fibers, respectively, after the fracture. The direction of propagation of the crack is indicated by the red arrows.[16]

1.2. Helicoidal arrangement of natural fibrillar nano-composites for mechanical reinforcement

Beyond the self-assembly and nanoconfinement of molecular chains into fibrillar arrangements, natural materials develop more complex higher-level structures in which nanofibrils are further bundled into bigger fibrils of various diameters up to the micrometer scale, aligned into 2D layered structures, and stacked into complex 3D architectures.[2,4,17]

The hierarchical organization of cellulose and chitin molecules present in wood and in the arthropod exoskeletons respectively is schematically depicted in Figure 1.3. The lower-levels of the structural hierarchy of these materials are similar and analogous to that of other nanofibrillar composites such as silk, i.e., individual polymer chains (poly(*D*-glucosamine) in cellulose and

poly(*N*-acetylglucosamine) in chitin) assemble into nanoconfined fibrillar structures composed of crystalline and amorphous domains and further bundle into bigger fibrils, wrapped with hemicelluloses and lignin in the case of cellulose or with proteins in the case of chitin. From this point, the higher levels of the hierarchical organization of fibrillar biocomposites differentiate into specific structures to satisfy the particular mechanical and functional properties of each material. The cell walls of wood are composed of distinct concentric layers of cellulose fibers: a primary layer with cellulose fibrils randomly distributed in the plane of the layer, and three secondary layers, S1, S2, and S3, with cellulose fibrils helically wound in varying patterns in each one.[5] As for the arthropod exoskeletons, layers of parallel chitin fibers are stacked in a progressively rotated configuration to form a helicoidal structure commonly referred to as twisted plywood or Bouligand structure[18] after Yves Bouligand, who was the first to identify this motif and its

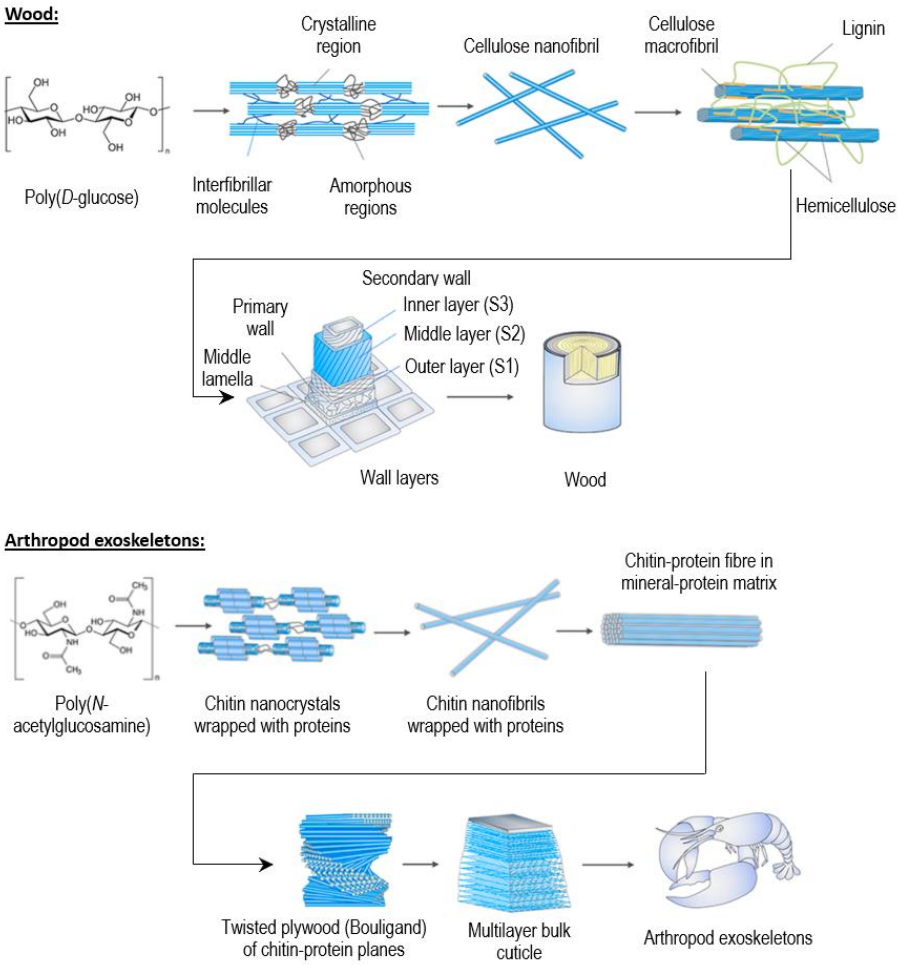

Figure 1.3: Schematic of the hierarchical organization of cellulose in wood (top) and chitin in the arthropod exoskeletons (down).[33]

similarity to the cholesteric liquid crystalline phase of some materials.[19] The twisted plywood configuration is not exclusive to arthropods nor to the animal kingdom, though. As a matter of fact, helicoidal arrangements of cellulose microfibrils are more widespread in plant taxa than it was initially realized.[20]

The reinforcing characteristics of the Bouligand ultrastructure have been recognized in many biological materials.[21–25] Mechanically, the Bouligand configuration provides the material with increased toughness and isotropy in multiple directions. Moreover, studies in the scales of the *Arapaima gigas* Amazonian fish showed that the lamellae of the Bouligand structure can reorient in response to the in-plane loading conditions, re-aligning towards the tensile axis to deform in tension through stretching/sliding mechanisms.[23,26]

One of the most remarkable and well-known examples of sophisticated damage-tolerant biomaterials whose outstanding mechanical properties have been associated with the presence of the Bouligand configuration is the mineralized hammer-like dactyl clubs of the stomatopods, commonly called mantis shrimp (*Odontodactylus scyllarus*). This crustacean delivers fast and powerful punches with this appendage to shatter the shells of its prey, many of which are themselves considered a benchmark of super-tough biocomposites.[27] The dactyl strike is one of the fastest and most powerful impacting events observed in nature, with accelerations over 10^5 m/s^2, speeds over 20 m/s, and instantaneous forces up to 1500 N, thousands of times the bodyweight of the animal.[28,29] The remarkable ability of this material to withstand thousands of such highly energetic strikes without catastrophic damage[30] has been recognized to be the result of different toughening mechanisms arising from the multiphase composite nature of the material, schematically depicted in Figure 1.4.

The dactyl club is divided into two distinct regions, an outer impact region, and an internal periodic region. The outer region is composed of a gradient of amorphous calcium carbonate and fluorapatite,[31] as well as a herringbone structure region of compacted sinusoidal arrangements of mineralized nanofibrils of chitin.[32] The inner region is made of a helicoidal array of chitin fibrils partially mineralized with amorphous calcium carbonate. This Bouligand arrangement

provides several toughening mechanisms that hamper the catastrophic propagation of cracks within the material. Particularly, it forces the cracks to propagate following a helicoidal path between the chitin fibers, which dissipates a higher amount of energy than a crack propagating straight. Additionally, cracks propagating straight into the material encounter an elastic modulus oscillation due to the anisotropic stiffness of neighboring layers that hampers the propagation across layers.[25]

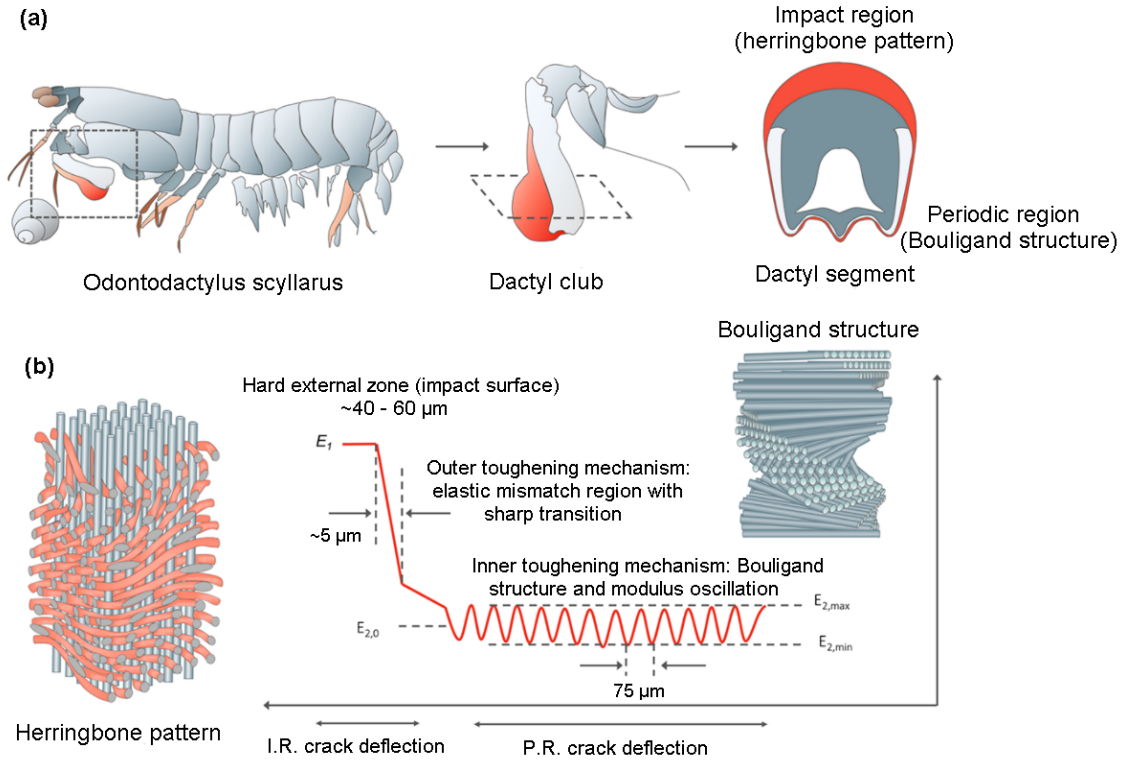

Figure 1.4: (a) Illustration of the dactyl club from *O. scyllarus*. (b) Schematic of the rotating fibers and interpenetrating fibrous pore canal tubules present in the impact region (left). Toughening mechanisms of the dactyl club (middle), based on a hard outer-layer, a modulus transitional region for crack deflection between the impact surface and the bulk of the impact region, and a periodic region with a helicoidal pattern and modulus oscillation for crack shielding. Representation of the Bouligand structure of chitin fibers (right).[33]

1.3. Optical functionality of helicoidal biomaterials

The hierarchical arrangement of small building blocks in biological materials is not only responsible for enhanced mechanical responses but in many cases, it results in the integration of one or multiple functionalities to the materials. One such functionality is related to the effective

interaction with light toward fulfilling biological functions such as camouflage, signaling, communication, heat regulation, and vision/light detection.[33,34] The helicoidal alignment of fibrillar composites has been associated with two optical effects in several animal and plant tissues, namely structural coloration and selective reflection of circularly polarized light.

Unlike the coloration mechanism based on the presence of pigment molecules that selectively absorb certain visible wavelengths, structural coloration is produced by the interaction of light with the internal micro- or nano-structures present in many biological materials.[35] Helicoidally stacked microfibrils form multilayers with a refractive index that varies periodically in space, this arrangement acts as a photonic crystal giving rise to the Bragg reflection phenomenon:[36] when the periodic distance defined by half of the helicoidal pitch ($P/2$) is comparable to the wavelength of visible light, a photonic bandgap is formed that leads to light being reflected in a particular wavelength range centered at a λ_{max} determined by the Bragg-Snell law:[37]

$$m\lambda_{max} = \bar{n} \cdot P \cdot \sin(\theta) \qquad \text{(Eq. 1.1)}$$

where m is the order of diffraction, $\bar{n}$ is the average refractive index and θ is the angle of the incident light.

Very good examples of structural coloration are provided by the fruits of *Pollia condensata* and *Margaritaria nobilis*, whose metallic appearance and strong iridescent blue coloration (Figure 1.5) are associated with the Bouligand arrangement of cellulose microfibrils in their epidermal cell walls as verified by electron microscopy.[38,39] Other examples are found in the leaf of Malaysian understory plants[40] and in the iridescent cuticle of many beetles.[41–45]

Additionally, the helicoidal photonic structures exhibit a preferential reflection of circularly polarized light with the same chirality than that of the helicoidal structure, mostly left-handed (L-CPL).[43,45–48] Only very few examples of materials reflecting right-handed circular polarized light (R-CPL) are reported, among them, the exocuticle of the beetle *Chrysina resplendens* that reflects both handednesses simultaneously due to the inclusion of an anisotropic layer between two separated left-handed layers, which acts as a half-wave retarder.[42]

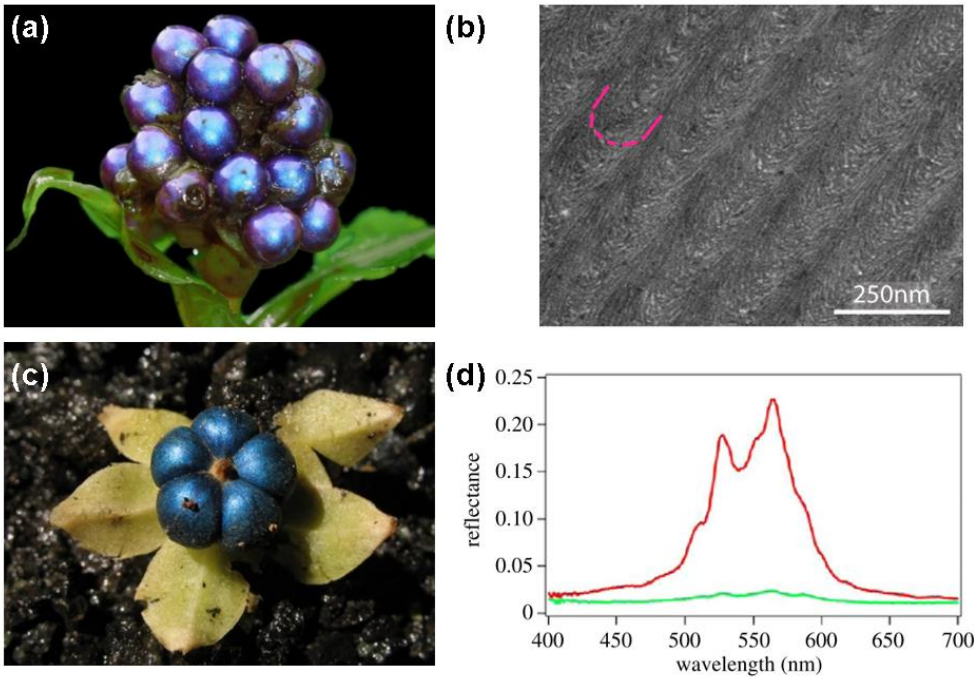

Figure 1.5: (a) Photography of the shiny blue berries of the tropical *Pollia condensata* plant. The diameter of each fruit is about 5 mm.[49] (b) TEM of the cellulose microfibrils that constitute the thick cell wall in the external layer of the fruit of *P. condensata*. The red lines highlight the twisting direction of the microfibrils.[38] (c) Photograph of the fruit of *Margaritaria nobilis*.[50] (d) Reflectance spectra of circularly polarized light measured on *M. nobilis*. Only left (red) CPL is reflected.[39]

The occurrence of circular polarization in nature is very rare and its utility for the organisms remains mysterious. Yet a certain family of Scarabaeidae beetles (often referred to as scarab beetles) are able to convert unpolarized incident light into L-CPL by reflection,[51] and some stomatopod crustaceans are capable of detecting circularly polarized light, allegedly to mediate sexual signaling or contrast enhancement in turbid environments.[52]

1.4. Nanocellulose as a building block for nanocomposite materials

The increasing global interest in the development of products made from renewable resources has encouraged the research on cellulose-based materials as an environmentally friendly alternative to petroleum-based ones. Cellulose is estimated to be naturally generated at a rate of 1.5 x 10^{12}

tons per year,[53] which makes it the most abundant organic polymer on Earth and a virtually inexhaustible source of sustainable polymeric raw material available for human use.

Besides being bio-sourced, cellulose combines plenty of properties of interest for many technical applications, such as hydrophilicity, chirality, biodegradability, non-toxicity, low density, or broad chemical modifying capacity. Moreover, owing to its hierarchical structure and semicrystalline nature, cellulose nanoparticles with remarkable mechanical properties and reinforcing capabilities can be extracted using top-down deconstructing strategies. All these favorable characteristics make cellulose an ideal candidate to be incorporated into polymer nanocomposites. In the present section, we introduce the most relevant characteristics of cellulose and the different morphologies and nanostructures in which it can be found.

Cellulose is present in plants, algae, and many forms of fungi, serving as a structural element within the hierarchical construction of their cells, typically accompanied by hemicelluloses and lignin.[54] Moreover, bacteria of the genera *Gluconacetobacter*, *Agrobacterium*, *Pseudomonas*, *Rhizobium*, and *Sarcina* can also synthesize cellulose from glucose and various other carbon sources.[55,56] Cellulose is a carbohydrate polymer whose molecular structure is shown in Figure 1.6. It is formed by D-anhydroglucose units linearly connected through β-1,4 glycosidic bonds. To accommodate the preferred bond angles of the acetal oxygen bridges, every second anhydroglucose unit (AGU) is rotated by 180°. The degree of polymerization, DP, varies considerably depending on the source and treatment of the raw material between 100 up to 20000.[57] One end of the cellulose molecule contains an anomeric C atom linked by the glycosidic bonds (non-reducing end) whereas the other end has a D-glucopyranose unit in equilibrium with the aldehyde function (reducing end group).

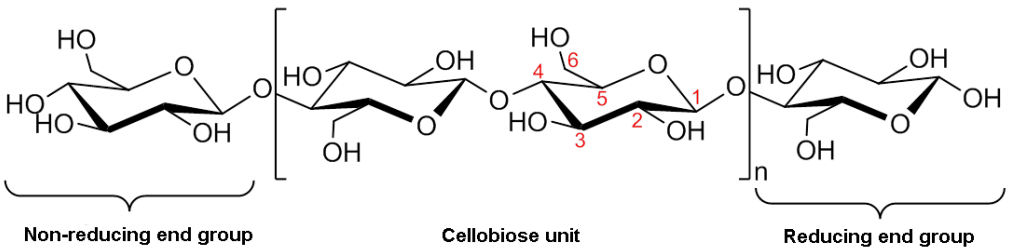

Figure 1.6: Molecular structure of cellulose (n = DP).

The three hydroxyl groups of the AGU, as well as the oxygen atoms in the backbone of the cellulose molecule, interact with each other within the chain or with neighboring cellulose molecules by forming intra- and inter-molecular hydrogen bonds, which have a significant influence on the properties of cellulose, including the limited solubility in most solvents, the reactivity of the hydroxyl groups, the crystallinity, and the ability to self-assemble.[54]

The regular structure of native cellulose (cellulose I) leads to its crystallization. Cellulose from different sources possesses comparable crystallinity (around 50%) although in different proportions of two polymorphic phases. Plant cellulose mainly crystallizes in the triclinic I_β phase, whereas bacterial cellulose mainly consists of I_α monoclinic crystals. Native cellulose is also commonly treated with aqueous sodium hydroxide (mercerization) or it is dissolved, precipitated, and regenerated to produce textiles and technical products; this regenerated cellulose crystallizes in a different and thermodynamically stable form of cellulose II, also with a monoclinic cell but with a different arrangement of the cellulose chains within it. Models of these different crystalline structures of cellulose are schematically displayed in Figure 1.7**Error! Reference source not found.**. Both cellulose I and II can be further converted into less stable cellulose III and IV allotropes by chemical treatment although they are less technically relevant.

As introduced earlier, plant cellulose organizes into a morphological hierarchy defined by elementary fibrils, microfibrils, and microfibrillar bands. The elementary fibrils are composed of the longitudinal assembly of individual molecules held together by hydrogen bonds and van der Waals forces, and they have crystalline and amorphous domains. The lateral dimensions of the elementary fibrils are between 1.5 – 3.5 nm, those of the microfibrils are between 10 – 30 nm, whereas the microfibrillar bands are on the order of 100 nm.[53] This hierarchical structure of native cellulose can be deconstructed to isolate nanofibrils and nanocrystals with potential applications in many technological industries ranging from paper and packaging to construction, food, personal care, among many others.[58]

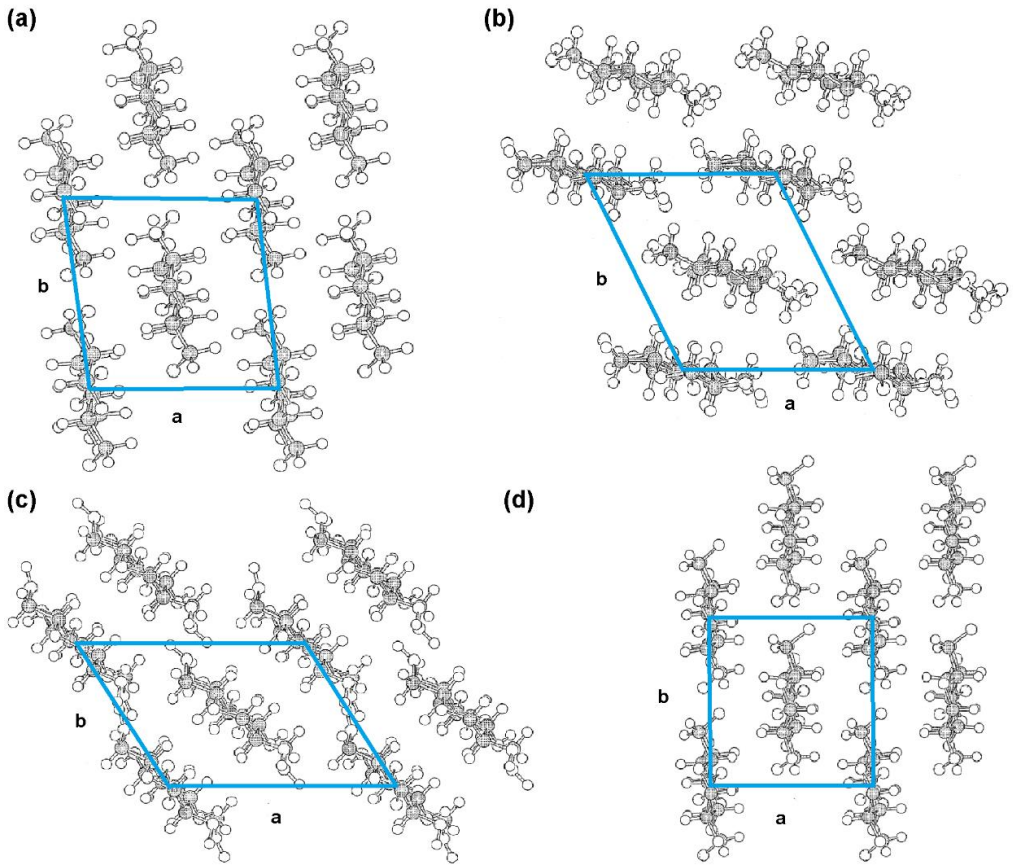

Figure 1.7: Models of (a) cellulose I_β, (b) cellulose II, (c) cellulose III_1, and (d) cellulose IV_1.[59] The blue parallelograms represent the projections of the unit cell onto the a – b plane, where "a" and "b" are two unit cell vectors.

Figure 1.8 shows the increasing number of scientific publications related to the use of these nano-manifestations of cellulose over the past 20 years. But it is as a biobased reinforcing nanofiller that such materials have attracted more interest, particularly after the work of Favier et al. who first reported the use of cellulose nanocrystals as reinforcing filler of poly(styrene-*co*-butyl acrylate)-based nanocomposites.[60] Nanocellulosic materials have great potential for the development of nanocomposites as they combine the desirable properties of cellulose, such as high strength and low density, with the reinforcing characteristics of nanoparticles, namely high surface area and high aspect ratio. We present below three types of cellulosic nanomaterials commonly investigated for reinforcement applications.

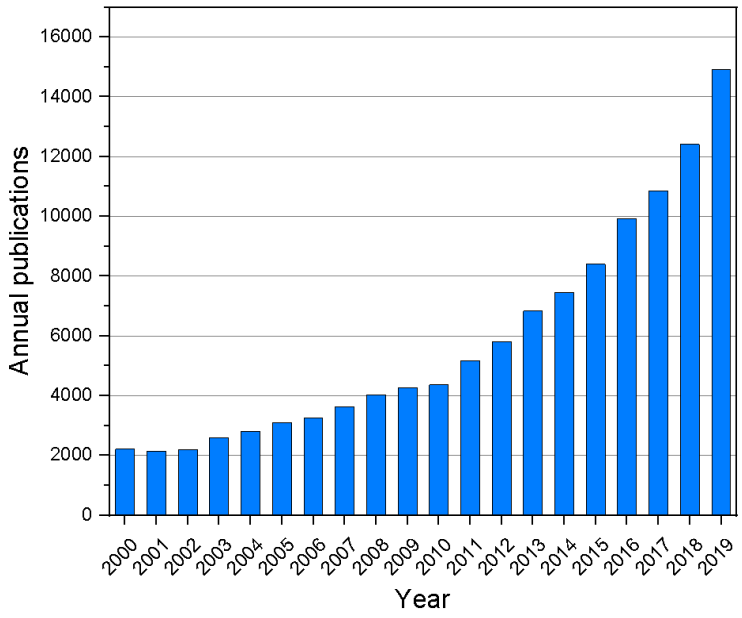

Figure 1.8: Annual publications from 2000 to 2019 on the subject of nanocelluloses. Data obtained using the ScienceDirect platform and the following keywords: nanocellulose, microfibrillated cellulose, bacterial cellulose, microbial cellulose, CNF, NFC, CNC, cellulose nanocrystals, and cellulose nanowhiskers.

1.4.1. Cellulose Nanocrystals (CNCs)

Individual cellulose crystallites can be isolated by the acid hydrolysis of native cellulose. These crystals assemble into rigid rod-like (or "needle-like") cellulose particles commonly referred to as cellulose nanocrystals (CNCs) or cellulose nanowhiskers. Due to differences in the hydrolysis kinetics between amorphous and crystalline domains, the amorphous regions are preferentially hydrolyzed when subjected to strong acids such as sulfuric or hydrochloric acid, leaving the crystalline regions unaffected[61] (Figure 1.9). These are recovered after washing with successive centrifugations and dialysis against distilled water to remove free acid molecules.

Being "entirely" crystalline, CNCs stand out compared with other nanocelluloses due to their rigid structure, superior strength, chemical purity, optical properties, and reproducibility of its production.[62,63] The most common feedstocks for CNCs are lignocellulosic plants such as wood pulp and cotton, although other sources such as algae, bacteria, and tunicates may also be used (tunicates are the only known animal source of cellulose). The dimensions of the nanocrystals depend largely on the source from where they are extracted and the hydrolysis conditions. Typical

sizes for CNCs originating from different cellulose sources are summarized in Table 1.1. The crystal width varies from a few nanometers to tens of nanometers while their lengths span from hundreds of nanometers to several micrometers. The isolation of the nanocrystals by acid treatment, most commonly performed with sulfuric acid, also imparts a negative surface charge that provides good colloidal stability,[64] which is beneficial for the practical use of CNCs.

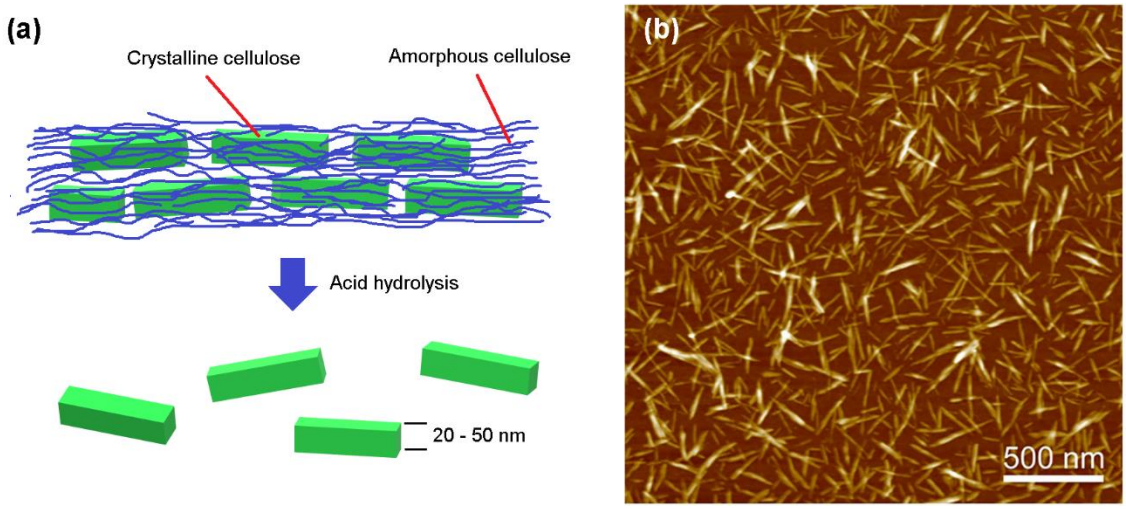

Figure 1.9: (a) Schematic representation of the extraction of cellulose nanocrystals using acid hydrolysis. (b) Topographical AFM height image showing the whisker-like shape of cellulose nanocrystals extracted from wood pulp via sulfuric acid hydrolysis.[57]

The nanoscale dimensions, high aspect ratio, and high surface-to-volume ratio of the CNCs make them an interesting material to be incorporated as the reinforcing phase for nanocomposites. The Ashby plot presented in Figure 1.10 illustrates the advantageous mechanical performance of cellulose nanoparticles (in general) compared to many common engineering materials. The specific elastic modulus (E/ρ) and specific strength (σ_b/ρ) of cellulose ($\rho \approx 1.6$ g/cm^3)[65] outperform most of these materials, which justifies the interest in the development of composite materials based on this abundant and renewable feedstock. The axial elastic modulus of native cellulose crystals from cotton and tunicates, respectively, has been reported between 105 – 143 GPa,[66,67] while theoretical calculations estimate a value of 167.5 GPa,[68] which surpasses the specific modulus of Kevlar® and steel.

Table 1.1: Examples of length and width of CNCs from various sources.

Source	Length (nm)	Width (nm)	Technique	Ref.
bacterial	100 – 1000	10 – 50	TEM	[69]
cotton	100 – 150	5 – 10	TEM	[70]
cotton linter	100 – 200	10 – 20	SEM – FEG	[71]
ramie	150 – 250	6 – 8	TEM	[72]
sisal	100 – 500	3 – 5	TEM	[73]
tunicate	1000 – 3000	15 – 30	TEM	[74]
Valonia	>1000	10 – 20	TEM	[75]
soft wood	100 – 150	4 – 5	AFM	[76]
hard wood	140 – 150	4 – 5	AFM	[76]

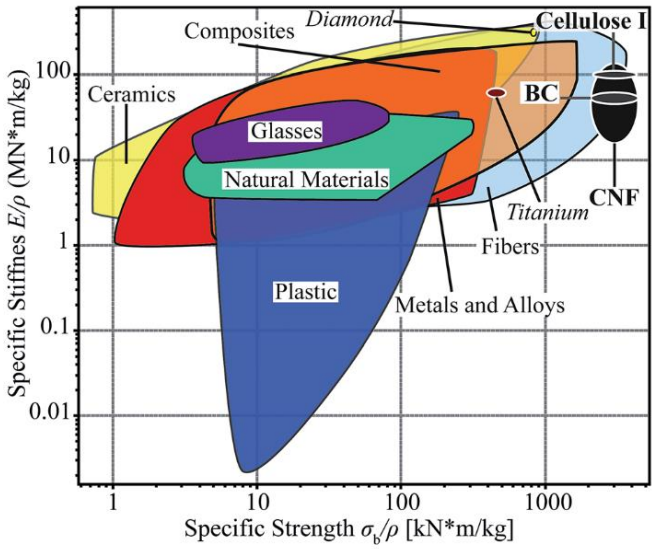

Figure 1.10: Ashby plot of the specific stiffness and specific strength comparing cellulose I, CNFs, and BC versus different engineering materials.[77]

Besides their attractive mechanical properties, CNCs were found to form a stable chiral nematic crystalline phase in suspension,[78] which boosted an additional interest in this material owing to its optical properties. The chiral nematic phase (also called cholesteric phase) is characterized by a helical modulation of the direction of alignment of the rigid nano-rods which might be retained upon solvent removal. Having a pitch (in the dry state) in the submicrometric range, it results in Bragg reflection of visible light and striking iridescent color of the resulting films.[79] Additionally, the helical assembly of CNC nanorods within the dry films renders the material chiral and sensitive to circular polarization, thus of great interest for photonic applications.

1.4.2. Micro- and Nano-Fibrillated Cellulose (MFC and NFC)

Instead of the complete hydrolysis of the amorphous phase, both crystalline and amorphous domains of the native cellulose fibers can be broken into smaller semicrystalline nano- and micro-fibers (Figure 1.11) by mechanical disintegration processes such as grinding, mechanical homogenization at high pressure and cryocrushing,[61] as well as by chemical methods such as hydrolysis in high-concentration acid and subsequent regeneration in water or any anti-solvent.[80] The shear forces exerted by the different mechanical processes promote the fibrillation of the native cellulose, which are moderately degraded and opened into a highly web-like entangled network of nanofibrils (microfibrillated cellulose, MFC).[81] To facilitate the process, which is highly energy consuming, different pre-treatments, such as enzymatic hydrolysis or the introduction of charged groups through carboxymethylation or 2,2,6,6-tetramethylpiperidine-1-oxyl (TEMPO)-mediated oxidation, are conventionally used.[82–85] The combination of mild enzymatic hydrolysis or TEMPO oxidation with high-pressure shear forces allows the isolation of individual cellulose nanofibrils, CNF (or nanofibrillated cellulose, NFC), having a width of 3 – 5 nm[54,82,85,86] and a length that can be more than 1 µm.[87]

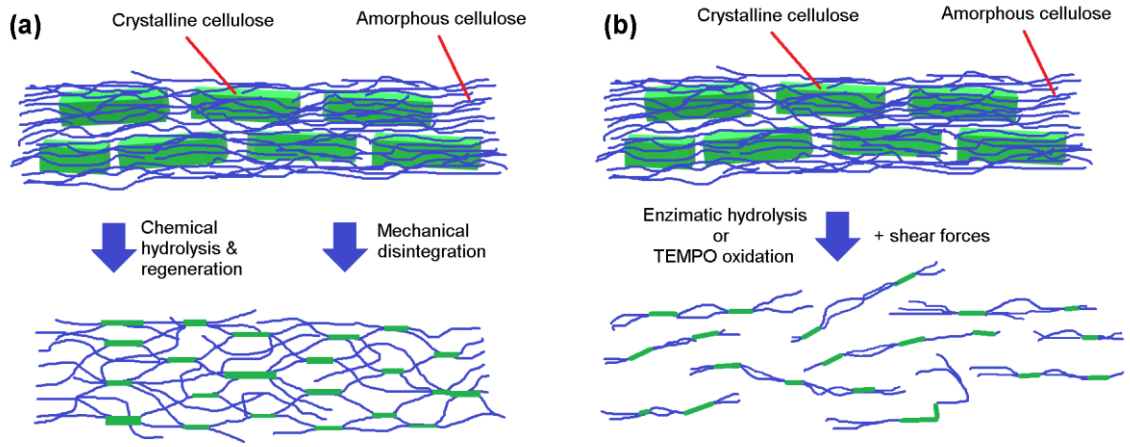

Figure 1.11: Schematic representation of the routes used for the extraction of (a) microfibrillated cellulose and (b) cellulose nanofibrils by breaking the hierarchical macrostructure of cellulose either chemically or mechanically.

Given that the surface of the cellulose nanofibrils bears a high concentration of hydroxyl groups, it can be functionalized by various heterogeneous reactions including esterification and

etherification. TEMPO-oxidation converts the hydroxyl groups into carboxyl groups introducing negative charges that help stabilization of the colloidal dispersion of CNFs. Other possible chemical treatments and functionalization opportunities include carboxymethylation, hydrophobization, acetylation, as well as the inclusion of reactive vinyl moieties, polymer chains, or corona plasma treatment.[88–91]

The higher aspect ratio of CNF compared to nanocrystals grants the former with improved mechanical reinforcement capabilities. Different theoretical and experimental values of the longitudinal elastic modulus of cellulose microfibrils (or bundles) have been reported, being 100 GPa a good approximation to an average value.[92] Table 1.2 compares the elastic modulus of a number of engineering material commonly used to reinforce polymeric matrices.

Table 1.2: Modulus and density of common reinforcing materials compared to microfibrillated cellulose

Material	Modulus (GPa)	Density (Mg/m^3)	Specific modulus ($GPa\ m^3/Mg$)	Ref.
carbon fibers	200 – 500	1.8	110 – 270	[93]
nanoclay	150 – 400	2.5	60 – 160	[94]
carbon nanotubes	1000 – 1700	1.4	715 – 1215	[95]
glass	69	2.5	28	[96]
microfibrillated cellulose	100	1.6	60	[92]

1.4.3. Bacterial Nanocellulose (BC)

An alternative to the disintegration of plant cellulose is the harvesting of cellulose produced by a bacteria of the genus *Gluconacetobacter xylinum*, an acetic acid bacteria that secretes an abundant 3D network of cellulose fibrils under aerobic conditions, using glucose as a carbon source.[97] The first report regarding the production of cellulose from bacteria was done by Brown in 1886,[98] who investigated the biosynthesis of cellulose by this bacteria. Bacterial cellulose is similar to plant cellulose, with the added value of being purer because it does not contain hemicelluloses nor lignin. Additionally, it exhibits higher crystallinity (around 80%), a higher degree of polymerization, and smaller diameters, therefore better mechanical properties and reinforcing capabilities. The major challenge of its industrialization, though, is the high cost of mass production.[61]

1.5. Strategies to prepare nanostructured thin films: Nano architectonics

Nanoscience and nanotechnology are terms in vogue these days, even transcending the scientific community. They are often used interchangeably, but they mean somewhat different things. Nanoscience deals with the making, imaging, and manipulating objects having at least one spatial dimension in the range of 1 – 100 nm whereas nanotechnology implies the application of nanoscience for the development of useful materials, devices, or processes. Although nanoscience has revealed various interesting phenomena, its translation into useful technological breakthroughs is not straightforward. One of the most important challenges of nanomaterials is the development of simple and efficient methods of organizing materials into precise, predetermined nanostructures. Let us consider the example of the hierarchical structuring of biological materials: the main characteristics of the building blocks, their organization at different length scales, and the link with the macroscopic functionalities and properties exhibited by many of these materials have been unveiled (and continue being investigated) thanks to advances in imaging and probing techniques with sub-micrometer resolution. Yet, the synthetic fabrication of useful functional materials bearing such complex structures is, in most cases, impossible to achieve with existing methods. The term “nanoarchitectonics”, first coined in 2000 by Masakazu Aono, has been growing popularity in the literature to refer to the technology system aimed at arranging nanoscale structural units to construct functional materials.[99]

Methods to fabricate nanostructures are normally classified according to whether they follow one of two opposite approaches: top-down or bottom-up. In the top-down approach, bulk macroscopic material is gradually carved by means of precision tools until reaching the desired size and shape. In the bottom-up approach, on the contrary, small components (molecules, colloids, etc.) combine either by physicochemical phenomena or by externally applied driving forces to build larger and more complex systems. These two approaches are schematically depicted in Figure 1.12.

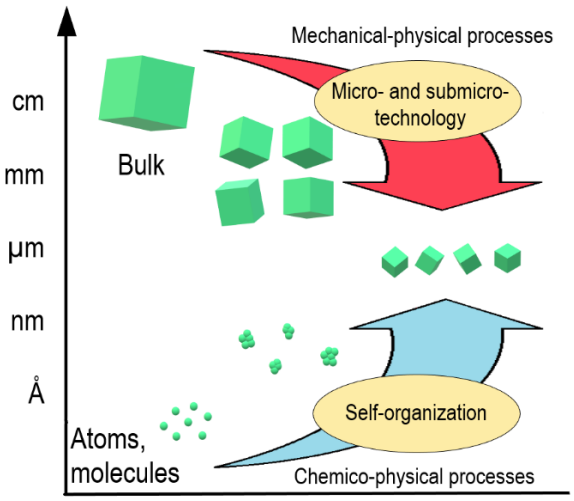

Figure 1.12: Schematic representation of the top-down vs bottom-up approaches.

1.5.1. "Top-down" strategies

The scheme shown in Figure 1.13 illustrates a list of common top-down fabrication methods and their accessible length scales compared to the size of natural and artificial objects.

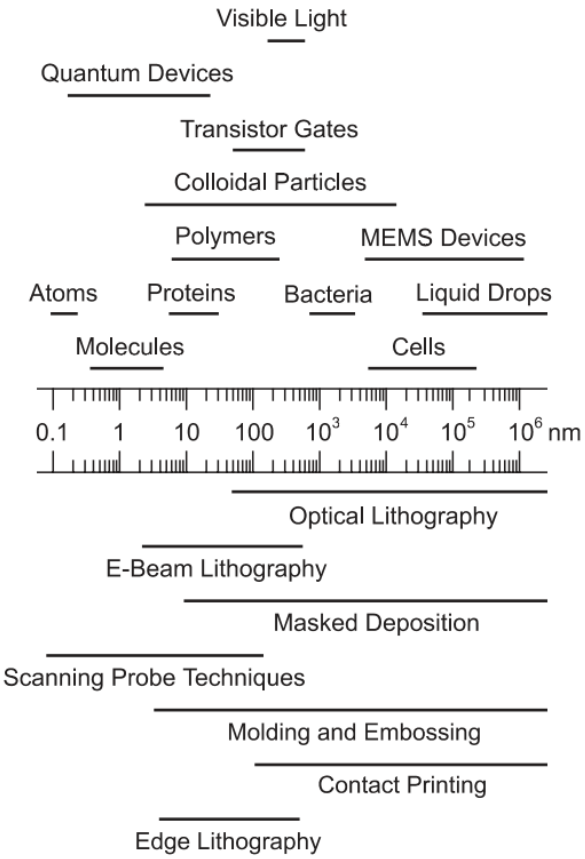

Figure 1.13: Accessible length scales by top-down methods compared to the dimension of common objects.[100]

Optical lithography is, by far, the technique most commonly used for the micro- and submicron-patterning of surfaces, owing to its universality in the manufacturing of microelectronic devices. This technique exploits various processing methods to form highly reproducible noble metal nanostructures through the application of a set of process steps such as masking, patterning, imprinting, and treatment procedures to a resist (radiation-sensitive) material and thin metal film on a flat substrate surface.[99] A simplified scheme of the process is summarized in Figure 1.14(left) for the case of using an oxidized Si wafer as the material of interest and a negative photoresist system (typically a polymer that becomes insoluble by crosslinking upon exposure to light). The oxidized Si wafer is coated with a 1-μm thick layer of the photoresist and exposed to radiation through a patterned mask. The unexposed areas are removed by a developing solution, which leaves a pattern of bare oxide on the wafer surface. In the next step, the unprotected SiO_2 layer is etched by acid solutions; the photoresist protects the oxide areas it covers. Then, the remaining photoresist is removed by a strong acid such as H_2SO_4 that does not attack the oxide or the silicon. After all these steps, the wafer with the etched window in the oxide layer is ready for further processing such as further etching of the Si with the patterned SiO_2 working now as the etch mask.[101]

Although traditional photolithographic techniques suffer from resolution limitations related to the wavelength of the used light, state-of-the-art nano-lithographic methods allow the fabrication of features with lateral dimensions in the order of 30 nm using laser light combined with sophisticated immersion optics, phase-shifting masks, and multiple exposures.[102]

Scanning beam techniques use a highly focused beam of either electrons (Electron Beam Lithography, EBL) or ions (Focused Ion Beam lithography, FIB) to scan across a thin layer of resist, which is subsequently used as a mask for etching and metal deposition to yield the desired metal nanopattern. The main advantage of these two methods is the ability to produce virtually any 1D or 2D shape with resolutions <10 nm.[99] The main disadvantage is the long time needed to pattern large areas and, therefore, the difficulty of scale-up.

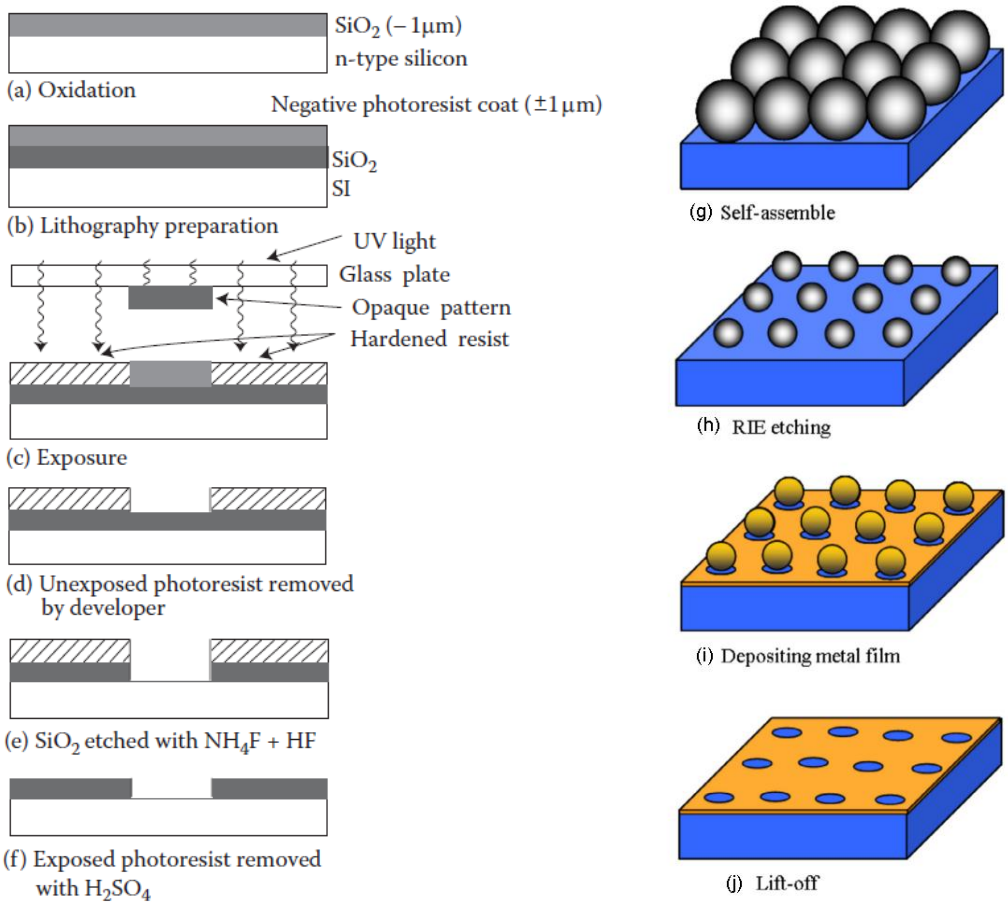

Figure 1.14: (left) Basic process steps of photolithography and pattern transfer.[101] (right) Schematic illustration of the colloidal lithography process.[103]

Non-lithographic techniques based on scanning probe methods such as Atomic Force or Scanning Tunneling Microscopes (AFM or STM, respectively) reach the maximal resolution limit of moving individual molecules and atoms[104] (Figure 1.15) but they all suffer from long processing times and thus very low throughput. An economical alternative to the scanning methods is to use colloidal particles as a mask for subsequent evaporation and/or etching processes to fabricate nanostructure arrays (colloidal lithography), however, this method is only viable for very specific patterns. For example, Li et al.[103] used colloidal polystyrene spheres self-assembly reactive ion etching (RIE), metal deposition, and lift-off processes to fabricate nanometallic holes working as color filters (Figure 1.14(right)).

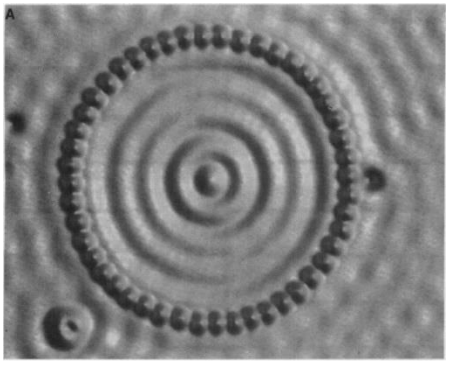

Figure 1.15: STM image of the so-called "quantum corral" formed by 48-atom Fe ring constructed on Cu(111) by individual positioning the atoms with the tip of a Scanning tunneling Microscope. The diameter of the ring is 142.6 Å.[104]

Some other top-down nanopatterning techniques are based on the replication of features from hard or soft stamps in a thermoplastic or photocurable resist by embossing or molding. This is the so-called Nanoimprint Lithography (NIL), which is capable of patterning features with lateral dimensions <10 nm on the cm^2 area scale.[105]

Most of the techniques introduced above are either very expensive and require sophisticated tools and facilities or mostly applied to planar surfaces and tolerate little variation in the materials that can be used. All these constraints limit the consideration of top-down approaches for the preparation of complex hierarchical structures.

1.5.2. "Bottom-up" strategies: self-assembly and directed assembly

Bottom-up approaches use the self-assembly and self-organization of smaller building blocks such as molecules to form the desired functional structures. Molecules may organize by different types of interactions including ionic, covalent, or hydrogen bonding, which may result in new properties of the assembly. Moreover, larger building blocks (e.g. colloids) may also self-assemble driven by capillary, van der Waals, electric or magnetic interactions, among others. Self-assembly typically employs asymmetric building blocks that are pre-programmed to organize into well-defined supramolecular assemblies. Most common are amphiphilic surfactant molecules or polymers composed of hydrophobic and hydrophilic parts.[106] The self-assembly may be also

directed by different types of templates or external stimuli, as well as it may be chemically or lithographically directed.

The most well-known self-assembly giving rise to pattern formation is the so-called self-assembled monolayers (SAMs) of amphiphilic molecules[107] which is exploited by various techniques to coat and pattern surfaces. For instance, the well-established Langmuir-Blodgett (L-B) method relies on the transfer of a SAM formed at the air-liquid interface onto a substrate that is immersed (or pulled) vertically into (or from) the liquid.[108] The repetition of this step enables the formation of multilayers. Chen et al. [109] used the L-B transfer process and substrate-mediated condensation of L-α-dipalmitoylphosphatidylcholine (DPPC) molecules to create a pattern of alternating stripes with widths of about 800 nm separated by channels of about 200 nm in width (Figure 1.16) over areas of square centimeters.

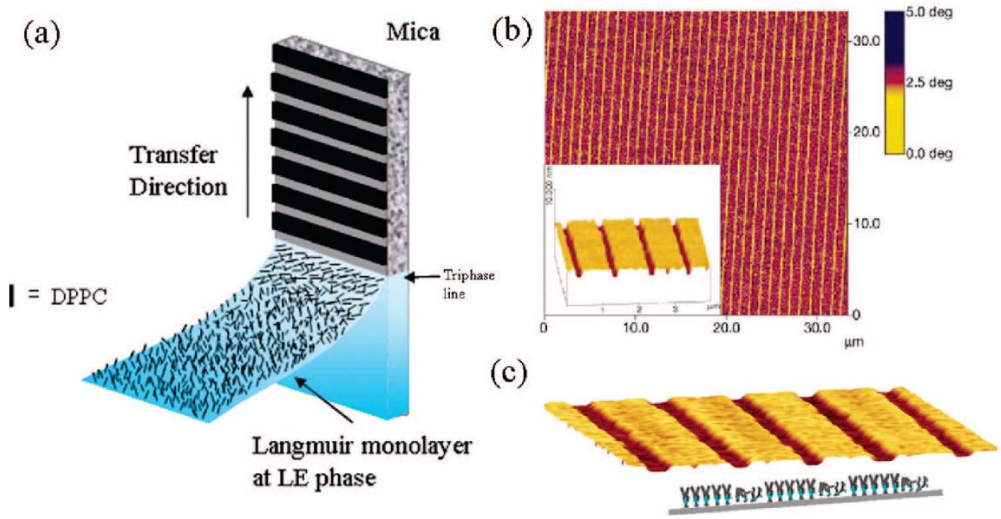

Figure 1.16: (a) Schematic representation of the meso-pattern formation by L-B transfer. (b) AFM phase image of the microchannels formed on mica (topography image in the inset). (c) Composition of the DPPC pattern: expanded molecules in the channels and condensed molecules in the stripes. [109]

Some patterning methodologies may combine "top-down" solid-state engineering physics and "bottom-up" molecular-chemistry methods to fabricate nanostructures, being microcontact printing (μCP)[110] a perfect example. This "soft-lithographic" method uses an elastomeric stamp (typically poly(dimethylsiloxane), PDMS) to transfer patterns of SAMs of long-chain thiols or silanes present in the "ink" to the substrate through conformal contact (Figure 1.17). This

remarkably simple procedure provides routes to high-quality patterns and structures with lateral dimensions of few nanometers on the cm^2 area scale.

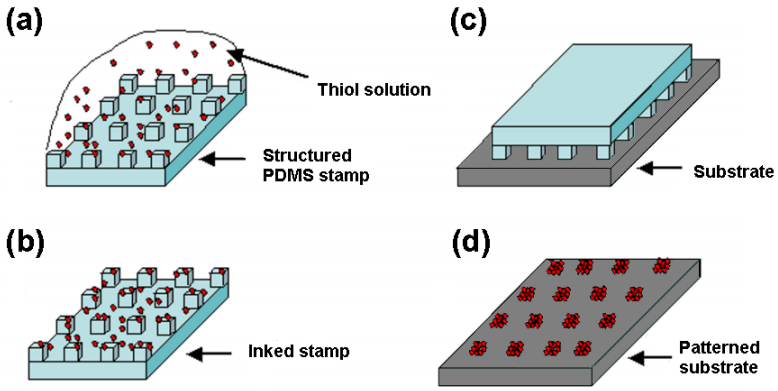

Figure 1.17: Schematic representation of the microcontact printing technology. (a) Inking of a PDMS stamp with a thiol solution for a given time. (b) The thiol self-assembles on the surface of the stamp. (c) Contact between the stamp and the substrate of interest. (d) The self-assembled thiol is transferred on the substrate along patterns corresponding to the relief structure of the PDMS stamp. Adapted from [111].

1.5.3. Layer-by-layer (LbL) deposition technique[112]

A versatile bottom-up technique that allows the preparation of multilayer thin films with a controlled organization at the nanoscale is the so-called layer-by-layer (LbL) deposition technique introduced by G. Decher.[113–115] This simple method is based on the sequential adsorption of oppositely charged materials onto a surface by electrostatic interaction, although such multilayer assembly has also been demonstrated for other types of interactions such as hydrogen bonding[116–119] and covalent bonds,[120–122] among others.[123–126]

A simplified depiction of the electrostatic LbL assembly principle is illustrated in Figure 1.18. A positively charged surface (in this example) is initially exposed to a polyanion solution by dipping the substrate into it. The polymer adsorbs onto the surface due to charge complexation ("ion-pairing") between negative charges of the polyelectrolytes and positive charges on the surface of the substrate. The flexible polymer molecule deposits forming loops of non-paired segments that create an overcompensation and reversal of the surface charge. This charge reversal limits the amount of adsorbed material to form a nanometer-thick layer. The coated substrate, now bearing

negative charges, is then dipped into a polycation solution for a similar adsorption process of the second polyelectrolyte layer. Optionally, a rinsing step in pure solvent (typically water) may be inserted between the adsorption steps to remove weakly bound molecules, as well as a drying step to "freeze" the obtained conformations. The build-up process can be iterated as many times as desired. In the absence of diffusion of the components, the film thickness grows steadily after every deposition step (linear growth).[115] In some systems, the diffusion of at least one of the components leads to its storage inside the film and thus to an increasing amount of extra charge available for ion-pairing at each deposition step. The consequence is the continuous speed up of the thickness growth that is referred to as super-linear (or exponential) growth.[127,128]

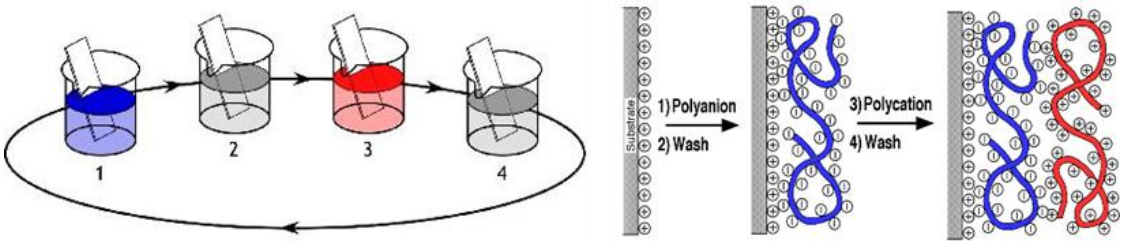

Figure 1.18: (left) Schematic of the cyclic film deposition process by alternately dipping a charged substrate into a polyanion (blue) and a polycation (red) solution, steps 2 and 4 represent washing steps. (right) Simplified depiction of the alternating deposition of the polyanion and polycation on a positively charged substrate.

The two main advantages of the LbL methodology is its simplicity and versatility. It does not require sophisticated equipment and various parameters can be varied to control the layer properties including exposure time, temperature, pH, concentration, and ionic strength of the polyelectrolyte solutions.[112] Moreover, a large number of different materials can be incorporated into different layers to bring about tuned properties of the films. The building components are not restricted to polyelectrolytes: organic and inorganic nanoparticles and crystals, biomolecules, lipids, and viruses may be used, which is of great interest for the preparation of bio-inspired composite materials. For instance, Tang et al. fabricated a nanoscale version of the brick-and-mortar structure (Figure 1.19) responsible for the high toughness observed in natural nacre by the sequential deposition of poly(diallyl dimethylammonium chloride) polycation (PDDA) and anionic montmorillonite clay (MTM).[129] This coplanar structural order of nanoplatelets and

nanosheets is a well-established application of the LbL assembly, being successfully used for the preparation of multilayered nanostructures made out of different materials such as silicates,[130] unilamellar titania crystallites,[131] clays,[132,133] among others.

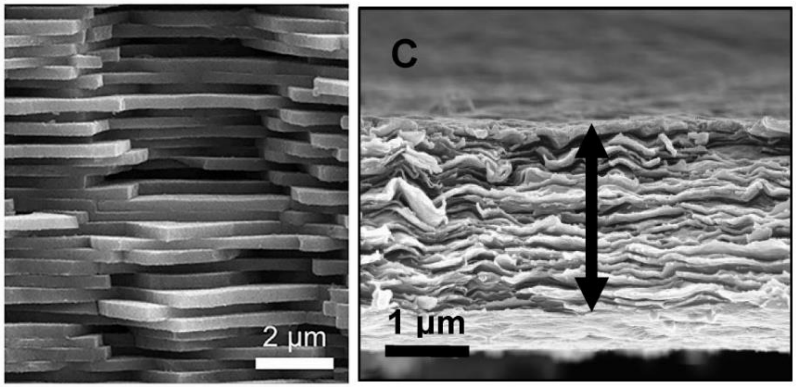

Figure 1.19: (left) Brick and mortar structure of natural nacre.[134] (right) SEM images of cross-sections for free-standing films of $(PEI/MTM)_{100}$ prepared by LbL.[135]

To speed up the LbL deposition process, spray-assisted[136,137] and spin-assisted[138,139] methods were developed, which shortened considerably the fabrication times and increased the attractiveness of the technique for scaling-up and industrialization. The adsorption process in dipping is diffusion-controlled, therefore, reaching the saturation and charge reversal of the surface during every deposition step may take tens of minutes. Conversely, both spraying and spinning methods force the interaction of the adsorbates with the surface by shear and evaporation, respectively, reducing the deposition time to only a few seconds.

The LbL assembly enjoys great acceptance in nanoarchitectonics due to its adaptability. Not only it allows the incorporation of a multitude of building blocks of various kinds, but its contour-following characteristic also enables the deposition of functional coatings on many types of surfaces independently of their shape and size. LbL multilayer coatings have been successfully reported for irregular surfaces such as fabric,[140] nanofluidic channels,[141] nanopores,[142] or nanoparticles.[143] The remarkable versatility of LbL approaches has led to the development of functional materials for a broad spectrum of applications including superhydrophobic surfaces,[144] drug delivery systems,[145,146] anti-fouling coatings,[147] chemical sensors,[148,149] among many others.

1.5.4. State-of-the-art on the fabrication of helicoidally aligned nanocellulose-based films

In the previous sections, we have seen some of the most common methods used for the preparation of 2D patterned nanostructures and coplanar nanocomposite films. Many other methods have also been suggested for controlling the assembly and in-plane alignment of anisometric nano-objects.[150,151] However, these methods are limited in their ability to fabricate more complex 3D nano-architectures, they are restricted to a small number of components, or are extremely costly. Self-assembly (and directed self-assembly) can thus be considered the most obvious route to the fabrication of such nanostructured materials since this is the approach by which complex natural microstructures are formed. A promising approach that employs self-assembly for the fabrication of helicoidally aligned nanomaterials is the so-called evaporation-induced self-assembly (EISA), first used for the production of mesoporous solids templated by the spontaneous co-assembly of surfactant-silica mesophases upon solvent removal.[106]

Revol et al.[78,152] first reported the retention of the chiral nematic organization of CNCs suspensions in solid films after evaporation-induced self-assembly, which paved the way to the increasing interest for the development of cellulose-based photonic materials. The chiral nematic mesostructure of films prepared in this way behaves as a one-dimensional photonic crystal. When half of the pitch ($P/2$) of the chiral structures of the resulting films is comparable to the wavelength of the visible light, the material exhibits structural coloration, as introduced in § 0. Moreover, the reflected light is circularly polarized with a handedness determined by the chiral sense of the structure (left-handed for CNC films).

The wavelength of the reflected color of CNC films can be tailored by manipulation of the helical pitch, which has been accomplished by variations in the ionic strength of the suspension,[153] the drying conditions,[154] as well as by the influence of magnetic[155,156] and electric fields.[157] Moreover, the handedness of the reflection of circularly polarized light on CNC films has also been effectively manipulated after the work of Fernandes et al. They impregnated chiral CNC

films with a nematic liquid crystal (4-cyano-4'-pentylbiphenyl, 5CB) that filled the micrometer gaps (or cracks) attributed to non-equilibrium states during the solvent evaporation. The resulting photonic structure consisted of an anisotropic domain, acting as a half-wave retarder, sandwiched between left-handed cholesteric layers, analogous to the morphology of the cuticle of the scarab beetle *Chrysina resplendens*. Both natural and synthetic materials reflect both RCP and LCP light according to the model shown in Figure 1.20.[158]

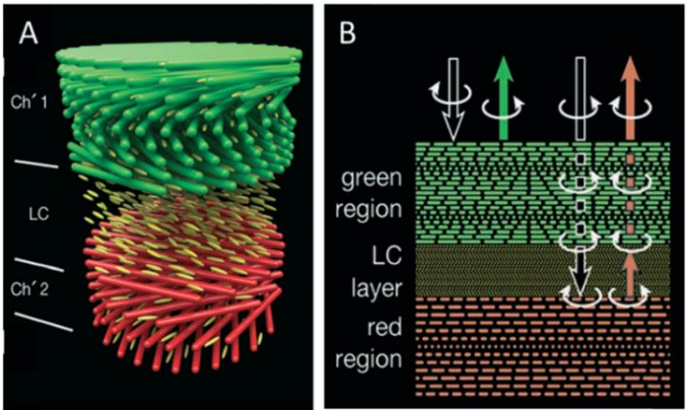

Figure 1.20: Scheme of the sandwiched structure, reflection, and transmission optical characteristics of the CNC-based film with a liquid-crystal layer acting as a λ/2 plate.[158]

Materials with promising sensing applications have also been prepared by the co-assembly of CNCs with additives during EISA. Yao et al.[159] incorporated poly(ethylene glycol) (PEG) into the CNC suspensions before solvent evaporation to obtain solid films showing uniform structural colors by changing the proportion of CNC and PEG (Figure 1.21). The films demonstrated reversible and smooth changes in their colors in response to the relative humidity between 50% and 100% owing to the reversible swelling and dehydration of the chiral nematic structure.

An important step forward toward the scaling-up of the directed self-assembly of helicoidal nanostructures for responsive photonic materials has been recently taken by the group of Vignolini. They demonstrated a large area and cost-effective roll-to-roll (R2R) method for fabricating hydroxypropyl-cellulose (HPC) stimuli-responsive photonic laminates to map pressure distributions over large areas.[160]

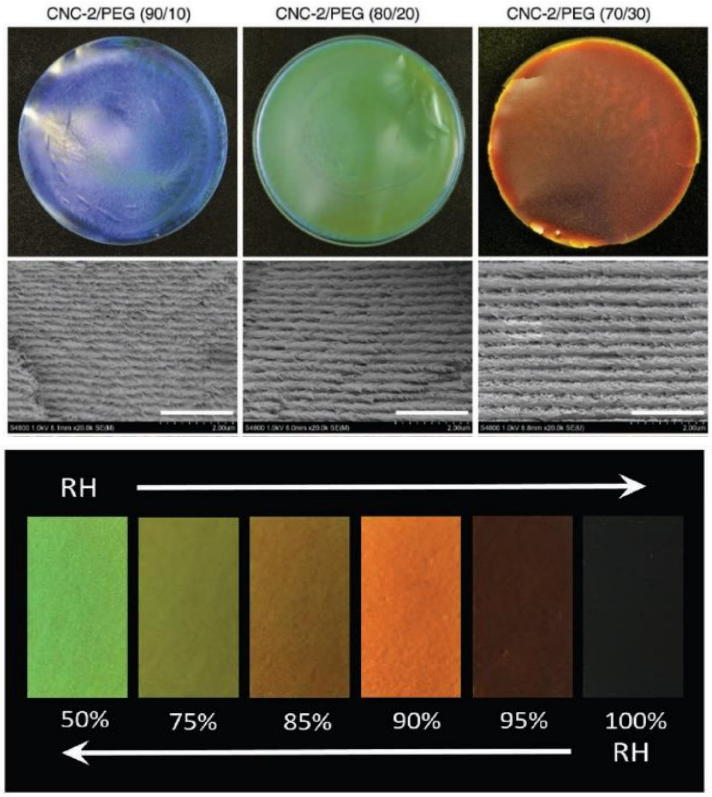

Figure 1.21: (Top) Photograph of CNC/PEG composite films showing different structural colors under white illumination (diameter of the film = 9 cm). (Center) SEM images of the cross-section of the films showing the different helical pitches (scale bar = 2 µm). (Bottom) Reversible structural color change of the CNC/PEG (80/20) film at different RH.[159]

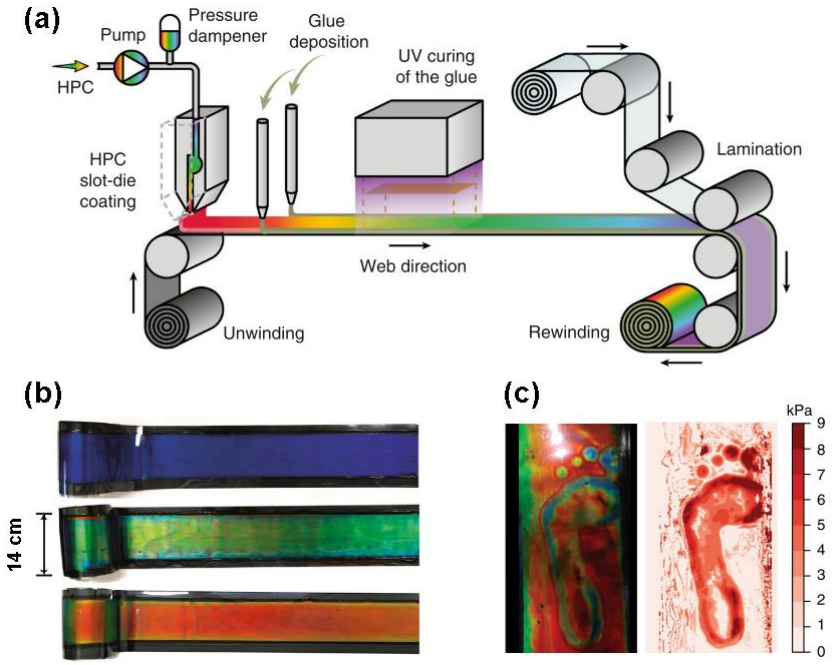

Figure 1.22: (a) Schematic of the R2R fabrication of HPC-laminated films. (b) Black PET-baked product rolls of red, green, and blue HPC laminates with HPC concentrations of 63, 66, and 70 wt%, respectively. (c-left) Footprint recorded on R2R red HPC laminate. (c-right) False-color pressure maps of the footprint.[160]

1.5.5. LbL for hierarchical nanoarchitectures

Beyond the fabrication of functional surfaces, rational LbL approaches have demonstrated great potential for the fabrication of hierarchical structures owing to the combination of spontaneous self-assembly and stepwise directed assembly. Katagiri et al. developed artificial bilayer vesicles (baptized "cerasome") with a silicate framework that were further integrated into multilayer stacks with either PDDA or oppositely charged cerasomes by an alternating layer-by-layer methodology (Figure 1.23(a)). The authors regarded such structures as tissue mimics with the potential for constructing artificial multicellular systems.[161,162] Ji et al. pre-synthesized carbon capsules with mesoporous channels in their shells, which were dispersed in water with the aid of surfactants and further LbL-assembled with either PDDA or poly(styrene sulfonate) (PSS) into multilayer thin films (Figure 1.23(b)) that exhibit excellent absorption capabilities for volatile aromatic hydrocarbons.[163]

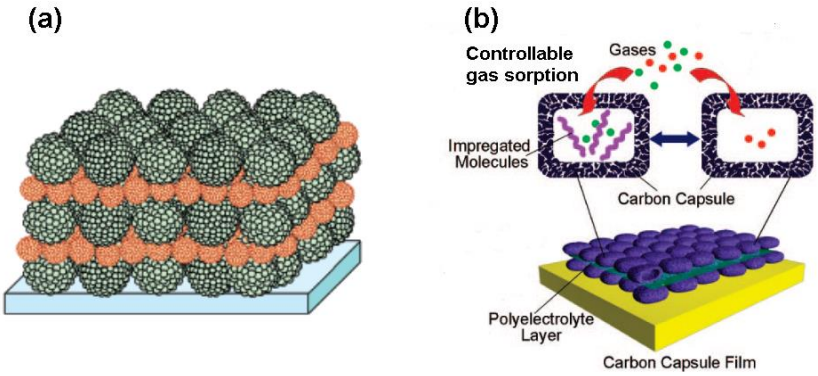

Figure 1.23: (left) Schematic drawing of a three-dimensional assembled structure of anionic and cationic Cerasomes.[162] (right) Schematic illustration of dual-pore carbon capsule film.

Coming back to nanocomposites, the stratification characteristics of LbL films can be used to improve the spatial distribution of the reinforcing phase within the polymeric matrix. For example, Mamedov et al. assembled single-wall carbon nanotubes (SWCNT) with polyelectrolytes to obtain strong films with a tensile strength approaching that of hard ceramics.[164] Although hybrid materials polymer/SWCNT are well-documented, their mechanical properties are noticeably below their highly anticipated potential because the filler is highly prone

to phase segregation. The layer-by-layer approach for nanocomposite film fabrication prevents phase segregation and allows for much higher filler loading.

The build-up of cellulose-based LbL-films with polyelectrolytes has also been extensively reported in the literature. Cranston et al.[165] first assembled polyelectrolyte multilayers (PEMs) of colloidal CNC and poly(allylamine hydrochloride) (PAH) and investigated the morphology and anisotropic optical properties of the resulting film. Wågberg et al.[87] further prepared PEMs made of carboxylated MFC and cationic polyelectrolytes: poly(ethyleneimine) (PEI), poly(diallyldimethylammonium chloride) (PDDA), and PAH. Freestanding CNF-based PEMs with improved mechanical properties have been prepared by either dip-assisted or spin-assisted LbL.[166,167]

A simple and novel modification of the spray assisted LbL with advantageous potential for nano-architected thin films was recently introduced by Blell et al.,[168] the so-called Grazing Incidence Spraying (GIS). They sprayed colloidal dispersions of cellulose nanofibrils at a grazing angle (5° – 10°) with respect to the receiving surface, which produced the effective in-plane alignment of the nanofibrils parallel to the spraying direction (Figure 1.24). Sekar et al. further oriented gold nanorods and silver nanowires of different aspect ratios but with the same surface chemistry to demonstrate that the quality of the alignment is improved the larger the nano-objects are.[169]

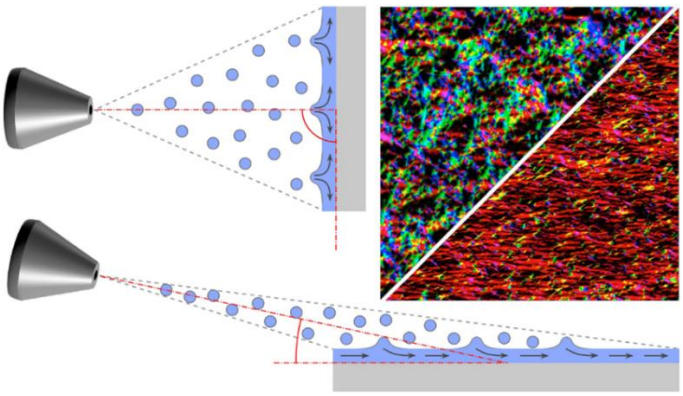

Figure 1.24: Schematic depiction of the grazing incidence spraying. When the colloidal dispersion of CNFs was sprayed in an orthogonal direction to the substrate (top image), the nanofibrils deposited without any preferential direction of alignment (multiple colors indicate multiple directions). On the contrary, when the suspension was sprayed at a small angle with respect to the substrate (bottom image), the shear forces aligned the nanofibrils in the direction of spraying, as demonstrated by the homogeneously colored nanofibrils.[168]

Finally, the combination of the grazing incidence spraying (GIS) methodology with the LbL assembly allowed the build-up of nanocomposite thin films of silver nanowires displaying highly anisotropic optical properties: multilayer films containing four layers of nanowires oriented in the same direction reached a polarization efficiency of up to 97% in the near-infrared region.[170] Furthermore, preliminary work within our research group (not yet published) showed the fabrication of thin films composed of three layers of silver nanowires in which the direction of alignment of every layer was rotated with respect to the below layer to form chiral structures exhibiting exceptional circular dichroism (several thousands of millidegrees).

1.6. Purpose of the thesis and research overview

The topics brought up into discussion in the previous sections highlight the technical relevance of finding effective ways to prepare hierarchical structures of nanofibrillar building blocks to achieve materials with the desirable properties and functionalities exhibited by natural materials. The benefits of using bio-sourced nanoparticles such as cellulose nanofibers and nanocrystals as building blocks for such materials were also emphasized.

The present research work is based on the premise that the combination of the LbL methodology with the grazing incidence spraying (GIS) of rod-like nanoparticles can be regarded as an additive manufacturing process in which the direction of alignment of the anisotropic reinforcement can be rationally designed to obtain thin-film materials possessing a complex internal structuring of the reinforcing phase. We rely on this directed assembly approach to fabricate thin films of CNF/polyelectrolyte possessing a helicoidal arrangement of the nanofibrils, inspired by the interesting damage tolerance and optical properties associated with this architecture in biological materials.

The scientific research presented in this thesis is divided into two main objectives: *(i)* to prepare multilayer CNF/polyelectrolyte films with a unidirectional and helicoidal arrangement of the reinforcing nanofibrils, and *(ii)* to investigate the resulting mechanical and optical properties of the nanostructured films. The methodology followed for the different studies and the

characterization methods employed are described in Chapter 2. In Chapter 3, the processing conditions required to obtain an independent and high-degree alignment of the CNF layers are discussed, as well as the preparation of “thick” nanostructured films by the combination of GIS and LbL. Chapter 4 describes the optical characteristics of unidirectionally and helicoidally reinforced films, as determined by transmittance measurements, circular dichroism spectroscopy, and Mueller matrix spectroscopic ellipsometry, whereas Chapter 5 discusses the mechanical behavior of the nanostructured CNF/polyelectrolyte films characterized by nanoindentation. A summary of the more relevant obtained results, concluding remarks, and suggested directions for futures research are presented at the end of this manuscript.

Chapter 2. Materials and Methods

2.1. Materials

Poly(dimethyldiallylammonium chloride) solution (PDDA, 20 wt.% in H_2O, $\overline{M_w}$ = 100,000 – 200,000 g/mol), poly(ethylene imine) solution (PEI, 50 wt.% in H_2O, $\overline{M_w}$ ~750,000 g/mol), chitosan from shrimp shells (CHI, practical grade), reference standard buffer (pH 4.00 ± 0.01, 7.00 ± 0.01, and 10.00 ± 0.01), deuterium oxide (99.9 atom % D), and glutaraldehyde solution (GA, grade II, 25% in H_2O) were purchase from Sigma-Aldrich (Lyon, France). Sodium chloride (≥ 99%, Ph.Eur.), magnesium chloride (≥ 98.5%, anhydrous), silica gel blue pearls (2 – 4 mm, with humidity indicator), and acetic acid (99%, for synthesis) were purchased from Carl Roth GmbH (Karlsruhe, Germany).

Poly(vinylamine) (PVAm, tradename LUPAMIN 9095, 20 wt.% in H_2O, $\overline{M_w}$ = 340,000 g/mol) was freely provided by BASF (Ludwigshafen, Germany). Carboxymethylated Microfibrillated Cellulose (CNF) (generation 2) was supplied as a pulp (2.26 wt.% in H_2O) by Innventia AB (Stockholm, Sweden). A CNC suspension (0.7 wt.% in H_2O) extracted from tunicates was supplied by Bruno Jean from CERMAV-CNRS (Grenoble, France). Montmorillonite (MTM) clay EXM 2039 was provided by Clariant Produkte GmbH (Moosburg, Germany) as a ground clay powder.

200 mm (100)-silicon wafers used as substrates for the construction of LbL films were purchased from WaferNet, Inc. (San Jose, CA, U.S.A.). Quartz slides (25 x 25 x 1 mm) were purchased from

Agar Scientific Ltd (Stansted, U.K.). Ultrapure water with a resistivity of 18.2 MΩcm used for the preparation of all solutions, suspensions, film samples, and experiments was obtained using a Milli-Q® Advantage A10 water purification system from Merk-Millipore (Molsheim, France).

2.1.1. Preparation of polyelectrolyte solutions

PVAm and PDDA were diluted in Milli-Q water to obtain solutions at a concentration of 1 mg/mL, PDDA was further filtered using cotton wool to remove insoluble. The pH of the PVAm solution was then adjusted using a 0.5M solution of either NaOH or HCl. PEI was dissolved in Milli-Q water under bath sonication to a final concentration of 2.5 mg/mL. CHI was first dissolved in a 1M solution of acetic acid to a concentration of 10 mg/mL by magnetic stirring overnight, it was then diluted 10 times in Milli-Q water, centrifuged at 8000 rpm for 20 minutes in a ROTINA 420R centrifuge (Hettich Zentrifugen, Germany) and filtered using cotton wool. The final concentration was determined from dry mass measurements to be 1.2 mg/mL after drying overnight a known volume of the solution in a FreeZone 4.5 Liter – 105C lyophilizer (Labconco, Kansas City, MO, USA).

2.1.2. Preparation of nanoparticle suspensions (CNF, CNC, MTM)

The gel-like CNF suspension was dispersed in Milli-Q water to a theoretical concentration of 2 mg/mL and sonicated with a sonic dismembrator model 505 (Fischer Scientific, U.S.A.) for 20 minutes at 30% amplitude. The suspension was then centrifuged for 1 hour at 9500 rpm. The resulting supernatant was first filtered on cotton wool and then with 5-µm PVDF syringe filters Millex-SV (Merck, Germany) to remove big particles. The final concentration was typically about 1.4 mg/mL as determined from dry mass measurements; it was further diluted to the required concentration.

The CNC suspension was used as received. It was further diluted to the desired concentration by sonication in an ultrasonic bath for 15 minutes. MTM clay powder was suspended at 10 mg/mL

in Milli-Q water under magnetic stirring for 3 days. The suspension was then centrifuged for 2 hours at 7500 rpm. The resulting supernatant was used without further dilution (about 4 mg/mL as determined from dry mass measurements).

2.2. Samples preparation

2.2.1. Substrate cleaning

Both the silicon wafers and the quartz slides were submerged in a 50:50 solution (v/v) of H_2O:ethanol and sonicated for 15 minutes in an ultrasound bath. After drying with compressed air, they were cleaned/activated by 3-minutes plasma treatment in a plasma cleaner PDC-002 (Harrick Plasma, U.S.A.) at high RF power (~30 W).

2.2.2. Dip-assisted LbL assembly

The plasma-activated substrate was immersed in a beaker containing the polycation solution for 10 minutes (PEI was used as the first layer in all multilayer samples throughout this work). After this step, the substrate was rinsed by immersing it 3 times into Milli-Q water for 1 minute each. The substrate was then dried with compressed air and dipped into a beaker containing the negatively charged suspension for 10 minutes with identical rinsing steps as for the previous solution. The iteration of these deposition steps was continued until reaching the desired number of layers. Thickness measurements by ellipsometry were occasionally performed after a certain number of layer pairs (in the case of films prepared on silicon wafers).

The fabrication of films with a large number of layers was generally accomplished with the help of a dipping robot made in-house consisting of a 3-axis arm and a multi-axis stepper controller from Isel France (Houdan, France), a drying station with compressed air, and a LabView program.

2.2.3. Spray-assisted LbL assembly

Conventional spray-assisted LbL was carried out using AIR-BOY spray bottles (Carl Roth GmbH, Karlsruhe, Germany). They were filled with the polyelectrolyte solutions or nanoparticle suspensions and pressurized manually. The solutions/suspensions were sprayed for 5 seconds orthogonally to the activated receiving surface, which was held vertically for the drainage of the liquid. Then, rinsing water was sprayed similarly for 10 seconds followed by drying with compressed air. PEI was always used as the first layer in all samples. The oppositely charged solution/suspension was then sprayed following the same cycle. The iteration of these deposition steps was continued until reaching the desired number of layers. Thickness measurements by ellipsometry were occasionally intercalated after a certain number of layer pairs in the case of films prepared on silicon wafers.

Grazing Incidence Spraying (GIS) was performed semi-automatically with the help of a spraying system made in-house, schematically illustrated in Figure 2.1. The colloidal suspension of cellulose nanoparticles was pumped by a liquid handling pump M50 (VICI AG, Schenkon, Switzerland) through fluorinated ethylene-propylene (FEP) microfluidic tubing until a stainless-steel air atomizing nozzle 1/4J (Spraying Systems, Glendale Heights, IL, U.S.A.), which was likewise supplied with compressed air piloted by gas flow controllers Red-y (Vögtlin Instruments GmbH, Aesch, Switzerland). The sample was kept in a vertical position on a rotating platen by means of a rubber stopper and pulling vacuum. The spraying direction was always pointing downward and the angle of the nozzle with respect to the substrate surface was kept fixed at 10°. The top border of the sample (in the spraying direction) is used as a reference to discuss relative positions within it. The *x*-*y* position of the platen, as well as its rotation around the *z*-axis, was numerically controlled by servomotors programmed in the automation software Kynon (Galaad, France). The spraying sequence was commanded by a LabView program that allows the accurate control of the spraying time and the flow rates of both the liquid and the compressed air. The polyelectrolyte solutions and the rinsing water were sprayed manually with AIR-BOY spray bottles (orthogonal spraying).

The liquid flow rate of the cellulose suspension was varied between 1 – 5 mL/min, the airflow rate, between 20 – 40 L/min, the spraying time, between 10 – 60 s, and the CNF concentration, between 0.1 – 1 mg/mL. Optimal spraying conditions to attain a high degree of alignment of the CNFs and CNCs are discussed in Chapter 3.

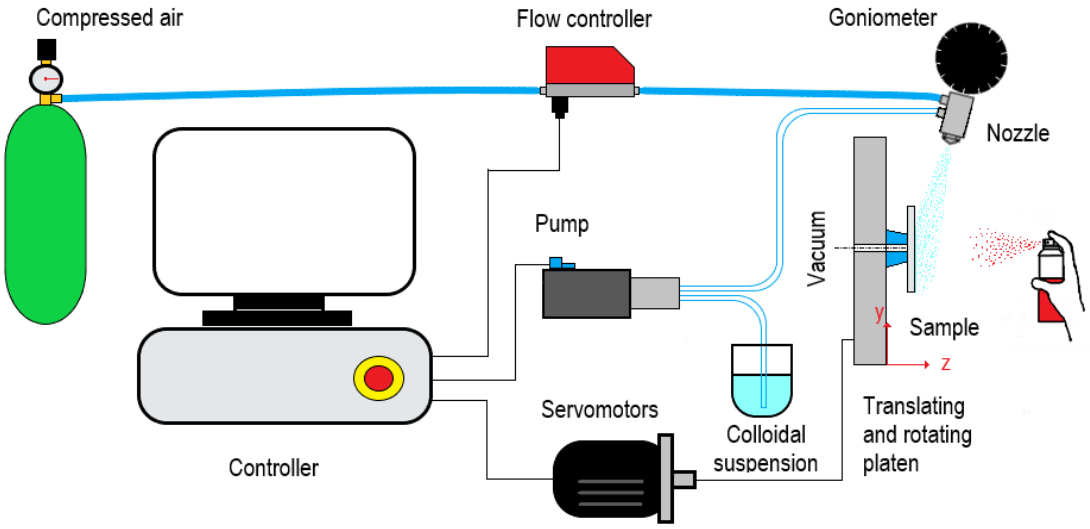

Figure 2.1: Schematic illustration of the GIS setup.

2.3. General characterization methods

2.3.1. Quartz Crystal Microbalance with Dissipation monitoring (QCM-D)[171]

The quartz crystal microbalance (QCM) is a technique that uses acoustic waves generated by the oscillation of a piezoelectric quartz crystal to measure mass with a nanogram sensitivity. A QCM sensor consisting of a single quartz crystal sandwiched between two metal electrodes is excited to a resonant condition by applying an AC voltage that induces an oscillating expansion and contraction of the crystal lattice owing to quartz's property of piezoelectricity (Figure 2.2(a)). Any mass adsorbed on the surface of the sensor produces a frequency change that is detected by the instrument and that is linearly related to the adsorbed mass by the Sauerbrey equation:[172]

$$\Delta m = \frac{C}{n}\Delta f \qquad \text{(Eq. 2.1)}$$

where *n* is the harmonic number and *C* is a coefficient of proportionality grouping the thickness of the crystal, its density, and its resonant frequency (it is approximately −17.7 Hz ng/cm^2 for a 5-MHz crystal). This linear relationship is valid as long as the depositing material adsorbs rigidly and homogeneously over the active area of the crystal. These assumptions are not generally fulfilled when depositing soft materials such as polymers because they often incorporate viscous contributions to the frequency change.

QCM with dissipation monitoring (QCM-D) allows the characterization of mass deposits with frictional dissipative losses due to their viscoelastic character. For this, the driving power is momentarily switched off which causes an amplitude decay of the oscillatory movement that depends on the properties of the oscillator and the contact medium (Figure 2.2(b) and (c)). The dimensionless dissipation parameter is defined as

$$D = \frac{E_{dissipated}}{2\pi E_{stored}} \qquad \text{(Eq. 2.2)}$$

with $E_{dissipated}$ being the energy dissipated during one oscillatory cycle and E_{stored} being the energy stored in the oscillatory system.

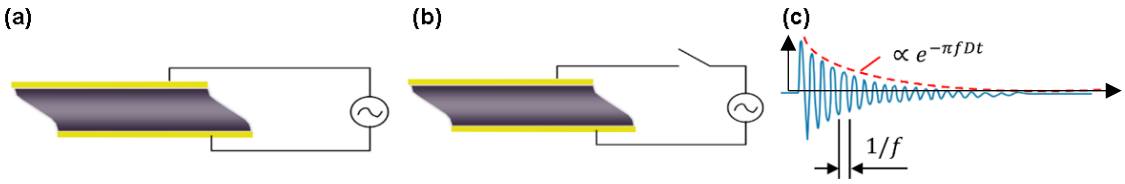

Figure 2.2: Schematic of the operation of QCM-D. (a) Quartz crystal with alternating current applied across Au electrodes. (b) Short-circuiting of the alternating current. (c) Oscillation decay as the quartz disk comes to rest (the horizontal axis corresponds to time and the vertical axis corresponds to amplitude).[171]

We monitored the growth of some LbL films on a QCM-D QSense E4 (Biolin Scientific, Gothenburg, Sweden). Quartz sensors QSX 301 coated with gold (Biolin Scientific, Gothenburg,

Sweden) were first cleaned as described in § 2.2.1, they were then introduced in the measurement cells and rinsed with Milli-Q water. The temperature of the experiment was set to 20°C and the sensors were rinsed with water sufficient time to reach a stable baseline of both frequency (*f)* and dissipation (*D)*. LbL films were assembled onto the QCM sensors by following iterative polycation/rinsing/polyanion/rinsing steps. Typically, 600 µL of the corresponding solution was injected into the QCM cell at 300 µL/min. In every deposition step, the solutions were left in contact with the sensor until both the frequency and the dissipation signals reached a plateau.

We also performed a solvent exchange experiment in which, after selected deposition steps, we replaced the H_2O in the flow cells by D_2O for about 10 minutes until both the frequency and the dissipation factor stabilized, then Milli-Q water was injected again into the cells.

2.3.2. Polarized light microscopy[173]

The polarized light microscope is designed to generate contrast in samples with optical anisotropic properties. It is equipped with a polarizer positioned before the specimen and an analyzer (a second polarizer) located after the specimen (Figure 2.3). A birefringent sample splits the incident plane-polarized light into two polarized wave components that are perpendicular to each other (called the ordinary and extraordinary wavefronts). The velocities of these components are different and vary with the propagation direction through the specimen. The light components become out of phase after traversing the sample, and they are recombined with constructive and destructive interference when they pass through the analyzer. Thus, the intensity of light transmitted through an anisotropic sample varies with the angle of in-plane rotation. Isotropic materials, on the other hand, have one unique refractive index, and light propagates through them at the same speed in every direction. Therefore, light polarized microscopy is used to distinguish between isotropic and anisotropic samples.

A Leica DM-RX microscope was used to verify the anisotropy of some of the prepared film samples. The polarizer and the analyzer were oriented perpendicular to one another. Micrographs of the samples were acquired at every 15° of in-plane rotation using an objective with 10x

magnification and a CMOS camera TrueChrome AF (Tucsen Photonics, China). Images were taken using consistently the same microscope and camera settings for all samples. The grey intensities of the different micrographs were measured using the image processing software ImageJ (National Institute of Health, U.S.A.).

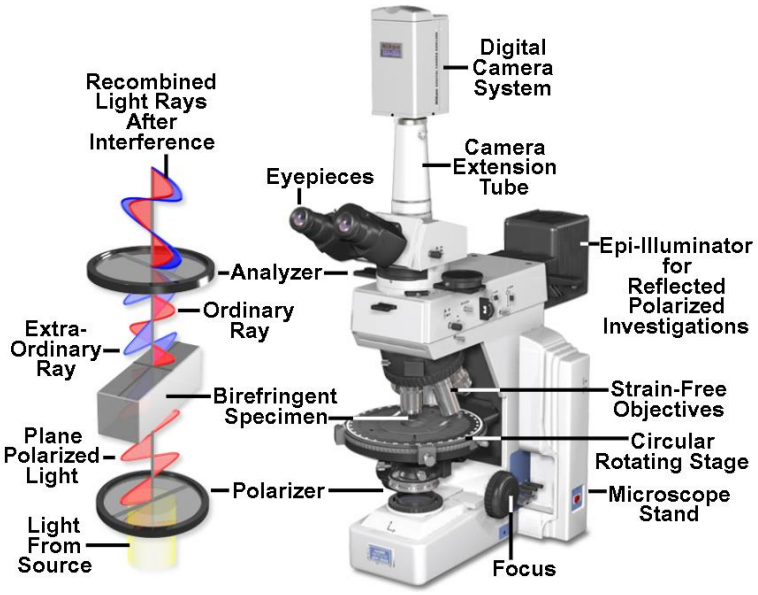

Figure 2.3: Polarized light microscope configuration.[173]

2.3.3. Atomic Force Microscopy (AFM)[174]

AFM is a very-high-resolution type of scanning probe microscope that measures the interaction force ("atomic force") between a very sharp probe located at the free end of a cantilever and the sample's surface to generate topographical images.

The force acting on two atoms separated by a certain finite distance is schematically depicted in Figure 2.4. At a long distance, attractive forces (van der Waals, electrostatic, etc.) act on the atoms whereas at short distances the wavefunctions of electrons associated with these atoms overlap, producing strong repulsive forces (Pauli's exclusion principle). The balance point between these attractive and repulsive forces determines the equilibrium atomic distance. The probe attached on

the cantilever feels a force similar to the one shown in Figure 2.4 which deflects the cantilever. If the deflection is small enough, the restoring force, *F*, obeys Hooke's law, expressed as

$$F = k(z - z_0) \qquad \text{(Eq. 2.3)}$$

where *k* is the spring constant of the cantilever and $z - z_0$ is the cantilever deflection. When the cantilever approaches the sample from far away, it bends toward it due to the attractive forces. After crossing the balance point, it bends backward as a consequence of the repulsive forces.

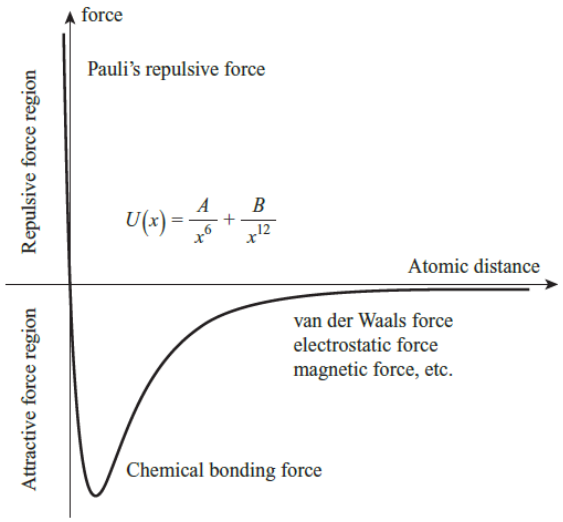

Figure 2.4: Atomic force acting between two atoms.[174]

The AFM probe traces the surface topography using the cantilever deflection as the feedback signal (contact mode). However, the damage to both surface and tip by the frictional force is inevitable and sometimes very serious. To overcome these problems, tapping mode was developed in the earlier 1990s and it has become a standard mode of commercial AFM instruments since then (Figure 2.5). In this mode, the cantilever is vibrated at a frequency near its resonant frequency. The amplitude of the oscillation decreases when the probe starts interacting with the sample's surface, tapping mode uses this amplitude signal for feedback control. In this way, the contact with the sample is limited to very short periods.

The AFM images presented in this manuscript were acquired in tapping mode on a Bruker AFM Dimension Icon (Bruker, U.S.A.) with a Nanoscope V controller. AFM cantilevers having a

nominal resonant frequency of 300 kHz, nominal spring constant of 42 N/m, and a nominal tip radius of 7 nm were used. Phase and height imaging channels were recorded simultaneously using a scan rate of 1.0 Hz with a resolution of 512 x 512 pixels. The images were analyzed with the software NanoScope Analysis v.1.9 (Bruker, U.S.A).

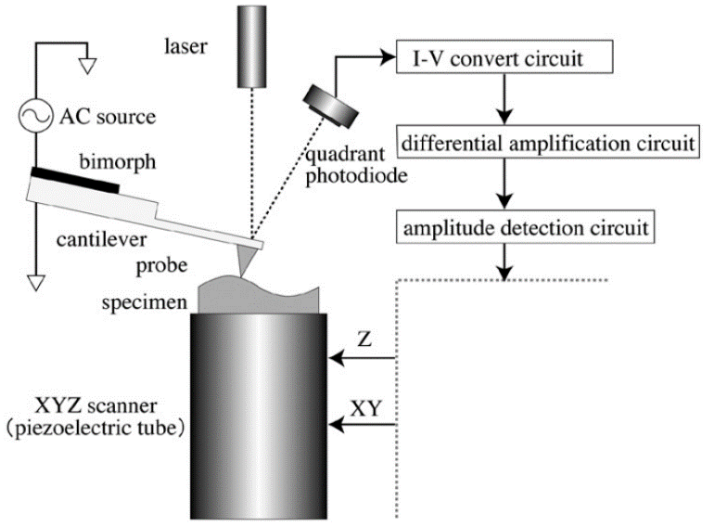

Figure 2.5: Schematic representation of the AFM tapping mode.[174]

For the morphological characterization of CNFs and CNCs, 100 µL of the highly diluted colloidal suspensions were deposited on PDDA-coated silicon wafers for 2 minutes, washed with water, and allowed to air-dry. We used PDDA instead of PEI as the anchoring layer to the substrate because it showed a smoother surface and thus improved the accuracy of the height measurements on the AFM images.

2.3.4. Orientation Analysis

The alignment of the CNFs and CNCs was determined by the analysis of the AFM images obtained either on monolayers or in thicker multilayers with cellulose as the top layer. The distribution of the angle θ between the nanofibrils (or nanocrystals) principal axis and the spraying direction was extracted from the AFM pictures using the directional image analysis plug-in OrientationJ[175] (Biomedical Imaging Group, EPFL, Switzerland) developed for ImageJ. This method is based on the analysis of the local structure tensor in the local neighborhood of each

pixel of the image. As a result, the angle of orientation of every pixel is calculated and represented by the software as a given color. A complete description of the principle of operation of the plug-in can be found elsewhere.[175] A 2D nematic order parameter (S_{2D}) was calculated from the distribution of the angles of orientation as:

$$S_{2D} = \langle 2cos^2\theta - 1 \rangle \quad \text{(Eq. 2.4)}$$

where the chevrons denote the weighted average over the distribution of θ. S_{2D} can take values between 0 and 1, the limits corresponding to a random distribution (isotropic film), and to perfectly parallel alignment of all nanoparticles (unidirectional film), respectively.

The raw AFM images were flattened to center the data and remove tilt and bow before analyzing them with OrientationJ. To properly perform the analysis, a window size (number of pixels) that properly represented the diameter of the nanofibrils was selected. The S_{2D} parameter was sensitive to this value. Therefore, the selected value was kept constant for all images of the same size. For instance, most AFM images of CNF were 2 x 2 μm^2; in this case, a window of 2 pixels with a Gaussian gradient was used for all the pictures. The angle distribution was non-weighted (i.e., 1 pixel = 1 count), but the pixels with a value of coherency or energy below 10% were not included in the calculation as these pixels are often artifacts.[175] Whenever the substrate was detected underneath the deposited layers, a surface coverage was determined after thresholding the greyscale images in ImageJ.

2.3.5. Scanning Electron Microscopy (SEM)

Scanning Electron Microscopy enables the observation of very small surface structures by scanning the sample with a focused electron beam. From the spot illuminated by the electron beam, various signals are emitted such as secondary electrons, backscatter electrons, or characteristic X-rays (Figure 2.6). SEM forms an image of the sample by detecting the electrons reflected or generated from the surface of the specimen.

Most SEM images are generated by detecting secondary electrons. As the intensity of the generated secondary electrons varies with the angle of incidence of the incident electrons, subtle variations in the roughness of the surface can be detected according to the signal intensity. SEM resolution can be as high as 0.5 – 4 nm.

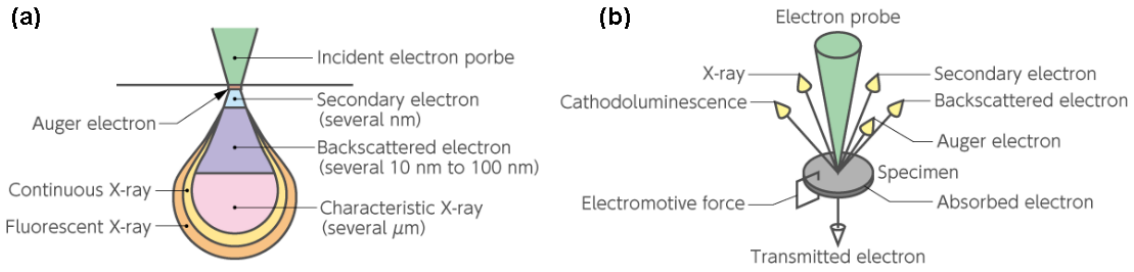

Figure 2.6: (a) Depth of quantum emission and spatial resolution probed by SEM. (b) Information obtained from the specimen.[176]

To image the cross-section of thin multilayer films, the supported sample was first crosslinked by dipping it into a glutaraldehyde (GA) solution (5% in H_2O) for two hours. After this time, it was rinsed in Milli-Q water for 5 minutes. Then, the film was subjected to dehydration in sequential EtOH/water solutions with increasing concentrations of ethanol (25%, 50%, 75%, and 100%) for 10 minutes each. Immediately after, the film was carefully fractured inside liquid N_2 and dipped once more in the GA solution to crosslink the exposed cross-section. This procedure was adopted to try to obtain a brittle fracture of the film without distortion of the internal structure. The sample was glued vertically to a cross-section holder using conductive carbon cement Leit-C (Agar Scientific, U.K.) and imaged with a Field Emission Gun Scanning Electron Microscope (FEG-SEM) SU8010 (Hitachi, Japan) with secondary electron detector, at an accelerating voltage of 1 kV.

2.4. Optical characterization methods

2.4.1. Principles of optics[177]

In this section, we briefly introduce the basic principles of optics required to understand the optical characterization methods employed in this work.

2.4.1.1. Propagation of light

As it is well-known, light has electromagnetic properties, i.e. synchronized oscillations of an electric field, *E*, and magnetic field, *B*, that are perpendicular to each other. The direction of light propagation is perpendicular to both *E* and *B* (Figure 2.7). When light passes from one medium to another it may change its direction at the interface. This phenomenon, called refraction, is determined by the refractive index *n* defined by

$$n \equiv c/s \qquad \text{(Eq. 2.5)}$$

where *s* represents the speed of light in the medium and *c*, the speed of light in a vacuum (c = 2.99792 x 10^8 m/s). Accordingly, the propagation of light waves becomes slower in a medium with high *n*.

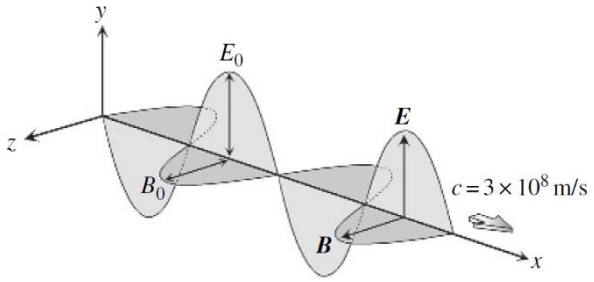

Figure 2.7: Propagation of an electromagnetic wave. *E* and *B* denote the electric field and magnetic induction, respectively, *c* is the speed of light waves.[177]

The refractive index alone does not consider the effect of light absorption exhibited by some media. Light absorption has no effect on wavelengths (λ), but it decreases the amplitude of the

electromagnetic wave along the *x*-direction with exp($-2\pi kx/\lambda$). Thus, the propagation of light through media is better described by a complex refractive index *N* that includes a second material property: the extinction coefficient, *k*. This complex refractive index is in turn related to the magnitude of the polarization generated by the propagation of light within a dielectric material, expressed by the dielectric constant, ε (also referred to as permittivity). Then:

$$N \equiv n - ik \equiv \sqrt{\varepsilon} \qquad \text{(Eq. 2.6)}$$

If there is no light absorption, $\varepsilon = n^2$.

In optical measurements, light intensity in media is characterized by Beer's law:

$$I = n|E|^2 = I_0 \exp(-\alpha d) \qquad \text{(Eq. 2.7)}$$

where α is the absorption coefficient ($\alpha = 4\pi k/\lambda$) of the medium and *d* is the distance from the surface.

2.4.1.2. Reflection and transmission of light

The reflection and transmission of light are determined by the complex refractive indices of media. Figure 2.8(a) illustrates light propagation at oblique incidence at the interface between two media with different refractive indices (the phase of the electric field is indicated by lines). During the time *t* in which the incident wave travels from point B to D, the transmitted wave advances from point A to E, and the reflected wave, from A to C. From Figure 2.8(a), it is clear that:

$$\frac{\sin\theta_i}{\overline{BD}} = \frac{\sin\theta_t}{\overline{AE}} = \frac{\sin\theta_r}{\overline{AC}} = \frac{1}{\overline{AD}} \qquad \text{(Eq. 2.8)}$$

where θ_i, θ_t and θ_r are the angles of incidence, transmission, and reflection, respectively. From Eq. 2.5, light advances ct/n during the time *t*. Therefore $\overline{BD} = ct/n_i$; $\overline{AE} = ct/n_t$; $\overline{AC} = ct/n_r$, where n_i, n_t, and n_r are the refractive indices for the incident, transmitted, and reflected

light, respectively. Given that $n_i = n_r$, we notice that $\overline{BD} = \overline{AC}$, thus we obtain the law of reflection that states that the angle of reflection is equal to the angle of incidence. From Eq. 2.8, the well-known Snell's law that describes the relationship between the angles of incidence and refraction is also derived:

$$n_i sin\theta_i = n_t sin\theta_t \qquad \text{(Eq. 2.9)}$$

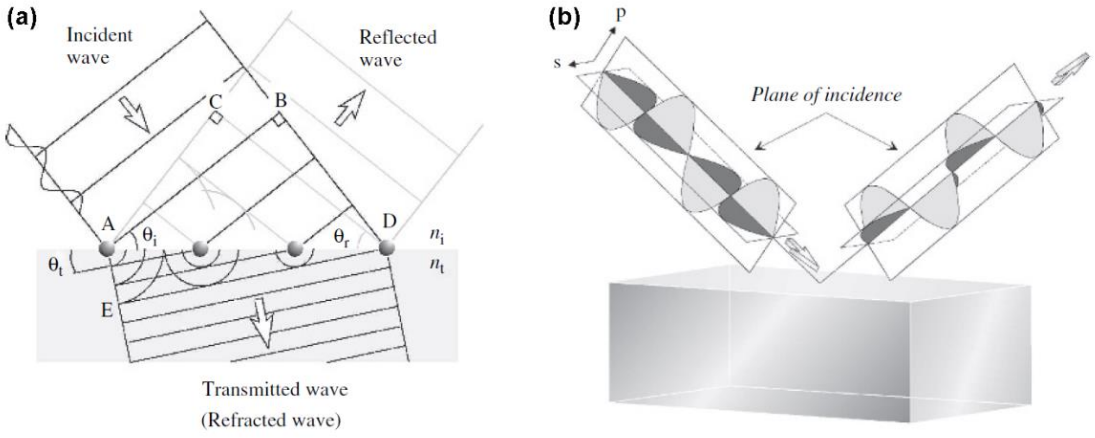

Figure 2.8: (a) Light reflection and transmission at oblique incidence when $n_i < n_t$. (b) Reflection of p- and s-polarized light waves.[177]

Light reflected or transmitted by samples at oblique incidence is classified into p- and s-polarized light waves depending on the oscillatory direction of its electric field. In p-polarization, the electric field of the incident and the reflected light waves oscillate within the same plane (the plane of incidence). In s-polarization, the electric field of the incident and the reflected light waves oscillate in a plane perpendicular to the plane of incidence. Figure 2.9 shows the reflection and transmission of p- and s-polarized waves.

The amplitude reflection and transmission coefficients for p- and s-polarized light are defined by the Fresnel equations:

$$r_p \equiv \frac{E_{rp}}{E_{ip}} = \frac{n_t \cos\theta_i - n_i \cos\theta_t}{n_t \cos\theta_i + n_i \cos\theta_t} = |r_p| \exp\,(i\delta_{rp}) \qquad \text{(Eq. 2.10)}$$

$$r_s \equiv \frac{E_{rs}}{E_{is}} = \frac{n_i \cos\theta_i - n_t \cos\theta_t}{n_i \cos\theta_i + n_t \cos\theta_t} = |r_s|\exp\,(i\delta_{rs}) \qquad \text{(Eq. 2.11)}$$

$$t_p \equiv \frac{E_{tp}}{E_{ip}} = \frac{2n_i \cos\theta_i}{n_t \cos\theta_i + n_i \cos\theta_t} = |t_p|\exp\,(i\delta_{tp}) \qquad \text{(Eq. 2.12)}$$

$$t_s \equiv \frac{E_{ts}}{E_{is}} = \frac{2n_i \cos\theta_i}{n_i \cos\theta_i + n_t \cos\theta_t} = |t_s|\exp\,(i\delta_{ts}) \qquad \text{(Eq. 2.13)}$$

where $|r_p|, |t_p|, \delta_{rp}, \delta_{tp}$,$|r_s|, |t_s|$ and δ_{rs}, δ_{ts} represent the change in the amplitude and phase of p- and s-polarized light upon reflection and transmission, respectively.

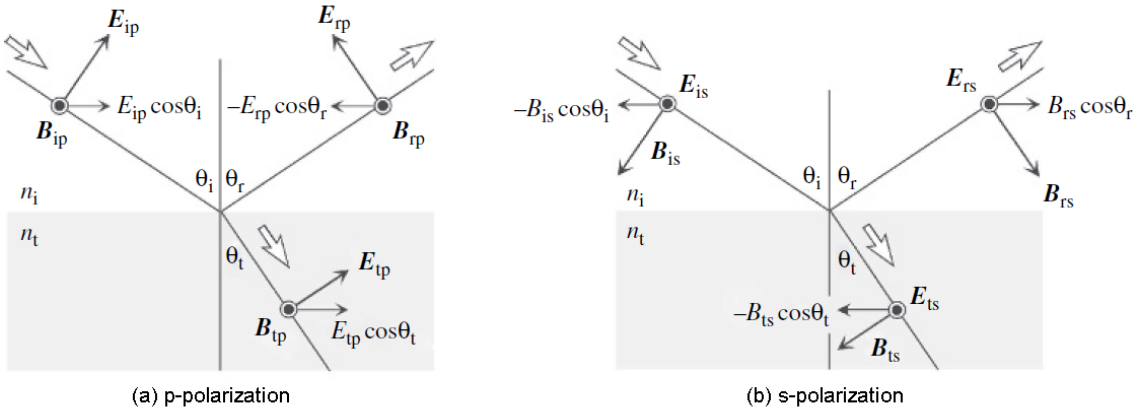

Figure 2.9: Electric field *E* and magnetic induction *B* for (a) p-polarization and (b) s-polarization. In these figures, *B* in (a) and *E* in (b) are perpendicular to the plane of the paper and are pointing to the reader. The subscript ip, rp, and tp represent the incidence, reflection and transmission of p-polarized light, respectively. The subscript is, rs, ts represent the incidence, reflection, and transmission of s-polarized light, respectively.[177]

2.4.1.3. Polarization of light

Polarized light refers to light waves in which the electric fields are oriented at specific directions. The polarization state of light traveling along the *z*-axis, for example, is described by the superimposition of two electric fields whose directions are parallel to the *x* and *y* axes. The vector sum of the electric fields E_x and E_y gives the resulting electromagnetic wave. Different polarization states result from the phase difference $\delta_y - \delta_x$ between the two orthogonal electric

fields as shown in Figure 2.10. When there is no phase difference ($\delta_y - \delta_x = 0$), the light is linearly polarized with a resulting vector ($E_x + E_y$) at 45° in the x – y plane (Figure 2.10(a)). However, the amplitude of the resulting vector is $\sqrt{2}$ times larger than either E_{x0} or E_{y0}. When the phase difference between E_x and E_y is 90° ($\delta_y - \delta_x = \pi/2$), the resulting vector rotates in the x – y plane as the light propagates, which is referred to as circular polarization (Figure 2.10(b)). A clockwise rotation (from the point of view of the observer) of the resulting vector is called right-handed circular polarization (R-CPL) whereas an anticlockwise is called left-handed circular polarization (L-CPL). For any intermediate value of the phase difference ($0 < \delta_y - \delta_x < \pi/2$), the resulting light is elliptically polarized (Figure 2.10(c)).

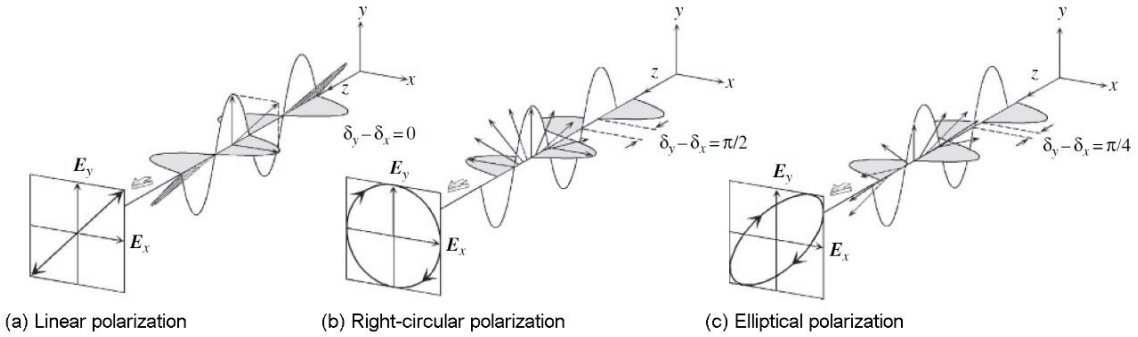

Figure 2.10: Representations of (a) linear polarization, (b) right-circular polarization and (c) elliptical polarization. Phase differences between the electric fields parallel to the *x* and *y* axes ($\delta_y - \delta_x$) are (a) 0, (b) $\pi/2$, and (c) $\pi/4$.

The states of polarization of light can be visualized with the polarization ellipse represented in Figure 2.11, which traces the path of the electric field of polarized light in a fixed *xy*-plane (when light propagates along the *z*-direction). The two parameters needed to describe light polarization are, thus, the azimuth angle θ between the major axis and the *x*-axis, and the ratio between the length of the minor axis *b* and the major axis *a* (ellipticity, $e = b/a$). When $e = 0$, light is linearly polarized, whereas $e = \pm 1$ implies right- and left-handed circularly polarized light respectively. The ellipticity angle is defined as $\varepsilon = \arctan e$.

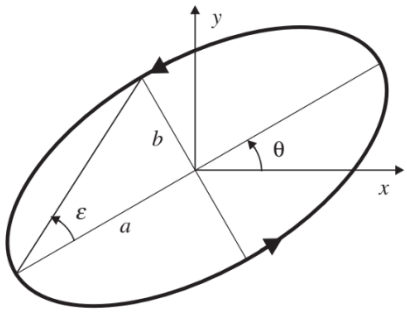

Figure 2.11: The polarization ellipse for visualization of the state of polarization of light.[178]

2.4.1.4. Stokes – Mueller formalism

In the Stokes – Mueller formalism, the polarization states of light beams are represented by Stokes vectors (*S*) and the sample is characterized by a 4 x 4 Mueller matrix *M*. The Stokes vector is defined by four components described in terms of the irradiance (optical power per unit area):

$$S = \begin{bmatrix} I \\ Q \\ U \\ V \end{bmatrix} = \begin{bmatrix} I_x + I_y \\ I_x - I_y \\ I_{+45^\circ} + I_{-45^\circ} \\ I_R - I_L \end{bmatrix} \quad \text{(Eq. 2.14)}$$

Here, I_x and I_y denote irradiance of linear polarization in the *x* and *y* directions, respectively, I_{+45° and I_{-45° denote irradiance of linear polarization in the $+45^\circ$ and -45° directions, respectively and I_R and I_L denote irradiance of right- and left-handed circular polarization, respectively.

The Mueller matrix M = $\{M_{ij}\}$ with real-valued elements transforms an incident Stokes vector (S_i) into the exiting (reflected, transmitted, or scattered) Stokes vector S_0, according to

$$S_0 = MS_i \quad \text{(Eq. 2.15)}$$

or explicitly:

$$\begin{bmatrix} I_0 \\ Q_0 \\ U_0 \\ V_0 \end{bmatrix} = \begin{bmatrix} m_{11} & m_{12} & m_{13} & m_{14} \\ m_{21} & m_{22} & m_{23} & m_{24} \\ m_{31} & m_{32} & m_{33} & m_{34} \\ m_{41} & m_{42} & m_{43} & m_{44} \end{bmatrix} \begin{bmatrix} I_i \\ Q_i \\ U_i \\ V_i \end{bmatrix} \quad \text{(Eq. 2.16)}$$

This matrix representation allows the mathematical description of optical measurements. That is, variations in the polarization of light after interaction with the sample can be expressed by applying matrix calculus, even when there are many optical elements in a measurement.

In most cases, we are concerned only about polarization and depolarization properties of the analyzed sample and not about the absolute values of transmission or reflectance. Therefore, it is customary to normalize the Mueller matrix to the first element ($m_{11} = 1$) and the Stokes vector of the incident light to the first parameter ($I_i = 1$).

After interaction with the sample, the light beam will generally emerge partially polarized with a degree of polarization given by

$$P = \frac{\sqrt{Q^2 + U^2 + V^2}}{I} \qquad \text{(Eq. 2.17)}$$

Moreover, the polarized component of the emerging beam will be, generally, elliptically polarized with ellipticity and azimuth angle given by:

$$e = \tan\left(\frac{1}{2} arcsin \frac{V}{\sqrt{Q^2 + U^2 + V^2}}\right) \qquad \text{(Eq. 2.18)}$$

$$\theta = \frac{1}{2} arctan \frac{U}{Q} \qquad \text{(Eq. 2.19)}$$

2.4.2. Spectroscopic ellipsometry[177]

Ellipsometry is an optical characterization technique that measures the change in the polarization of light upon reflection (or transmission) on (or through) a sample. This allows the characterization of the optical constants (n, k) and thickness of thin films with very high sensitivity (~0.1Å). Additionally, it is a fast and non-destructive technique. However, it is an indirect characterization method that requires the definition of an optical model.

Upon reflection on a sample, p- and s-polarizations of light show different changes in amplitude and phase. This makes that incident linear polarized light becomes elliptically polarized after being reflected (Figure 2.12). The same applies to transmission. Ellipsometry measures the complex reflectance ratio ρ, which is the ratio of the amplitude reflection coefficients for p- and s-polarizations (Fresnel Eq. 2.10 and Eq. 2.11, respectively):

$$\rho \equiv \frac{r_p}{r_s} \equiv \frac{\left(E_{rp}/E_{ip}\right)}{\left(E_{rs}/E_{is}\right)} \equiv \tan\psi \exp(i\Delta) \qquad \text{(Eq. 2.20)}$$

where $\tan\psi = |r_p|/|r_s|$ is the amplitude ratio and $\Delta = \delta_p - \delta_s$ is the phase shift upon reflection. Spectroscopic ellipsometry measures these two values (ψ , Δ) as a function of the wavelength of light. In order to evaluate the optical constants and thickness of samples from spectroscopic ellipsometry, it is necessary to construct an optical model to fit the theoretical dielectric function to the measured (ψ , Δ) spectra.

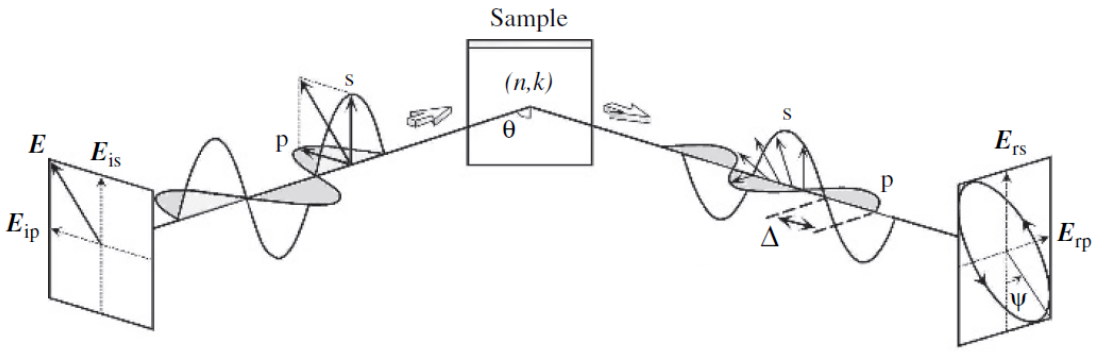

Figure 2.12: Measurement principle of ellipsometry.[177]

Throughout this thesis, the film thickness of samples deposited on silicon wafers was measured on a spectroscopic ellipsometer SENpro (SENTECH Instruments GmbH, Germany) and its built-in software SENpro v.1.2.4. The (ψ , Δ) spectra were obtained in the spectral range between 400 – 800 nm using an incident angle of 70°. The optical model used to fit the (ψ , Δ) spectra was composed of three layers, as depicted in Figure 2.13. The deposited film was approximated to an effective medium with homogeneous refractive index n = 1.559, as previously done by others in our group for CNF-based multilayer films.[167] Cross-sectional SEM and step measurements on

AFM images of thick films allowed us to verify the good agreement of the thickness values determined by ellipsometry using this refractive index. The thickness of the thin SiO_2 layer of the silicon wafer was measured prior to the deposition of the film, right after plasma treatment. All the values of the film thicknesses reported throughout this manuscript represent the average and associated standard deviation of at least five measurements recorded at different spots on the sample.

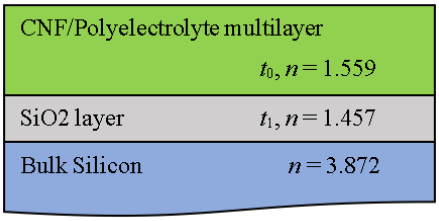

Figure 2.13: Optical model used for thickness measurements by ellipsometry.

2.4.3. Ultraviolet-visible-near infrared (UV-Vis-NIR) spectroscopy[179]

The UV-Vis-NIR spectroscopy is a technique used to characterize the absorbance or transmission of light by solutions and transparent solid samples. Quantitative absorption spectroscopy allows determining the concentration of the analyte in a given sample. The determination is based on the measurement of the intensity (I) of light transmitted from a reference beam (I_0) as it passes through the sample. The absorbance, A, and the transmittance, T, are defined as:

$$A = -\log_{10}\left(\frac{I}{I_0}\right) \quad \text{(Eq. 2.21)}$$

$$\%T = \left(\frac{I}{I_0}\right) \times 100 \quad \text{(Eq. 2.22)}$$

We relied on this non-destructive technique to measure the transparency of the CNF/polyelectrolyte films, reported as the $\%T$. For this, we prepared the desired films on quartz slides. The transmittance spectra were recorded on a Cary 5000 UV-Vis-NIR spectrometer (Agilent Technologies, Inc., U.S.A.) in the spectral range between 200 – 800 nm.

2.4.4. Circular Dichroism (CD) spectroscopy

CD spectroscopy is a form of light absorption spectroscopy that measures the difference in absorbance of left- and right-handed circularly polarized light (L-CPL and R-CPL, respectively) rather than non-polarized light as in UV-Vis-NIR spectroscopy. An optically active chiral compound absorbs preferentially one of the directions of circularly polarized light (CPL) over the other. The difference in absorbance is defined as

$$\Delta A = A_{LCPL} - A_{RCPL} \qquad \text{(Eq. 2.23)}$$

where A_{LCPL} and A_{RCPL} correspond respectively to the absorbance of L-CPL and R-CPL. Although ΔA is usually measured, CD data is commonly reported in degrees of ellipticity, *e* (see Figure 2.11):[180]

$$e = \tan(\varepsilon) = \frac{b}{a} \equiv \frac{E_R - E_L}{E_R + E_L} = \frac{\left(I_R^{1/2} - I_L^{1/2}\right)}{\left(I_R^{1/2} + I_L^{1/2}\right)} \qquad \text{(Eq. 2.24)}$$

where E_R, I_R, E_L, I_L are the magnitudes of the electric field vectors and irradiance of the R-CPL and L-CPL, respectively. Generally, the circular dichroism effect is small and $\tan(\varepsilon)$ can be approximated to ε in radians. Moreover, *I* can be substituted by Beer's law (Eq. 2.21) in natural logarithm to finally inter-convert between ε and ΔA:

$$\varepsilon(rad) \approx \tan(\varepsilon) = \frac{e^{\Delta A \frac{\ln 10}{2}} - 1}{e^{\Delta A \frac{\ln 10}{2}} + 1} \qquad \text{(Eq. 2.25)}$$

$$\varepsilon(deg) \approx \Delta\mathrm{A}\left(\frac{\ln 10}{4}\right)\left(\frac{180}{\pi}\right) = 3298.2\ \Delta A \qquad \text{(Eq. 2.26)}$$

Circular dichroism spectra of film samples prepared on quartz slides were recorded on a Jasco J1700 CD spectrometer (JASCO, Tokyo, Japan) in the spectral range between 190 – 800 nm at a scan rate of 100 nm/min.

2.4.5. Mueller matrix ellipsometry

The Mueller matrix of selected film samples fabricated on quartz slides was obtained by Yann Battie at the University of Lorraine on a spectroscopic ellipsometer UVISEL (HORIBA, Japan) in the spectral range 270 – 800 nm (limits of the equipment). This ellipsometer only allows determining the first three columns of the Mueller matrix, the last column can be obtained by symmetry provided that the depolarization of the sample is negligible. This was verified by a second ellipsometer (dual rotating retarder ellipsometer in the spectral range 400 – 800 nm).

2.5. Mechanical characterization by nanoindentation

2.5.1. Principles of nanoindentation[181,182]

Also called Instrumented Indentation Technique (IIT), nanoindentation is a characterization method for measuring the mechanical properties of materials. It is particularly well suited for determining the elastic (Young's) modulus (E) and hardness (H) of small volumes of materials such as thin films. In nanoindentation, a hard tip called indenter, typically made of diamond, is pressed into contact with the test material surface while the force and penetration values are continuously recorded. Common geometries of the indenter are illustrated in Figure 2.14.

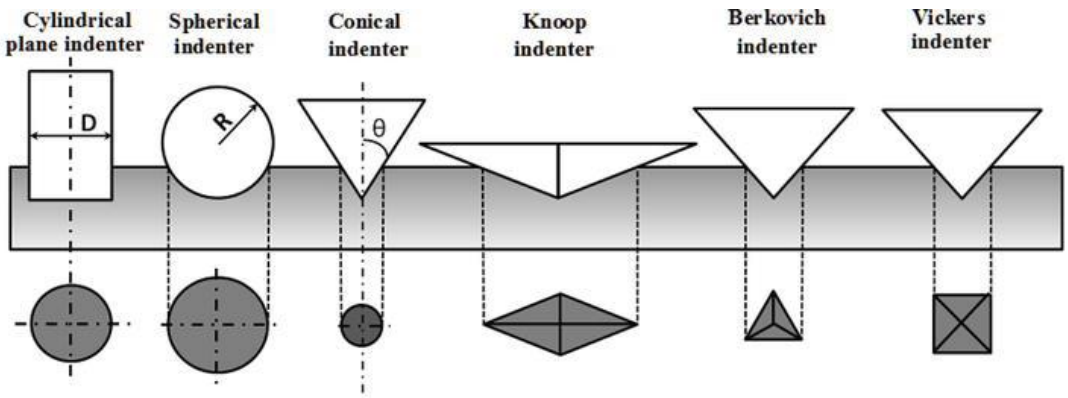

Figure 2.14: Schema of the different types of indenter geometries.[183]

In a typical nanoindentation experiment, the load is applied from zero to a set value and then back to zero. If plastic deformation occurs, a residual impression is left on the surface of the specimen. The size of this residual imprint is usually too small to be measured accurately with optical techniques, however, the knowledge of the penetration depth and the geometry of the indenter provides an indirect method to determine the projected area of contact under load, from which the mechanical properties can be estimated. A characteristic compliance curve (force-displacement) obtained by nanoindentation is shown in Figure 2.15. The depth of contact h_c and the slope of the elastic unloading dP/dh allow the calculation of the specimen modulus and hardness. h_r is the depth of the residual impression, and h_e is the displacement associated with the elastic recovery during unloading.

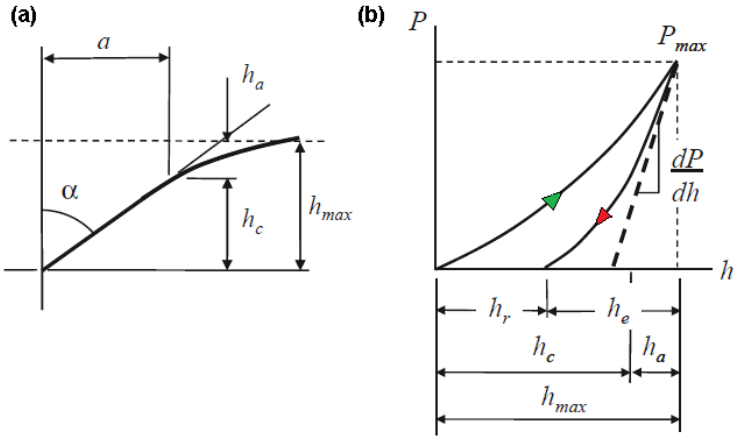

Figure 2.15: (a) Geometry of contact with a conical indenter. (b) Typical compliance curves of loading (green arrow) and unloading (red arrow) from a nanoindentation experiment with maximum load P_{max} and maximum depth beneath the sample surface h_{max}. dP/dh is the slope of the elastic unloading, a is the contact radius, h_c is the depth of the contact circle, h_r is the depth of the residual impression, h_e is the displacement associated with the elastic recovery during unloading, and h_a is the depth of the circle of contact from the specimen free surface.[181]

The analysis of the results is based on the procedure first proposed by Oliver and Pharr.[184] They observed that the unloading data are well described by a simple power-law relation of the form

$$P = A(h - h_f)^m \qquad \text{(Eq. 2.27)}$$

where *A*, h_f, and *m* are all determined by a fitting procedure. The initial unloading contact stiffness, *S*, is then found by differentiating Eq. 2.27 with respect to displacement and evaluating at the maximum displacement:

$$S = \left.\frac{dP}{dh}\right|_{h_{max}} = Bm(h_{max} - h_f)^{m-1} \qquad \text{(Eq. 2.28)}$$

The contact depth is then calculated by:

$$h_c = h - \epsilon P/S \qquad \text{(Eq. 2.29)}$$

where ϵ is a geometrical correction factor for the type of indenter (ϵ = 0.75 for pyramidal indenters). The importance of this model is that it enables to compute the contact area as a function of the contact depth, $A = f(h_c)$, directly from the compliance curve. For an ideal Berkovich indenter (the most commonly used), $A = 24.56h_c^2$. However, for accurate measurements at shallow indentations (< 2 μm), the area function is typically obtained by calibration with standard materials to account for the rounding at the apex and the non-ideal shape of the indenter.

The knowledge of the contact area allows the determination of the hardness, *H*, defined as the mean contact pressure at full load,

$$H = \frac{P_{max}}{A} \qquad \text{(Eq. 2.30)}$$

as well as the reduced modulus, E_r, and Young's modulus of the test specimen, *E*:

$$E_r = \frac{\sqrt{\pi}}{2}\frac{S}{\sqrt{A}} \qquad \text{(Eq. 2.31)}$$

$$E = (1 - \nu^2)\left[\frac{1}{E_r} - \frac{1 - \nu_i^2}{E_i}\right]^{-1} \qquad \text{(Eq. 2.32)}$$

where ν is the Poisson's ratio, and the subscript *i* represents the properties of the indenter material.

2.5.2. Nanoindentation of thin films[185]

An important difficulty encountered when characterizing the mechanical properties of supported thin films by nanoindentation is to avoid the involuntary probing of the properties of the underlying substrate. Therefore, special care must be taken for the interpretation of the results in such cases. For accurate determination of the film hardness (*H*), a fully developed plastic zone within the film must be guaranteed (Figure 2.16(a)) because under this condition the mean contact pressure becomes independent of the load. A common practice is to report the value of *H* of the plateau typically observed in plots of *H* vs penetration depth. Generally, the influence of the substrate is negligible for penetration depths below 10% of the film thickness. This observation is necessary but not sufficient for measurements of the elastic modulus as the elastic deflections of both the substrate and the film contribute to support the indenter load (Figure 2.16(b)). Some mathematical models used to deconvolute the properties of the film and the substrate from the experimental data will be discussed in Chapter 5.

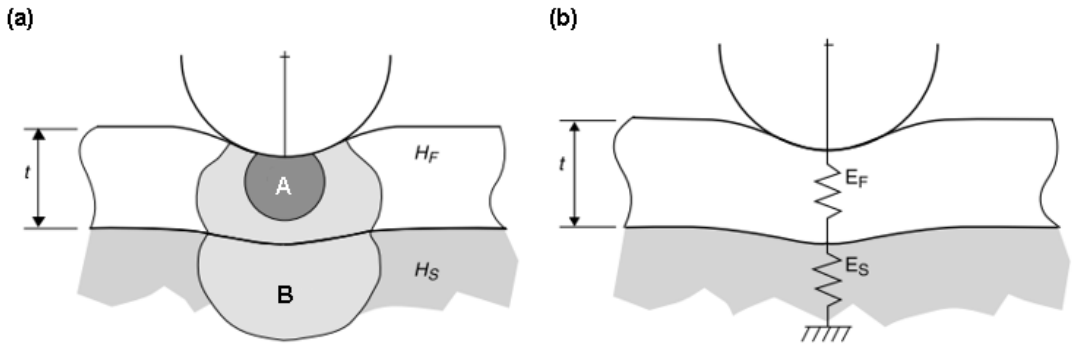

Figure 2.16: (a) Plastic zone in thin-film systems (of thickness = *t*) on hard substrates (A) and soft substrates (B). (b) Elastic response of the film/substrate system represented by two springs connected in series.[185]

Apart from the effect of the substrate, other factors may affect considerably the nanoindentation test data of thin supported films. Particularly important are those factors reducing the accuracy of the projected area of contact used in Eq. 2.30 and Eq. 2.31 since this value is determined indirectly from the measurements of load and depth assuming the conformal contact of an indenter with ideal geometry. In practice, various errors are associated with this assumption. For instance, the actual contact area of a real indenter with non-ideal geometry is often larger than the computed

with the nominal dimensions as depicted in Figure 2.17(a). Moreover, the tip radius of the pyramidal indenter is not perfectly sharp; in practice, the actual tip radius of these indenters may be about 100 nm (Figure 2.17(b)). As introduced earlier, to account for these imperfections the area function of the indenter is calibrated by performing a series of indentations at various maximum loads on standard test specimens of known elastic modulus and Poisson's ratio. For the present work, this calibration procedure was performed on a polycarbonate standard before any indentation.

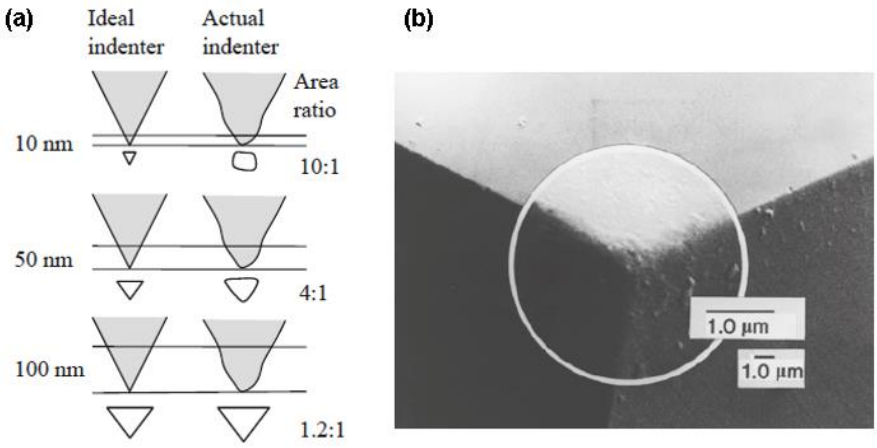

Figure 2.17: (a) Schematic of comparison of areas of contact with an ideal conical indenter and a real indenter with a non-ideal shape. (b) The tip of a Berkovich indenter with a tip radius on the order of 100 nm.[181]

2.5.3. Continuous Stiffness Measuring (CSM) methodology

To investigate the mechanical properties of the supported thin films, we relied on the application of the so-called Continuous Stiffness Measuring (CSM) methodology, first introduced by Oliver and Pethica,[184,186] which is based on the superimposition of a small harmonic oscillation to the monotonic load of the indenter.

We used a NHT^3 nanoindenter and a Berkovich diamond indenter B-K78 from CSM Instruments (now Anton Paar, Austria). The area function of the indenter was calibrated before the experiment using a polycarbonate standard of known elastic modulus. The supported film samples were conditioned at the testing relative humidity (RH) level for at least 24 hours before the experiment

by keeping them in closed desiccators together with silica gel (for RH < 5%), a saturated solution of magnesium chloride (for RH ~33% at 20 – 25 °C), or a saturated solution of sodium chloride (for RH ~75% at 20 – 25 °C).[187] The RH was monitored with Testo 174H data loggers (Testo SE & Co., Germany). All nanoindentation experiments were performed inside a hermetically closed chamber at room temperature (T ~23 °C) and controlled RH. The samples were transferred at least two hours before the experiments into the enclosure and equilibrated at the testing conditions.

The CSM experiment was carried out up to a peak force of 80 mN by applying a loading profile such that the indentation strain rate was constant:

$$\frac{\dot{P}}{P} = \frac{1}{P}\frac{dP}{dt} = 0.05\ s^{-1} \qquad \text{(Eq. 2.33)}$$

A constant strain rate is recommended for the loading of polymers and other viscoelastic materials because it ensures similar loading conditions if different polymeric samples have to be compared; it is also recommended in cases where more data is required at low penetration depths.[188,189] A sinus excitation with 5 Hz frequency and 5 mN amplitude was imposed during loading. Because the CSM method does not make use of the data acquired during unloading, a fast (50 µm/min) linear withdraw of the indenter was used after reaching the peak force. At least 15 measurements were performed on each sample and humidity condition at different locations on the surface.

2.5.4. Nanoindentation with Knoop geometry

A diamond indenter with Knoop geometry (see Figure 2.14) provided by Anton Paar, Austria, was mounted on the nanoindenter machine and its area function was calibrated with a polycarbonate standard before the experiment. A quasi-static indentation loading at a constant strain rate $\dot{P}/P = 0.05\ s^{-1}$ was applied up to a peak force of 5 mN followed by a hold period of 120 s at peak force and unloading at the same constant strain rate used for the loading. The

experiment was performed at a controlled RH < 5% after following the same conditioning process described in § 2.5.3. At least 15 measurements were performed on every sample.

2.5.5. Nano-contact fatigue test

We employed a nanoscale repetitive "impact" testing methodology adapted from the one proposed by Beake et al.[190] The Knoop tip geometry was used for this nano-contact fatigue experiment because its sharp geometry exerts higher stresses to the film at shallow indentations. Once the tip sensed the surface of the sample, it was accelerated to a peak force of 7.5 mN at a loading rate of 450 mN/min so that it took one second to the tip to reach the final load. Once at peak force, the tip retracted to a minimum force of 0.05 mN at the same unloading rate to complete one stress cycle that was immediately repeated 150 times at the same location. Under these experimental conditions, the probe remained in contact with the surface for a "gentle" experiment that provides information on impact wear resistance.[191] Eight repeat tests were performed at three azimuth angles (0°, 45 °, and 90°) between the direction of alignment of the long axis of the indenter with respect to the spraying direction of the CNF suspension during the fabrication of the films (see § 5.3). The evolution of the surface damage was followed by continuously monitoring the probe position (depth vs. the number of cycles).

2.6. Statistical treatment of data[192]

Whenever sufficient replication data was obtained, statistical tests were used to compare different samples/testing conditions. This was particularly the case of the nanoindentation experiments. The data were treated with the statistical software Minitab v.18.1 (Minitab, U.S.A.) using a significance level $\alpha = 0.05$.

The normality of the data was assessed using the Ryan-Joiner test. Any normally distributed set of data is always reported as the mean ± its standard deviation, whereas a not-normal set of data is presented as the median and the interquartile range (IQR). Two or more normally distributed

set of samples were compared by means of one-way ANOVA with Tukey *post hoc* test. All statistical tests are reported according to the APA format:

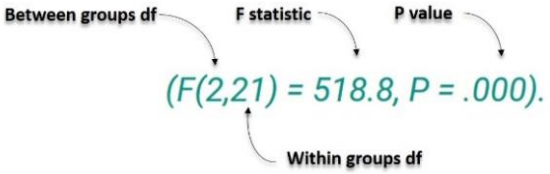

where "df" stands for degrees of freedom. Whenever box plots are presented, the following legend applies:

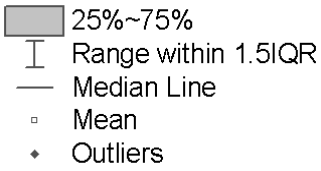

A full factorial design of experiments (DOE) to test the effect of four GIS parameters (concentration of the colloidal suspension, liquid flow rate, airflow rate, and spraying time) on the alignment of the cellulose nanoparticles and on the surface coverage was performed and analyzed using the statistical software Minitab. The selection of the factor levels (i.e. the settings of the process variables) will be further discussed in Chapter 3. Detailed information about the DOE approach can be found elsewhere.[193,194] The values of the measured responses (i.e. the nematic order parameter or the surface coverage) were evaluated by analysis of variance (ANOVA). This method attempts to explain experimental data in terms of two contributions: a set of experimental conditions (i.e. a model) and an error term grouping the data not accommodated by this model. The logic behind the ANOVA treatment is illustrated in Figure 2.18. The response at each factor level can be thought of as a normally distributed population (group) defined by a mean value and a constant variance (square root of the standard deviation). If the average variation between groups is large enough compared to the average variation within groups, then it can be concluded that at least one group mean is not equal to the others. ANOVA compares the variance attributed to the changes in the factor levels (treatment mean square, MS_{TR}) and the variance attributed to natural randomness of the measurement (error mean square, MS_{E})

by calculating the *F*-ratio = MS_{TR}/MS_{E}. If the investigated factors do not affect the response, the *F*-ratio will be close to 1. On the other hand, if at least one of the investigated factors does affect the response, then $F > 1$. More information on ANOVA can be found elsewhere.[195]

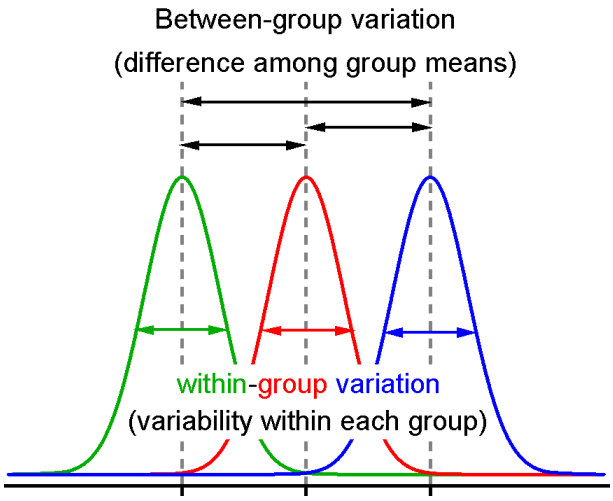

Figure 2.18: Schematic illustration of the logic behind ANOVA.

Besides the values of the *F*-statistics, the Minitab software uses other analytical tools to interpret the results from the DOE, namely Pareto plots, main effect plots, and interaction plots.[194] The Pareto plot represents the absolute values of the standardized effects to identify the factors and interactions that are most important to the process. The standardized effects are *t*-statistics that test the null hypothesis that the effect is 0. This chart also plots a reference line indicating the factors and interactions that are potentially important at the selected significance level (α). This reference line is drawn at *t*, where *t* is the $(1 - \alpha/2)$ quantile of the t-distribution. The main effect plot shows the mean response value at each level of the process variable (factor), which allows comparing the relative strength of the effects of various factors: the sign of the slope illustrates the direction of the effect (i.e. if the average response value increases or decreases) while the absolute value of the slope indicates the strength of the effect. On the other hand, the interaction plot shows the mean response of two factors at all possible combinations of their settings. Parallel lines indicate no interactions between the factors, while non-parallel lines imply the interaction between the factors.

Chapter 3. Isotropic and anisotropic cellulose-based nanocomposites

In Chapter 1, we highlighted the technical relevance of finding effective ways to prepare hierarchical structures of nanofibrillar building blocks to achieve materials with the desirable performance and functionalities exhibited by natural materials. We introduced that, while nature masters the organization of anisotropic nano-objects like nanocelluloses into complex superstructures, the development of synthetic materials with precisely controlled nano-architectures is hindered by the lack of suitable approaches for their preparation. Following the work of Blell[168] and Hu,[170] we set to use the grazing incidence spraying (GIS) technique to deliver unidirectional in-plane alignment to cellulose nanofibrils (CNFs) during the layer-by-layer (LbL) assembly of thin composite films with polyelectrolytes. However, we propose that the deliberate variation of the direction of orientation of individual nanocellulose layers could be exploited for preparing films with well-defined internal nano- and micro-structural arrangements of the reinforcing nanofibrils, ranging from the fundamental unidirectional array to the more complex cross-ply and helical configurations of controlled characteristics (e.g. handedness and pitch). These internal structuring of the films may lead to interesting mechanical and optical properties as introduced in Chapter 1.

In this chapter, we first investigate the assembly of cellulose nanofibrils into LbL films with different polyelectrolytes and montmorillonite (MTM) clay. Then, we analyze the effects of the

different spraying parameters on the quality of the parallel in-plane alignment of the CNFs and verify that independent directions of orientation can be obtained in consecutive CNF layers. The same procedure is validated for cellulose nanocrystals (CNCs). The last sections of the chapter are dedicated to the preparation and characterization of thick multilayer films with specific internal superstructures of CNFs, namely unidirectional, cross-ply, and helical arrangements.

3.1. Spray-assisted LbL assembly of isotropic CNF-based films

3.1.1. Morphological characterization of the CNFs

Before the preparation of the nanocomposite films, we characterized the dimensions of the CNFs used. Individual nanofibrils were directly measured from AFM images obtained on sub-monolayers deposited on PDDA-coated silicon wafers (Figure 3.1). Considering that AFM suffers from tip convolution/broadening, the cross-section of the nanofibrils was determined by measuring their height profiles.

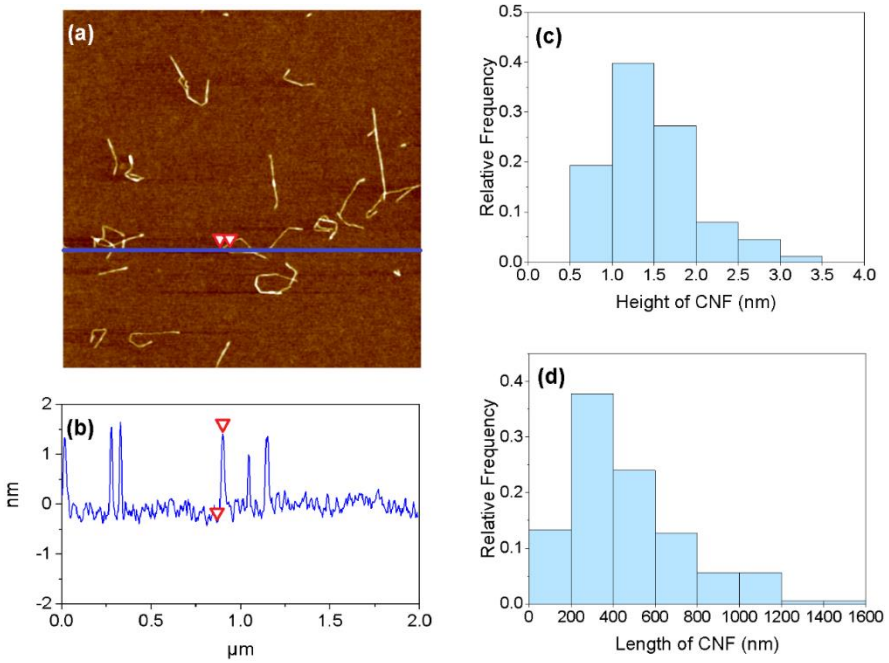

Figure 3.1: (a) Representative AFM image (2 x 2 µm^2) of individual CNFs deposited on PDDA-coated silicon wafer. (b) Cross-sectional analysis of individual CNFs. Height (c) and length (d) distributions of the CNFs.

The measurement of more than 80 individual and isolated nanofibrils on the AFM images revealed that the CNFs used in the present study had a median height of 1.5 nm (IQR 1.1 – 1.8 nm) and a median length of 400 nm (IQR 240 – 590 nm), which results in an aspect ratio of approximately 260. These sizes are slightly lower than the ones typically reported in the literature (5 – 15 nm width and > 1 µm long),[87] however, it is well-known that the size of the CNFs varies considerably depending on their source and fibrillation process.[54,82,86]

3.1.2. Isotropic CNF/polyelectrolyte nanocomposites

Previous work in our team showed the preparation of both isotropic and anisotropic CNF-based LbL films using either chitosan or poly(vinylamine) as a binding polyelectrolyte.[167,168] Moreover, many other components have also been reported for the preparation of cellulose nanocomposites.[196–199] Motivated by the need to prepare micron-thick multilayer films required for the envisioned mechanical characterization, the relative growth rate of isotropic films prepared with three different polycations, namely chitosan (CHI), poly(vinylamine) (PVAm), and poly(diallyldimethylammonium chloride) (PDDA), were compared by ellipsometry (Figure 3.2). The samples were prepared by conventional orthogonal spray-assisted LbL deposition of the polyelectrolyte solutions and the CNF suspension (0.15 mg/mL) onto PEI-coated silicon wafers.

Since the pH of weak polyelectrolyte solutions affects the degree of dissociation of the ionizable groups on the polymer chains, this parameter controls the conformation of the molecules in solution and therefore also during their deposition.[112,167,200] Two different pH values were used for the PVAm and chitosan solutions as they are weak polyelectrolytes. On the contrary, the ionization degree and conformation of PDDA, a strong polyelectrolyte, are unaffected by the pH of the solution so it was kept constant (at pH = 4). Figure 3.2 shows that CNF-based LbL films assembled with PVAm and PDDA exhibited a linear growth of the film thickness with respect to the number of deposited layer pairs, only a slight deviation from linearity was exhibited at the initial stages of build-up (first 3 – 4 layer pairs), which is typically ascribed to the influence of the substrate.[112,201] The thickness growth of the film prepared with CHI exhibited the so-called

"super-linear" behavior, i.e., an increasing growth rate with the number of layer pairs. The fastest growth rate was observed for films built with PVAm and the lowest for films assembled with chitosan.

As expected for weak polyelectrolytes, the increase in thickness was faster at higher pH, being more than double for PVAm at pH 10 than at pH 8, with thickness increments of about 13 nm/layer pairs and 5.4 nm/layer pairs, respectively. The faster thickness growth of the multilayer film built at higher pH was associated with the reduced surface charge of the polyelectrolyte and the consequently higher number of molecules depositing to compensate the opposite charges of the film surface, as it has been previously reported.[202–204] In the case of chitosan, only a slight faster thickness growth was distinguished for the film prepared at pH = 5.7 than for the film prepared at lower pH. Working at a higher pH was unfavorable as it negatively affects the solubility of chitosan.[205] In view of these results, PVAm was selected as the more convenient polycation to combine with CNF, motivated by the need for a smaller number of layers to reach the desired micron-thickness and therefore shorter fabrication times. The selection of a weak polycation is also advantageous as it offers room for fine-tuning the film thickness by means of pH changes of the depositing solution.

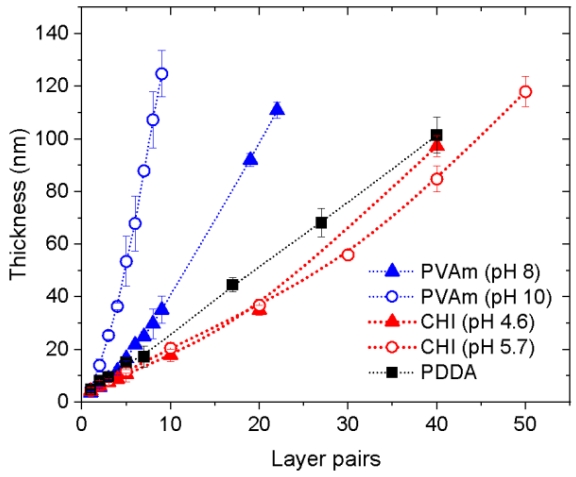

Figure 3.2: Variation of the thickness for CNF-based films prepared with different polycations at different pH as a function of the number layer pairs. Dotted lines are a guide for the eye.

The homogeneity of the film thickness can be assessed by comparing the size of the error bars (standard deviation) of the data points in Figure 3.2. For most of the films, the error bars were

small except for the one prepared with PVAm at pH 10, suggesting a higher roughness for this film. This assumption was confirmed by comparing the topographical AFM pictures of the films assembled with PVAm (Figure 3.3). Even though the thickness of these films was comparable (111 ± 3 nm and 125 ± 9 nm, respectively), the root-mean-square (RMS) roughness of the film prepared at the highest pH was more than three times larger (21.0 ± 1.0 nm) than that of the film prepared at lowest pH (5.6 ± 0.5 nm).

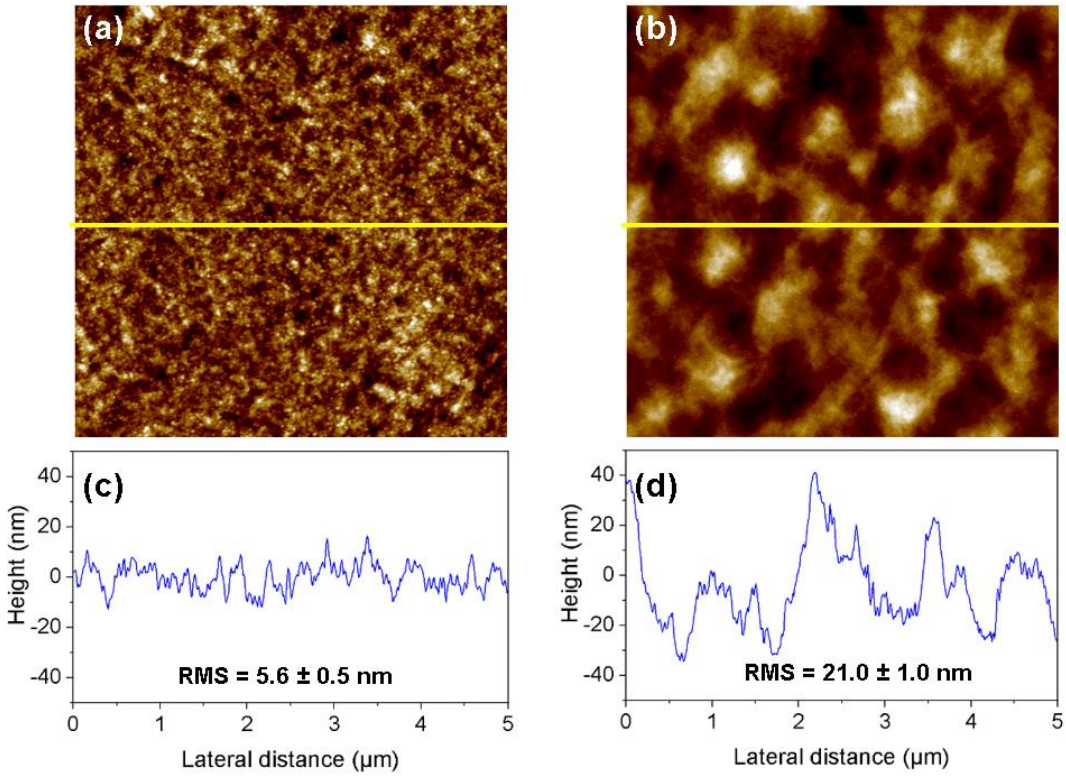

Figure 3.3: Topographical AFM images of the samples prepared with PVAm at pH = 8 (a) and PVAm at pH = 10 (b). (c) and (d) are the extracted height profiles at the position of the yellow lines in (a) and (b), respectively.

3.1.2.1. QCM-D analysis of (CNF/PVAm)$_n$ multilayer films prepared at different pH

The growth of (CNF/PVAm)$_n$ films with PVAm at pH = 8 and at pH = 10 was also investigated in the wet state using quartz crystal microbalance with dissipation monitoring (QCM-D). The diffusion-controlled deposition of the film components onto the quartz sensors cannot be directly

compared to the enforced-deposition imposed by the spraying process, however, it might reveal clues about internal characteristics of the films associated exclusively with the difference in pH.

A representative portion of the QCM data is presented in Figure 3.4(a) to illustrate the adsorption kinetics of the multilayer systems onto the gold surface of the quartz crystal. Only a small segment of the data is presented because of the very long measuring time of the experiment (approximately one week). This zoomed area corresponds to the time span in which the adsorption of the seventh CNF/PVAm layer pair took place, the adsorption of the other layer pairs showed the same behavior though. The injection of the CNF suspension into the QCM cell produced an initial rapid drop of the frequency followed by a further slower decrease of the signal, which indicates instantaneous adsorption of the nanofibrils followed by a re-arrangement of the layer until saturation. This decline in frequency (associated with the incorporation of mass to the films) was accompanied by an augmentation of the dissipation factor ΔD indicating the parallel increase of the viscoelasticity of the film/CNF suspension system. The subsequent rinsing with Milli-Q water led to no significant frequency changes, meaning no desorption of CNFs from the surface, together with a decrease of the dissipation factor associated with the change of the viscoelastic properties of the solution above the crystal (water instead of CNF suspension). The positive difference between the dissipation values measured before CNF injection and after water rinsing indicates a significant increase in the viscoelastic properties of the deposited film. When PVAm was injected into the cell, the frequency further dropped and the dissipation increased until reaching steady states (approximately half of the change associated with CNF). After rinsing with water, both signals increased slightly indicating minor desorption of PVAm and the formation of a highly hydrated layer of PVAm (or of the whole film). The peaks detected at the injection points are attributed to pressure changes associated with the exchange of liquids in the cell.

Figure 3.4(b) shows the monotonically accumulated changes in the normalized resonance frequency (Δf/n) and the dissipation factor (ΔD) of the third harmonics during the complete build-up of the films. The changes in resonance frequency and dissipation factor during the deposition of the first-three layer pairs were similar for the two samples. In this initial regime, the growth of

the film is affected by the substrate (e.g. different roughness and surface charge of gold compared with the bulk film). Starting from the seventh layer, though, the drop in frequency and the corresponding rise in the dissipation of the film built with the PVAm solution at pH 10 became more pronounced than for the system prepared at pH 8. Hence, the film prepared at higher pH must be thicker and less rigid. The contribution of CNF (even number of layers) to the adsorbed mass and viscoelasticity of the multilayer systems is greater than the contribution of PVAm (odd number of layers) as denoted by the stairs-like pattern of the Δf and ΔD curves. This is more evident for the film built at pH 10. After the initial slow regime, the increase of the adsorbed amount of material in both films reached a steady buildup as better revealed by the plot of the absolute value of Δf as a function of the number of layers presented in Figure 3.4(c). The linear fits of the curves (removed from substrate effect) revealed that the growth rate of the film deposited using PVAm at pH 10 was twice the rate of the system built at pH 8, which is in good agreement with the results obtained by ellipsometry (i.e., in the dry state).

In the previous paragraphs it has been introduced that, owing to the marked difference in dissipation values, the films deposited from polycation solutions at different pH must present differences in their rigidity. To properly compare this property, the dissipation factor is presented in Figure 3.4(d) as a function of the normalized frequency. This representation removes time as an explicit parameter and allows the comparison of the energy dissipation of both films at comparable mass (proportional to the frequency change). In both films, the increase in energy dissipation was basically proportional to the decrease in frequency, thus the viscoelasticity of the films was constant throughout the buildup, even during the slow-growing regime of the first three-to-four layer pairs. The steepest slope observed for the data of the film built at pH 10 confirms that this film was not only thicker than the film built at pH 8 but it was also less rigid.

The viscoelasticity of the LbL films can be influenced by the contribution of two main factors. On one hand, the amount of water hydrodynamically coupled to the film's material. On the other hand, the intrinsic rigidity of the material, defined by the density of ionic interactions between the

CNF and the PVAm: the more densely charged the polyelectrolytes are, the more ionically "crosslinked" the film will be (thus, more rigid).

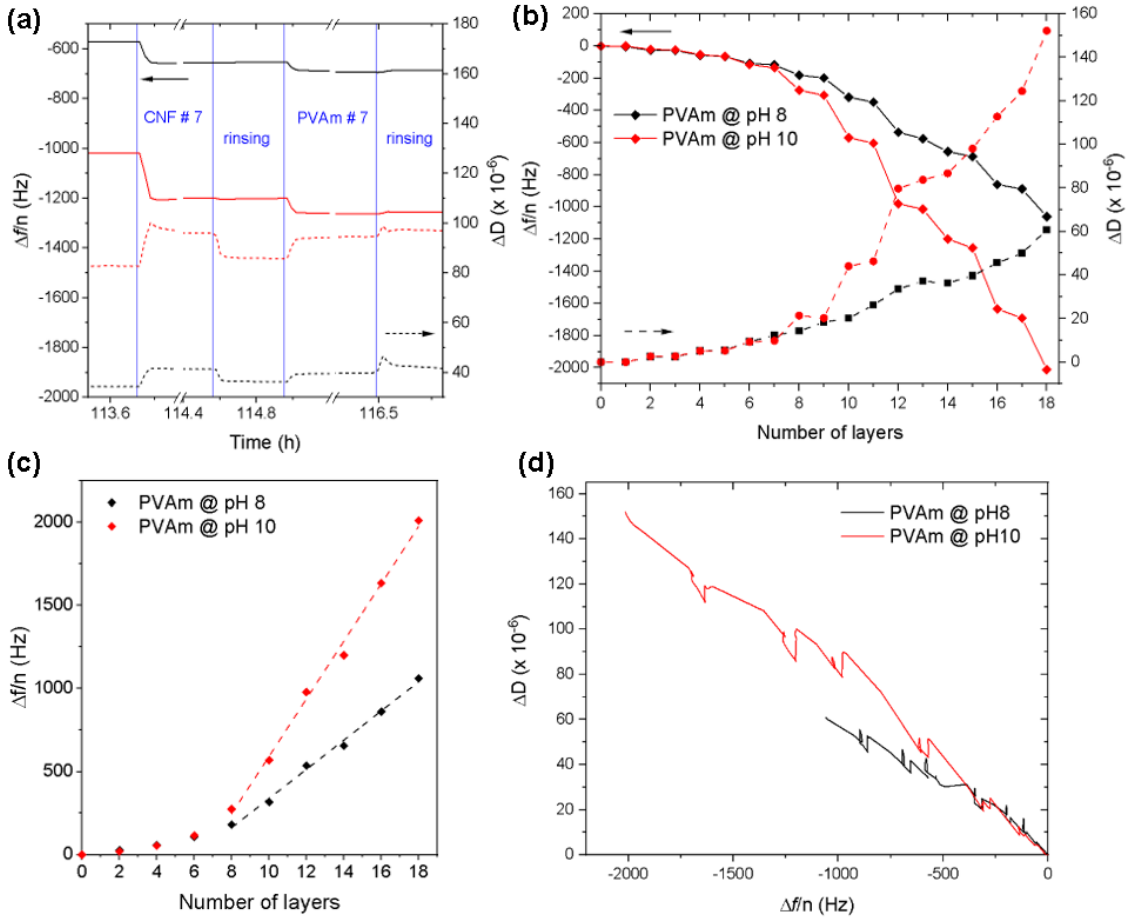

Figure 3.4: (a) Frequency and dissipation changes during the construction of LbL films on QCM sensors at pH 8 (black curves) and pH 10 (red curves). (b) Accumulated changes in the resonance frequency and the dissipation factor during the complete build-up of the multilayer films. (c) Absolute value of the frequency changes as a function of the number of layers. (d) Dissipation factor as a function of the changes in frequency for both films. All graphs correspond to the data of the 3rd harmonics.

The density of the ionic crosslinking is strongly affected by the pH of the system during film buildup because both cellulose[206] and PVAm[207] are weak polyelectrolytes. The carboxylic group of the CNF (pKa ≈ 4.5) is completely dissociated at neutral pH 7.0,[208] thus the cellulose nanofibrils are completely charged during the entire buildup of both films. On the contrary, PVAm (pKa ≈ 10) is partially charged at pH 8 but only weakly charged at pH 10.[209] Weakly charged polyelectrolyte chains (i.e., at higher pH) deposit in coiled conformations that form thicker and loosely attached films owing to the lower density of available complexation sites.

They might also form a more open structure (i.e., porous films) than highly charged polyelectrolyte molecules (at lower pH). The latter are adsorbed in elongated conformations and form thinner, denser, and stiffer films with a higher density of charge compensation.

With respect to the amount of water, we remark that the cellulose nanofibrils possess a huge surface area full of -OH groups able to form strong hydrogen bonds with water molecules. Therefore, CNF is known to be highly hygroscopic. Moreover, having the highest density of primary amine groups of any polymer, PVAm is also a highly hygroscopic material. Therefore, the CNF/PVAm multilayer films must be highly hydrated as it has been observed by others for polysaccharide-based multilayer systems[210,211] and for colloidal complexes of PVAm and carboxymethyl cellulose (CMC).[209]

3.1.2.2. Determination of water content by solvent exchange experiment in QCM-D

To gain information on the contribution of coupled water to the viscoelastic response of the multilayer films, the liquid fraction was determined by a solvent exchange procedure monitored by QCM-D as first reported by Craig and Plunkett.[212] This method is based on the measurement of the change in resonance frequency caused by the replacement of the solvent by its deuterated analogous. Figure 3.5 shows the measured changes of frequency ($\Delta f_n/n$) at three different buildup stages of the $(CNF/PVAm)_n$ multilayer systems built with PVAm at pH = 8 and at pH = 10 when switched from H_2O to D_2O and back to H_2O. The Δf value measured during the solvent exchange procedure carried out after the deposition of the third layer pair (PVAm as the top layer) was considerably lower than that observed after the CNF and PVAm layers of the sixth layer pair, probably because the adsorption process at this stage was still influenced by the surface of the sensor. Thus, no significant differences were detected at this initial stage between the amount of coupled water in both films. A different scenario was evidenced during the deposition of the sixth layer pair, where the substrate no longer affects the deposition process. In this case, the decrease in frequency associated with the injection of D_2O was higher for the sample prepared with a

PVAm solution at pH 10 than for the one prepared at pH 8. This decrease in frequency is associated with the amount of water trapped within the multilayer, for instance in "porous structures", and not with the so-called hydration water, i.e. water stoichiometrically bound to the PEM.

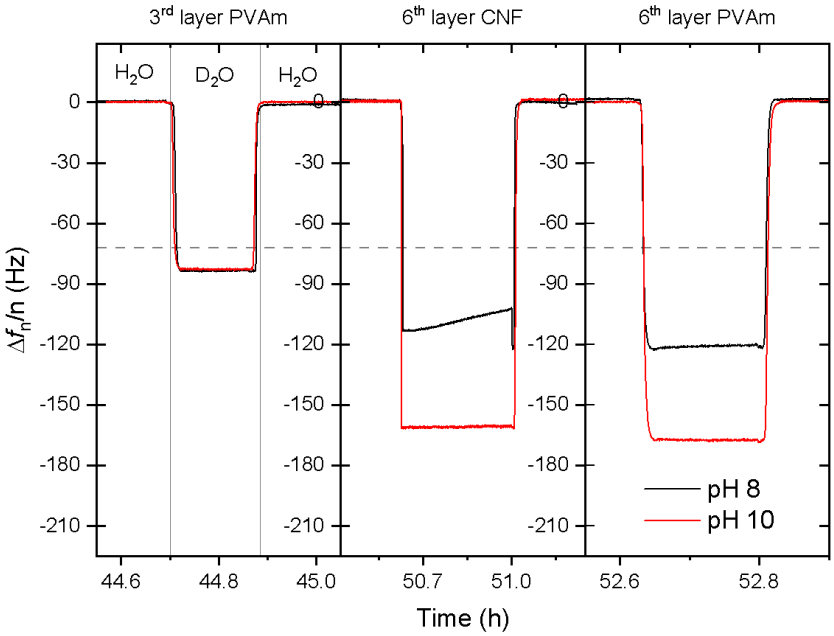

Figure 3.5: Representative solvent exchange data (3rd overtone) obtained at three different stages of the fabrication of the $(CNF/PVAm)_n$ films prepared at two different pHs.

The mass fraction of water within the film was calculated according to:[212]

$$S_{fraction} = \frac{\Delta f_s - \Delta f_d}{\Delta f_s(1 - \rho_d/\rho_s)} \qquad \text{(Eq. 3.1)}$$

where Δf_d is the frequency difference between the bare crystal and the crystal with the deposited film in D_2O, Δf_s is the frequency difference between the bare crystal and the crystal with the deposited film in H_2O, ρ_d and ρ_s are the densities of D_2O and water, respectively. The resulting mass fractions of water within the multilayer films, averaged from the data of the five measured resonance frequencies, are presented in Table 3.1. Conducting the solvent exchange procedure after the deposition of two consecutive layers (the sixth layer pair) put in evidence that, in the case of the lower pH, the amount of trapped water depended on the outermost layer of the film,

being 30% higher when PVAm was the top layer. On the contrary, the amount of water trapped in the film prepared at higher pH was independent on the top layer. In the absence of data for thicker films, it seems that the film prepared at higher pH absorbs an average of 24% more water than the film prepared at lower pH, which contributes to the higher viscoelasticity of the former.

Table 3.1: calculated water contents of the CNF/PVAm films (PEI is the first layer).

	Mass fraction of water		
	7th layer (PVAm)	**12th layer (CNF)**	**13th layer (PVAm)**
PVAm @ pH = 8	0.80 ± 0.20	0.60 ± 0.05	0.78 ± 0.04
PVAm @ pH = 10	0.74 ± 0.04	0.84 ± 0.01	0.87 ± 0.01

The "odd-even" effect on the hydration of polyelectrolyte multilayers, in which the nature of the outermost layer determines the amount of water absorbed by the whole film, has been previously observed for PEMs in which at least one of the components is a weak polyelectrolyte.[213–217] Wong et al. found that PSS-terminated PAH/PSS multilayer films were swollen in water to a higher extent than PAH-terminated films due to the higher hydrophilicity of the PSS surface.[214] In views of this explanation, and assuming that PVAm is more hydrophilic than CNF (at equal volumes), the odd-even effect detected in the CNF/PVAm system at pH 8 may be interpreted in terms of a lower fraction of PVAm at the film surface. It is well established that an increased amount of weakly charged molecules (e.g. weak polycations at high pH) are adsorbed on reference cellulose, also forming a thicker layer.[167,203] Therefore, the CNF-terminated film (whose outermost layer is rather intermingled CNF and PVAm) prepared at pH 10 should have an increased fraction of hydrophilic PVAm that absorbs more water than the CNF-terminated film prepared at pH 8. The difference in water uptake between the two films vanishes when PVAm is the top layer.

Differences in the amount of extrinsic binding sites (i.e. polymer/counterion pairs) inside the PEMs[218] have also been used to justify the asymmetric swelling behavior since the counterions of the extrinsic binding sites induce an osmotic pressure which forces the PEM to uptake water.[216] In this respect, the big and rigid nanofibrils (relative to the polyelectrolyte molecules) do not compensate for all the charges of the coiled and thick layer of PVAm adsorbed at pH 10,

thus the excess of counterions found within the film promotes an increased water uptake. On the other hand, at lower pH, the PVAm molecules deposit in a thinner and smoother layer whose charges are much easier balanced by ion-pairing with the negative charges on the CNFs. Therefore, a lower osmotic pressure induces the absorption of comparatively less water.

The phenomenon of the odd-even effect in swelling is not fully understood and it is out of the scope of this work. However, we have learned through the QCM-D experiment that the films prepared at two different pH exhibit differences in their viscoelastic behaviors, to a large degree associated with differences in the amount of trapped water.

3.1.3. Isotropic CNF/clay nanocomposites

Besides polyelectrolytes, many other types of constituents have been LbL-assembled with CNFs for the preparation of functional films, e.g. hybrid films with clay nanoplatelets have been reported in the literature for various applications.[219–221] Given the technical interest of this hybrid system, we set to investigate the feasibility of the incorporation of clay nanoplatelets into our sprayed multilayer films. In the present sub-section, the assembly of films combining CNFs and montmorillonite (MTM) clay nanoplatelets was followed by ellipsometry. Since both nano-objects are negatively charged, PVAm was used as a gluing polycation (at pH 10 for faster film growth). The relative growth rate of films prepared with and without clay is presented in Figure 3.6. We noticed that the reference film containing only MTM and PVAm grew very slowly (1.6 nm per layer pair) in comparison to the film without clay (14 nm per layer pair). Meanwhile, the sample combining both reinforcing components, MTM and CNFs, showed an intermediate thickness increment of 6.8 nm per layer pair. Therefore, the incorporation of clay reduced significantly the growth rate of the CNF/PVAm system.

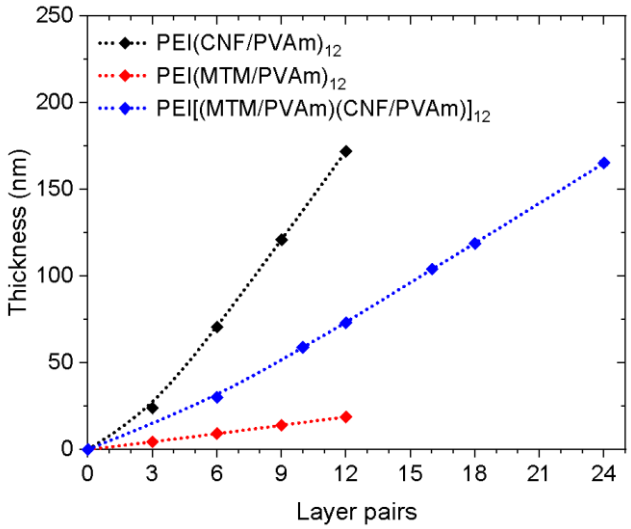

Figure 3.6: Thickness increment for $(CNF/PVAm)_n$ films prepared with and without MTM clay. Small error bars are hidden by the data points. Dotted lines are guides for the eye.

The morphology of the used MTM nanoplatelets can be seen in the height AFM image of the first layer of MTM deposited on the PEI-coated silicon wafer (Figure 3.7(a)). Moreover, the incorporation of both reinforcing materials within the LbL film is clearly identified in the phase AFM image of the second MTM layer of the hybrid film (Figure 3.7(b)), in which CNFs of the underlayer are recognized through gaps on the top MTM layer. The incorporation of clay to the CNF-based films is therefore feasible.

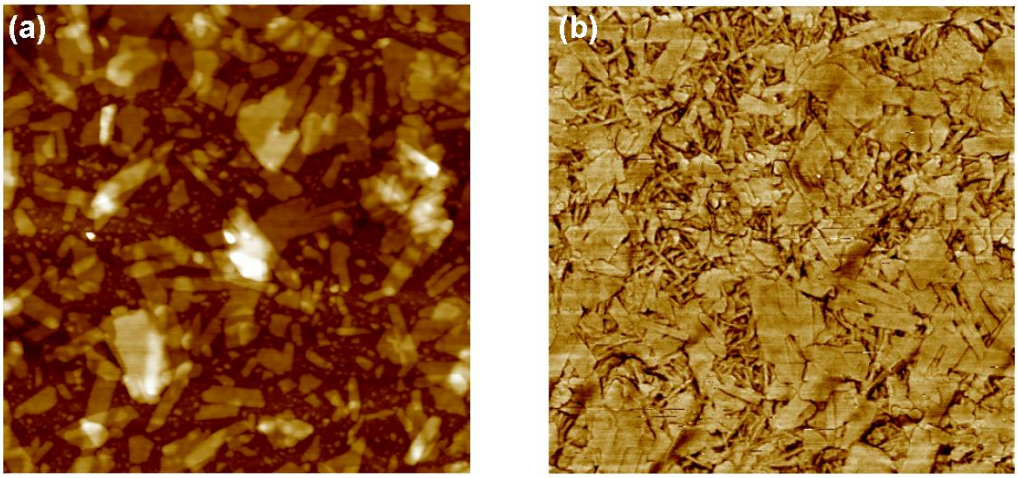

Figure 3.7: (a) Height AFM image of the first layer of clay deposited onto PEI-coated silicon wafer. Image size: 1x1 μm^2, vertical range = 10 nm. (b) Phase AFM image of the second clay layer of the film $PEI[(MTM/PVAm)(CNF/PVAm)]_{12}MTM$. Image size: 1x1 μm^2, vertical range = 24°.

3.2. GIS-assisted LbL assembly of aligned nanocellulose-based films

3.2.1. CNF monolayers

The envisioned concept of preparing cellulose films with controlled helicoidal structures is based on the premise of being able to align independently the cellulose nanofibrils in each layer of the film. As introduced in Chapter 1, previous work in our group carried out with cellulose nanofibrils allowed the introduction of the Grazing Incidence Spraying (GIS) alignment technique.[168] In her doctoral thesis, Rebecca Blell explored the influence of three key parameters on the alignment of CNF monolayers on PEI-coated silicon wafers, namely the liquid flow rate of the spraying suspension, the airflow rate of the carrying gas, and the concentration of the CNF suspension.[222] Her results were obtained using a One-Variable-At-a-Time (OVAT) approach, i.e., varying one parameter at a time keeping all other variables fixed, which is a fair enough method for gaining insights on the main effect of the studied process variables on the output functional performance. When it comes to the optimization of the process parameters, however, the OVAT approach fails to recognize interactions among the variables and their results could be misleading because there is no guaranty whatsoever that the effect of one variable will be the same when the conditions of the other variables change. In the present section, we varied the spraying parameters simultaneously and used statistical methods to obtain predictable estimates of factor effects and their interactions, with the purpose of finding optimum spraying conditions to attain the highest possible alignment of CNF monolayers.

A monolayer of the prepared suspension of anionic CNFs was deposited on PEI-coated silicon wafers by grazing incidence spraying. Since the number of experimental trials, i.e., the number of all possible combinations of experimental conditions, increases exponentially with the number of variables, only four process parameters (factors) were varied; those that are considered to influence the most the alignment of the CNF, namely the concentration of the CNF suspension

(*C*), its liquid flow rate (*LF*), the airflow rate of the compressed air (*AF*), and the spraying time (*t*). On the contrary, based on previous studies in our team, the spraying angle and the distance of the nozzle to the sample were kept constant at 10° and 1 cm, respectively. Each factor was studied at two levels representing the two extreme settings reasonably attainable. These limits were arbitrarily selected based on either technical limitations (e.g. maximum or minimum settings of the gas flow controller and liquid pump, respectively, or the typical concentration of the CNF suspension obtained with the used protocol) or practicality and meaningfulness of the settings, e.g. too low *AF* would not align the nanofibrils whereas too long times are not practical nor necessary.

The full factorial design of experiments with four factors tested at two levels requires $2^4 = 16$ trial runs to test all possible combinations of the factor levels. These runs were executed in random order to remove the influence of biased factors, and some of them were replicated to guarantee reproducibility. A 2D nematic order parameter (S_{2D}), extracted from the image analysis of AFM pictures, was used to quantify and compare the alignment of the CNF monolayers.

Table 3.2 shows the design layout of the experiment with response values averaged from at least three AFM images per condition (taken at the center of the sample, ~3.5 cm from the top border). The highest degree of alignment was achieved when using spraying condition #10, i.e., the one that combined a long spraying time, a diluted CNF suspension, the lowest liquid flow rate, and the highest airflow rate. This combination of factor levels produced a parallel alignment of about 85% of the imaged nanofibrils (S_{2D} = 0.85). All other combinations produced a degree of alignment that was at least 20% smaller. An example of the different degree of alignment is shown in Figure 3.8, where representative AFM pictures of samples prepared with two different combinations of the spraying parameters are compared.

To gain a better understanding of the relative effect of every spraying parameter, the data from Table 3.2 were evaluated by Analysis of Variance (ANOVA) using Minitab software. The Pareto plot shown in Figure 3.9(a) displays the absolute values in decreasing order of the standardized effects of the individual factors and their interactions on the order parameter S_{2D}. On it, bars that

crossed the reference line (determined by the Minitab software) were statistically significant at a 5% significance level. The airflow rate of the carrying gas (*AF*) was the variable with the highest influence on the alignment of CNF, followed by the concentration of the spraying suspension (*C*). The spraying time (*t*) and the liquid flow rate (*LF*) affected the alignment both by themselves and in combination with other parameters (*t***AF* and *C***LF*), having these last ones equal or higher effects than the individual factors.

Table 3.2: Design layout of the experiment with response values.

	Factor levels				Response
Run	**Spraying time (*t*) [s]**	**Concentration (*C*) [mg/mL]**	**Liquid flow (*LF*) [mL/min]**	**Airflow (*AF*) [L/min]**	**S_{2D} parameter**
1	10	0.15	1.0	20	0.52 ± 0.13
2	60	0.15	1.0	20	0.59 ± 0.04
3	10	0.80	1.0	20	0.15 ± 0.06
4	60	0.80	1.0	20	0.44 ± 0.01
5	10	0.15	5.0	20	0.33 ± 0.02
6	60	0.15	5.0	20	0.54 ± 0.06
7	10	0.80	5.0	20	0.28 ± 0.09
8	60	0.80	5.0	20	0.50 ± 0.08
9	10	0.15	1.0	40	0.67 ± 0.06
10	60	0.15	1.0	40	0.85 ± 0.01
11	10	0.80	1.0	40	0.55 ± 0.10
12	60	0.80	1.0	40	0.61 ± 0.04
13	10	0.15	5.0	40	0.52 ± 0.03
14	60	0.15	5.0	40	0.48 ± 0.01
15	10	0.80	5.0	40	0.62 ± 0.01
16	60	0.80	5.0	40	0.35 ± 0.03
control	35	0.50	3.0	30	0.49 ± 0.04

Because the Pareto chart only displays the absolute value of the effects, the mean value of S_{2D} at each level of the spraying parameters are presented in Figure 3.9(b) to show the direction of the individual effects. These mean values are determined by averaging the responses measured with every fixed variable. For instance, the "Min." black point in Figure 3.9(b) corresponds to the average value of the spraying conditions #1, 3, 5, 7, 9, 11, 13, and 15 of Table 3.2 (spraying time = 10 s) while the "Max." black point corresponds to the average response of conditions #2, 4, 6, 8, 10, 12, 14, and 16 (spraying time = 60 s). The effect of CNF concentration and liquid flow rate determined in this way were negative, i.e., the mean value of S_{2D} decreased when these parameters passed from their low levels to their high levels. On the contrary, the apparent effects of *AF* and *t* were positive since the mean value of S_{2D} increased when either the airflow or the spraying time rose.

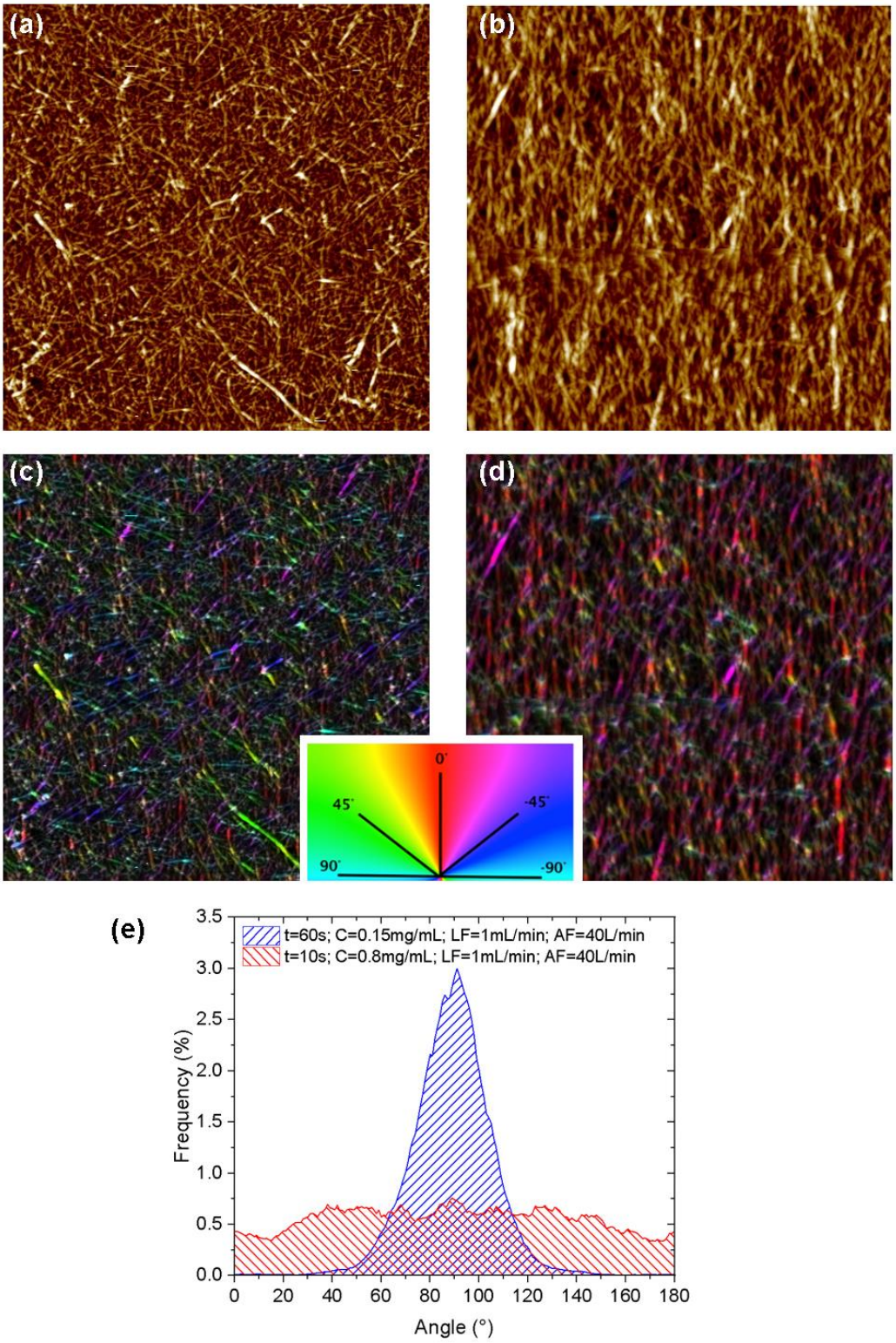

Figure 3.8: (a) AFM height image of the sample prepared with the conditions of run #11 in Table 3.2 (S_{2D} = 0.55). Image size 2x2 μm^2, vertical range 10 nm. (b) AFM height image of the sample prepared with the conditions of run #10 in Table 3.2 (S_{2D} = 0.85). Image size 2x2 μm^2, vertical range 19 nm. (c and d) Color survey of the orientation of the CNF in images in (a) and (b), respectively, obtained by OrientationJ. (e) Distribution of orientation of the CNF extracted from images (c) and (d).

However, the effects of the individual factors cannot be accurately analyzed without considering their interactions because at least two of them demonstrated to be statistically significant. Therefore, the interaction plots of Figure 3.10 show how the response of the S_{2D} parameter to the change in one factor depends on the value of the second factor. This time, the mean of S_{2D} is calculated by averaging the response values measured with the two variables of interest fixed. By inspection of these interaction plots, it becomes clear that when the airflow was set to its low level (20 L/min), the alignment of CNF was improved by using longer spraying times. On the contrary, when *AF* was set to its high level (40 L/min), good alignment of CNF was obtained independently of the spraying time. Similarly, an increased S_{2D} could be obtained when using the more diluted CNF suspension provided that it was sprayed at the lowest flow rate.

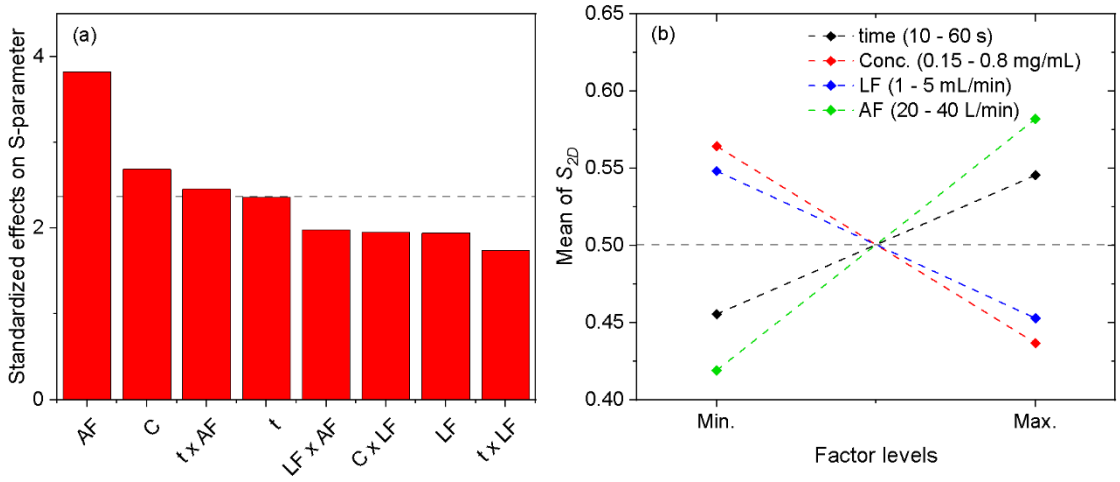

Figure 3.9: (a) Pareto chart representing the effect of the different process parameters of the grazing incidence spraying on the value of S_{2D}. The factors surpassing the reference line on the chart calculated by Minitab indicate which factors are statistically significant at $\alpha = 0.05$. (b) Main effects plot showing how different levels of the studied factors affected the mean value of S_{2D}. Dashed lines are guides for the eye.

The evaluation of the obtained data using the Minitab software allowed to go further on the correlation of the degree of alignment of CNFs to the specific settings of the spraying conditions: the 2D nematic order parameter S_{2D} was mathematically modeled using an *a priori* first-order linear model given by:

$$S_{2D} = a_0 + a_1 t + a_2 C + a_3 LF + a_4 AF + a_{12} t \cdot C + a_{13} t \cdot LF + a_{14} t \cdot AF + a_{23} C \cdot LF + a_{24} C \cdot AF + a_{34} LF \cdot AF + a_{123} t \cdot C \cdot LF + \cdots \quad \text{(Eq. 3.2)}$$

where a_i is a coefficient that represents the effect of the corresponding factor, a_{ij} is the effect of the second-order interaction between factors *i* and *j*, and a_{ijk} is the effect of third-order interactions among factors *i*, *j*, and *k*. Analysis of Variance (ANOVA) showed that the variations of S_{2D} were likely due to the modification in the factor levels and not to random error ($F(9,6) = 8.17$, $p = 0.01$). After removing the less-significative third- and second-order interaction, the coefficients of Eq. 3.2 were estimated by Minitab resulting in:

$$S_{2D} = 0.233 + 0.00298t - 0.417C - 0.0553LF + 0.01358AF + 0.00169t \cdot LF + 0.000024t \cdot AF + 0.0737C \cdot LF + 0.00062LF \cdot AF - 0.000077t \cdot LF \cdot AF \quad \text{(Eq. 3.3)}$$

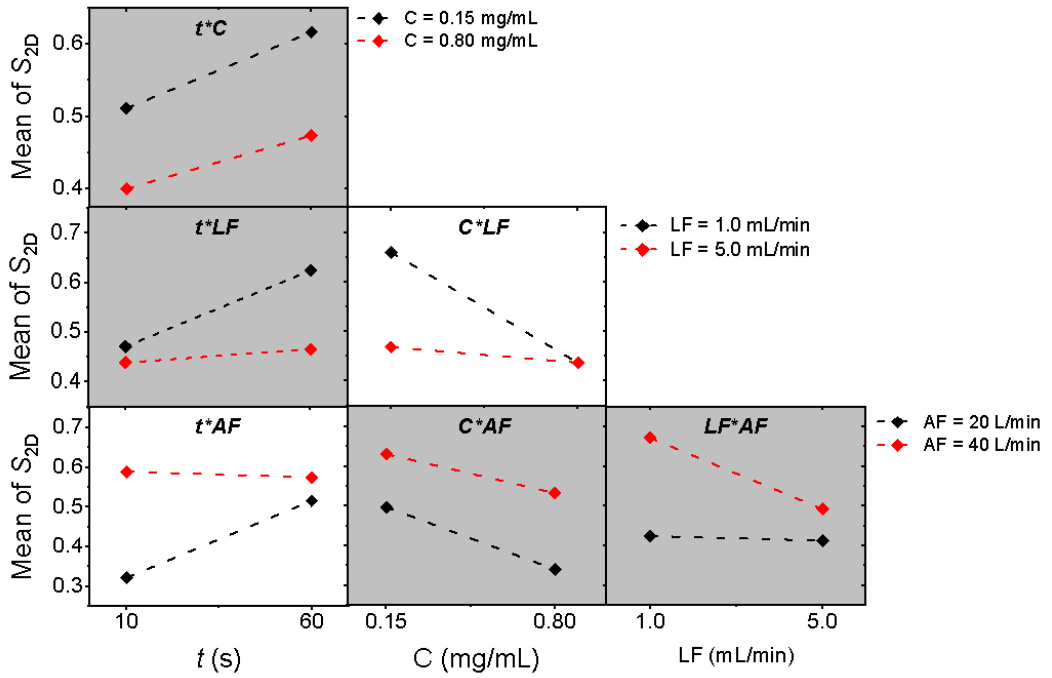

Figure 3.10: Interaction plots showing how the relationship between the factors and the response depends on the value of the second factor.

The coefficient of determination R^2 of the mathematical fit was 0.92, which confirms that the proposed linear fit describes well the GIS process. The accuracy of the mathematical model was experimentally validated by comparing the predicted and the measured S_{2D} values of the control experiment of Table 3.2. This sample was prepared using values of the parameters approximately in the middle point of the tested range. The predicted value was 0.50 ± 0.07, where the error was given by the root-mean-square error (RMSE) calculated by the ANOVA procedure, while the

experimental value was 0.49 ± 0.04. Eq. 3.3 describes the effect of the four spraying parameters investigated on the alignment of the cellulose nanofibrils; it allows the prediction of the value of the order parameter S_{2D} as a function of the selected settings of the spraying process parameters (within the studied range).

Being CNF a precious working material, it was also desirable to optimize its consumption during the preparation of the succeeding samples. Consequently, both the liquid flow rate and the concentration of the cellulose suspension were kept at their respective low levels. To optimize the spraying time parameter, new samples were prepared using three intermediate settings of this factor while keeping the airflow rate at its high (optimum) level. The S_{2D} values determined at 3.5 and 4.5 cm from the top border of the samples are plotted in Figure 3.11. In both cases, the order parameter increased until reaching a constant value at around 35 s. The lower values of S_{2D} measured at 4.5 cm corroborates that the CNF alignment decreases with the distance from the nozzle.

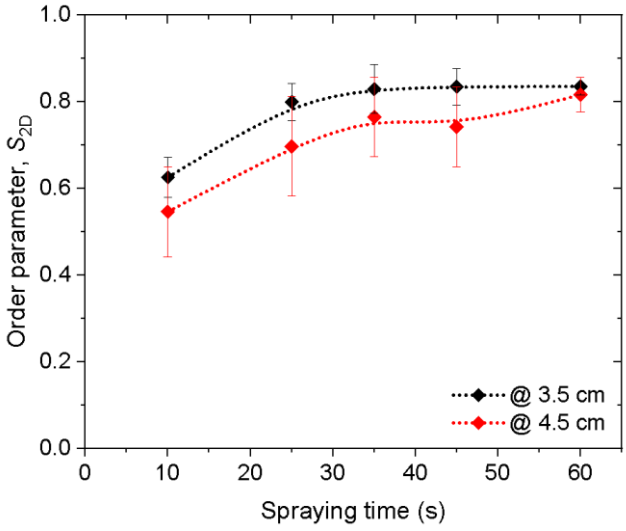

Figure 3.11: Variation of the 2D nematic order parameter S_{2D} as a function of the spraying time and the distance from the top border of the sample. Samples prepared with C = 0.15 mg/mL, LF = 1 mL/min, AF = 40 L/min. Dotted lines are guides for the eye.

Given that the underlying silicon wafer was clearly detected in the images acquired for the samples sprayed for 10 s, the thresholding of the grayscale pictures allowed us to determine that the nanofibrils covered approximately 80% of the surface under this condition. On the contrary,

the samples sprayed for longer times showed a denser packing of the CNFs so that the substrate was not accurately identified. Thus, we considered that the surface coverage of the samples sprayed for 35 s and 60 s reached practically 100%. Figure 3.12 shows representative AFM images of the samples prepared using 10 s and 35 s of spraying time, respectively. Moreover, ellipsometry measurements showed that the thickness of the CNF monolayer sprayed for 10 *s* was 4.3 ± 0.1 nm, while the ones of the samples sprayed for 35 s and 60 s was 6.6 ± 0.3 nm and 6.4 ± 0.3 nm, respectively. These results imply that at 10 s the saturation of the surface was not yet reached.

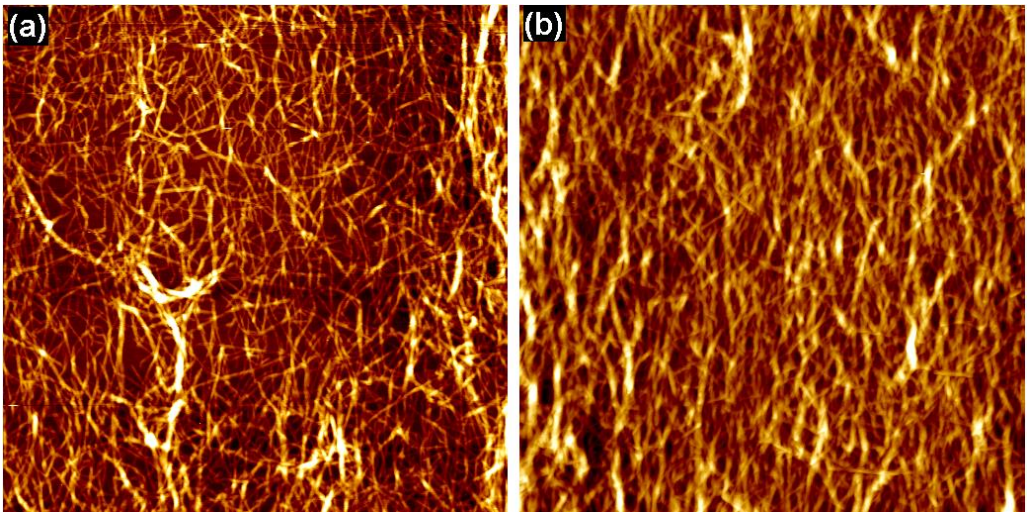

Figure 3.12: AFM height images of a monolayer of CNF on PEI sprayed for (a) 10 s and (b) 35 s. Samples prepared with C = 0.15 mg/mL, LF = 1 mL/min, and AF = 40 L/min. The images sizes are 2x2 μm^2 and the vertical ranges are 16 nm, and 25 nm, respectively. Spraying direction pointing up.

By combining the results of the surface coverage and thickness of the monolayer with the values of S_{2D} shown in Figure 3.11, it becomes clear that the saturation of the surface is favorable to obtain the highest degree of alignment of the CNFs. We recall that the electrostatic nature of the interactions responsible for the LbL assembly of polyelectrolytes and charged components limits the amount of material adsorbed in every deposition step. Thus, there is a critical time above which no further material is adsorbed. If the spraying process ends before an equilibrium charge complexation state has been reached at the film surface, the CNFs would deposit without the preferential alignment induced by the shearing flow of the suspension. The use of spraying times longer than this critical time during the GIS process is, thus, imperative for reaching complete

surface coverage as well as the high and reproducible quality of the unidirectional alignment of the CNFs.

The values of the order parameter (S_{2D}) and the mean angle of orientation (θ) measured at different locations on the sample prepared using the optimum spraying condition (run #10 in Table 3.2) were used to investigate the homogeneity of the alignment of the CNFs in the monolayer. The resulting mapping of these two parameters is shown in Figure 3.13.

The value of S_{2D} increased along the centerline of the spraying cone, reaching values $S_{2D} > 0.65$ at approximately 22 mm from the top border (Figure 3.13(a)). This degree of alignment remained constant for at least 30 mm; no more data was obtained in this direction in the benefit of getting more images in the lateral direction. In this last case, the degree of alignment decreased toward the lateral borders of the spraying cone so that $S_{2D} > 0.65$ was observed in a range of approximately 10 mm around the centerline of the spraying.

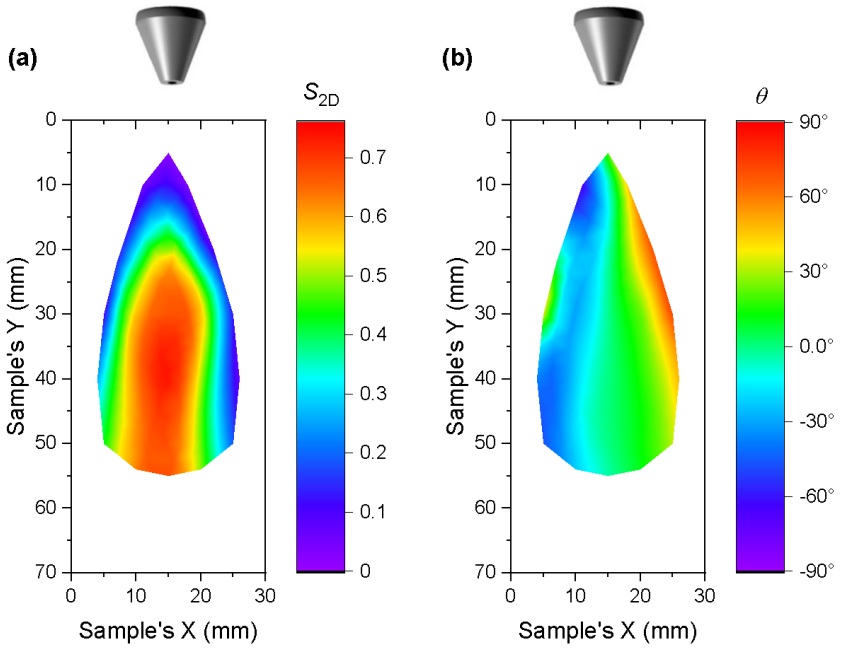

Figure 3.13: Contour plots showing the mapping of (a) the nematic order parameter (S_{2D}) and (b) the mean angle θ of preferential alignment of the CNFs.

As for the direction of the preferential alignment of the nanofibrils, θ changed following the diverging flowlines of the spraying pattern (Figure 3.13(b)), as reasonably expected and as

previously observed by Rebecca Blell.[222] In the central area defined by $S_{2D} > 0.65$ the angle of alignment varied between approximately ± 30°. The mapping of θ showed some artifacts at the right border of the spraying cone due to the low alignment of the CNFs in this region, which rendered meaningless the determined angles of preferential orientation in this area.

3.2.2. Independent orientation of consecutive CNF layers

The studies on the alignment of CNF shown so far have been performed on polished silicon wafers coated with a thin layer of PEI having a sub-nanometer RMS roughness. However, as the film grows by the addition of subsequent layers, the surface roughness increases. The question then arises as to whether this increased roughness significantly affects the orientation of the successive CNF layers. Rebecca Blell[222] studied the alignment of a cationic CNF layer sprayed by GIS onto the first layer of negatively charged CNF and verified that the top layer was also aligned in the direction of the spray. Moreover, she corroborated that thicker multilayer films built with chitosan and unidirectionally-oriented CNFs were birefringent, indicating that the net macroscopic orientation of nanofibrils in thick films prepared by GIS was preserved.[168] We have seen however that films prepared with chitosan grow much thinner than the films built with PVAm (see Figure 3.2), and it is reasonable to speculate that the surface roughness of both systems is not comparable. Therefore, before moving forward to the fabrication of multilayer films with helicoidal microstructures, it was necessary to verify that the effective alignment of the nanofibrils within multilayer films of the system of interest $(CNF/PVAm)_n$ was also preserved. Furthermore, not only the surface roughness but also the direction of orientation of the top layer may influence the arrangement of the depositing CNF layers. Therefore, in the present section, we investigate the effect of these two parameters on the alignment of the top CNF layers.

The 2D nematic order parameter, film thickness, and root-mean-square (RMS) roughness were determined at different stages of the fabrication of $PEI(CNF/PVAm)_{10}$ films prepared with PVAm solutions at pH = 8 and pH = 10. To account for the effect of the direction of orientation of the top layer, one set of samples was prepared by spraying successive CNF layers in the same

direction (unidirectional alignment), while the second set of samples was prepared by spraying consecutive CNF layers with an in-plane rotation angle of 90° between them (cross-ply alignment). On one hand, when the upper layer is sprayed in the same direction as the layer below, the latter might work as a template of the former, promoting a better alignment. On the other hand, when the upper layer is sprayed in a perpendicular direction to the one below, the latter might interact destructively in the alignment of the former. Therefore, these conditions represent the two extreme cases in which the alignment of the top layer could be influenced by the direction of orientation of the layer beneath. It is assumed that if the top layers can be effectively aligned under these two extreme conditions, they would also be aligned when using any other intermediate angle between consecutive CNF layers. Both sets of samples were prepared using the optimum spraying conditions discussed in § 3.2.1.

Figure 3.14 shows the superposition of AFM pictures taken to the first and second CNF layers of the cross-ply samples. In this image, the perpendicular orientation of the nanofibrils in both layers is clearly visualized, which demonstrates that CNF can be effectively oriented by GIS independently of the direction of orientation of the nanofibrils present on the layer beneath. We noticed, though, that the nanofibrils of the second layer seemed to be wider than those of the first one. This implies that the nanofibrils of the top layer form bundles instead of depositing as individual nanofibrils, probably promoted by the interactions with the PVAm layer between them. The evolution of S_{2D} as a function of the number of layer pairs is shown in Figure 3.15. It must be pointed out, however, that the discrimination of individual nanofibrils on the AFM images became harder as the number of layers increased, which rendered difficult to accurately quantify the alignment. The values plotted in Figure 3.15 are therefore to be analyzed with caution, particularly those of the thicker films, in which the global orientation of the pixels of the image might not correspond to the actual orientation of the individual nanofibrils. In any case, the apparent orientation of the CNF layers seems to decrease slightly after the initial layer and stabilize in values above 0.65 – 0.70, which are still reasonably good for the purpose of inducing anisotropy to the film.

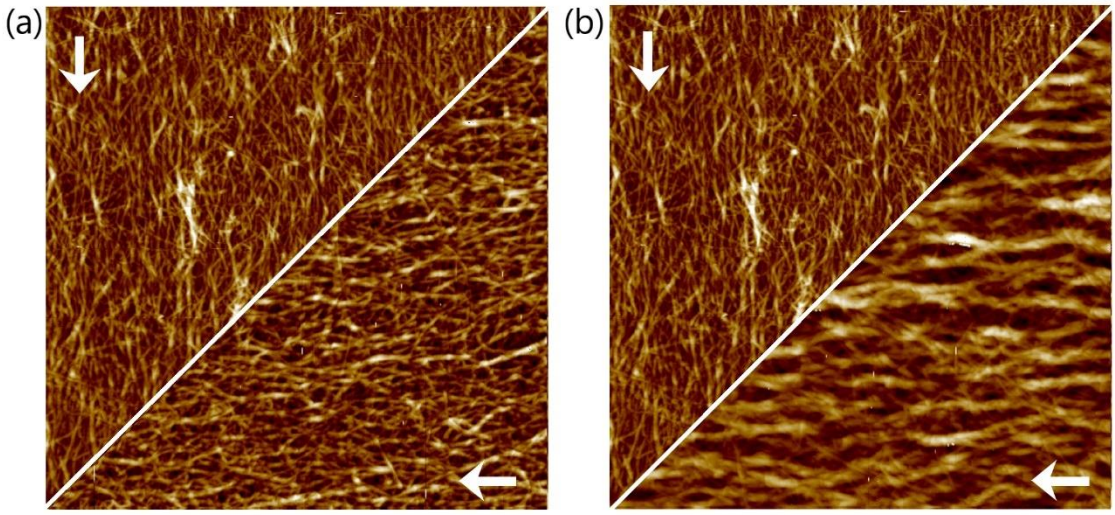

Figure 3.14: Superposition of representative AFM pictures of the first and the second CNF layers sprayed in perpendicular direction using (a) PVAm at pH 8 and (b) PVAm at pH 10. The vertical arrows indicate the spraying direction of the first layer and the horizontal arrows, the spraying direction of the second layer. Image sizes are 2x2 μm^2.

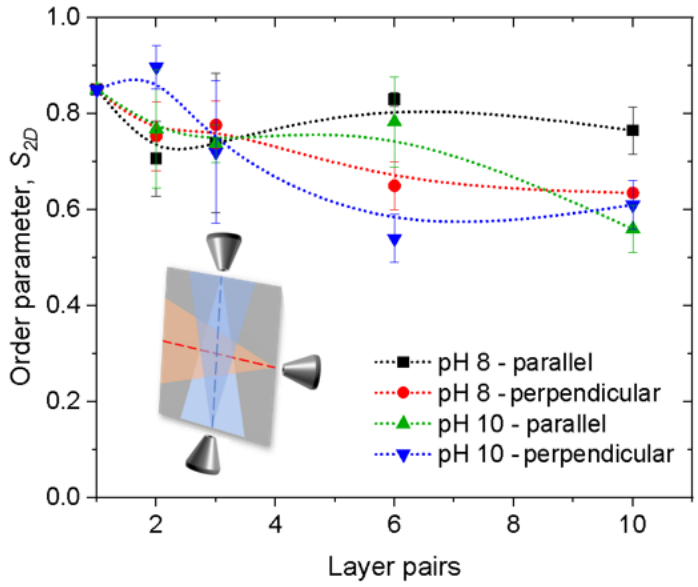

Figure 3.15: Variation of the order parameter S_{2D} as a function of the number of deposited PVAm/CNF layer pairs, the pH of the PVAm solution, and the spraying direction of alternated CNF layers. The dotted lines are guides for the eye.

The AFM images of Figure 3.16 better illustrate the loss in nanofiber resolution with the increasing number of CNF layers. Individual nanofibrils are distinguishable in the AFM picture corresponding to the first CNF layer because these are deposited on a smooth and rigid substrate. On the contrary, the PVAm molecules find a nanometer-rough surface composed of negatively charged cellulose nanofibrils and empty spaces, therefore they deposit on top of the nanofibrils.

In turn, the second layer of cellulose interacts with the PVAm-covered nanofibrils from the previous layer, aggregating into bundles of CNFs and increasing the size of the pores and the surface roughness instead of forming a uniformly flat surface (see the height profiles in Figure 3.16). This indistinguishability of individual nanofibrils implies the unsuitability of the determination of the S_{2D} parameter to compare the orientation of the CNFs in multilayer films.

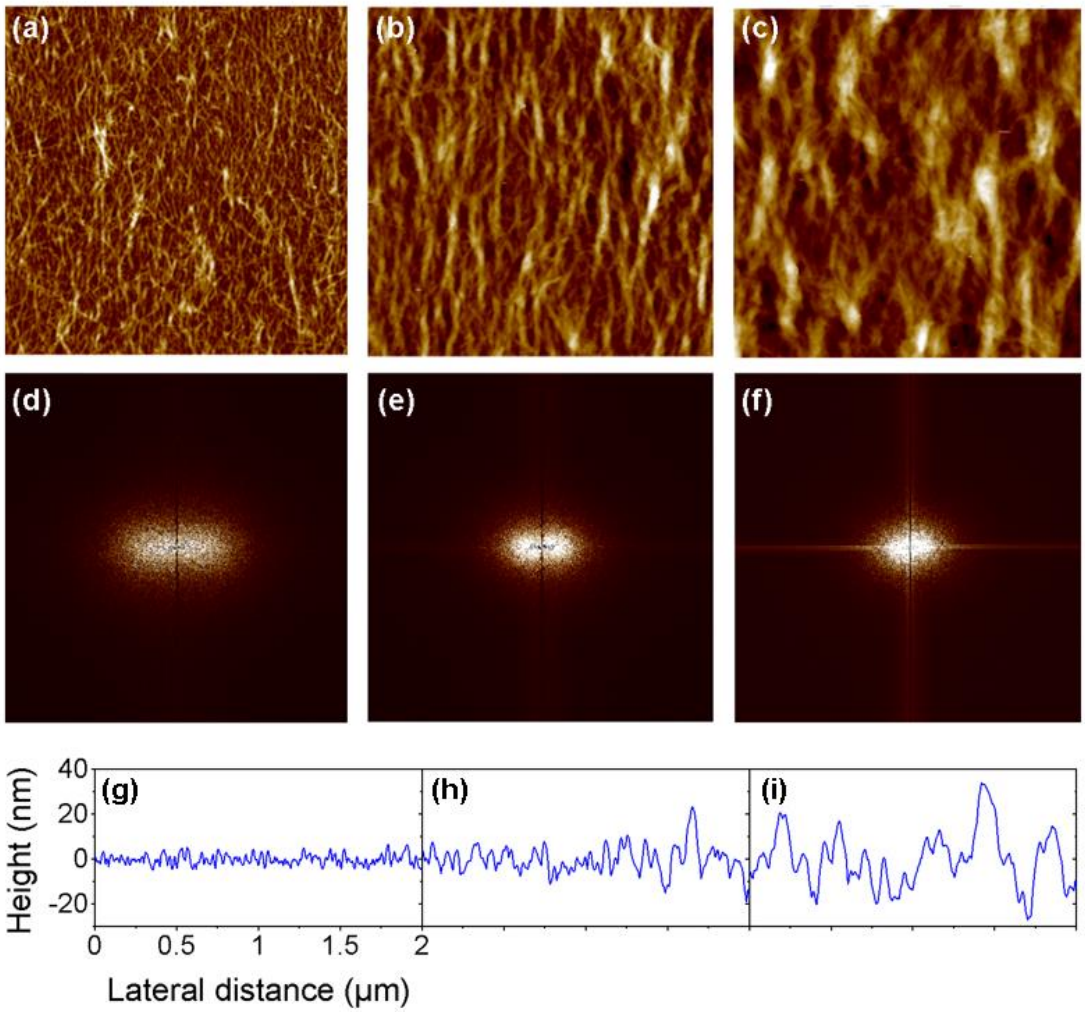

Figure 3.16: Topographical AFM of the (a) first CNF layer, (b) second CNF layer, and (c) third CNF layer of a $(CNF/PVAm)_n$ film prepared by spraying all cellulose layers in parallel directions (PVAm at pH =10). Images size 2x2 μm^2, vertical ranges of 15 nm, 42 nm, and 71 nm, respectively. (d – f) Fast Fourier Transform of the images (a), (b), and (c), respectively. (g – i) Height profiles extracted at the center of the AFM images in (a), (b) and (c). Scales are shown on the left panel.

The degree of parallel alignment of the nanofibrils can be inferred, though, from the elongation of the Fast Fourier Transform (FFT) of the AFM images (panels (d) to (f) in Figure 3.16). The

longest the oval feature of the FFT gets, the higher the degree of alignment of the corresponding AFM image.

Figure 3.17 shows the evolution of the thickness and roughness of the multilayer samples. Analogous to the samples prepared by conventional spraying, the films prepared by GIS using PVAm at pH = 10 grew faster and rougher than the films prepared at lower pH. Moreover, none of them showed significant growth differences associated with the angle of the in-plane orientation of the CNF layers. On the contrary, the roughness of the film prepared at pH = 10 was higher when the cellulose layers were sprayed in alternated perpendicular directions. At lower pH, the roughness was independent of the orientation of the CNFs.

The fast development of the surface roughness (that surpasses a tenth of the film thickness) together with the inability to distinguish individual nanofibrils as the multilayer gets thicker leads to questioning the ability to impart orientation on the top layers of thick films. However, the detection of orientation by OrientationJ and by FFT suggests the retaining of the microscopic alignment of the reinforcing phase, although in the form of bundles instead of individual fibrils.

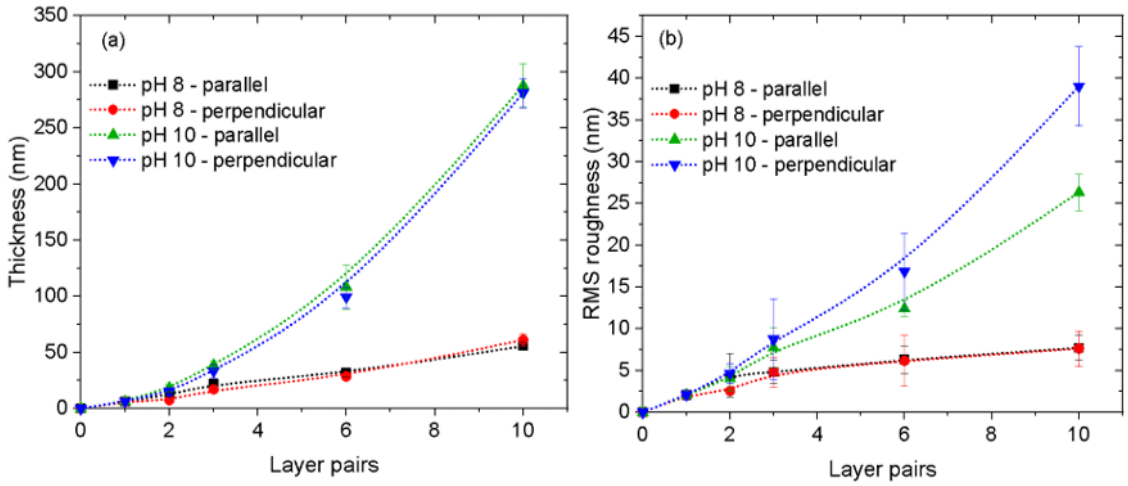

Figure 3.17: Variation of (a) thickness and (b) RMS roughness for two sets of samples as a function of the pH of PVA, the number of layer pairs, and the orientation of the CNF layers in multilayer systems (parallel and perpendicular layers). Dotted lines are guides for the eye.

3.2.3. Alignment of CNCs

Even though the present work focuses on the preparation of nanocomposite films with cellulose nanofibrils, we recognize the increasing interest within the scientific community for other forms of nanocelluloses, particularly for the rod-like nanocrystals (CNCs), as introduced in Chapter 1. In the present section, we demonstrate that these nanoparticles can also be aligned by means of the grazing incidence spraying technique. We worked with a suspension of CNCs extracted from tunicates and kindly provided by Bruno Jean (CERMAV, Grenoble, France). To characterize their size distribution, CNCs were deposited on PDDA-coated silicon wafers from highly diluted suspensions and imaged by AFM. A representative AFM image used in the morphologic characterization is shown in Figure 3.18 along with the obtained distributions of height and length. The measurement of more than 100 individual and isolated nanocrystals revealed that the CNCs used in the present study have a median height of 11.0 nm (IQR 8.7 – 15.0 nm) and a median length of 1390 nm (IQR 850 – 1980 nm), which results in an aspect ratio of approximately 115 (IQR 72 – 190).

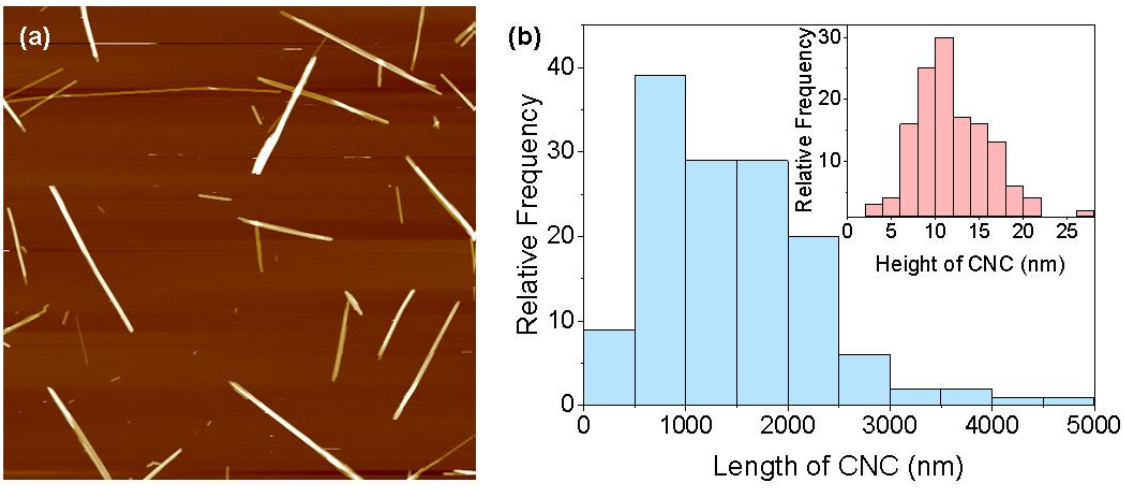

Figure 3.18: (a) Representative AFM image of single cellulose nanocrystals deposited from diluted suspensions onto PDDA-coated silicon wafers. Image size: 5 x 5 μm^2. Vertical scale: 40 nm. (b) Distributions of length and height of the CNCs.

Following the same methodology used to study the effects of the spraying parameters on the alignment of the cellulose nanofibrils, we prepared monolayers of anionic CNCs deposited on

PDDA-coated silicon wafers by grazing incidence spraying. In this case, only three process parameters were varied: the concentration of the CNC suspension (*C*), the airflow rate of the compressed air (*AF*), and the spraying time (*t*). The flow rate of the suspension, the incidence angle, and the distance of the nozzle to the sample were kept constant at 1 mL/min, 10°, and 1 cm, respectively. Each factor was studied at two levels representing the two extreme setting conditions. Figure 3.19 shows an AFM image taken at the center of the sample displaying the preferential alignment of the nanocrystals, as further demonstrated by the elongated shape of its FFT.

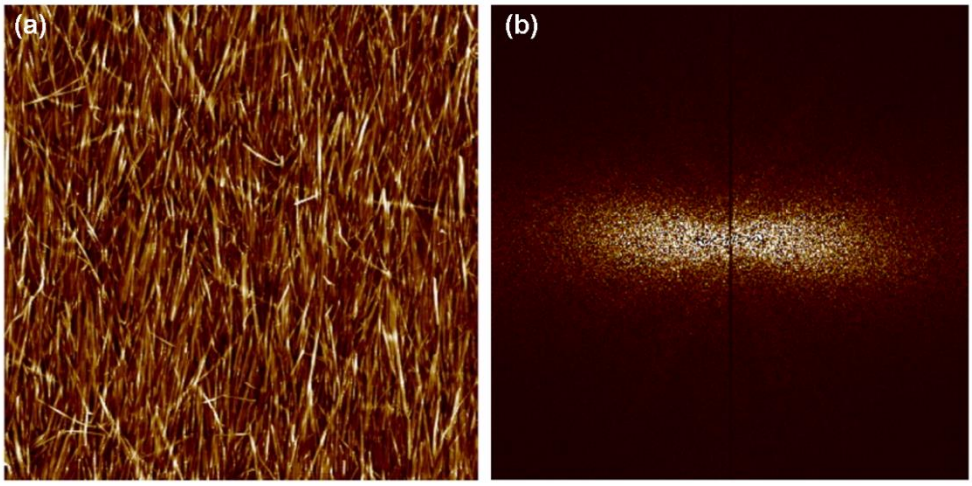

Figure 3.19: (a) AFM image of aligned CNCs using condition #8 in Table 3.3 (AF = 40 L/min, t = 45 s, C = 1 mg/mL). The image size is 8x8 μm^2 and the vertical range is 43 nm. Spraying direction pointing up. (b) Fast Fourier Transform of the image in (a).

The eight possible combinations of the factor levels are shown in Table 3.3 together with the average values of the studied responses. The alignment of the nanocrystals was characterized by the 2D nematic order parameter (S_{2D}) calculated from the image analysis of AFM pictures taken at the center of the samples. The underlying silicon wafer was visible in most of the AFM images, unlike in the case of the flexible nanofibrils, which allowed us to investigate the fraction of the surface covered by the CNCs as one of the studied responses. Analysis of variance showed statistically significant differences among some of the groups for both responses: $F_{S\text{-}parameter}$ (7, 8) = 4.78, p = 0.021, and $F_{coverage}$ (7, 8) = 4.90, p = 0.020. However, the minimal difference among

the mean values of S_{2D} suggested that this statistical significance was meaningless in practice and therefore we concluded that an excellent alignment of CNCs ($S_{2D} \approx 0.9$) can be attained independently of the combination of spraying parameters used, as long as they are set within the studied ranges. This confirms the expected enhanced ease of alignment of the nanocrystals compared to the nanofibrils owing to their rigidity.

Table 3.3: Design layout of the experiment with response values for the monolayer of CNC.

	Factor levels			**Response**	
Run	**Airflow (AF) [L/min]**	**Spraying time (t) [s]**	**Concentration (C) [mg/mL]**	**S_{2D} parameter**	***Coverage***
1	25	15	0.2	0.87 ± 0.01	58.49 ± 1.41
2	40	15	0.2	0.86 ± 0.03	46.20 ± 1.33
3	25	45	0.2	0.89 ± 0.01	50.83 ± 1.48
4	40	45	0.2	0.91 ± 0.01	52.47 ± 0.70
5	25	15	1.0	0.91 ± 0.01	86.90 ± 0.71
6	40	15	1.0	0.90 ± 0.01	76.99 ± 1.53
7	25	45	1.0	0.91 ± 0.01	66.29 ± 1.27
8	40	45	1.0	0.92 ± 0.01	68.71 ± 0.71

Figure 3.20(a) presents the Pareto plot of the effect of the spraying parameters on the surface coverage of the nanocrystals. It shows that the concentration of the CNC suspension was the most important parameter controlling the surface coverage. On the contrary, the airflow rate was not significant as better revealed by the main effects plot of Figure 3.20(b). Additionally, the most significant interaction was that of *AF*t*, shown in Figure 3.20(c). The fact that a higher fraction of covered surface is reached when using shorter spraying times suggests that the deposited CNCs might be also removed by effects of the shear forces, implying that the GIS is a harsher methodology for the rigid CNCs than for the flexible CNFs.

As for the extent of the effective alignment of CNCs, both the S_{2D} parameter and the surface coverage were measured at different spots along the centerline of the sprayed area. The obtained results are presented in Figure 3.21; both parameters decreased significantly with the increasing distance from the top border.

Finding optimum spraying conditions to maximize the surface coverage without compromising the good alignment of the CNCs was out of the scope of the present work. However, we have

demonstrated that good alignment of cellulose nanocrystals by using GIS is possible. Before going back to the study of the multilayer films of CNFs, we demonstrated also the effective independent alignment of a second CNC layer. For doing that, PVAm at pH = 10 was used as polycation and three different angles of in-plane rotation between the successive layers were used, namely 0°, 45°, and 90°. Representative AFM images of the top layer taken at the center of the samples are displayed in Figure 3.22. The color surveys obtained from OrientationJ allowed better visualization of the direction of the preferential alignment of the nanocrystals. Moreover, since the CNCs do not cover completely the film's surface, the orientation of the beneath layer can be

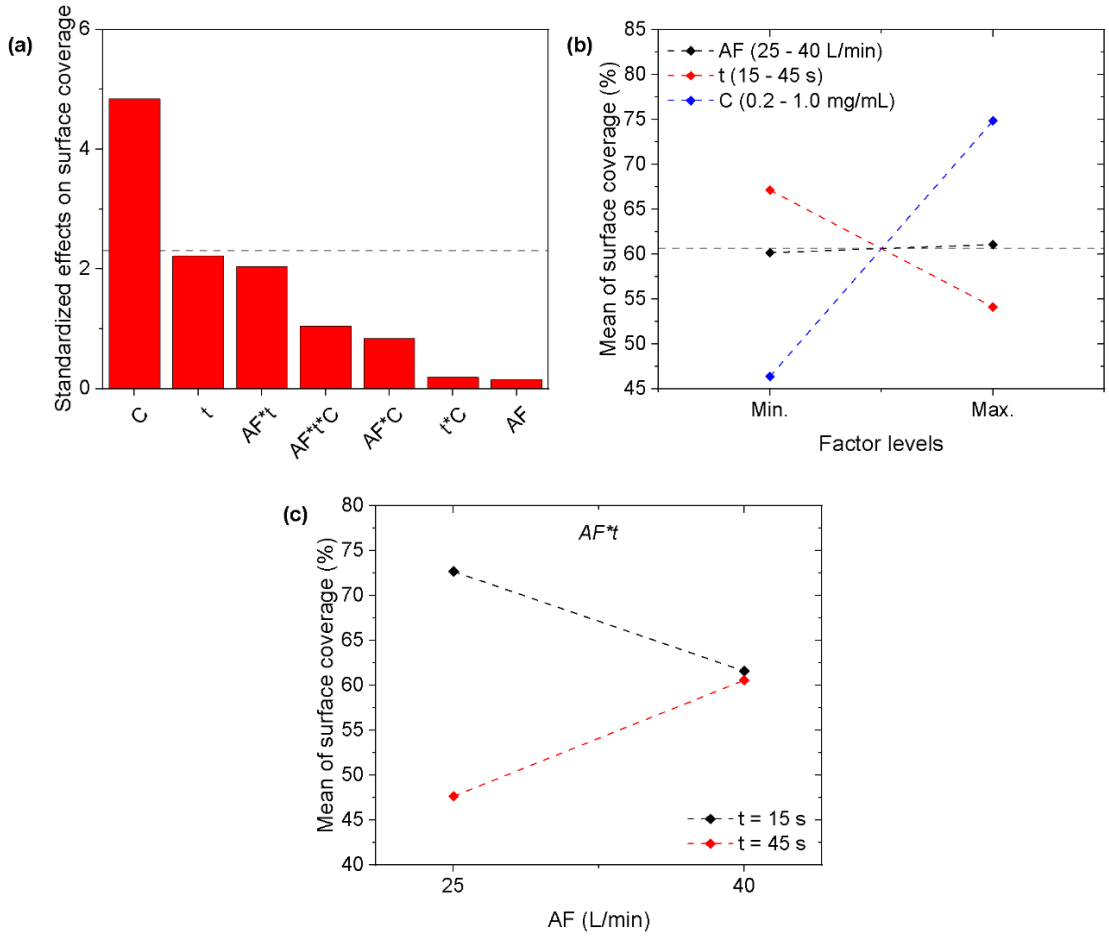

Figure 3.20: (a) Pareto chart representing the effect of the different process parameters of the grazing incidence spraying on the value of the surface coverage of CNCs. (b) Main effects plot showing how different levels of the studied factors affected the mean value of the surface coverage. Dashed lines are guides for the eye. (c) Interaction plot of the airflow rate and the spraying time.

also detected in some of the images. This is particularly evident in the pictures of the samples prepared with perpendicular directions of both CNC layers. Beyond the visual analysis of the AFM images, the comparison of the distribution of the preferential angle of orientation shown in Figure 3.22 also demonstrates the independent alignment of the two nanocrystal layers. In the case of parallel alignment, a unique strong peak at 0° was obtained. At 45°, a smaller and broader peak was observed as a consequence of the detection of the below-layer; the position of the peak was not at 45° due to the alignment of the sample on the AFM stage. Finally, for the sample prepared with two perpendicular CNC layers, two small peaks shifted by 90° were observed corresponding to the orientation of both layers.

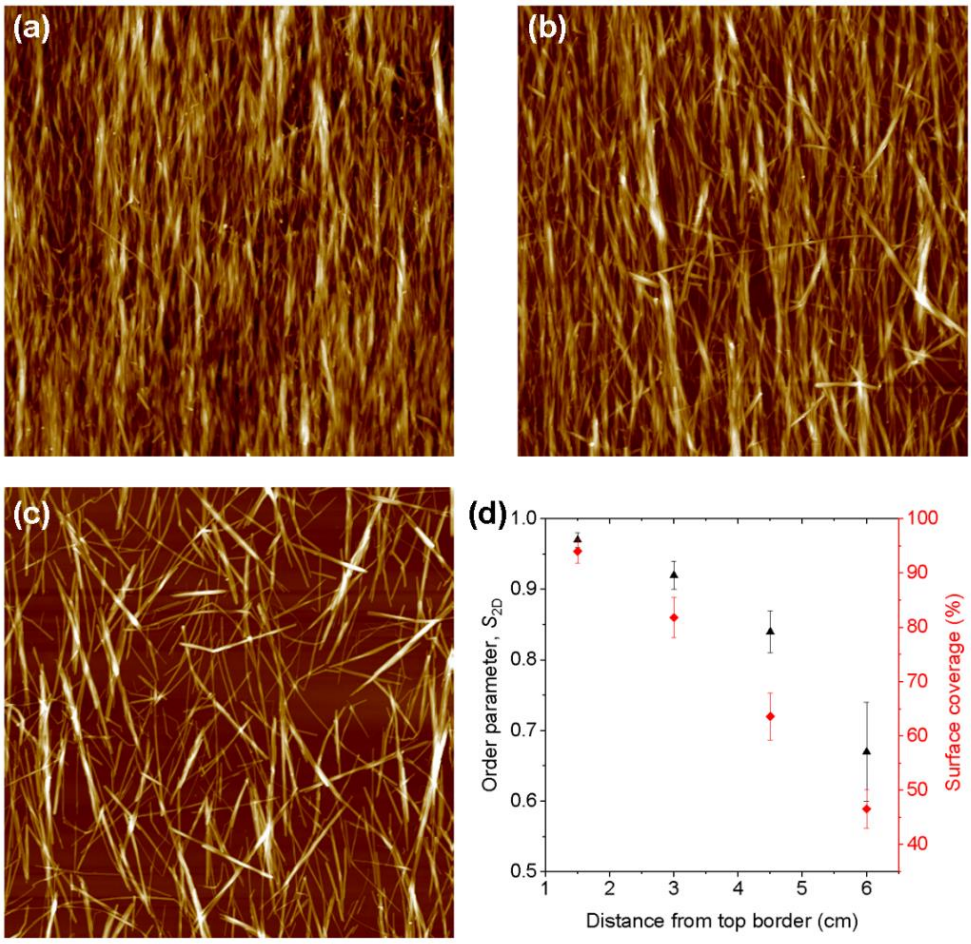

Figure 3.21: AFM images of CNCs sprayed by GIS over PEI-coated silicon wafers taken at 1.5 cm (a), 3 cm (b), and 6 cm (c) from the top border of the sample. Spraying direction pointing up. The size of the images is 8x8 μm^2 and the z-range is 100, 110, 75 nm, respectively. (d) Variation of the order parameter (black triangles) and the surface coverage (red diamonds) of CNC monolayers as a function of the distance from the top border of the sample.

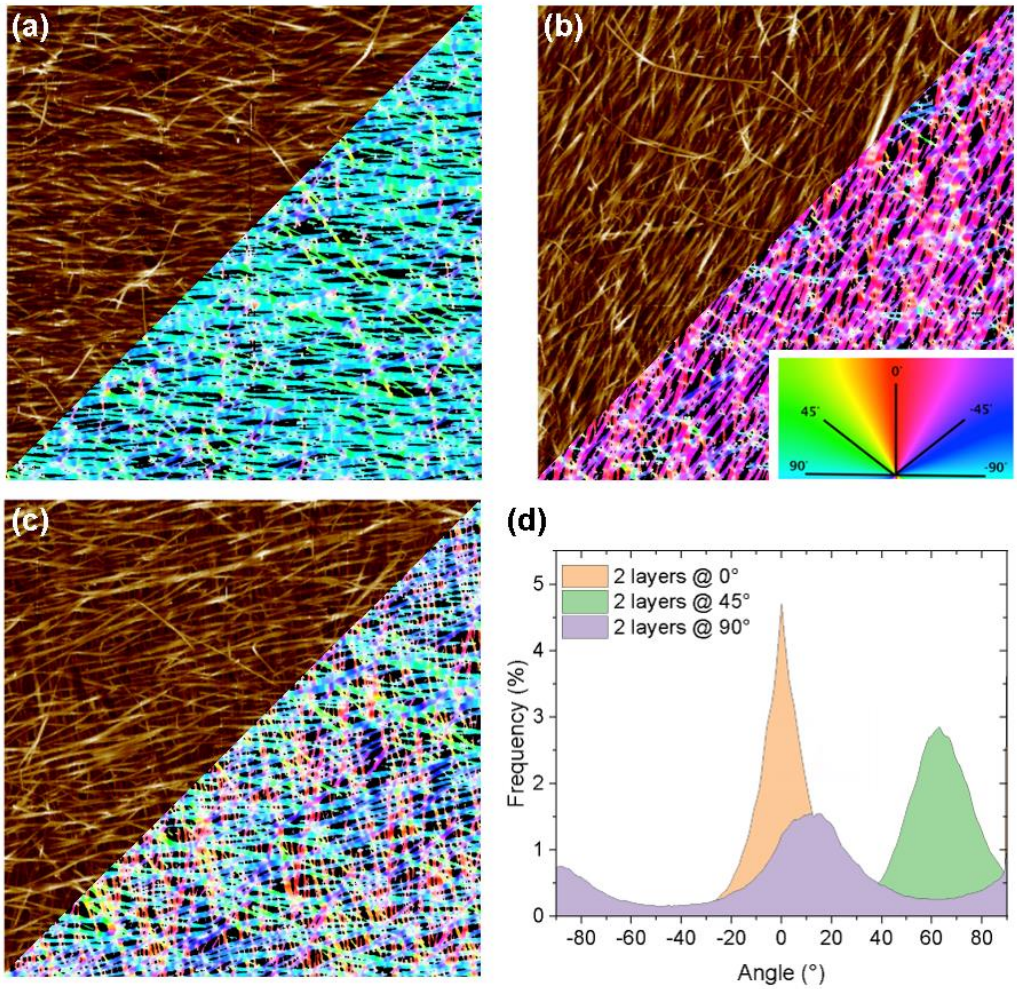

Figure 3.22: Representative AMF images of the second layer of CNCs sprayed at (a) 0°, (b) 45°, and (c) 90° with respect to the direction of the below layer. Half of the images are superimposed with the color surveys determined by image analysis with OrientationJ for better visualization of the direction of alignment. All images are 8 x 8 μm^2. (d) Distribution of orientation extracted by image analysis with OrientationJ of the AFM images in (a) to (c).

3.2.4. Thick CNF-based multilayer films

3.2.4.1. Unidirectionally-aligned films

After having studied how the degree and direction of orientation of the cellulose nanofibrils vary in monolayers (§ 3.2.1), we were interested in preparing micron-thick oriented films that could be used for characterizing their mechanical properties. Films with 100 layer pairs, $(CNF/PVAm)_{100}$, were prepared by spraying all CNF layers in the same direction using the

optimum spraying conditions previously identified. PVAm was sprayed at pH = 10 for faster film growth.

A concentric pattern of interference colors developed and became clearer with the increasing number of layers, as shown in the optical pictures of Figure 3.23. Thin-film coloring resulting from constructive interference of light reflecting off the film's surface and off the substrate interface is related to the thickness of the film (*d*) and the wavelength of the light (λ) through Bragg's law:

$$2d\ sin\theta = n\lambda \qquad \text{(Eq. 3.4)}$$

where θ is the angle of incidence. Therefore, homogeneity of the observed colors is commonly associated with the uniformity of the LbL film thickness at the microscale.[87] The disparate color fringes observed on the reflection pictures of Figure 3.23 can, thus, be ascribed to differences in the film thickness as a result of the spraying pattern. This was verified by measuring the film thickness by ellipsometry at increasing distances along the central axis of the sample and following its evolution at different stages of the film build-up (Figure 3.24). The film thickness decreased over the distance from the top border. Moreover, the difference between the initial and the final measured points accentuated with the number of deposited layers, indicating that more material deposited at the beginning of the spraying cone. When the sample started becoming too

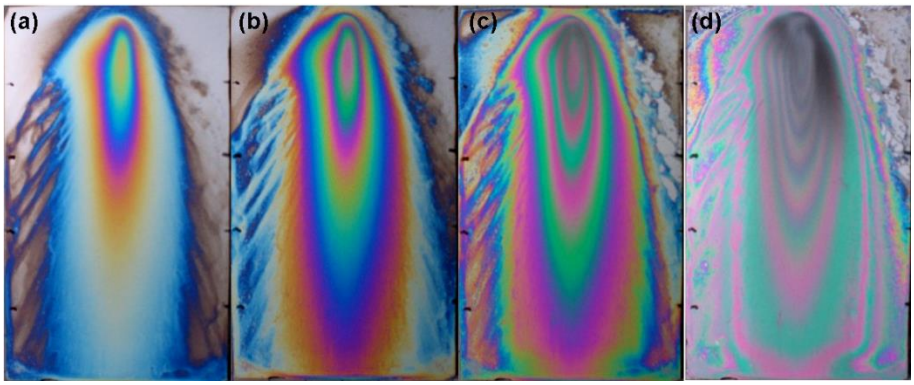

Figure 3.23: Optical images of the colored patterns observed in the unidirectionally sprayed GIS-samples with the increasing number of layer pairs (LP): 20 LP, 30 LP, 50 LP, and 100 LP (from (a) to (d)). The development of opaque areas around the initial impact area of the spraying cone is visible at the top of the image (d).

thick (~1µm), i.e. after the spraying of several tens of layer pairs, the interference colors were hidden by the development of a grey coloration probably due to the scattering of light by the increasing roughness of the surface. Particularly, in the vicinity of the initial impact area of the spraying jet, a blackened area developed probably associated with the harshness of the spraying process in this area. When the film started becoming opaque, the ellipsometry model no longer fitted the experimental data, so it was not possible to determine the thickness of these grey areas.

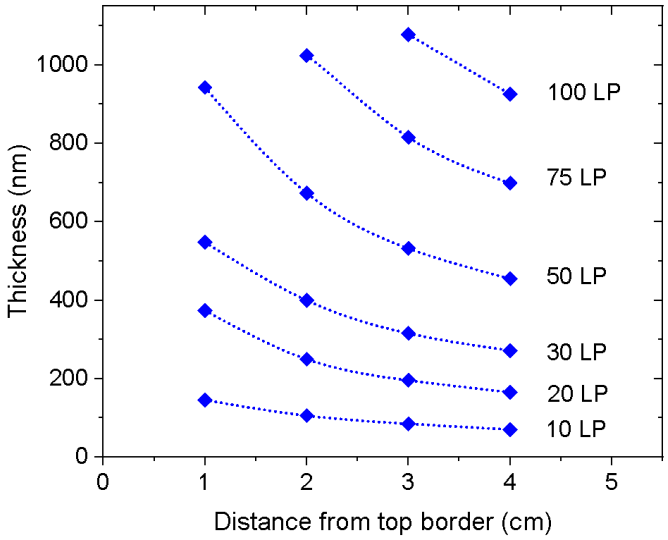

Figure 3.24: Thickness profiling of the unidirectional $(CNF/PAVam)_{100}$ sample with increasing distances along the central axis of the sample (measured from the top border) at different stages of the film buildup. Dotted lines are guides for the eye.

For the fabrication of thick unidirectional films with homogeneous thickness, an alternating 180° rotation of the spraying direction between consecutive CNF layers was adopted although this approach did not prevent the formation of opaque films (Figure 3.25(a)). Transmittance measurements on unidirectionally-aligned multilayer films prepared on quartz slides showed that the decay of the transparency with the increasing number of layer pairs was linear and much steeper for samples prepared at pH 10 than at pH 8 (Figure 3.25(b)).

Cross-sectional SEM and topographical AFM images (Figure 3.26) of the sample shown in Figure 3.25(a) exposed the development of roughness features comparable to the thickness of the film, which was judged excessive for what would be expected as intrinsic roughness of the multilayer

system, particularly when compared with the natural roughness of similar samples prepared by other fabrication methods such as dip-assisted or spin-assisted assembly.[167,204] Thus, the grey coloration observed in the thick sprayed samples was ascribed to the scattering of light on the excessively rough features of the film surface. Similar excessive roughness and grey coloration were also observed in thick CNF-based films prepared by orthogonal spraying, so this issue seems to be associated with the spraying process in general, and it is not exclusive to GIS.

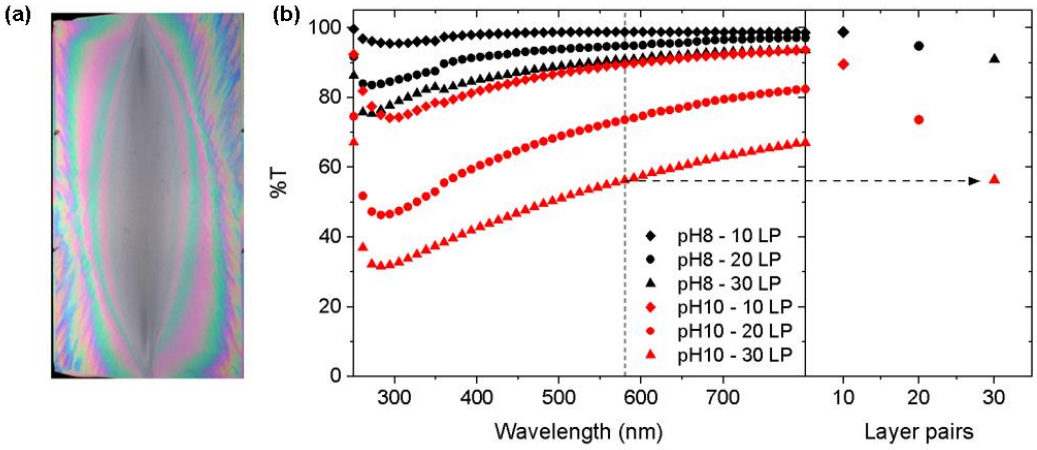

Figure 3.25: (a) Optical image of a unidirectional sample $(CNF/PVAm)_{100}$ sprayed with an alternated 180 degree rotation of the nozzle between consecutive CNF layers. The sample is 7 cm long. (b) Transmittance spectra of unidirectional samples prepared on quartz. Spectra recorded at three different stages of the build-up of the films (left panel) along with the corresponding %T measured at 580 nm as a function of the number of layer pairs (right panel).

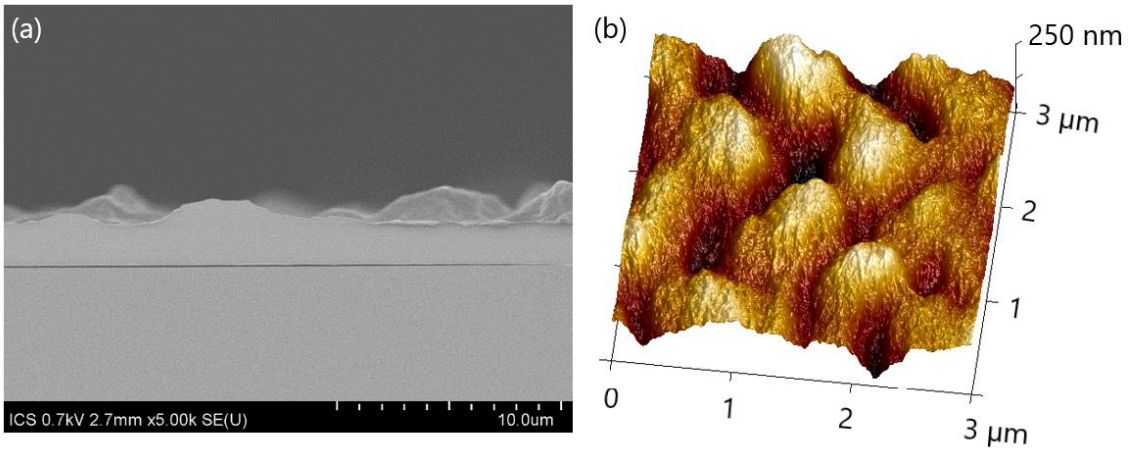

Figure 3.26: (a) Cross-sectional SEM image and (b) 3D topographical AFM rendering acquired at the center of a $(CNF/PVAm)_{100}$ multilayer film prepared by unidirectional GIS.

The variation of the spraying parameters (e.g. the concentration of the CNF suspension, spraying times, airflow rate, etc.), spraying conditions (rinsing and drying cycles), or salt concentration of the PVAm solution did not prevent the formation of opaque films, as judged qualitatively (with the naked eye). The pH during the buildup of the film was the only parameter found to influence the level of attained roughness, as demonstrated by comparing the topographical AFM images and the height profiles shown in Figure 3.27. A film prepared with PVAm at pH = 10 was found to be almost three times rougher than a film prepared at pH = 8, even though the thickness of the former was almost half that of the latter. We believe that the development of the excessive roughness of the thick spray-assisted films might be due to swell-induced instabilities as the ones reported for thin hydrogel layers supported on rigid substrates,[223–225] however a thorough investigation that goes beyond the scope of the present work would be necessary to understand and prevent the formation of such rough and opaque sprayed films.

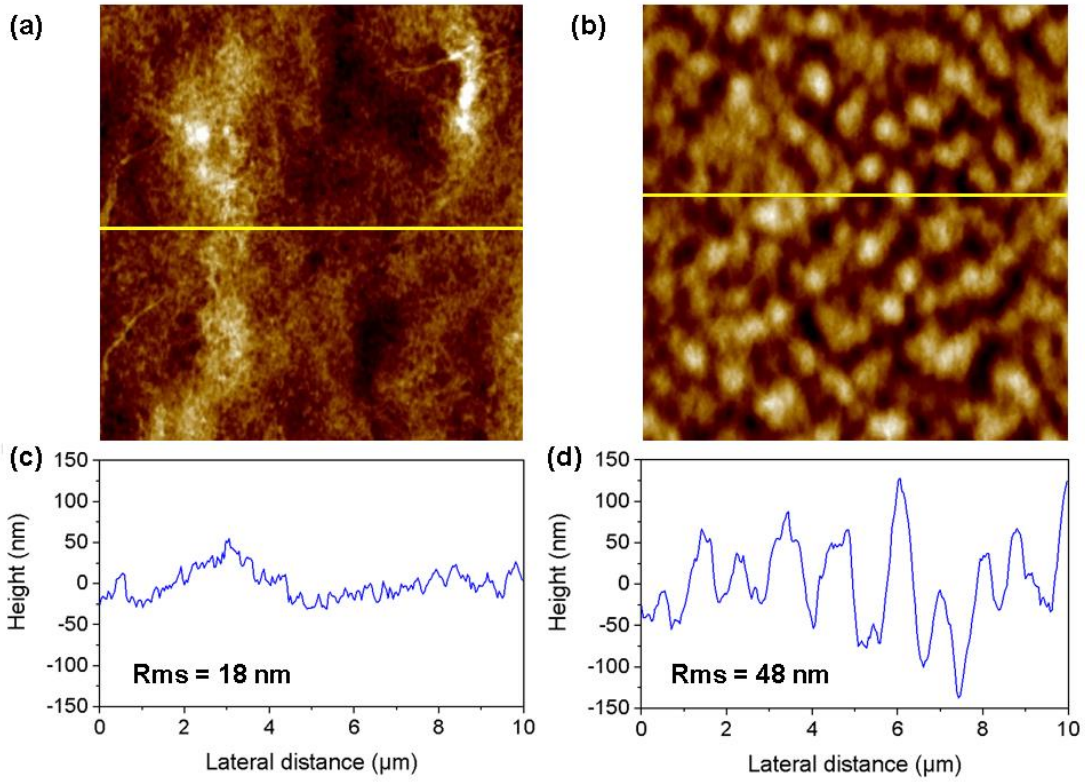

Figure 3.27: Topographical AFM images of (a) an 800-nm thick unidirectional $(CNF/PVAm)_{70}$ film prepared with PVAm at pH = 8, and (b) a unidirectional $(CNF/PVAm)_{30}$ film prepared with PVAm at pH = 10 (~490 nm thick). Images size is 10x10 μm^2, vertical ranges of 150 nm and 350 nm, respectively. (c) and (d) Height profiles extracted at the location of the yellow lines shown in (a) and (b), respectively.

To verify the unidirectional alignment of the CNFs in the thick sample shown in Figure 3.25(a), the center of the film was observed between crossed-polarizers under a polarized light microscope. Micrographs were obtained at different angles of in-plane rotation around the central point and they were numerically analyzed to quantify the brightness of the surface as a function of the azimuth angle. Figure 3.28(a) and (b) show the reflection optical micrographs taken at a rotation of 45° and 0°, respectively, zero degrees corresponding to the parallel alignment of the first polarizer with respect to the spraying direction. As expected for an anisotropic sample, the total extinction of light occurred when the spraying direction (and therefore fibril orientation) was parallel to either polarizer, while maximum reflection occurred every 45° rotation with respect to both polarizers. The relative intensity of the reflected light is presented in Figure 3.28(c) as a function of the azimuth angle. For comparison, the results obtained for a control sample prepared by conventional orthogonal spraying without preferential alignment of the CNFs are also shown. The optical anisotropy detected in the unidirectionally-oriented sample is a consequence of the structural anisotropy of the material, therefore it confirms that the in-plane alignment of the CNF layers was maintained in the sub-micron range instead of being destroyed by the developed roughness as it could be presumed. As discussed previously, the anisotropic alignment of the nanofibrils within the multilayer film may not be in the form of individual nanofibrils stacked in idealized stratified layers but more probably as intertwined bundles of them.

Previous data reported by our group on the angular variation of the relative brightness of a pure polysaccharide (CNF/chitosan) anisotropic multilayer film showed an unexpected asymmetric response in which the reflected intensity measured upon rotation of the sample to the right was about 3.5 times smaller than the one measured upon similar rotation to the left.[168] This puzzling observation was tentatively attributed to the effect of the intrinsic chirality of the film components. Our results on the CNF/PVAm system did not show such asymmetric response and the small differences, judged negligible, among the brightness peaks in Figure 3.28(c) are ascribed to inexact parallel alignment of the optical axis of the sample with the direction of the polarizer.

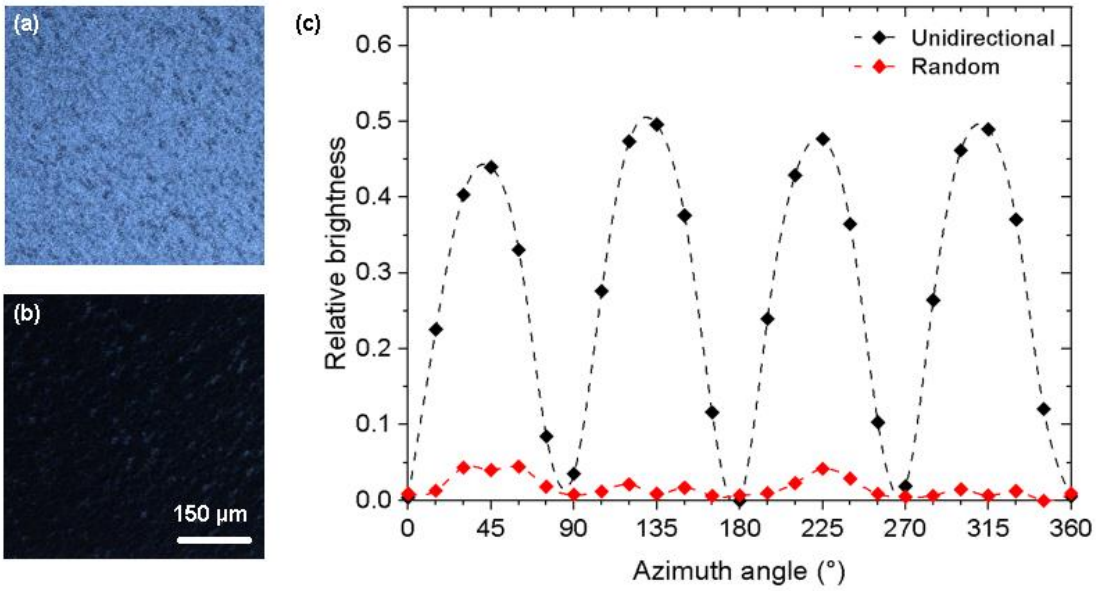

Figure 3.28: Optical micrographs taken between cross polarizers at the center of the unidirectional $(CNF/PVAm)_{100}$ film when the angle between the spraying direction and the polarizer was (a) 45° and (b) 0°. (c) Angular variation of the relative brightness for random and unidirectionally-oriented films.

We also remarked that the intensity of the light reflected off the random sample did not show an ideally isotropic response. A minor peak at 45° (≈ 225°) confirms our suspicions that the samples prepared by orthogonal spraying are not perfectly random but instead, they exhibit a weak anisotropy resulting from the drainage flow of the polyelectrolyte solutions.

3.2.4.2. CNF-based films with a cross-ply structure

The next step was to prepare a sample with a cross-ply alignment of the CNF layers, i.e., a sample in which the orientation of every cellulose layer was rotated by 90° with respect to the adjacent layers. 80 layers of cellulose were sprayed by GIS (using the optimum parameters already discussed) in combination with PVAm at pH = 10 sprayed orthogonally to the silicon wafer. A reflection picture of the sample is shown in Figure 3.29(a), in which the fringed color pattern took the shape of a cross. Optical micrographs taken at the center of the sample between cross-polarizers at different azimuth angles showed an optical isotropic behavior (Figure 3.29(b)), comparable to that of the random sample shown in Figure 3.28(c). When the micrographs were taken outside the center of the sample (4 mm and 8 mm away along the spraying axes), an

anisotropic response was detected, characterized by maximum reflection and total extinction of light alternating every 45° of in-plane rotation. Thus, demonstrating that the sample was indeed oriented in both spraying directions. The slight difference in the intensity peaks at 45° and 225° with respect to those at 135° and 315° might be due to non-perfectly symmetric spray patterns (as effectively observed qualitatively during the preparation of the samples) or the offset of the imaging spot with respect to the optic axis of the sample.

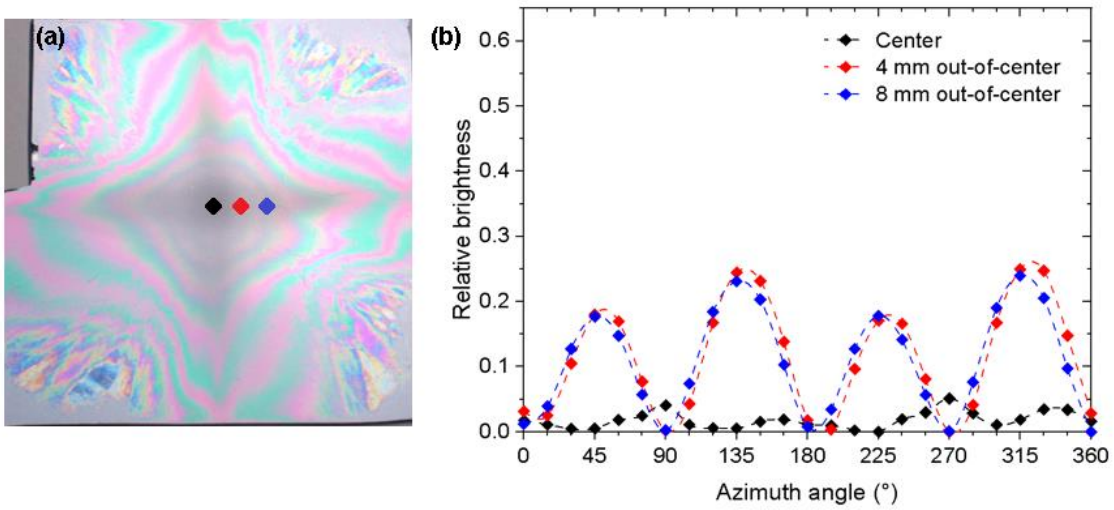

Figure 3.29: (a) Optical micrographs of the $(PVAm/CNF)_{80}$ film with a cross-ply structure. (b) Angular variation of the relative brightness measured in images taken under crossed polarizers at the center and at 4 mm and 8 mm away along the spraying axes from the center of the film shown in (a).

3.2.4.3. Helicoidally aligned film

Finally, we prepared helicoidally-oriented $(CNF/PVAm)_n$ films by rotating the spraying direction of the CNF suspension by a constant angle after every set number of layers. The rotational angle could be selected either clockwise or counterclockwise to deliberately fabricate films with either handedness. Moreover, the pitch of the helicoid could be tailored by adjusting either the angle of in-plane rotation between layer stacks or the number of mono-oriented stacked layers between rotations, or both. Although the film growth was slower the lower the pH of the PVAm solution, all helicoidally aligned films discussed throughout this work were prepared at pH = 8 to guarantee a better surface quality.

When helicoidal films were sprayed, the fringed color patterns due to the gradient thickness took the shape of concentric circles as visualized in Figure 3.30. The variation of the relative brightness measured at different azimuth angles both at the center of the sample and out-centered by 8 mm for a sample with two helicoidal right turns is shown in Figure 3.30. As for the cross-ply sample, the relative brightness detected out of the center demonstrates that the CNF layers are aligned. At the center of the sample, weaker variations in the relative brightness at different angles were detected, having a maximum every 180° rotation. This could be understood as the combination of constructive and destructive interferences of the reflections from the different oriented layers within the film.

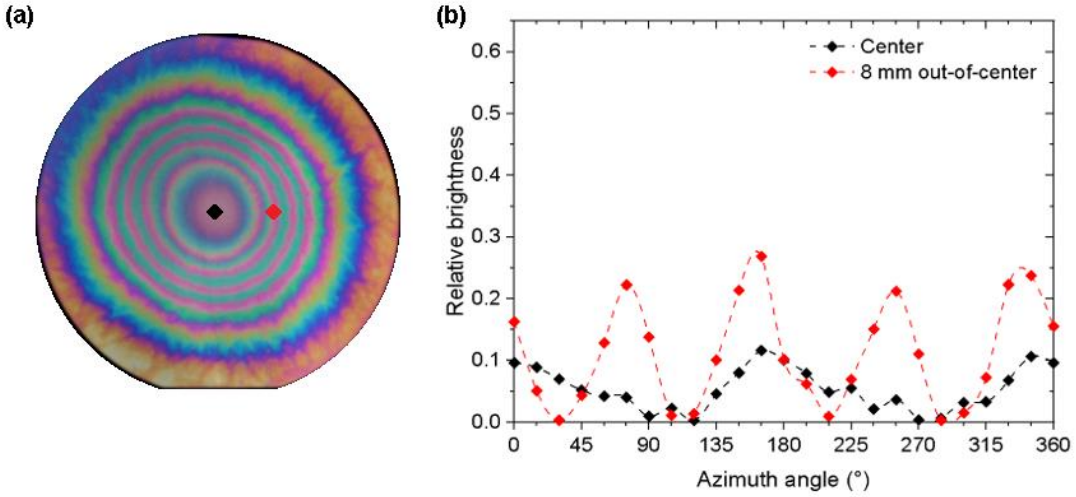

Figure 3.30: (a) Optical photograph showing the interference colors observed for a right-handed helicoidal film composed of 144 layers pairs with 2 turns (rotation of 5° after each layer pair). The film has a thickness of 1470 nm ± 60 nm, as determined by ellipsometry. (b) Angular variation of the relative brightness measured in images taken under crossed polarizers at the center and at 8 mm away from the center of the film shown in (a).

To verify the helicoidal alignment of the CNFs within the films, cross-sectional SEM pictures were acquired with the aim to observe the twisting pattern of the nanofibrils. A sample with two helicoidal turns, one to the left and one to the right, of 500 nm theoretical pitch was sprayed on top of a dipped-prepared film (for the purpose of increasing the total thickness of the film). This pitch was accomplished by rotating the spraying direction by 15° after every two unidirectionally-

sprayed layers of the CNFs. A representative SEM image of the cross-section of the film is presented in Figure 3.31(b). The very small diameter of the nanofibrils (1 – 2 nm) and possibly the high level of hydration of the film prevented the direct observation of a conceivable twisting pattern of the CNFs, in spite of the protocol adopted to try to obtain a brittle fracture of the film without distortion of the internal structure (namely, dehydration, rupture under liquid nitrogen, and crosslinking with glutaraldehyde). Nevertheless, a 4-layered ultrastructure was easily distinguished in all the images, whose number and dimensions corresponded to the half-pitch of the helicoid as schematically depicted in Figure 3.31(a). This stratification was interpreted as being caused by the difference in the rupture behavior of the periodical layers aligned parallel to the fracture plane compared with the layers aligned in any other direction, and it was thus accepted as indirect evidence of the successful helicoidal alignment of the CNFs with the desired characteristics. In the next chapter, we will present further proofs of such helicoidal alignment based on optical characterization methods.

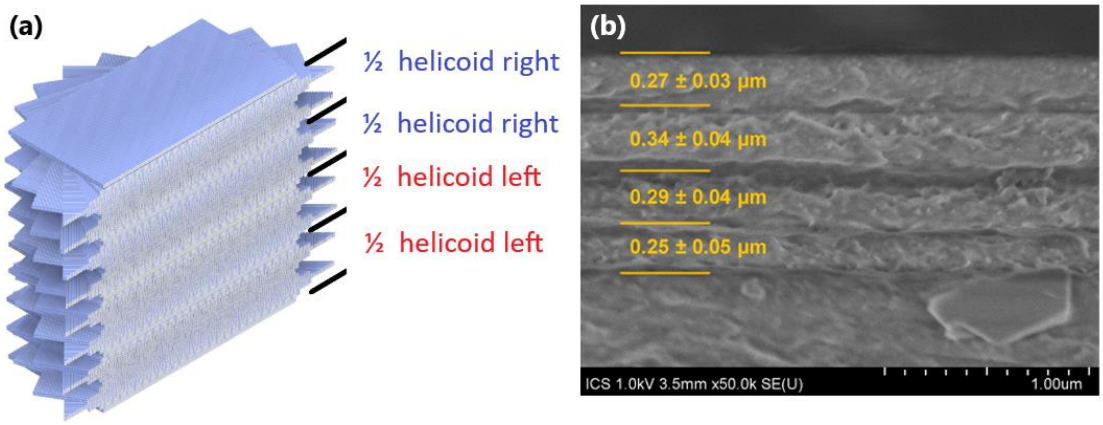

Figure 3.31: (a) Cross-sectional isometric view of a 3D rendering of the twisted cross-plywood configuration of the CNFs in the prepared helicoidal film. This 3D model was prepared by CAD by stacking 10-nm thick layers of parallel cylinders following the same alignment sequence as the experimental sample. (b) Cross-sectional SEM image of the helicoidal sample exhibiting a 4-layered ultrastructure corresponding to four half-pitches of the helicoids. The thickness of these thick sub-layers was measured in multiple locations in at least six different pictures, the errors shown correspond to the standard deviation of the measurements.

Based on the combination of the grazing-incidence spraying technique and the layer-by-layer fabrication approach we have successfully prepared isotropic and anisotropic CNF-based

composite films with an increasing complexity of the internal arrangement of the reinforcing nanofibrils. In the following chapter, we use optical characterization methods to further investigate the internal structures of the GIS-LbL films as well as the optical properties resulting from the conscious alignment of the CNFs.

Chapter 4. Optical characterization of GIS-structured CNF-based films

In the previous chapter, we verified the independent alignment of the CNF layers within films prepared layer-by-layer, which enabled the fabrication of thin films possessing complex internal arrangements of the reinforcing nanofibrils. In the present chapter, we rely on optical characterization techniques to (*i*) verify the internal structure attained in the GIS-LbL films and (*ii*) investigate their optical behavior. We characterize the transmittance, the circular dichroism, and the Mueller matrix of thin $(CNF/PVAm)_n$ films prepared on quartz slides using the optimum GIS conditions discussed in Chapter 3 (with PVAm at pH 8). We focused on two types of films that are considered the most elementary structures that can be fabricated by the deliberate rotation of the aligned CNF layers, namely samples with either a unidirectional or a helicoidal arrangement of the reinforcing nanofibrils. We envision that these two superstructures might be stacked in different combinations for the fabrication of thin films with even more complex architectures to achieve specific photonic responses. The measured properties were compared to a control sample prepared by dip-assisted LbL in which the nanofibrils deposited without any preferential orientation or structure (hereinafter referred to as "random" film).

Three main parameters were varied during the preparation of the helicoidal samples, namely the number of consecutive layers of CNF sprayed in the same direction, the angle (α) of in-plane rotation between consecutive layers or stacks of layers, and the handedness of the rotation (see

Figure 4.1). The pitch (*P*) is defined as the thickness accomplished after one turn (360° rotation) of the helicoid; it was varied either by keeping constant the rotation angle and changing the number of consecutive unidirectional layers, or vice versa. The nomenclature used throughout this chapter to refer to the different samples prepared is exemplified by the samples 97R1x15° and 50L2x30°, where the former denotes a right-handed (R) helicoidal film composed of 97 CNF/PVAm layer pairs and prepared with a 15° rotation after every single CNF layer, while the latter denotes a left-handed (L) helical film composed of 50 layer pairs and assembled with a 30° rotation after two consecutive CNF layers.

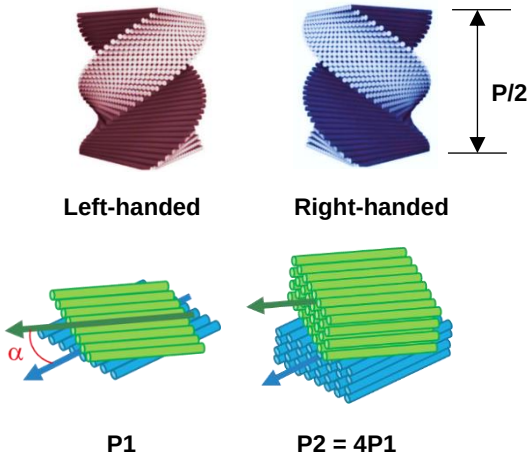

Figure 4.1: Representation of the three parameters varied to modify the helical structure of the samples. The right-handed rotation was considered as a clockwise rotation of the top CNF layers while left-handed rotation indicates counterclockwise rotation.

If not stated otherwise, all film samples were fabricated with 97 CNF/PVAm layer pairs, i.e. the number of layers needed to accomplish four helical turns with an in-plane rotation of 15° after every CNF layer. Given that these films did not absorb light in the UV-vis region, it was not possible to quantify their thickness by spectroscopy. On the other hand, as they were fabricated on transparent substrates, accurate ellipsometry measurements were not possible either with the available ellipsometers (in reflection mode). The thickness of the films was thus estimated by ellipsometry measurements of selected films prepared on silicon wafers using identical fabrication conditions. The thickness growth of all the monitored films was found to be similar indistinctly of the direction of spraying of their layers (Figure 4.2), as it was also observed in the previous chapter (see Figure 3.17). Therefore, a consolidated linear fit was used to predict the

thickness of the $(CNF/PVAm)_{97}$ samples (R^2 = 0.9873). We recall that the growth of the initial layers is typically slower due to the influence of the substrate, that is why the intercept of the linear fit was different from zero. The films grew at a rate of 8.7 nm per layer pair so that the 97-layer pair films were estimated to be around 840 nm thick.

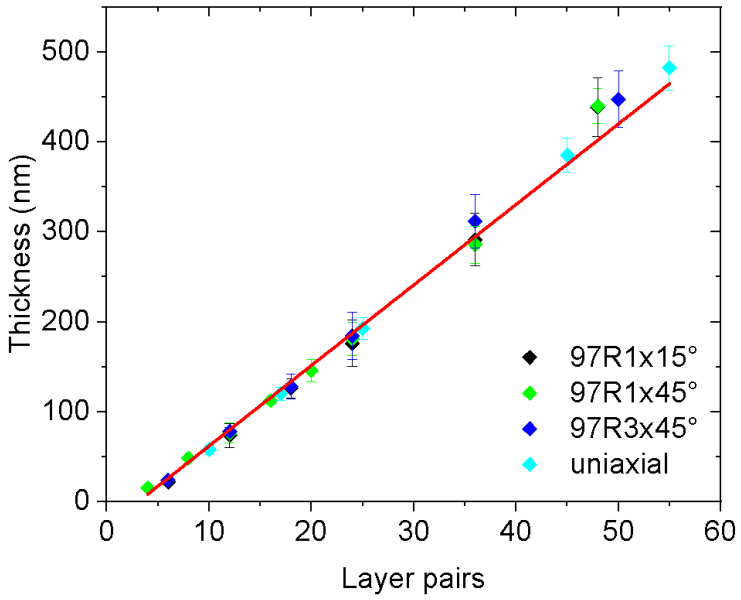

Figure 4.2: Thickness growth rate of $(CNF/PVAm)_{97}$ multilayer films with different internal structures fabricated by GIS on silicon wafers.

4.1. Transparency of CNF-based films prepared by GIS

The transmittance spectra of all the fabricated samples are shown in Figure 4.3(a). The spectra of most of the films were very close to each other and did not exhibit any significant trend related to their internal structures. For the sake of simplicity, an average spectrum for these samples is shown in red along with its standard deviation (error bars). Their total transmittance was between 60% and 80% in the visible range. On the other hand, a sample prepared by dip-assisted LbL having comparable thickness was found to have a transmittance of 97% (black curve). This huge difference in transmittance was ascribed to the scattering of light promoted by the high roughness of the GIS-LbL films discussed in the previous chapter (see Figure 4.3(b)). The average root-mean-square (RMS) roughness determined by AFM on these samples was 81 ± 3 nm.

A couple of helicoidal films prepared in a different batch with several weeks of difference with respect to the rest of the samples were considerably more transparent than the previous samples (green and blue spectra in Figure 4.3(a)). Based on our experience with the spraying system, this difference in transparency was attributed to slight variations in the fabrication conditions rather than to actual differences in the internal structures of the films. In general, GIS-LbL films are highly reproducible in terms of thickness growth, alignment, and roughness. However, we observed that the quality of the films might be sensitive to the precise adjustment of parameters such as the spraying angle, the distance and alignment of the sample with respect to the nozzle, the purity of the solutions/suspensions, the quality of the compressed air, the operator, etc. Therefore, samples prepared by different persons and on different days might present differences in their quality. In spite of this, it is noteworthy that transparency levels comparable to the ones obtained by dipping might be achievable in GIS-films, which encourages the seek for improvements on the GIS-technique.

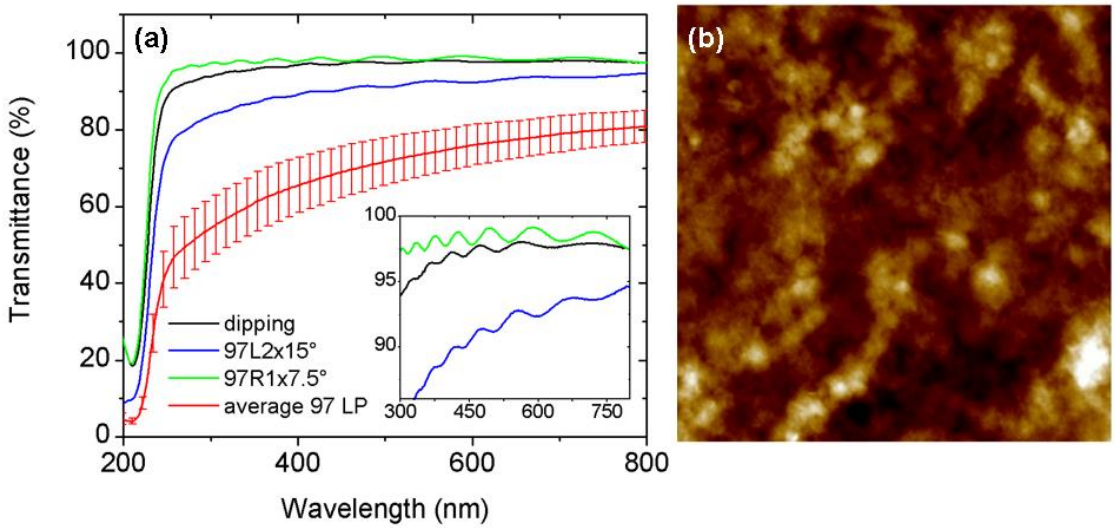

Figure 4.3: (a) UV-visible transmittance spectra of $(CNF/PVAm)_{97}$ films with different internal architectures. The red curve corresponds to the average spectra of seven films including one with uniaxial alignment of the CNFs. The inset shows a zoomed area of the spectra to highlight the presence of Fabry-Perot fringes. (b) Characteristic AFM topography image of the averaged samples. Image size is 20x20 μm^2 and the z-range is 560 nm.

Fabry-Perot fringes resulting from the interferences between beams reflected at the film-air and film-quartz interfaces were detected in the highly transparent samples (as better seen in the inset

of Figure 4.3(a)), which not only indicated an improved homogeneity and quality of the film (in terms of surface roughness) but also allowed the determination of the film thicknesses according to:[226,227]

$$\frac{1}{2nl} = \frac{1}{\lambda_p} + \frac{1}{\lambda_{p+1}} \qquad \text{(Eq. 4.1)}$$

where n is the refractive index of the film (assumed to be 1.559 as for the ellipsometry measurements), l is the film thickness, and λ_p and λ_{p+1} are the wavelengths of adjacent transmission maximum. The sample prepared by dipping was found to be 1310 ± 90 nm thick, while the helicoidal samples were around 1060 ± 60 nm, averaged from the thicknesses determined by the application of Eq. 4.1 to all the detected fringes. This last value was considerably higher than the estimated by ellipsometry (840 nm) and we believe that the difference might come from the incertitude associated with either the extrapolation of the data determined from the depositions on different substrates or the omission of a spectral variation of the refractive index in the case of the calculation from the Fabry-Perot fringes. For practical purposes, we averaged the results obtained from both methods and considered the thickness of the 97-layer pair films as being 950 nm.

4.2. Linear birefringent 1D nanocellulose-based films

In the present section, we use Mueller matrix spectroscopic ellipsometry (MMSE) to investigate the polarization properties of a $(CNF/PVAm)_{97}$ multilayer film with a unidirectional alignment of the nanofibrils. All the measurements were performed by Yann Battie at the University of Lorraine in transmission mode and normal incidence.

Figure 4.4 shows the first three columns of the Mueller matrix (M) measured at the center of the unidirectional sample for different angles of rotation around its normal (φ). Each element of M is presented using a polar coordinate system in which the radial coordinate corresponds to the wavelength and the angular coordinate to the angle of in-plane rotation of the sample (φ = 0 parallel to the spraying direction). Due to geometrical symmetry, only azimuth angles from 0° to

90° were measured. All Mueller matrices presented in this manuscript were normalized to the first element of the matrix (M_{11}) according to $m_{ij} = M_{ij}/M_{11}$, thus, $m_{11} = 1$ and all other elements have values in the range [-1,1].

Given that all the CNF-based films were nondepolarizing (as verified by means of a dual rotating-compensator ellipsometer), all of the polarization properties of the samples (diattenuation, retardance, depolarization, and their form, either linear, circular, or elliptical) could be extracted from the differential (logarithmic) decomposition of the measured Mueller matrix given by:[228–230]

$$M = e^{L}; \qquad L = \begin{pmatrix} 0 & LD & LD' & CD \\ LD & 0 & CB & -LB' \\ LD' & -CB & 0 & LB \\ CD & LB' & -LB & 0 \end{pmatrix} \qquad \text{(Eq. 4.2)}$$

where LD and LD' are the linear dichroism (diattenuation) along the *x*–*y* and ±45° axes, respectively, LB and LB' are the linear birefringence (retardance) along the *x*–*y* and ±45° axes, respectively, and CD and CB are the circular dichroism and circular birefringence, respectively.

We first observed that the elements m_{12}, m_{21}, m_{13}, and m_{31} in Figure 4.4 were zero throughout all the wavelengths and azimuth angles. Accordingly, the linear dichroism of the film must be negligible (i.e., there is no difference in the absorption of polarized light between the perpendicular axes). The matrix element m_{41}, associated with circular dichroism, was also negligible. On the contrary, m_{42} and m_{43} were non-zero and φ-dependent: $m_{42}(\varphi) = m_{43}(\varphi + 45°)$, which provides evidence of the uniaxial anisotropy of the sample. The matrix elements $m_{23} \approx m_{32}$ were also different from zero although their values were much smaller. Moreover, we noted that for the perpendicular azimuth angles 0° and 90°, the Mueller matrix takes the shape of a linear retarder (birefringent material):[177]

$$M = \begin{pmatrix} 1 & 0 & 0 & 0 \\ 0 & 1 & 0 & 0 \\ 0 & 0 & 1 & m_{34} \\ 0 & 0 & m_{43} & 1 \end{pmatrix} \qquad \text{(Eq. 4.3)}$$

where the fourth column can be written by symmetry after having verified that the depolarization was negligible. The optical axis of the system, i.e. the direction of propagation in which light suffers no birefringence, is parallel to φ = 0°.

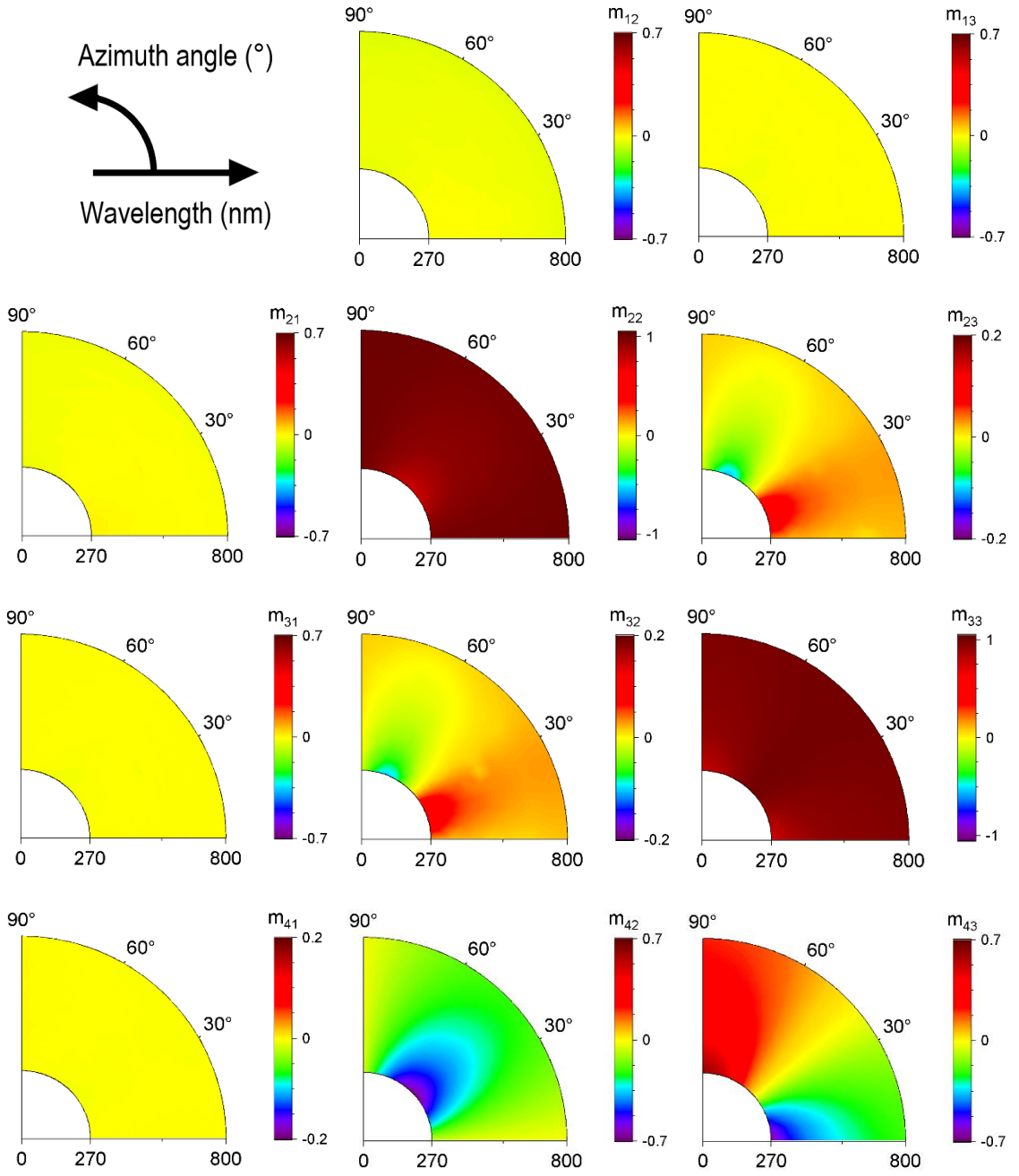

Figure 4.4: Contour polar plots of the first three columns of the Mueller matrix of the unidirectionally-aligned film. Note the different scaling of the off-diagonal elements (linear polarization) and anti-diagonal elements (circular polarization) because circular birefringence and circular dichroism tend to be orders of magnitude smaller than linear effects.[231]

The values of *LD*, *LB*, *CD*, and *CB* were obtained from the differential decomposition matrix *L* determined by the application of Eq. 4.2 to the experimentally-obtained Mueller matrices of both the unidirectional and the random films. In Figure 4.5 we compare the spectra of the polarization properties extracted at the azimuth angles 0° and 90°. We verified that *CD* and *CB* were negligible for both films, while *LB* and *LD* were non-zero in the unidirectional sample. Linear birefringence was the dominant polarization property of the unidirectional sample as *LB* was at least one order of magnitude higher than *LD*. Consequently, the sample presented an anisotropy of the refractive index. On the contrary, the random sample was isotropic, having all the off-diagonal elements of the *L* matrix equal to zero.

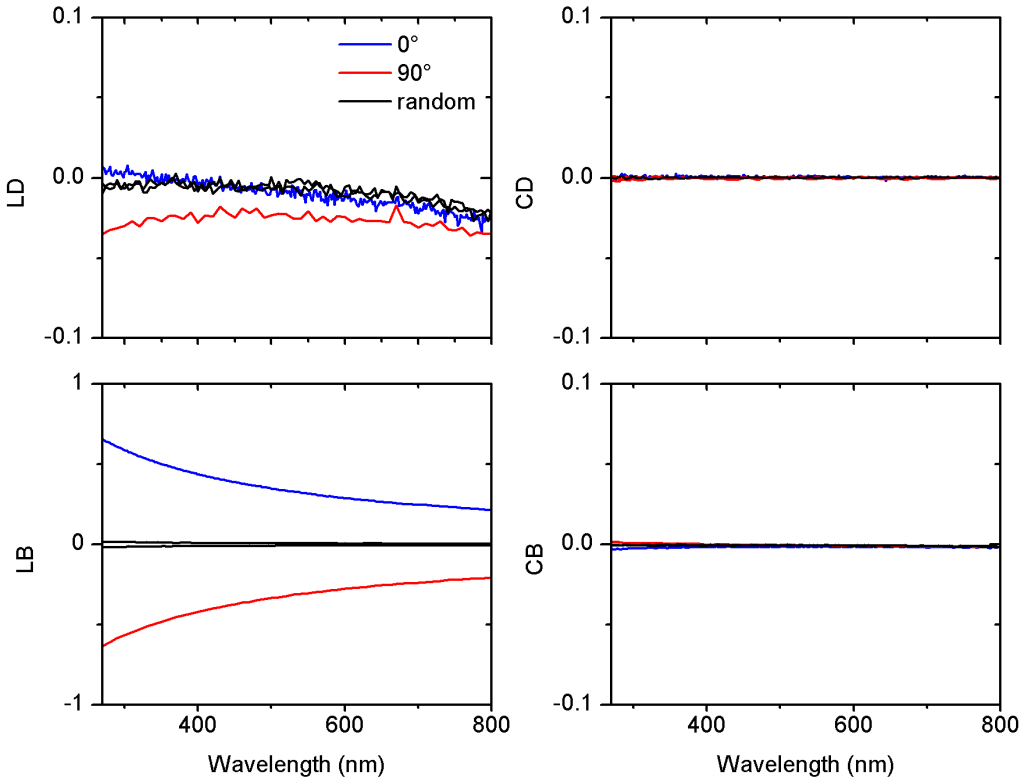

Figure 4.5: *LD*, *LB*, *CD*, and *CB* spectra extracted from the Mueller matrix of the unidirectional and the random samples at the azimuth angles 0° and 90°. For the sake of simplicity, the data for both angles of the random sample were plotted in the same color (black).

We calculated the effective birefringence $\langle \Delta n \rangle = \langle n_y - n_x \rangle$ of the unidirectional sample given by $|LB| = 2\pi|\Delta n|l/\lambda$, where l is the film thickness (950 nm). The resulting effective birefringence, averaged over all the wavelength range, was $\langle \Delta n \rangle = 0.029 \pm 0.003$, where the

error accounts for the assumed incertitude of the film thickness of ±10%. This value is about half of those reported for the birefringence of cellulose, which ranges from 0.045 to 0.062 depending on the source,[232] but it lies between those reported for birefringent films prepared with CNC by dip-coating[233] and spin coating.[234] A higher birefringence could be reached by replacing the CNF by CNC since the rigidity of the latter favors an even better alignment and packing of the nanoparticles than the former, as shown in § 3.2.3.

To evaluate the homogeneity of the sprayed film, we measured the Mueller matrix at different positions on the sample at a fixed wavelength of 300 nm (where *LB* was maximum). The contour mapping of the obtained *LB* is shown in Figure 4.6, where the shape of the spraying pattern is clearly recognized. Maximum birefringence was attained at the centerline of the sample and it decreased away from it, being null outside the deposition area.

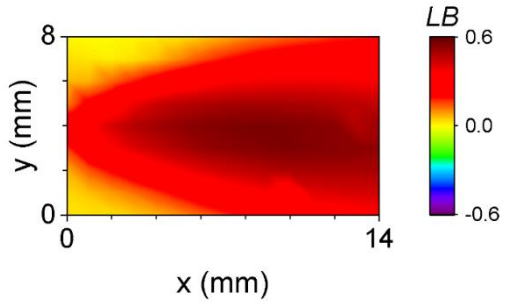

Figure 4.6: Contour plot of the linear birefringence, *LB*, of the unidirectional sample. Resolution: 1 mm.

We recognized the similarity of the contour mapping of Figure 4.6 to the one shown in Figure 3.13(a) in Chapter 3 which depicted the degree of alignment measured by AFM on a monolayer of CNF. Thus, Mueller matrix ellipsometry is a convenient technique to verify the unidirectional alignment of the reinforcing nanofibrils on thick films, which was not possible by AFM due to the lack of resolution of the individual nanofibrils confounded with the soft and rough surface of the thick samples. The Mueller matrix methodology is also less localized than AFM because the light beam diameter is in the millimeter scale and the acquisition of data at different spots of the sample takes noticeably less time. Additionally, the data acquired by transmission ellipsometry is not restricted to the surface of the sample but instead, they represent the properties of the whole thickness of the film.

Besides probing the optical properties of the film, the analysis and modeling of ellipsometric data have been shown adequate to quantitatively investigate internal characteristics of composite materials, including the size, orientation, and concentration of nanoparticles (NP) embedded in a dielectric matrix.[235–237] Battie et al. used a shape distributed effective medium theory (SDEMT) that accounts for the variation of depolarization parameter induced by NP shape distribution to model the effective dielectric function ε_{eff} of the material.[235,238] Following this methodology, we modeled the unidirectional CNF/PVAm film as an effective medium whose effective dielectric tensor is given by:

$$\varepsilon_{eff} = \begin{pmatrix} \varepsilon_e & 0 & 0 \\ 0 & \varepsilon_o & 0 \\ 0 & 0 & \varepsilon_o \end{pmatrix} \quad \text{(Eq. 4.4)}$$

where ε_o and ε_e are the ordinary and extraordinary permittivity, respectively. These properties can be directly related to the measured linear birefringence by:

$$LB = \frac{2\pi}{\lambda}\Delta n\, l = \frac{2\pi}{\lambda}\left(\sqrt{\varepsilon_e} - \sqrt{\varepsilon_o}\right) l \quad \text{(Eq. 4.5)}$$

The SDEMT model proposed by Battie et al. relates the ordinary and extraordinary dielectric functions of the composite film to the volume fraction occupied by the nanofibrils (*f*) and the dielectric functions of the matrix (ε_m) and the nanofibrils (ε_{nf}), respectively:[238]

$$\varepsilon_{e,o} = \frac{(1-f)\varepsilon_m + f\varepsilon_{nf}\beta_{e,o}}{(1-f) + f\beta_{e,o}} \quad \text{(Eq. 4.6)}$$

where the parameters $\beta_{e,o}$ for the extraordinary and ordinary waves, respectively, are given by:

$$\beta_e = \frac{\varepsilon_m}{\varepsilon_m + L_1\left(\varepsilon_{nf} - \varepsilon_m\right)}; \quad \text{(Eq. 4.7)}$$

$$\beta_o = \frac{1}{2}\sum_{i=2}^{3} \frac{\varepsilon_m}{\varepsilon_m + L_i\left(\varepsilon_{nf} - \varepsilon_m\right)} \quad \text{(Eq. 4.8)}$$

being L_1, L_2, and L_3 the depolarization parameters of spheroidal nanoparticles (NPs) along their three principal axes. These parameters only depend on the NP shape and vary from 0 to 1, satisfying $L_1 + L_2 + L_3 = 1$.

Modeling the nanofibrils as infinitely long cylinders results in $(L_1,\ L_2,\ L_3) = (0, 0.5, 0.5)$[239] and thus $\beta_e = 1$ and $\beta_o = 2\varepsilon_m/(\varepsilon_m + \varepsilon_{nf})$. Substitution of these terms in Eq. 4.6 and Eq. 4.5 demonstrates that the obtained *LB* is proportional to the film thickness (*l*) and the volume fraction of the CNFs (*f*):

$$LB = \frac{2\pi}{\lambda}\underbrace{\left[\frac{\varepsilon_{nf}}{2n_m}\left(\frac{\varepsilon_{nf} - \varepsilon_m}{\varepsilon_{nf} + \varepsilon_m}\right)\right]}_{B} fl \qquad \text{(Eq. 4.9)}$$

Thus, the knowledge of the thickness of the film and the optical constants of the polymeric matrix and the cellulose can be used to determine the relative composition of the sample. To do so, however, the mapping of Figure 4.6 must be first recalculated in a local coordinate system parallel to the mean axis of the nanofibrils at every considered point. To account for the gradients on the direction of orientation we considered that the nanofibrils in every measured point were locally oriented in a given direction defined by an azimuth angle θ with respect to the spraying direction. Therefore, the Mueller matrices measured at different spots corresponded to the Mueller matrix of a uniaxial sample rotated by θ, which can be expressed as:[240]

$$M(\theta) = R(\theta) \cdot M \cdot R(-\theta), \qquad \text{(Eq. 4.10)}$$

where $R(\theta)$ is the rotation matrix defined by:

$$R(\theta) = \begin{pmatrix} 1 & 0 & 0 & 0 \\ 0 & cos2\theta & -sin2\theta & 0 \\ 0 & sin2\theta & cos2\theta & 0 \\ 0 & 0 & 0 & 1 \end{pmatrix}$$

The application of Eq. 4.10 showed that $m_{42}(\theta) = m_{43} sin2\theta$ and $m_{43}(\theta) = m_{43} cos2\theta$, thus, the angle of the local orientation of the CNFs in the sample can be calculated by:

$$\theta = \frac{1}{2}\arctan\left(\frac{m_{42}(\theta)}{m_{43}(\theta)}\right) \qquad \text{(Eq. 4.11)}$$

The relevance of Eq. 4.11 is that, even though $m_{42}(\theta)$ and $m_{43}(\theta)$ depend on both the volume fraction of cellulose and the local thickness (in addition to the intrinsic birefringence of the CNF), the local orientation calculated from their ratio is independent of these factors. The local orientation of the CNFs throughout the film was then mapped in Figure 4.7(a). At the centerline of the sample, the alignment of the CNF was parallel to the spraying direction, but it was around ±30° toward the border of the deposition pattern. The gradient of this angle was consistent with the one measured by AFM on the CNF monolayer (Figure 3.13(b)), which further confirms the retaining of the alignment of the CNFs on the thick film.

Figure 4.7(b) shows the mapping of the linear birefringence of the unidirectional film corrected from the effects of the local orientation, i.e., the *LB* recalculated in the local frame parallel to the mean direction of the fibril alignment throughout the sample. This data can be used then in conjunction with Eq. 4.9 to further investigate the internal characteristics of the nanocomposite films.

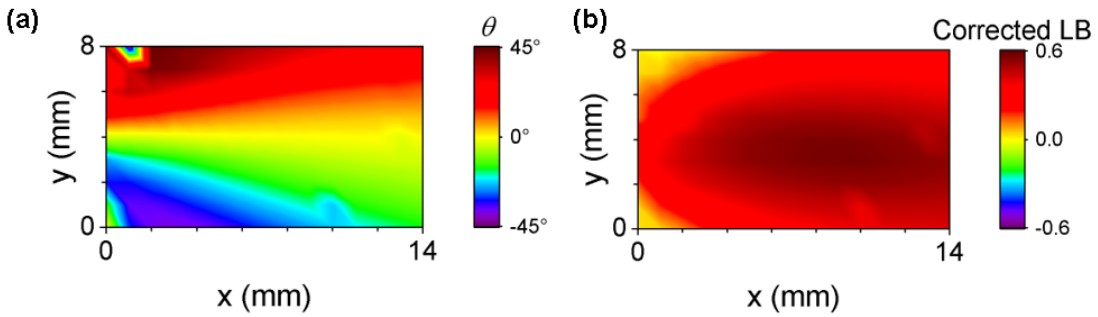

Figure 4.7: (a) Contour plot of the local orientation of the CNFs on the unidirectional sample, extracted from the Mueller matrix. (b) LB corrected in the local frame parallel to the mean direction of the fibril alignment.

We know from the § 3.2.4.1 that the thickness of the GIS-films is not homogeneous all along the sample surface; we attempted to map the local thickness of the film by optical profilometry, but the transparency of both the film and the substrate caused beams interferences that impeded the accurate detection of the film surface and the film/substrate interface. Mechanical (stylus)

profilometry was not suitable either for the characterization of the soft multilayer film due to damage to the sample surface. The lack of a thickness profile of the sample and accurate values of the optical constants of the individual film components (whose determination was out of the scope of this work) prevented the final determination of the volume fraction of the CNFs within the GIS-film. Such characterization remains pending for future work, but we have demonstrated that Mueller matrix ellipsometry is not only a simple, fast, non-destructive and large-scale method to investigate the optical anisotropy of multilayer films but it also provides a suitable approach to characterize the volume fraction of the reinforcing nanofibrils in the film, information that is elusive to determine by other means. In the next section, we investigate the optical properties of GIS-LbL films with a more complex internal arrangement of the reinforcing CNF.

4.3. Chiral multilayer films of cellulose nanofibrils

Previous works within our team[170,241] has proven the effective application of the GIS-assisted LbL methodology to prepare chiral films of silver nanowires exhibiting record values of circular dichroism owing to the combination of the chiral structure to the plasmonic coupling of the nanowires. However, films prepared with silver nanowires suffer from an elevated absorption of the incident light, which reduces their efficiency. On the contrary, cellulose does not absorb visible wavelengths (Figure 4.3(a)), thus, it may be a good candidate for the preparation of circular-polarization-sensitive non-absorbing filters provided that it is assembled into chiral structures. In this sense, we were interested in evaluating the resulting chiral properties of the CNF-based helicoidal films prepared by GIS-LbL.

The polarization properties of $(PVAm/CNF)_n$ multilayer films possessing different helicoidal arrangements of the CNFs were investigated by circular dichroism spectroscopy and Mueller matrix ellipsometry. As determined previously by ellipsometry, all samples having the same number of layers exhibited the same thickness, independently of the difference in their internal structures. If not stated otherwise, all the reported samples were composed of 97 pairs of layers

and had an estimated thickness of ~950 nm (averaged from ellipsometry and transmittance measurements).

The chiral properties of the prepared samples were investigated by means of circular dichroism (CD) spectroscopy. First, we compared two films whose only structural difference was the opposite handedness of the helicoidal alignment of the CNFs, namely samples 97R1x15° and 97L1x15°. The CD spectra obtained on these two samples are shown in Figure 4.8. For comparison, the spectra obtained on a random sample prepared by dipping, as well as those of the pure CNF suspension (1 mg/mL) and PVAm solution (10 mg/mL), are also plotted. Note that the concentration of the pure components was ten times higher than the concentration used for the preparation of the films.

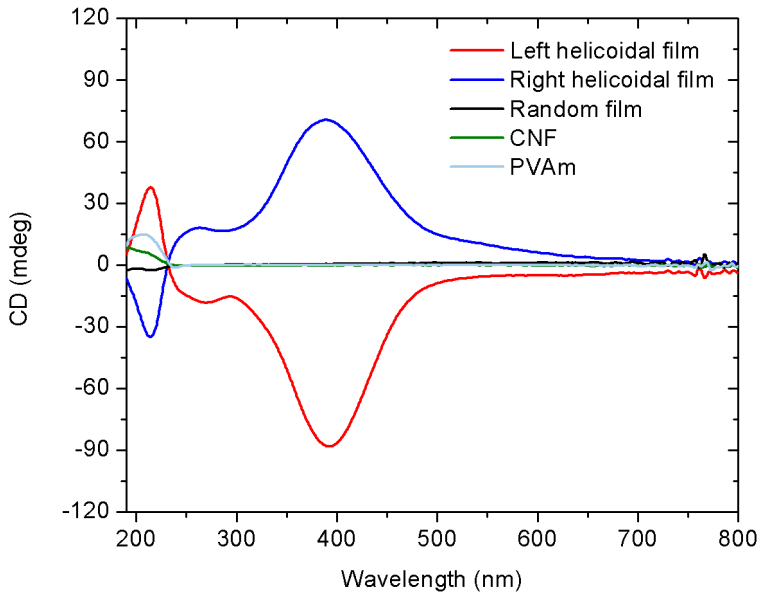

Figure 4.8: CD spectra of right- and left-handed helical films otherwise identical (samples 97R1x15° and 97L1x15°, respectively). For comparison, the spectra of a PVAm solution (10 mg/mL), a CNF suspension (1 mg/mL), and a random film prepared by dipping are also plotted.

The random (isotropic) sample did not exhibit any significant CD signal, while both pure components did show weak positive responses around 220 nm. The cellulose molecule is intrinsically chiral owing to the multiple chiral carbons along its backbone and moreover, their assemblies into nanofibrils are themselves chiral.[242,243] On the contrary, the CD signal exhibited by PVAm can only be ascribed to the presence of impurities and additives in the commercial product since the polymer does not have stereocenters in its structure. PVAm is synthesized by

the hydrolysis of poly(*N*-vinyl formamide),[244] the BASF grade used for the preparation of the samples (Lupamin 9095) has a degree of hydrolysis of around 90%,[245] so the non-hydrolyzed formamide groups may impart optical activity to the molecule as observed for some polyvinyl copolymers.[246–248]

The most obvious characteristic of the CD spectra compared in Figure 4.8, though, is the symmetrical response of the helicoidal films prepared with opposite handedness, which confirms the effective helicoidal assembly of the CNF within the films, giving rise to opposite chirality. The CD spectra of these films exhibited both positive and negative peaks at different wavelengths, changing signs around 230 nm, i.e., at the inception of the signals of the pure components. Moreover, the cellulose films absorb UV light at this low wavelength (see transmittance spectra of Figure 4.3), therefore the smaller peaks at around 200 nm correspond to the combined effect of many absorption processes and will not be further discussed. We were more concerned, though, with the broader and more intense peak located around 390 nm, which was attributed to the structural assembly of the CNFs. This peak presented a shoulder at around 260 nm that might be due to a higher-order Bragg diffraction. We focused on the analysis of the high structural peak. The positive peak of the right-handed helical film indicates that L-CPL was absorbed to a greater extent than R-CPL, i.e., circularly polarized light having the opposite handedness of the cholesteric structure of the film was preferentially transmitted, as is observed for the circular Bragg phenomenon.[249] The same observation applies to the negative CD signal measured in the left-handed sample. The selective Bragg reflection at normal incidence takes place in a spectral band centered at $k\lambda_{Bragg} = \bar{n}P$, where $\bar{n}$ is the in-plane average refractive index, P is the helix pitch, and k is an integer that labels the order of each maximum. Under the assumption of $\bar{n} = 1.559$ and $P = 950\,nm/4\,turns = 238\,nm$, we estimated a wavelength of selective Bragg reflection (k = 1) located at ~371 nm (±10% of assumed incertitude of the thickness), which is in good agreement with the structural CD peak at 390 nm.

The average intensity of the structural CD peak was ~80 mdeg, which represents a 0.2% efficiency in the filtration of circular polarization (defined as the achieved ellipticity with respect to perfectly

circular polarization, i.e. 45000 mdeg). Given that the CD signal is based on the measurement of light absorption, its intensity is related to the concentration of the attenuating species (Beer's law), e.g. the concentration of chiral molecules. In the case of chiral structured films such as the ones subject to this study, the intensity of the structural CD peak must depend mostly on the number of helical turns rather than on the actual concentration of CNF ($\propto$ thickness), e.g. see the absence of CD signals for a random film with the same thickness. Figure 4.9 shows the effectively monotonic increase of the intensity of the structural CD peak with the increasing number of helical turns. The CD intensity measured after only one turn was feeble possibly because the film thickness at this stage (~240 nm) was thinner than λ_{Bragg}.

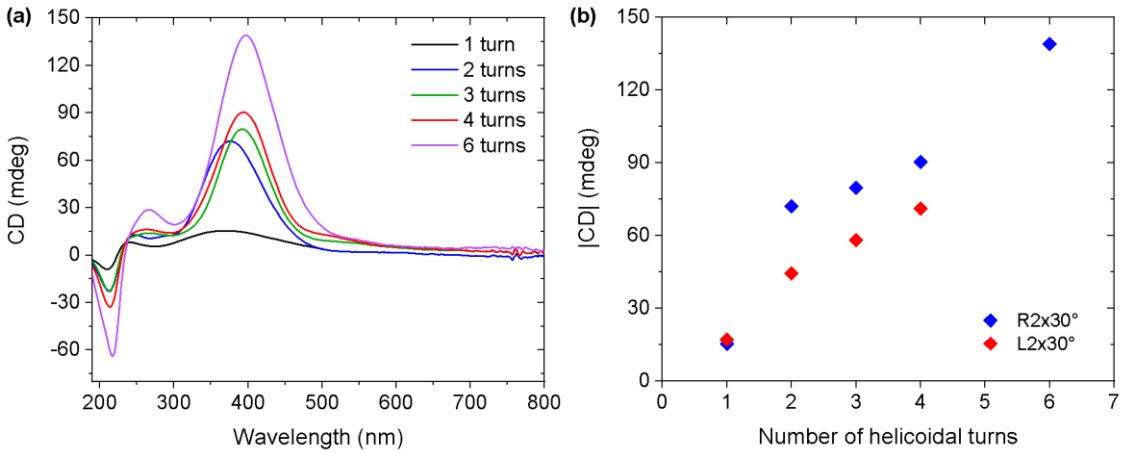

Figure 4.9: (a) CD spectra of sample 97R2x30° collected after the completion of different numbers of helical turns. (b) Intensity of the CD peak at ~390 nm vs. the number of helical turns of the film in (a) as well as the measured in a comparable sample with opposite handedness.

The symmetric CD signals detected for samples with opposite handedness (which was reproducible in all the tested films) seemed to be adequate proof of the effective helicoidal assembly of the CNFs within the bulk of the films. However, it has been recognized that linear anisotropies present in the samples may couple with small imperfection in the optical train of the instrument (strain birefringence) to give rise to artifactual CD signals.[250,251] Hence, the confirmation of the effective helicoidal alignment of the CNFs cannot rely exclusively on the results obtained from CD spectroscopy. As a matter of fact, we have seen in the previous section that samples possessing unidirectional alignment of CNFs do exhibit strong linear birefringence

and even some degree of linear dichroism; therefore, we determined the true CD spectra of selected samples by Mueller matrix spectroscopic ellipsometry for comparison.

Figure 4.10 shows the first three columns of the Mueller matrix obtained on the sample 97R1x15° having four right-handed helicoidal turns. We noticed that, apart from a possible artifact of the measurement at an azimuth angle of 60°, most elements of the Mueller matrix were featureless, except for m_{41} that showed maximum values between 400 nm and 500 nm independently of the azimuth angle. m_{42} and m_{43} indicate the presence of some remaining linear birefringence as well, which can be associated with the not-perfectly centered positioning of the sample during the measurement. Since our interest was to investigate the chiral properties of the films, we focused exclusively on the element m_{41} of the matrix.

After verification of the nondepolarizing nature of the samples, the extracted spectra of the four polarization properties of 97R1x15°, 97L1x15°, and the random sample were compared in Figure 4.11. Opposite CD signals were easily identifiable for the helical films around 430 nm, which confirmed that preferential absorption of left- or right-handed circular polarized light can be obtained in multilayer films with opposite handedness of the helicoidal assembly of the nanofibrils. Although small, remaining linear anisotropies were also present in the films.

Similar to the unidirectional sample, we evaluated the homogeneity of a helicoidal film by measuring the Mueller matrix at different positions throughout the sample 97R1x15° at a fixed wavelength of 430 nm, where the intensity of the signal was maximum. The obtained mapping of CD is shown in the contour plot of Figure 4.12. As expected, the maximum values of this property were observed at the center of the film, decreasing radially toward the borders of the sample.

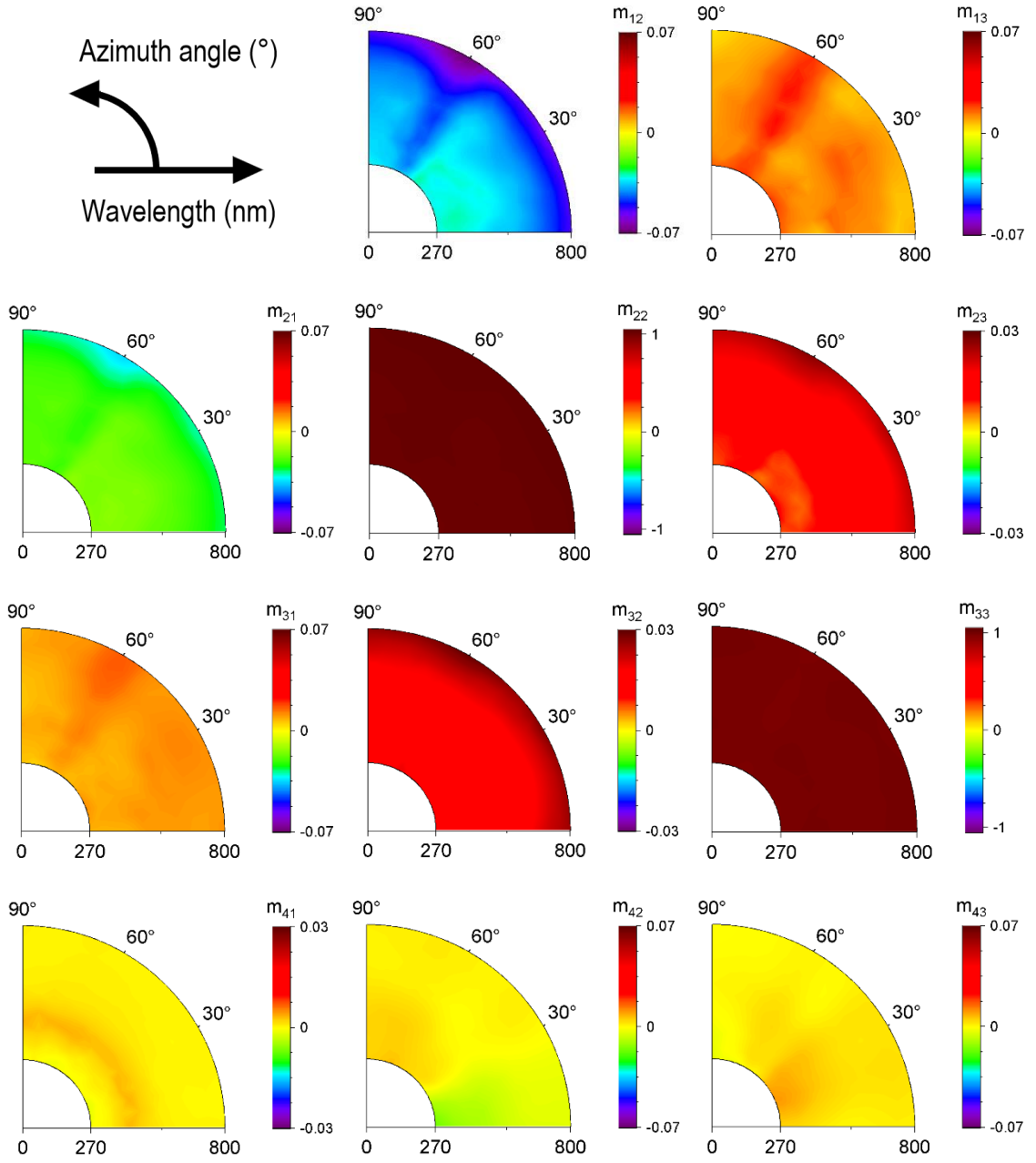

Figure 4.10: Contour polar plots of the first three columns of the Mueller matrix for the helical sample 97R1x15°. Note the different scaling of the off-diagonal elements (linear polarization) and anti-diagonal elements (circular polarization) because circular birefringence and circular dichroism tend to be orders of magnitude smaller than linear effects.[231]

In Figure 4.13 we compare the CD spectra obtained with both techniques, CD spectroscopy and Mueller matrix ellipsometry, on four different helicoidal films. We observed that the sign, shape, and magnitude of the CD signals obtained were comparable in both techniques, being only the position of the peaks consistently blue-shifted (40 ± 7 nm in all samples) when measured by CD spectroscopy. This offset of the CD signals measured by both techniques was significative and

might be due to systematic errors such as calibration of the spectrometer or change in the pitch due to swelling of the film by differences in the ambient humidity. In any case, the spectra obtained by CD spectrometry were not artefactual (except for the slight offset in the position of the peaks), and we relied on this latter technique to compare the circular dichroism of helicoidal films prepared with different structural characteristics since this technique was more accessible to us.

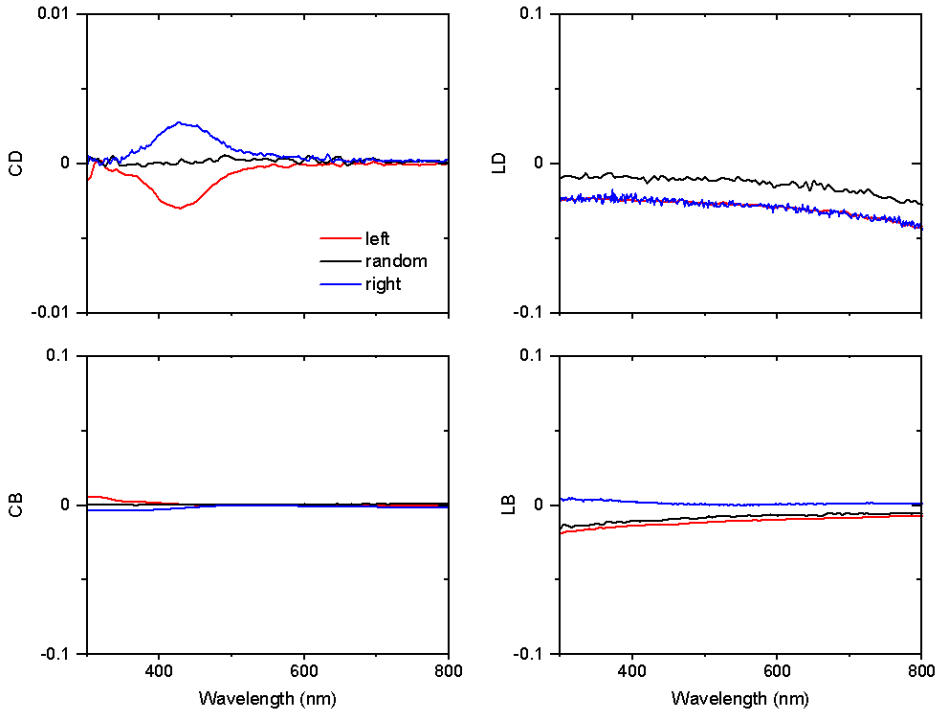

Figure 4.11: LD, LB, CD, and CB spectra extracted from the Mueller matrix of the 97R1x15°, 97L1x15°, and random samples at 0° azimuth angle.

We compared the circular dichroism of films having three different values of the helical pitch, accomplished by varying the azimuth angle between consecutive CNF layers, namely 7.5°, 15°, and 45°. All the samples had the same number of layer pairs distributed in 2, 4, and 12 complete turns of the helicoid, respectively. The estimated thickness of all three films was the same, 950 nm, which translates into approximate pitches of 80 nm, 240 nm, and 475 nm, respectively.

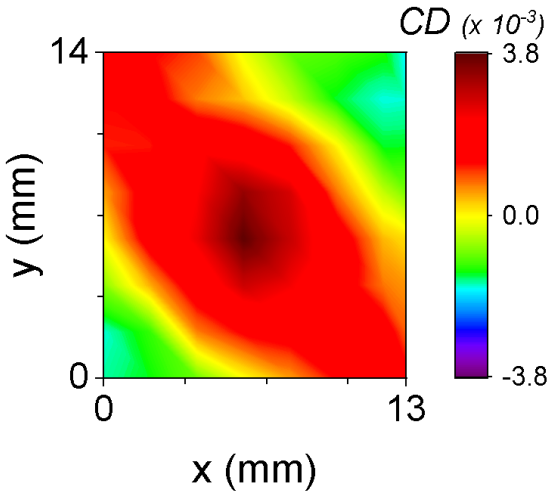

Figure 4.12: Contour plot of the circular dichroism, *CD*, of the helical sample L1x15°.

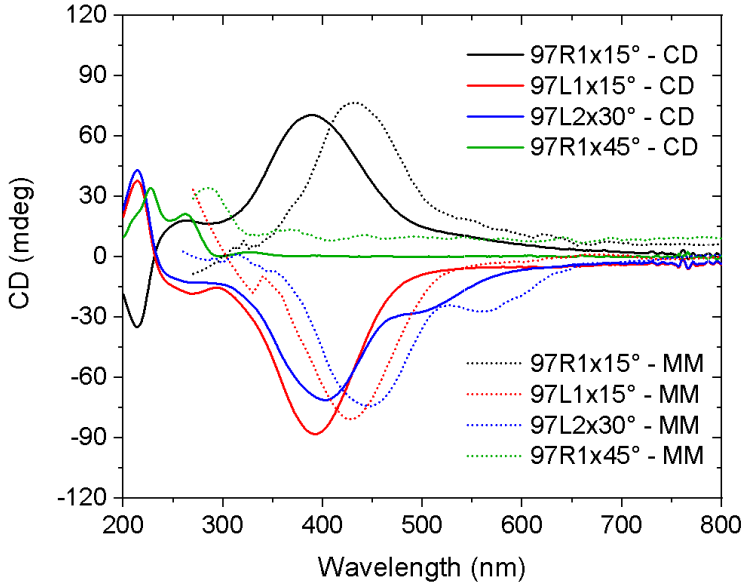

Figure 4.13: Comparison of the CD spectra obtained by CD spectroscopy and Mueller matrix spectroscopic ellipsometry (MMSE) on different helical samples.

The CD spectra of these films measured by CD spectrometry are shown in Figure 4.14(a). We observed significant differences in the positions of the structural peak, which left no doubts on the influence of the pitch on this parameter. The graph of the wavelength of maximum CD *vs* pitch depicted in Figure 4.14(b) shows that the position of the CD peak red-shifted linearly with the increment of the pitch as predicted by Bragg's law. The refractive index determined by the slope of the linear fit was 1.57 ± 0.03, which was consistent with the value used in ellipsometry to determine the thickness of the $(CNF/PVAm)_n$ films. Apart from the position of the peaks, we remarked obvious differences in the shape of the CD signals. First, the peaks seemed to broaden

as they moved toward higher wavelengths; furthermore, the spectra of the film with higher pitch exhibited a small signal around 500 nm given the impression of being part of interference oscillations, common to spectroscopic measurements. Similar oscillations have also been observed in the CD spectra of chiral films of silver nanowires with increasing spacing among layers.[241] Finally, the signal at low wavelengths, corresponding to the film with the smallest pitch was smaller than the peaks of the other two films and we believe that the signal overlapped with the negative peak observed for all films at this wavelength range as no negative CD was detected for this sample.

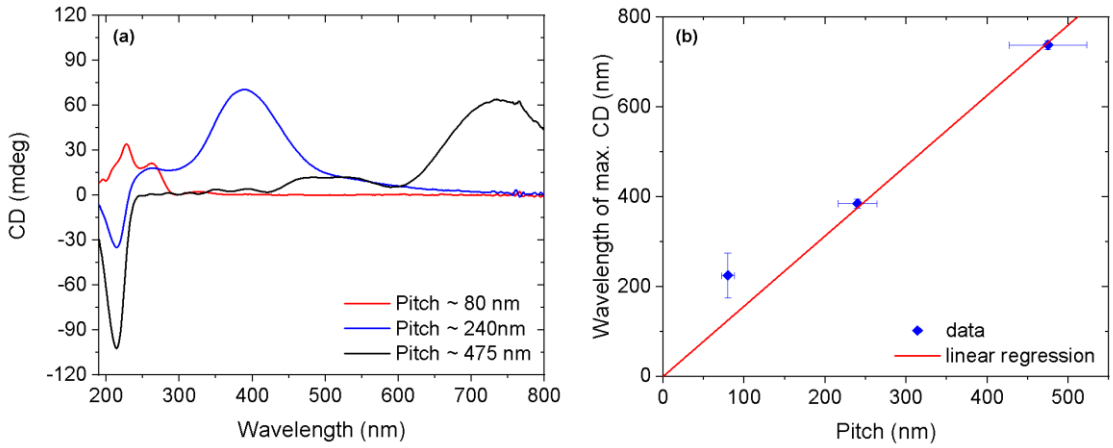

Figure 4.14: (a) CD spectra of three films with different pitches of the helical alignment. (b) Linear relationship between the position of the CD peak and the pitch.

In the framework of collaborative research, the optical transmittance behavior of the helicoidal samples was numerically simulated by Yann Battie from the University of Lorraine through the Berreman transfer matrix formalism.[252,253] The films were modeled as a stack of 98 unidirectional layers constantly rotated by a fixed azimuth angle. Each 10-nm layer was considered as having homogeneous anisotropic optical parameters defined in Figure 4.15(a). These indices were determined by fitting the reflection Mueller matrix measured at different azimuth angles on a 120-nm thick unidirectional film prepared on a silicon wafer. The simulated CD spectra of samples with identical characteristics except for opposite handedness are shown in Figure 4.15(b) superimposed to the experimental data obtained from CD spectroscopy. The theoretical modeling confirmed the experimental observations of reversed CD signals for samples with opposite

handedness. However, both the positions and intensities of the structural peaks obtained by the simulation were considerably different than the experimental values. The reasons might be associated with the idealization of the model, which considers homogeneous birefringent layers of identical compositions and thicknesses. Moreover, the ordinary and extraordinary refractive indices determined on the 120-nm thick layer might not represent the actual optical properties of the ~9 nm thick unidirectional monolayers forming the helicoidal stacking.

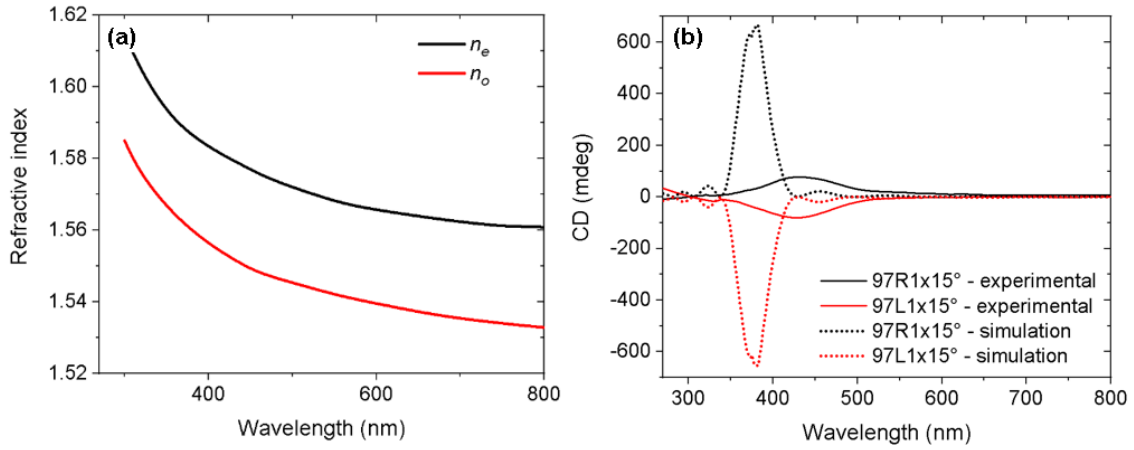

Figure 4.15: (a) Variation of the ordinary and extraordinary refractive index with wavelength used for the simulation of the optical response of helical films. (b) Experimental and simulated CD spectra of samples with opposite handedness.

The simulation of the optical behavior of samples with different pitches was also investigated. This was accomplished by increasing the number of helicoidal turns while keeping the thickness of the film constant. The simulated CD signals are presented in Figure 4.16. This result is in good agreement with our observation of the red shifting of the CD peak with the increasing pitch of the helicoidal arrangement of the nanofibrils, which confirms the structural nature of the signal. The linear fit of the wavelength of maximum CD *vs* pitch rendered a refractive index of 1.44 ± 0.03, which is lower than the determined on the experimental data. This implies that the theoretical model might not represent accurately the prepared films and that it needs to be improved.

Given that the films were modeled with the same thickness, the simulation also allowed us to verify that the intensity of the CD peak of the chiral films is not associated with the actual

thickness of the sample but is mostly a function of the number of helical turns, increasing monotonically with this parameter, as verified experimentally (Figure 4.9).

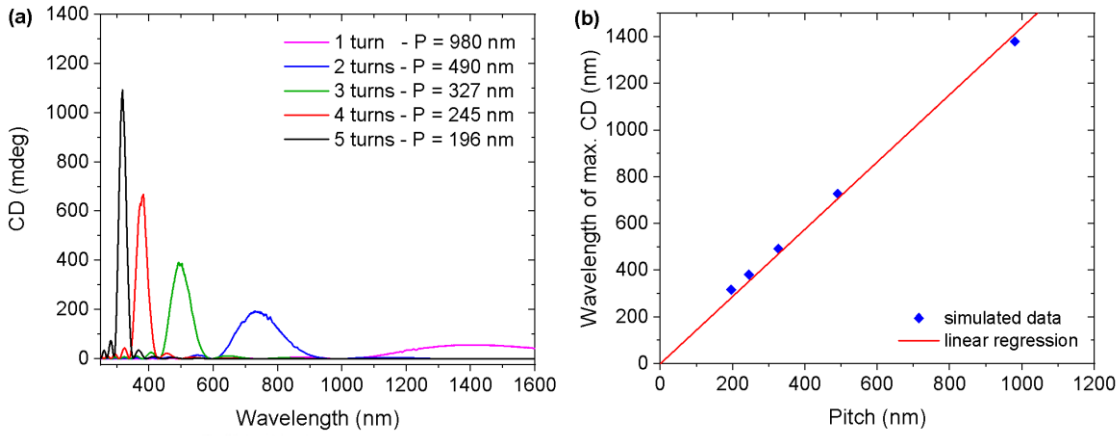

Figure 4.16: (a) Simulated CD spectra of right-handed helical films with an increasing number of helical turns at a fixed film thickness, resulting in a decrease of the helical pitch. (b) Simulated change of the CD peak with the structural pitch.

The qualitative agreement between the simulations and the experimental measurements of the polarization properties of microstructured $(CNF/PVAm)_n$ films signify that tailored optical behaviors can be easily designed theoretically before engaging in the time-consuming fabrication of the films by GIS-LbL. We have identified relevant parameters to design films with the desired optical behavior. Particularly, the localization of the selective Bragg reflection peak can be tailored by the adequate selection of the helical pitch and the handedness of selective transmission/reflection, by the choice of the handedness of the chiral structure. Broadband wave reflection/filtration might be accomplished by the stacking of helicoids with different pitches.

The efficiency of the selective filtration of circularly polarized light increases with the number of helicoidal turns, thus, many turns are necessary to attain high efficiency. A film thickness of around several tens of micrometers would be required for narrowband filtration and even thicker films, for broadband functionality. These values of thickness seem excessive for the practical application of the LbL deposition methodology; however, we believe that there is still much room for optimization in our approach.

The unidirectional and helicoidal arrangements of the CNF studied so far represent the most elementary structures that can be fabricated by the devised rotation of the aligned layers within the LbL films. More complex architectures can be engineered, though, by the alternation of stacks with opposite handedness or the intercalation of helicoidal and unidirectional stacks for the reflection of both handednesses of circularly-polarized light,[158] the stacking of gradient pitches for broadband filtration,[254] or a combination of all the above.

Chapter 5. Mechanical characterization of CNF-based multilayer films

5.1. Introduction

With the increasing demand for miniaturization of, for instance, electronic devices, mechanical testing equipment on small materials has been actively developed since the 1990s.[255] For nano- and micro-scale specimens, though, difficulties arise associated with specimen gripping and manipulation, precise loading, and accurate measurements of displacement and load. Some common mechanical tests, such as tensile test, have been successfully applied to freestanding thin films to evaluate their mechanical properties.[167] We initially planned to replicate such methodology for the mechanical characterization of the CNF-based films prepared throughout the present work, however, the small area with homogeneous thickness and effective alignment discussed in chapters 3 and 4 together with difficulties in the handling of freestanding film specimens made us consider nanoindentation techniques instead. In this type of test, the recording of the applied load and depth of penetration of an indenter into the specimen is used to indirectly determine the elastic modulus and hardness of the thin film. Other properties such as the strain-hardening index, fracture toughness, yield strength, and residual stresses can also be obtained under some conditions;[255,256] nonetheless, the discussion on the mechanical properties of the multilayer films throughout this chapter is limited to the elastic indentation modulus (E_{IT}) and the indentation hardness (H_{IT}).

The mechanical characterization of ~1 µm thick supported films made from CNF and PVAm was carried out by means of three experimental methodologies. Initially, a depth profiling of both E_{IT} and H_{IT} was performed with a Berkovich tip so that accurate values of these properties could be compared among different samples. Then, films with various internal microstructures were analyzed by single indentations with a two-fold symmetric Knoop indenter tip with the purpose of identifying anisotropic responses. Finally, a nano-contact fatigue methodology was adopted to describe different mechanical responses of the films at high strain rates associated with their internal nanostructures.

5.2. Estimation of the elastic modulus and hardness of the multilayer films by Continuous Stiffness Measurements (CSM)

As previously evoked in § 2.5.2, the main difficulty encountered when characterizing the mechanical properties of supported thin films by nanoindentation is to avoid probing the properties of the underlying substrate. To overcome this, it is a common practice to restrain the depth of penetration of the indenter to a maximum of 10% of the film thickness[185] because the volume of material involved in elastic measurements is about ten times the equivalent contact radius of the indenter.[257] Even so, the influence from the substrate on the measurements of elastic modulus is unavoidable. Consequently, many empirical or analytical ways to treat the experimental data have been developed, some of which were compared by Menčik et al.[258] Extracting the actual film hardness from experiments on film/substrate systems is even more difficult than for the modulus due to the complex nature of the plastic zone. In this case, the conventional 10% of the thickness rule is commonly used, which in the case of soft coatings on hard substrates can be enlarged to about 30%.[181]

To investigate the elastic modulus and hardness of the $(CNF/PVAm)_n$ multilayer films prepared throughout this thesis we relied on the application of the so-called Continuous Stiffness Measuring (CSM) methodology, first introduced by Oliver and Pethica,[184,186] which is based on

the superimposition of a small harmonic oscillation to the monotonic load of the indenter. This methodology allows investigating the evolution of both properties as a function of the depth of penetration of the indenter into the sample which can be used to identify gradients on the properties in the thickness direction or to deconvolute the intrinsic modulus and hardness of the films from that of the substrate by means of appropriated mathematical models.[188,259]

The resulting depth profiles of the mechanical properties measured on the supported multilayer films are exemplified in Figure 5.1, which shows the raw evolution of the indentation elastic modulus (E_{IT}) (filled circles) and indentation hardness (H_{IT}) (open triangles) of a 1-µm thick helicoidal sample composed of 97 (CNF/PVAm) layer pairs as a function of the relative penetration depth (h_c/t). Since the influence from the substrate on the measurements of the elastic modulus is unavoidable, the curve of the "apparent" modulus represents a composite response of the film/substrate system that grows monotonically with the depth of penetration. On the contrary, since the indentation depths were essentially less than the film thickness, and therefore the plastic deformation was contained within the film, the hardness measurements were only slightly affected by the substrate's properties, as it is expected in the case of soft films on hard substrates.[259,260]

As introduced earlier, some mathematical models can be found in the literature to extract the intrinsic values of the elastic modulus and hardness from the experimental curves $E_{IT} = f(h_c)$ and $H_{IT} = f(h_c)$ respectively, provided that the properties of the substrate and the thickness of the film are known. We adopted the analytical model proposed by Bec et al.[260] to extract and report the actual film modulus, E_f, from the global measurements. In this model, the global stiffness, K_z, of the film/substrate system is obtained from the reciprocal sum of the film stiffness and the substrate stiffness, each multiplied by correcting polynomial functions, resulting in the following expression:

$$\frac{1}{K_z} = \frac{1}{1 + 2t/\pi a_c}\left(\frac{t}{\pi a_c^2 E_f^*} + \frac{1}{2a_c E_s^*}\right) \qquad \text{(Eq. 5.1)}$$

where E_f^* and E_s^* are the reduced modulus of the film and substrate respectively, t is the film thickness, a_c is the contact radius, and the global stiffness K_z is related to the apparent reduced modulus E_{IT}^* of the film/substrate system through the relation $K_f = 2\,E_{IT}^* a_c$; ($E^* = E/(1-\nu^2)$; being ν the Poisson's ratio).

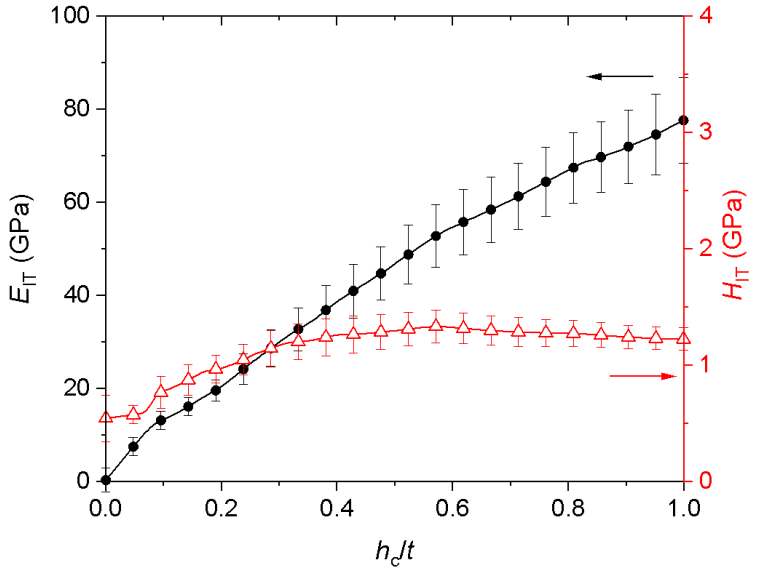

Figure 5.1: Evolution of the indentation modulus, E_{IT}, and indentation hardness, H_{IT}, as a function of the depth of penetration of a Berkovich tip into a $(CNF/PVAm)_{97}$ helicoidal film prepared by GIS. Average curves obtained from approx. 20 indentations at a controlled relative humidity < 3%.

There exist also several models to extract the hardness of a thin film, H_f, from indentation experiments performed on composite film/substrate systems; we applied and compared the results obtained from two of them; on one hand, the model proposed by Bhattacharya and Nix[261] for a soft film on a hard substrate, given by:

$$H_{IT} = H_s + (H_f - H_s)exp\left(-\frac{\sigma_f E_s}{\sigma_s E_f}\left(\frac{h_c}{t}\right)^2\right) \qquad \text{(Eq. 5.2)}$$

where H_{IT} is the composite hardness, H_s is the substrate hardness, h_c is the contact depth, and σ_f and σ_s are the yield strengths of the film and substrate, respectively. On the other hand, we also report the results obtained by the application of the analytical model introduced by Korsunsky et al.,[262] given by the following expression:

$$H_{IT} = H_s + (H_f - H_s)\left(\frac{1}{1 + k\left(\frac{h_c}{t}\right)^2}\right) \quad \text{(Eq. 5.3)}$$

where k is a fitting parameter that describes a wide range of composite and indenter properties such as coating brittleness, interfacial strength, indenter geometry, etc.

Since the application of the aforementioned mathematical models requires the properties of the substrate as input, we first performed the CSM experiment on a neat silicon wafer of (100)-orientation, identical to the one used as the substrate for the preparation of all films throughout this work. The evolution of the indentation elastic modulus (E_{IT}) (filled circles) and indentation hardness (H_{IT}) (open triangles) as a function of the depth of penetration is shown in Figure 5.2. We noticed that these properties were not ideally constant but showed a strong depth-dependence at shallow depths (under 150 nm) instead, which is caused partly by the combined effects of the non-ideal pyramidal geometry of the indenter, indentation size, and the tip bluntness. At deeper depths, the hardness reached a constant value of 11.9 ± 0.1 GPa (averaged between 150 nm and 500 nm). The elastic modulus also stabilized at an almost constant value although the "plateau" of this property was not perfectly flat, probably biased by the calibration of the indenter with polycarbonate. Even so, the average between 150 – 500 nm was 177 ± 2 GPa, with a variation of approx. 7% between the initial and the final modulus. These values are in good agreement with the ones reported in the literature, being the hardness of a (100)-silicon wafer typically reported in the range 9 – 16 GPa[263,264] and the modulus, in the range 130 – 188 GPa.[263,265] Further deeper, a pop-out event was observed in both curves above 500 nm, which is attributed to well-known pressure-induced phase transitions in the crystalline silicon material.[266–268]

Once the mechanical properties of the substrate were estimated under the CSM experimental conditions, the numerical fitting of the models described by Eq. 5.1, 5.2, and 5.3 to the experimental curves $E_{IT} = f(h_c)$ and $H_{IT} = f(h_c)$ allowed us to determine the intrinsic elastic modulus and hardness of the multilayer films prepared throughout this thesis; whose values are

discussed and compared in the following sections as a function of the different preparation parameters of the films and testing conditions.

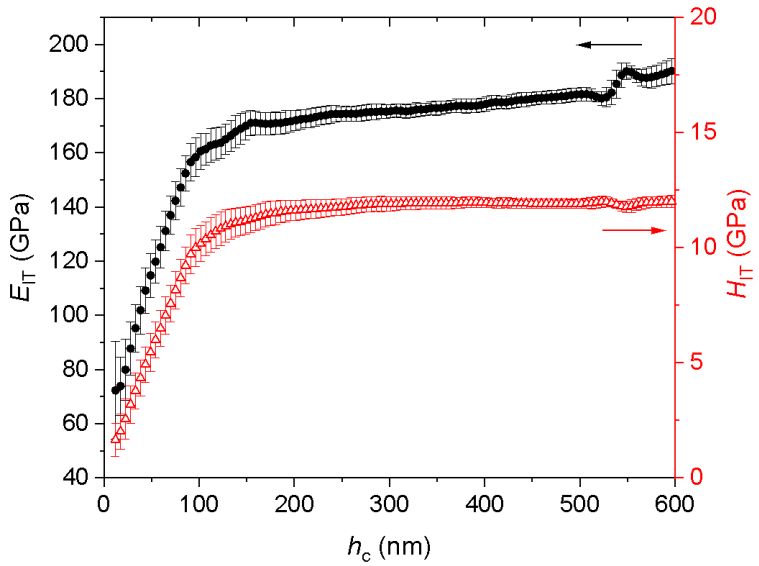

Figure 5.2: Evolution of the indentation modulus, E_{IT}, and indentation hardness, H_{IT}, as a function of the depth of penetration of a Berkovich tip into a neat (100)-silicon wafer. Average curves obtained from approx. 20 indentations at a controlled relative humidity < 3%.

5.2.1. Effects of the pH of the polycation solution used during film preparation

As introduced in § 3.4, the pH of the depositing solutions of weak polyelectrolytes during the LbL assembly of multilayer films influences the film thickness, constituent's organization, and film composition.[200,269] To evaluate possible differences in the mechanical responses associated with these characteristics, the elastic modulus and hardness of two films of $(CNF/PVAm)_n$ prepared from PVAm solutions at two different pH were compared. The ~1 µm thick samples were fabricated by orthogonal spraying, i.e., the reinforcing cellulose nanofibrils were deposited in a random fashion without any preferential direction of alignment.

Figure 5.3 shows the measured compliance ($1/K_z$) as a function of the contact radius, a_c, for films prepared by spraying the PVAm solution at pH = 8 and at a pH = 10, respectively. The dispersion of the measurements was considerably larger for the sample prepared at pH = 10, which can be ascribed to the presence of micron-sized rough features on the surface of the sample as shown in

the optical images of the remaining imprints in Figure 5.4. Surface roughness negatively affects the accuracy of the depth-sensing and the determination of the area of contact between the indenter and the film.

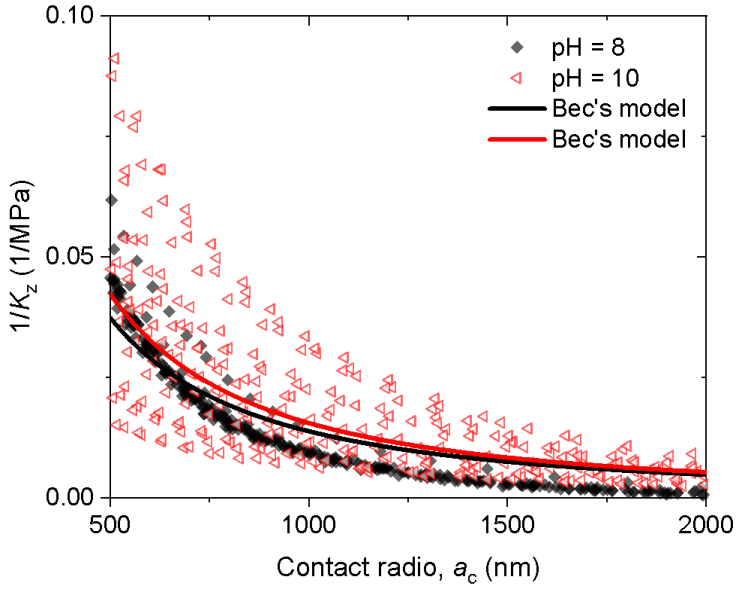

Figure 5.3: Apparent compliance as a function of the contact radius of $(CNF/PVAm)_{97}$ films prepared at two different pH of the polycation solution. The experiment was performed at a controlled RH < 3%.

The predictions of the Bec's model (continuous lines) are superimposed to the experimental data in Figure 5.3; they were obtained by fixing the film thickness to 1000 nm and the modulus of the substrate to 177 GPa during the non-linear regression procedure. To account for the indentation size effects argued in the previous section, only data points above a thresholding penetration depth $h_c \approx 150$ nm ($a_c = 500$ nm) were included in the fitting procedure (the same is valid throughout the chapter). We noted that the model described fairly well the data points obtained for the sample prepared at pH 10, owing to their high dispersion. On the contrary, the fitting of the data obtained on the film built at pH 8 was unsatisfactory (coefficient of determination, $R^2 = 0.77$), which results in an overestimation of the film modulus at shallow indentations and an underestimation at deeper penetration. This lack of fit was observed in all tested samples (as it will be seen later) and suggested a gradient in the elastic modulus of the film. Indeed, all the models used to remove the influence of the substrate on the mechanical properties of the films assume homogeneous and

isotropic properties of the films, which might not reflect the actual nature of the CNF/PVAm samples: being composed of an entangled network of flexible nanofibrils and empty space (eventually filled with water), the studied films can be regarded as porous instead of bulk material.

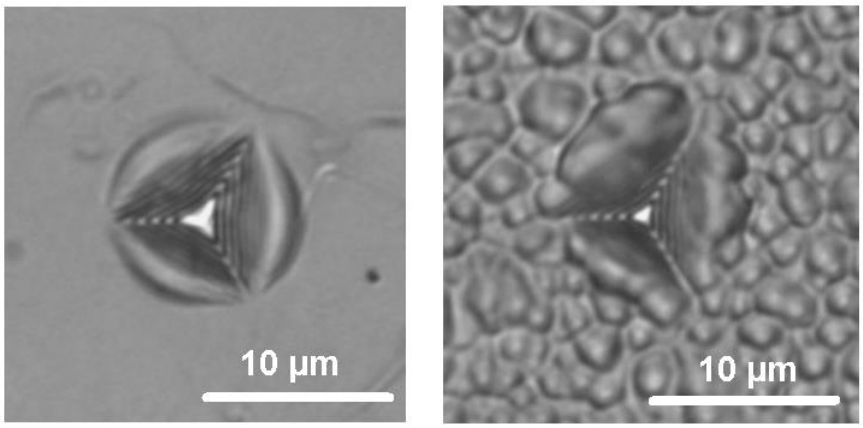

Figure 5.4: Optical micrograph of the residual imprint left after the CSM indentation on the multilayer films fabricated from a PVAm solution at pH = 8 (left) and at pH = 10 (right); visible pile-ups are observed around the indentation borders.

The values of E_f deduced by the Bec's model were 16.1 ± 0.5 GPa for the film prepared at pH = 8, and 14.1 ± 0.4 GPa for the film prepared at pH = 10. The slightly higher modulus of the film prepared at lower pH is consistent with the more rigid structure expected for a stronger ionically crosslinked nanofibrils network. Nonetheless, owing to the broad dispersion of the data obtained at the highest pH, this difference in the modulus is not statistically significant.

The evolution of the hardness due to the increment in the depth of penetration for both film samples is shown in Figure 5.5 along with the best-fit curves obtained from the application of the Korsunsky's model. Although not as pronounced as for the modulus curves, the hardness also increased monotonically with the penetration depth. Unlike the fitting of the Bec's model for the determination of the elastic modulus of the films, the models to determine the film hardness required the simultaneous fitting of at least two parameters, namely H_f and k in the case of Korsunsky's model, or H_f and $\chi = (\sigma_f E_s)/(\sigma_s E_f)$ in the case of Bhattacharya's. Moreover, by fixing the hardness of the substrate to the value obtained on the bare silicon wafer (H_s = 11.9 GPa) it was not possible to achieve the convergence of the models to the experimental data. Therefore,

this third parameter was also allowed to vary during the iteration process. Both models were only applied to the data points collected between 10% and 70% of the film thickness for all the samples reported from here on in order to guarantee good convergence of the fits; divergence below and above these depths were ascribed to indentation size effect and non-homogeneous characteristics of the films, respectively. Under these premises, the hardness values obtained by the fitting of Korsunsky's and Bhattachayra's models to the experimental data are presented in Table 5.1.

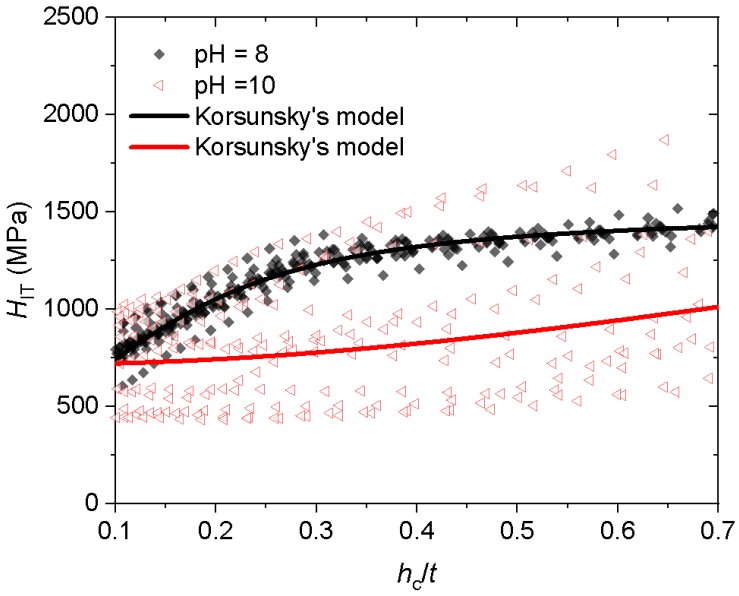

Figure 5.5: Evolution of the indentation hardness with the depth of penetration normalized to film thickness extracted from CSM indentations of $(CNF/PVAm)_{97}$ films prepared at two different pH of the polycation solution.

In all the samples and conditions tested it was observed that the values of the film and substrate hardness determined by Bhattacharya's model tended to be higher and lower, respectively than those estimated by Korsunsky's model. Hereinafter we compare the values of H_f and H_s averaged from the results obtained from both models. The high dispersion of the acquired data on the rough sample prepared at pH = 10 difficulted the good fitting of either model (see R^2 value in Table 5.1) and therefore accurate comparisons were not possible. On the contrary, both models described fairly well the variation of the hardness with the penetration depth for the film prepared at low pH, resulting in an average film hardness of 540 MPa. This value approaches the maximum value reported in the literature for LbL nanocomposites.[270]

Table 5.1: Coefficients determined by the application of Korsunsky's and Bhattacharya's models to the experimental data acquired on the film samples prepared at different pH of the PVAm solution.

Model	Parameter	PVAm @ pH = 8	PVAm @ pH = 10
Korsunsky	H_f **(MPa)**	513 ± 7	713 ± 2
	H_s **(MPa)**	1482 ± 7	2500 ± 1470
	R^2	0.9384	0.14985
Bhattacharya	H_f **(MPa)**	572 ± 5	710 ± 10
	H_s **(MPa)**	1376 ± 5	1740 ± 770
	R^2	0.92877	0.14956
Average	H_f **(MPa)**	540 ± 40	712 ± 2
	H_s **(MPa)**	1430 ± 75	2120 ± 540

In an attempt to reduce the influence of the surface roughness on the comparison of the mechanical properties of the films prepared at different pH, we determined the load/stiffness^2 parameter (H/E^2 = [4/π][P/S^2]) proposed by Joslin and Oliver,[271] which gives an indication of the material's resistance to plastic deformation. The determination of this parameter relies on the use of the recorded values of load, *P*, and the stiffness, *S*, obtained from the slope of the unloading curve, and thus it does not require a knowledge of the actual contact area. The drawback of this approach in the case of thin films is that the stiffness is not corrected from the influence of the substrate, therefore this parameter continually decreased with the indentation depth. The values extracted at 20% of the film thickness (chosen to reduce the influence of both the indentation size effect and the substrate) are reported in Figure 5.6 for comparison. Statistically, the resistance to plastic penetration, H/E^2, was higher at pH = 10 than at pH = 8 (2100 ± 800 nm^2/mN *vs*. 1600 ± 200 nm^2/mN; $F(1, 33) = 7.04$, $p = 0.01$). However, the high scattering of the reported parameter's values was not significantly improved, which suggests that the uncertainty in the determination of the contact area was not the only source of error. Indeed, since the indentation depths were comparable to the superficial roughness features, actual differences in the properties may arise depending on whether the tip of the indenter first probes the sample on or around a peak or a valley of the superficial asperities. For this reason, no definite conclusions could be drawn about the effect of the pH of the polycation solution used during film preparation on the mechanical properties of the films.

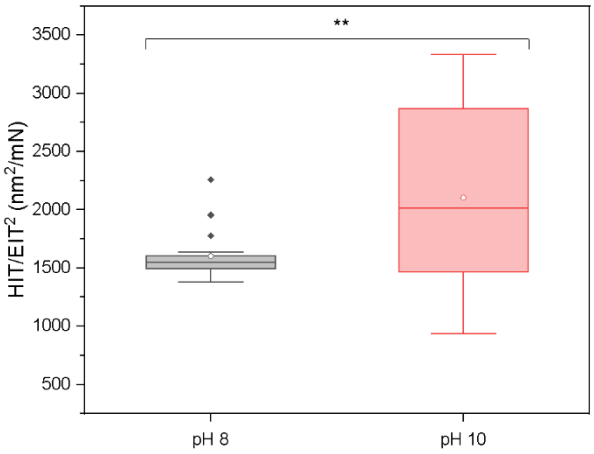

Figure 5.6: Comparison of the load/stifness^2 parameter determined for the two tested samples. ** indicates statistical significance at p = 0.01.

It is worth commenting on the huge difference between the hardness of the substrate H_s measured for silicon and the one estimated by the application of Korsunsky's and Bhattacharya's models (Table 5.1). In fact, since the plastic deformation is contained within the limits of the film thickness, the substrate is expected to have minimal or no influence on the determination of the hardness. Therefore, the elevated values of hardness measured deep into the bulk silicon are inaccessible under the testing conditions of the supported thin films. We propose, thus, that the monotonic increment of the hardness with increasing penetration depth corresponds to the densification by crushing of the porous material under the indenter, as it has been reported for other types of porous thin films.[272] As mentioned before, the CNF-based multilayers can be seen as a network of flexible nanofibrils and empty space. Under the increasing load of the indenter tip, the pores are first compressed before the confined nanofibrils are continually compacted as schematically depicted in Figure 5.7. This sequential pore crushing and nanofibril compaction give rise to a gradient of the mechanical properties of the film. Thus, the substrate hardness H_s reported in Table 5.1 corresponds partly to the hardness of the compacted CNF/PVAm layers and not only to the actual silicon substrate. This gradient model is consistent with the aforementioned crossing of Bec's model curve (describing a homogeneous film) with the experimental compliance data. The compacted film does not affect considerably the elastic response, though,

because the elastic-affected zone is far larger than the plastic zone, extending deep into the stiff silicon substrate.

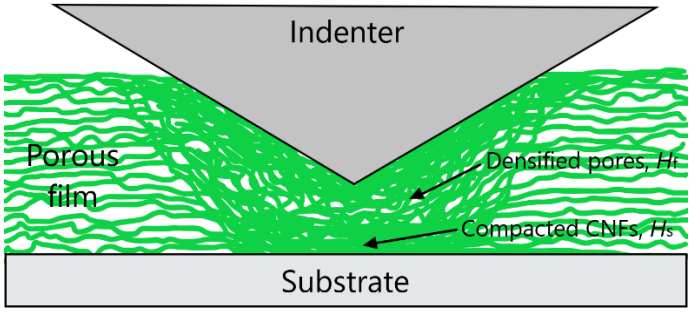

Figure 5.7: Schematic representation of the densification of the film under the indenter by crushing of the porous structure and compaction of the nanofibrils.

5.2.2. Effects of the incorporation of MTM clay to the multilayer system

Besides polyelectrolytes, we have also prepared some isotropic samples in which montmorillonite (MTM) clay has been incorporated into the multilayer structure of the nanocellulose film. In this section, we compare the mechanical properties of the resulting hybrid $(CNF/PVAm/MTM/PVAm)_n$ samples to those of the film composed exclusively of cellulose and polyelectrolyte. The experimental and fitted curves obtained for the compliance vs the contact radius of the organic and the hybrid film samples prepared at pH = 8 and pH = 10 are shown in Figure 5.8. We remarked that the incorporation of clay improved the quality of the surface of the film prepared at pH = 10, judged by the significantly narrowed scattering of the experimental data and by the qualitative comparison of the optical micrograph of the imprint shown in Figure 5.9 with that of the purely organic sample shown in Figure 5.4(right). Apart from this reduction in roughness and the consequent enhancement of the accuracy of the measurement at higher pH, no significant differences were encountered among the datasets of the samples with and without clay (Figure 5.8). Therefore, the incorporation of clay nanoplatelets to the CNF/PVAm film proved not to have any practical impact on the elastic modulus of the resulting films. The fitting of Bec's model to the experimental data was not improved either and the apparent compliance was overestimated all over the depth range.

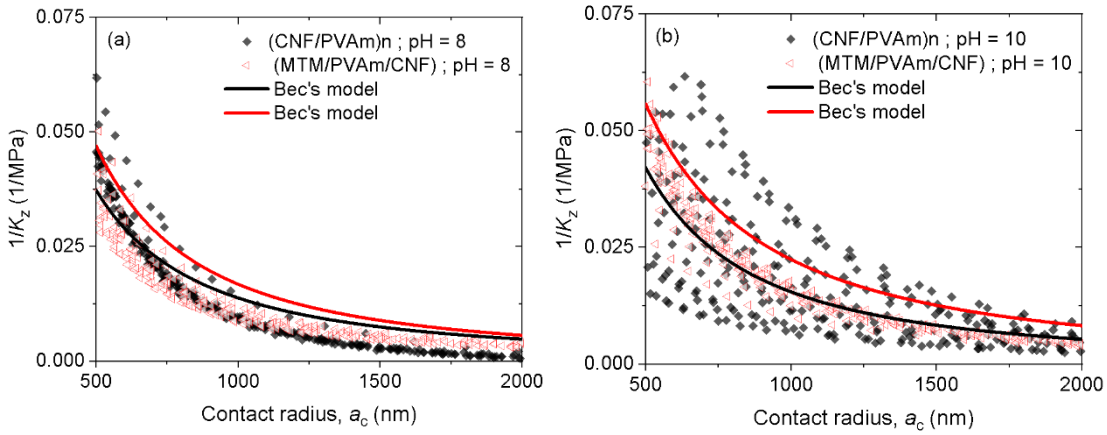

Figure 5.8: Composite compliance as a function of the contact radius extracted from CSM indentations of multilayer $(CNF/PVAm)_n$ films with and without clay prepared at pH = 8 (a) and pH = 10 (b). The experiment was performed at a controlled RH < 3%.

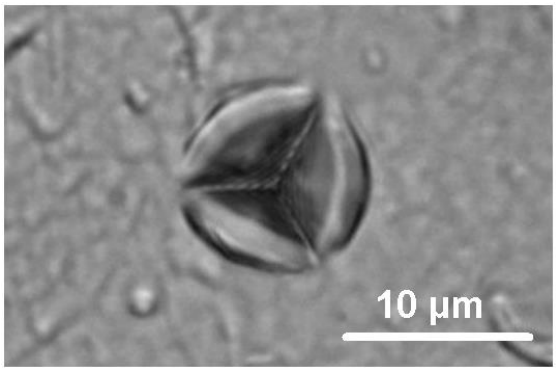

Figure 5.9: Optical micrograph of the residual imprint left after the CSM indentation on the film incorporating clay nanoplatelets within the multilayer structure, fabricated at pH = 10.

The depth profiles of the hardness of the films are shown in Figure 5.10 and the values of the best-fit parameters are summarized in Table 5.2. Comparisons at pH = 10 were not relevant due to the lack of fit of the data of the organic film. On the contrary, the data of the hybrid sample were well described by the mathematical models and it could be compared to the hybrid film prepared at lower pH: both the hardness of the film and the substrate (i.e., the compacted film) were higher on the samples prepared at pH 10. At pH = 8, the hardness of the film was found to be higher when the internal structure of the $(CNF/PVAm)_n$ multilayer was intercalated with inorganic clay nanoplatelets, as it is expected from a simple rule of mixture.

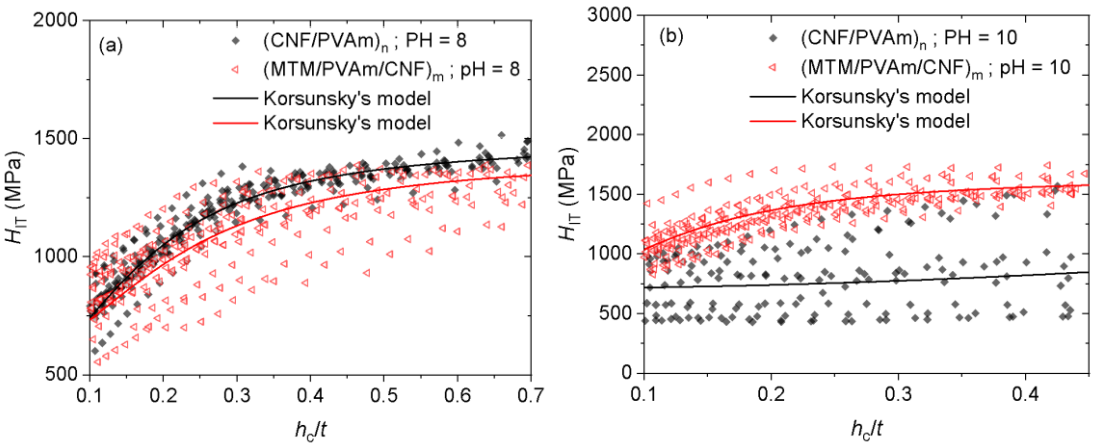

Figure 5.10: Evolution of the indentation hardness with the depth of penetration normalized to film thickness extracted from CSM indentations of thick films incorporating clay nanoplatelets prepared at pH = 8 (a) and pH = 10 (b).

Table 5.2: Average hardness determined by the application of Korsunsky's and Bhattacharya's models to the experimental data acquired on the film samples with and without MTM clay prepared at different pH.

Parameter	**PVAm @ pH = 8**		**PVAm @ pH = 10**	
	Organic	**Hybrid**	**Organic**	**Hybrid**
H_f **(MPa)**	540 ± 40	620 ± 40	-	680 ± 30
H_s **(MPa)**	1430 ± 75	1380 ± 60	-	1590 ± 90

5.2.3. The effect of hydration

The mechanical properties of polyelectrolyte complexes and polyelectrolyte multilayers are known to be strongly correlated with their water content, which acts as a strong plasticizing agent.[273,274] Water plasticizes the studied films by disrupting electrostatic interactions and by creating free volume in the porous network, thus enhancing chain and fibrils mobility.[275–278] For hydrophilic PEM systems, such as the $(CNF/PVAm)_n$ multilayer films fabricated in this study, the water content increases with the humidity of the atmosphere to which it is exposed. In the present section, we studied the effect of the relative humidity (*RH*) on the elastic modulus and hardness of the multilayer systems $(CNF/PVAm)_n$ and $(CNF/PVAm/MTM/PVAm)_m$ prepared with the PVAm solution at pH = 8. Samples prepared at pH = 10 were not considered in virtue of the negative effect of their excessive roughness on the accuracy of the determination of the mechanical properties.

Figure 5.11(a) and (b) show the depth profiles of the apparent compliance and hardness measured at three different levels of humidity for the purely organic sample, while the extracted values of the film modulus and hardness of both the organic and the hybrid samples are compared in Figure 5.11(c) and (d), respectively. Owing to the insufficient fitting of the Bec's model to the experimental data, the values of E_f reported in Figure 5.11(c) correspond to the apparent modulus measured at 20% of the film thickness and not to the values extracted from the model. As for the hardness, we report the average values of H_f and H_s extracted from the fitting of Korsunsky's and

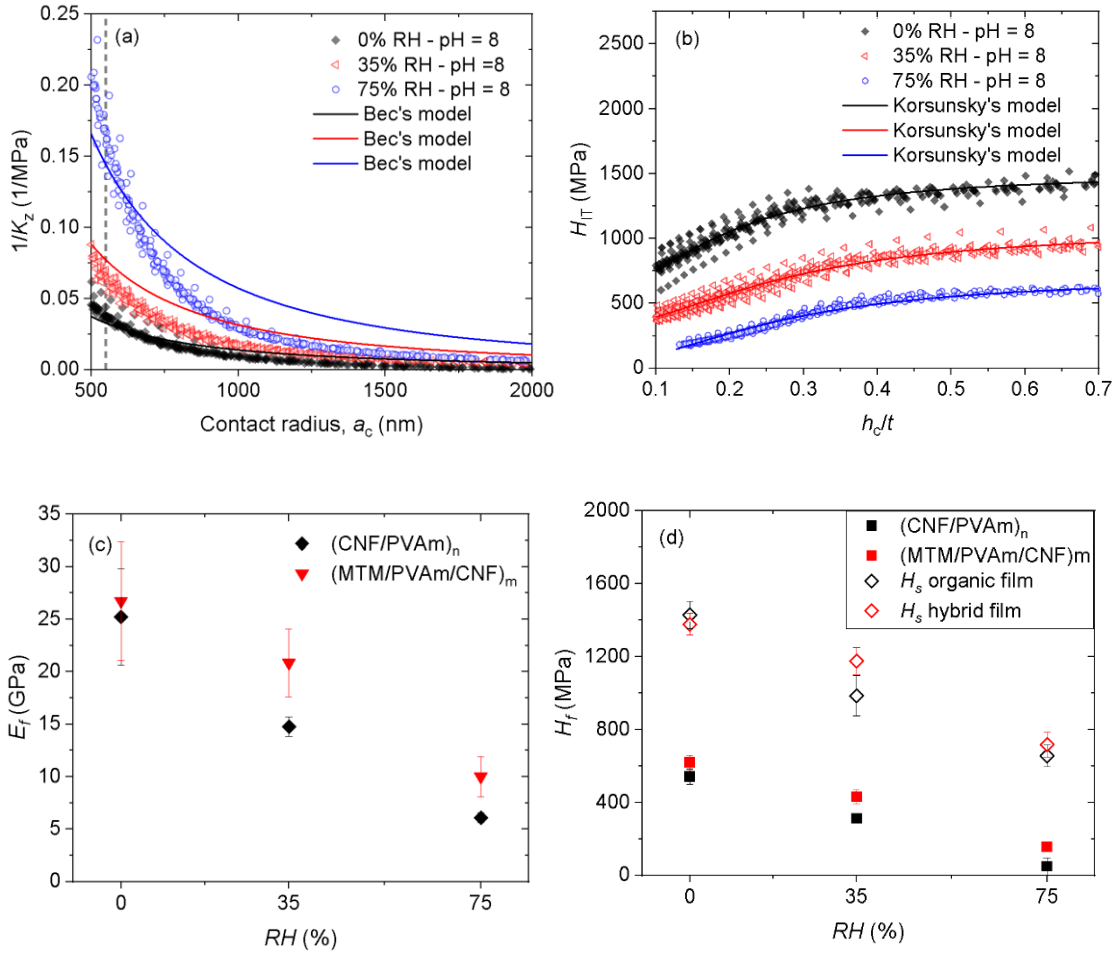

Figure 5.11: Comparison of the depth profiles of the reciprocal of the global stiffness (a) and the indentation hardness (b) measured at three different levels of relative humidity on the $(CNF/PVAm)_n$ films prepared at pH = 8. Decay of the film modulus (c) and the film hardness (d) of the organic and the hybrid film with the relative humidity.

Bhattacharya's models, which represented fairly well the experimental data of this property. As expected, both properties dropped considerably with the increment of the humidity level. Upon

hydration from < 3% RH (labeled 0% RH) to 75% RH, E_f dropped 76% in the purely organic sample and 63% in the hybrid film. The hardness of the film, H_f, was even more sensitive to humidity than the elastic modulus, falling 91% in the case of the organic film, and 75% in the hybrid one. The hardness of the compacted multilayer, H_s, also dropped linearly with the degree of humidity, proportional to the loss of performance of the film, as shown in Figure 5.11(d). These results imply that the incorporation of MTM clay into the CNF-based film slightly improved the resistance of both mechanical properties to humidity, as it has been reported before.[279]

5.2.4. Effect of the internal structure of the multilayer films

All samples characterized so far had in common that they were prepared by the orthogonal spraying of the CNF suspensions, which produced films with quasi-isotropic properties. We have seen in chapters 3 and 4, though, that the deliberate combination of GIS and LbL allows us to induce a well-defined alignment of the reinforcing cellulose nanofibrils within the films. In the present section, we investigate the mechanical responses of such anisotropic samples; in particular, we compare the modulus and hardness of films with unidirectional and helicoidal alignments (97L1x15°) of the CNFs to the values obtained for a control sample with "random" orientations of the nanofibrils. The values of modulus and hardness obtained for these samples are gathered in Table 5.3. As in the previous section, the reported moduli represent the values of the apparent moduli read at 20% of the film thickness because the Bec's model did not fit the data (Figure 5.12). These values are not corrected from the influence of the substrate and thus they do not represent the actual properties of the films, but they are used here to compare the relative stiffness of the different samples. Both the stiffness and hardness of the random and the helicoidal films were statistically the same, while both properties of the unidirectional film were higher. This result may suggest actual differences in the mechanical behavior of the films owing to the organization of the reinforcing nanofibrils, which are better packed when arranged parallel to each

other. But the measurement on the unidirectional sample may also be biased by the alignment of the internal anisotropy of the film and the edges of the Berkovich indenter.

Table 5.3: Comparison of the film modulus and hardness of film samples with different internal arrangements of the CNFs.

	Apparent modulus at 20% thickness (GPa)	***H_f* (MPa)**	***H_s* (MPa)**
Random	25 ± 5	540 ± 40	1430 ± 75
Unidirectional	34 ± 4	670 ± 50	1620 ± 60
Helicoidal	23 ± 3	570 ± 50	1360 ± 40

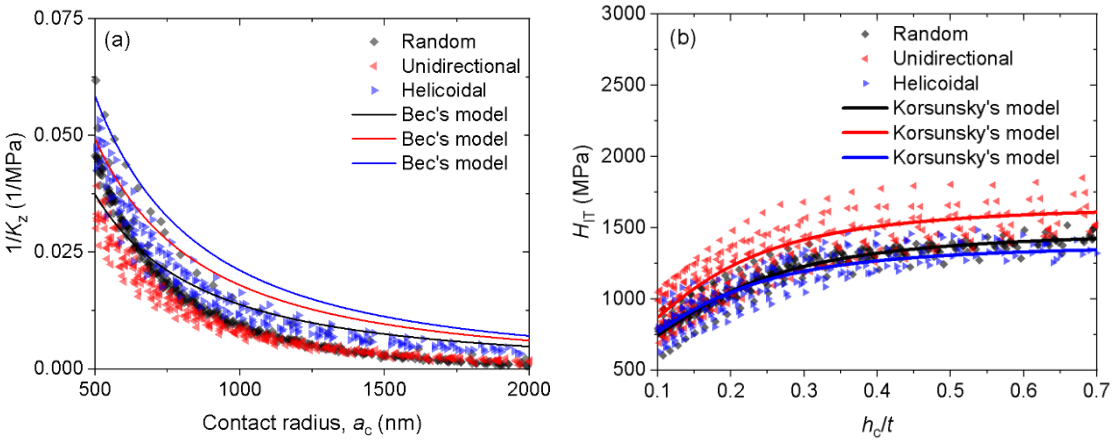

Figure 5.12: Depth profiles of the apparent compliance (a) and the indentation hardness (b) measured on $(CNF/PVAm)_n$ films with three different internal microstructures. Samples prepared with pH = 8 and measured at RH < 3%.

Figure 5.13 shows the variation of both mechanical properties with the relative humidity, where no significant differences were found among the sensitivity to hydration of the samples with different internal structures. The elastic modulus and the film hardness of all three samples decayed approximately 76% and 93%, respectively, when passing from the dry (< 3% RH) to the wet state (75% RH).

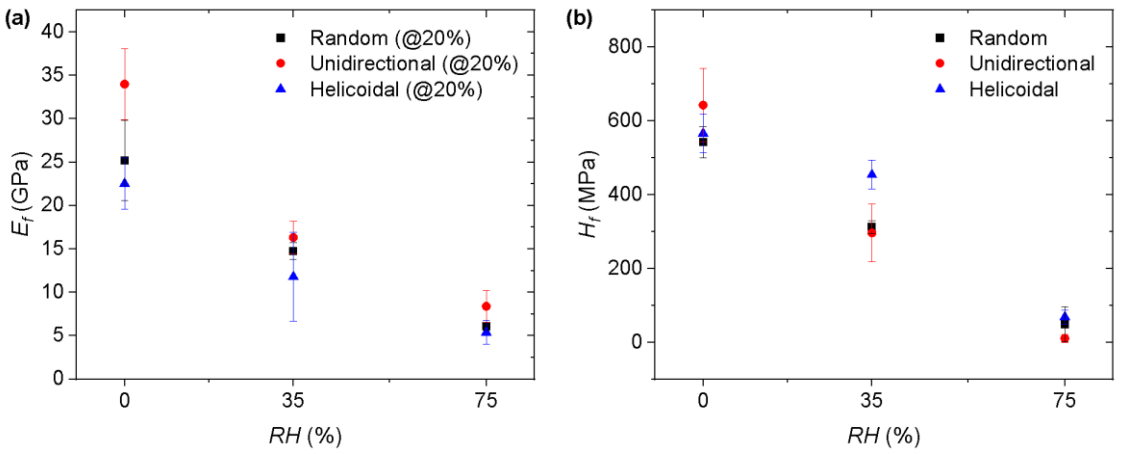

Figure 5.13: Decay of the film modulus (a) and the film hardness (b) with the humidity on samples with three different internal microstructures of the reinforcing cellulose nanofibrils.

5.2.5. Summary of results from the CSM measurements

At this point, we summarize the most important conclusions drawn from the nanoindentation experiments performed following a CSM methodology and the use of mathematical models to deconvolute the properties of the multilayer films from those of the silicon substrate. The high roughness of the film prepared at high pH impeded the accurate comparison of the properties of these samples, thus, no conclusions could be drawn about the effect of this parameter. However, the inadequate fitting of the elastic model proposed by Bec et al. provided insight into the internal characteristics of the CNF-based multilayer films; it suggested that the properties of the films were not homogeneous. This observation was further supported by the detection of two different values of hardness extracted from Korsunsky's and Bhattacharya's models. These models described well the experimental data but, given that the indentations were confined within the thickness of the film, the so-called "substrate hardness, H_s" could not correspond to the 10-times-harder silicon wafer. We recalled the observations made by AFM in Chapter 3 of the formation of pores and thus proposed that an internal porous structure is responsible for the gradient mechanical properties of the multilayer films. The incorporation of MTM clay slightly improved the hardness as well as reducing the sensitivity of both the elastic modulus and the hardness to the plasticizing effect of ambient humidity. The parallel alignment of the reinforcing nanofibrils

also seems to influence both properties, although the question remains whether this result reflects the intrinsic properties of the film or it is biased by the use of the non-axisymmetric Berkovich indenter. In the next section, we will further investigate the anisotropic response of the unidirectional film.

5.3. Anisotropic mechanical properties detected by nanoindentations with Knoop geometry

From the many existing geometries of indenting tools, the pyramidal one giving a diamond-shape indentation with a length that is about 7 times the width and 30 times the depth, is the one showing the highest sensitivity to shallow indentation, which first permitted the extension of the indentation tests to small specimens and brittle materials.[280] The non-symmetric geometry of the Knoop indenter has additionally been exploited for the identification of anisotropic mechanical properties in ceramics [281–283] and polymers,[284] as well as bi-axial residual stresses in steels[285] and polymers.[286]

In Chapter 3, we discussed the difficulties to characterize the unidirectional alignment of CNFs by AFM on the multilayer films once they are composed of more than a few layers. We have therefore resorted to optical methods such as birefringence and Mueller matrix ellipsometry to verify that the unidirectional alignment conferred by the GIS methodology to the individual "layers" of the CNFs was retained on thick films. In the present section, we exploit the Knoop tip sensitivity to material anisotropy to obtain mechanical evidence of the anisotropic characteristics of the unidirectional thick $(CNF/PVAm)_n$ films. For doing so, we measured the elastic modulus and hardness at three azimuthal angles between the theoretical direction of alignment of the nanofibrils and the longer diagonal of the Knoop tip (Figure 5.14). We compared the results obtained on thick unidirectional films prepared by GIS to those obtained on a control sample, ideally random, prepared by orthogonal spraying. The samples were prepared with PVAm at pH = 8 and were tested at RH < 3%.

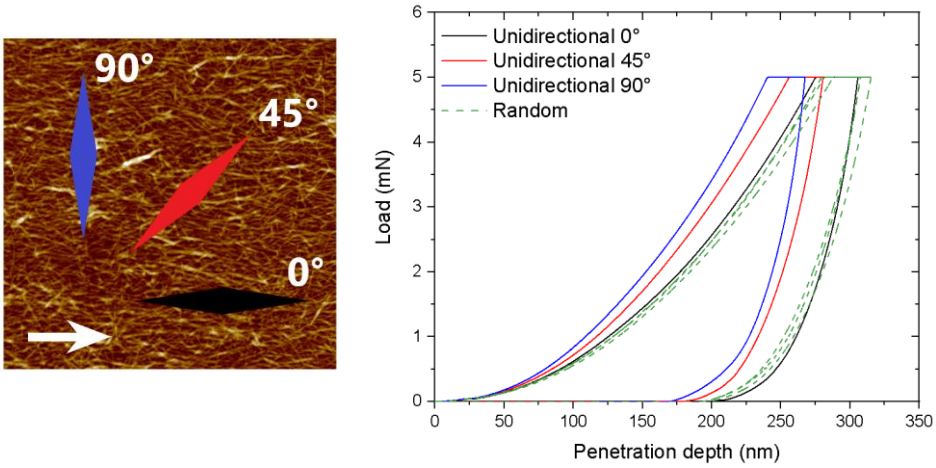

Figure 5.14: (left) Direction of alignment of the long axis of the Knoop indenter with respect to the GIS direction (white arrow) of the CNF suspension during the fabrication of the unidirectional sample. (right) Average compliance curves obtained at different azimuth angles on the unidirectional as well as the random sample.

Figure 5.14(right) shows the average compliance curves collected for both samples probed to a peak load of 5 mN. Clearly, increased depths of penetration were attained on the unidirectional sample when the azimuthal angle decreased from 90° (longer diagonal of the tip perpendicular to the direction of CNF alignment) to 0° (longer diagonal parallel to the direction of CNF alignment). On the contrary, virtually the same depth was obtained on the random sample independently of the azimuthal angle (all curves are shown in the same color for the sake of simplicity).

Some considerations were necessary before comparing the resulting elastic modulus and hardness of the specimen material obtained by nanoindentation with the Knoop geometry. In particular, owing to the different elastic recovery of the short diagonal of the residual impression compared to the long diagonal, the sides of the imprint "collapse" inward upon removal of the load, reducing the actual projected area of contact and leading to incorrect values of the mechanical properties. We applied the method proposed by Riester et al.[287] to correct the contact area to be input into the Oliver-Pharr equations used to determine the elastic modulus and hardness from the compliance curves. This method is in turn based on the dependence observed by Marshal et al.[288] of the recovered indentation size in terms of the geometry of the indenter and the ratio H/E, which,

in the assumption that the recovery along the long axis is negligible compared to that of the short axis, can be expressed as:

$$\frac{b'}{b} = 1 - \alpha \frac{d}{b} \frac{H}{E} \quad \text{(Eq. 5.4)}$$

where *d* and *b* are the lengths of the long and short diagonals at full load, respectively (*d*/*b* = 7.11); *b'* is the length of the recovered short diagonal after unloading, and α is a geometry factor found from experiments on a wide range of materials to be equal to 0.45.[288] Riester et al. then calculated a corrected semi-angle θ_2' for the pyramidal Knoop indenter which accounts for elastic recovery forces, given by:[287]

$$\tan \theta_2' = \left(\frac{b'}{b} tan\theta_2 \right) \quad \text{(Eq. 5.5)}$$

where θ_2 is the face angle of the short axis with the central axis of the indenter. The corrected projected area was then calculated by $A = 2h_c^2 \tan \theta_1 \tan \theta_2'$, with $\theta_1 = 86.25°$. The ratio *H*/*E* used in Eq. 5.4 was calculated using the values determined in § 5.2.4.

Other types of corrections of the contact area have also been proposed, for instance, the enlarged area in the case of piling-up around the indenter has been calculated by direct measurements of the height profiles extracted from AFM images of the imprints.[289] Indeed, AFM micrographs of the impressions left by the Knoop indenter (as the one shown in Figure 5.15) demonstrated that the $(CNF/PVAm)_n$ samples presented pile-ups around the lateral sides with heights of the order of 50 nm. However, given the difficulties encountered and the long time needed to acquire sufficient accurate AFM pictures of all the imprints *in-situ* after the experiment, no corrections of the pile-ups effects were performed. Nevertheless, the goal of the experiment was to compare the relative difference among the properties measured at different azimuth angles rather than assessing exact values.

The resulting values of the elastic modulus and hardness measured at different azimuth angles on the random and unidirectionally-oriented $(PVAm/CNF)_n$ films are compared in Figure 5.16. The

modulus of the film with random orientation, corrected from the effects of the elastic recovery, was nearly the same independently of the azimuthal angle of testing; only a slightly higher value of the modulus (~10%) was found for the measurements at 90°, but this small difference was judged insignificant in practice. Moreover, as it was discussed in Chapter 3, the samples prepared by orthogonal spraying are not perfectly random, but they may present a weak anisotropy resulting from the gravitational flow of the polyelectrolyte solutions during drainage; this weak anisotropy might be in part causing the slight difference in modulus at 90°. The same trend was found on the multilayer film composed of unidirectionally oriented nanofibrils ($F(2, 48) = 41.55$, $p < 0.001$), but in this case the difference in modulus between the perpendicular and the parallel direction was about 26% (63 ± 5 GPa and 50 ± 4 GPa, respectively). As for the hardness, a difference of about 28% was found between the values collected at the parallel and perpendicular directions, being the difference statistically significant as determined by one-way ANOVA ($F(2, 48) = 14.33$, $p < 0.001$). On the contrary, no statistical significance was found among the measurements realized at different azimuthal angles on the random sample ($F(2, 42) = 1.17$, $p > 0.321$).

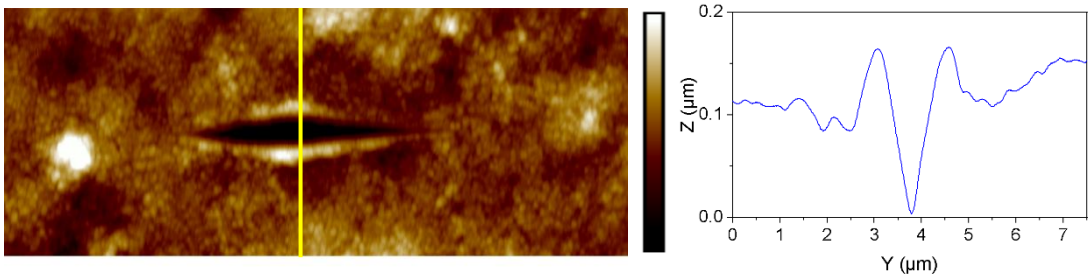

Figure 5.15: (left) topographical AFM image of the remaining imprint after nanoindentation with Knoop geometry on the unidirectional sample; image size: 19.5 x 7.7 µm^2, vertical scale range = 2 µm. (right) height profile extracted at the position of the yellow line on the AFM picture.

The anisotropic response of both mechanical properties on the unidirectional film, represented by the higher values detected when the long diagonal of the indenter was oriented perpendicularly to the spraying direction (and therefore, to the direction of alignment of most nanofibrils), results from the parallel alignment of the direction of higher stress concentration (that of the long diagonal of the indenter) with the weaker direction of the sample, i.e., that in which elastic and plastic deformations proceed by the separation of aligned fibrils bound together by weak

interactions (hydrogen bonds and ion-pairing with the PVAm). On the opposite case, when the direction of maximum stress concentration is perpendicular to the nanofibril orientation, the deformation requires the collective displacement of comparatively higher amounts of nanofibrils and the rupture of their strong covalent bonds, which causes higher resistance to both elastic and plastic deformation. This situation is depicted schematically in Figure 5.17.

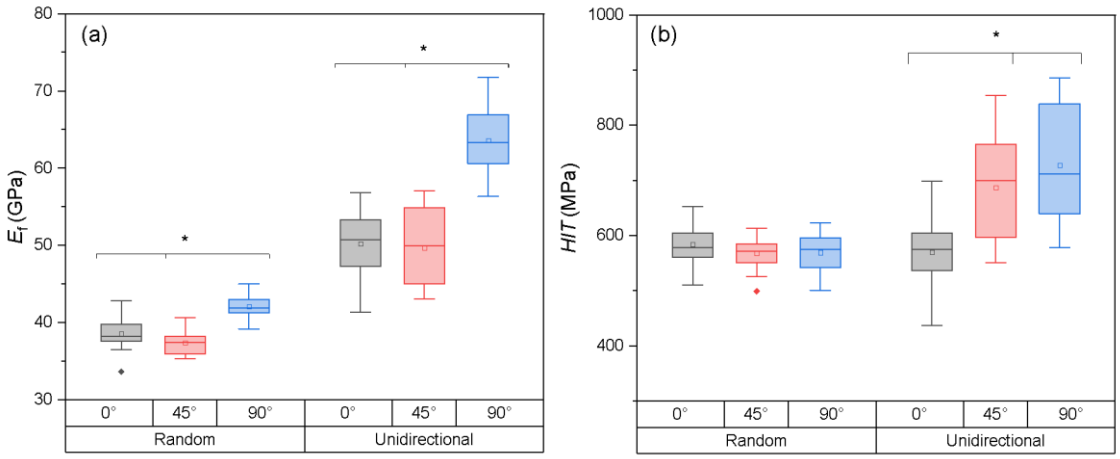

Figure 5.16: (a) Indentation modulus and (b) hardness of the random and unidirectional samples, measured at three different azimuth angles with respect to the GIS direction. * indicates a *p*-value < 0.001.

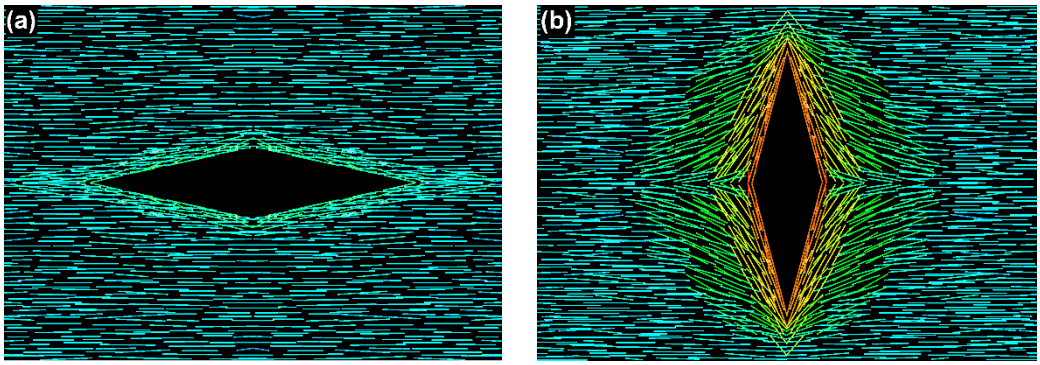

Figure 5.17: Schematic representation of the comparative extent of deformation attained when the long axis of the indenter is (a) parallel or (b) perpendicular to the main direction of alignment of the CNFs. The lines represent the parallel alignment of the cellulose nanofibrils, they deform under the application of the indentation load but the number of nanofibrils deformed depends on the orientation of the Knoop indenter. Different angles of alignment are colored differently by the OrientationJ plug-in of ImageJ.

As expected, the characterization of the helicoidal sample with a Knoop indenter resulted in no significant difference among either the modulus ($F(2, 46) = 0.15$, $p = 0.862$) or the hardness ($F(2,$

47) = 1.31, p = 0.280) measured at different azimuthal angles as it can be seen in Figure 5.18, so the sample can be regarded as a quasi-isotropic material.

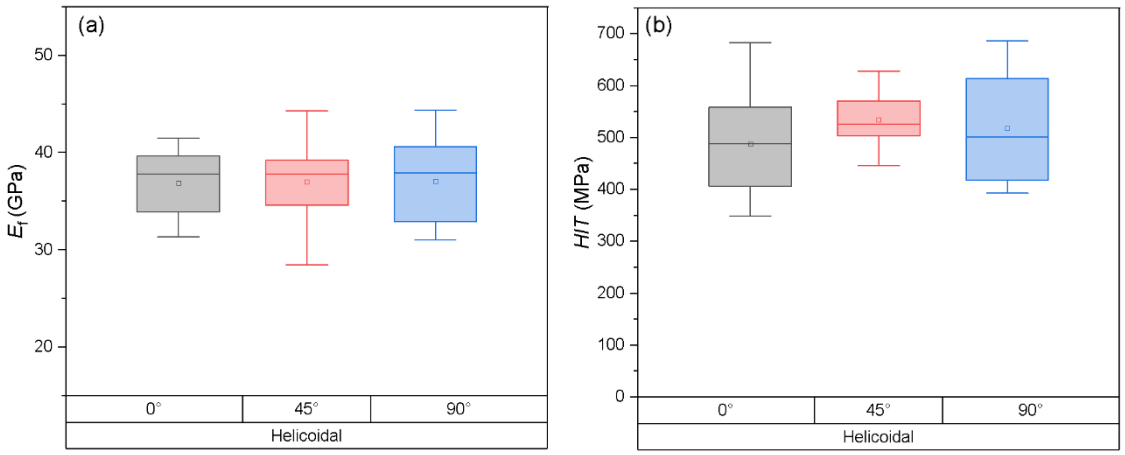

Figure 5.18: (a) Indentation modulus and (b) indentation hardness of a sample with helicoidal alignment, measured at three different azimuth angles.

Riester et al. showed that the values of the elastic modulus and hardness of some metals measured with a Knoop indenter and corrected from the elastic recovery were consistent with those obtained with other types of indenters.[287] The values of hardness that we determined with the Knoop indenter are also consistent with the ones reported in the previous section. The values for the random and the helicoidal samples, which are independent on the tested angle, were approximately 580 ± 34 MPa and 510 ± 84 MPa, respectively. Given the scale of the error, these values are close to the ones reported in Table 5.3, determined by CSM with a Berkovich geometry. On the other hand, the hardness of the unidirectional sample depended on the tested angle, reaching values about 25% higher than the random sample in the most extreme case (i.e. at 90°) and equal values when the long axis of the indenter was parallel to the main alignment direction of the nanofibrils.

In the case of the elastic modulus, the values estimated with the Knoop geometry were considerably larger than the ones determined in the previous section (at 20% penetration depth), although they followed the same trend: random = helicoidal < unidirectional. The difference in the absolute values comes from the higher penetration depths reached during the Knoop experiment, about 30%, thus been more influenced by the modulus of the silicon substrate. Still,

the lowest modulus measured in the unidirectional sample (at 0°) was 25% higher than the modulus of the random and the helicoidal sample, hence, the parallel alignment of the cellulose nanofibrils effectively increase the mechanical properties of the multilayer films, presumably due to an improved packing of the CNFs.

5.4. Nano-contact fatigue testing at high strain rates

The anisotropic mechanical properties of the unidirectionally-aligned films imply a preferential direction of propagation of the deformation (or damage, e.g. cracking), promoted by the low-energy-demanding separation of nanofibrils (or bundles of nanofibrils) as discussed in the previous section. This directionality is at the origin of the enhanced toughness observed in natural materials possessing helicoidal arrangements of the fibrillar reinforcement phase since it promotes the deflection of cracks/deformation following longer and tortuous paths that dissipate a higher amount of energy, as briefly introduced in Chapter 1. In this final section, we attempt to provide evidence of the enhanced mechanical behavior of the helicoidally GIS-structured CNF-based multilayer films when subjected to high strain rate solicitations. It is a difficult task, though, to probe the impact resistance of supported thin films such as the one prepared in the present work. For instance, the impact test methods commonly used to investigate the brittle-ductile behavior of polymers (e.g. Charpy or Izod) are designed for bulk samples with standardized geometries. Thus, we relied on a nanoscale repetitive fatigue testing technique[290] to investigate the deformation of the $(CNF/PVAm)_n$ multilayer thin films at high strain rates. This technique, initially designed for studying the brittle failure of hard coatings, was also shown to be sensitive to nano-/micro-structural variations in polymeric films.[190] The method is based on the repetitive stress-cycling ("impact") of the test probe while following the evolution of the induced damage in the film with time. For ductile materials, such as hydrated cellulose films, the amount of permanent deformation can be used as an indirect measure of the energy absorbed by the material during "impact".

The hysteresis curves shown in Figure 5.19 show the evolution of the accumulated depth (relative to the depth reached after the first stress cycle) as a function of the number of repeated cycles for the multilayer $(CNF/PVAm)_n$ films with random and unidirectional alignments of the CNFs. No statistically significant difference was found among the final accumulated depth measured at different azimuth angles in the random sample, as determined by one-way ANOVA ($F(2, 17) = 0.8$, $p = 0.102$). On the contrary, the accumulated depth of the unidirectional film was 14% higher when the experiment was performed with the long axis of the indenter oriented parallel to the direction of alignment (Figure 5.19(a)) for the reasons discussed in the previous section. Apart from this offset of the total accumulated depth, the curves obtained at all the tested azimuth angles showed exactly the same shape. For simplicity and for the sake of gaining statistical accuracy, the results of the accumulated depth vs the number of cycles presented hereinafter for all the films correspond to the mean curves averaged from the results obtained at the three tested azimuth angles.

Figure 5.19(b) compares the mean evolution of the accumulated depth measured on both the random and the unidirectional film. Both curves exhibited similar behavior during the initial ~15 cycles; in this first region, every bounce of the indenter caused an additional penetration of the tip. After approx. 15 cycles, a different behavior between the curves became apparent: the relative depth of the random sample stabilized around 20 nm and remained constant until the end of the experiment. On the other hand, the penetration depth of the unidirectional sample continued to increase linearly with every new bounce of the tip. After 150 stress-cycles, the accumulated depth was 45% higher for the unidirectional sample compared to the random one ($F(1, 35) = 14.35$, $p = 0.001$). The main information extracted from the experiment is not the final depth, though, but the shape of the curve itself since this is the parameter that highlights differences in the ductility (or damage) between both materials. Permanent deformation within the film requires less energy when separating nanofibrils bound together by polymer than by breaking the strong cellulose fibrils. Consequently, when all cellulose layers are preferentially aligned in one exclusive direction, the energy given to the film by every bounce of the indenter is sufficient to either extend

previously formed cracks along the main direction of alignment or to separate the nanofibrils of a below layer, resulting in the continue increment on penetration depth observed for the unidirectional sample. On the contrary, the random sample does not have a preferential direction for fibril separation, therefore, after a certain number of impacts no further damage is possible with the level of energy supplied to the material; further penetration would only proceed for an increased level of load.

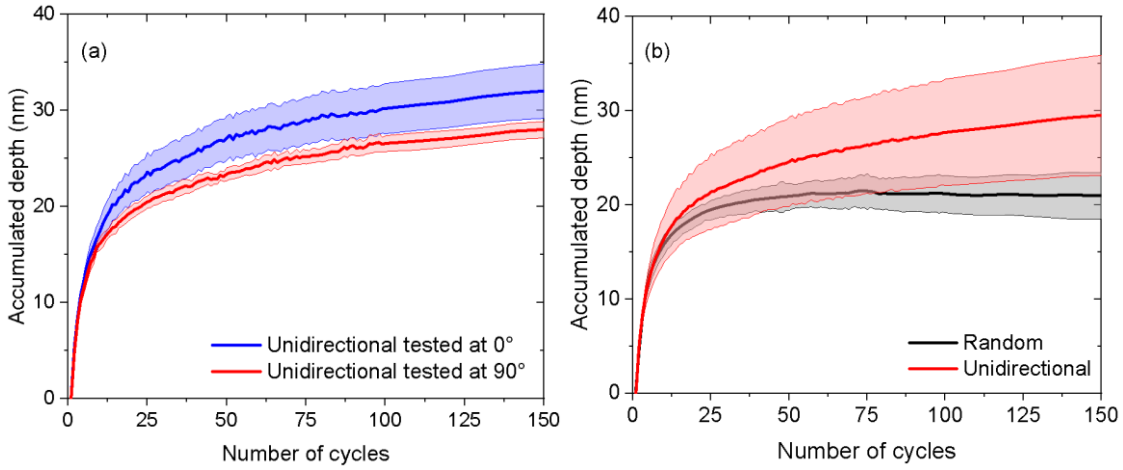

Figure 5.19: (a) Average accumulated depth vs the number of stress cycles produced on the unidirectional film tested at two different azimuth angles. (b) Comparison of the averaged accumulated depth curves for the random and the unidirectional samples. Shadowed areas correspond to the standard deviation of all measured curves.

The extent of the cyclic-induced deformation is a measure of the ductility of the film because ductile failures are associated with significant plastic deformation before failure whereas brittle failures usually involve little plastic deformation.[190] The fact that the film with the unidirectional alignment of the CNFs is more prone to deform permanently under high strain solicitations than the structureless film suggests that the parallel alignment of the reinforcing nanofibrils provides the multilayer film with a mechanism for impact energy dissipation that is not present in the sample with random orientation.

After having found that the contact-fatigue methodology employed was appropriate to detect differences in energy absorption between the random and the unidirectional films, which represent the two extreme cases of low and high ductility among all the prepared samples, we investigated

the response of a sample fabricated with a cross-ply configuration of the reinforcing cellulose layers, i.e., one in which consecutive mono-oriented layers of CNFs are rotated by 90°. The average curves obtained at two different areas of the cross-ply film are shown in Figure 5.20. The center of the sample exhibited a behavior resembling that of the random sample, i.e., the accumulated depth reached a plateau after a certain number of stress cycles (~50). This behavior was consistent with the quasi-isotropic nature of this configuration because the ease of propagation of the deformation given by the unidirectional alignment of each cellulose layer was perturbed by the perpendicular direction of propagation of the adjacent layers. However, when the experiment was performed at approx. 8 mm outside the center of the spraying sample, i.e., where one of the perpendicular directions was more important than the other (due to the narrow profile of the spraying pattern), the accumulated depth continued to grow constantly as observed on the entirely unidirectional sample. It did so in a feebler way, though, as it was expected due to the reduced number of parallel layers on the film.

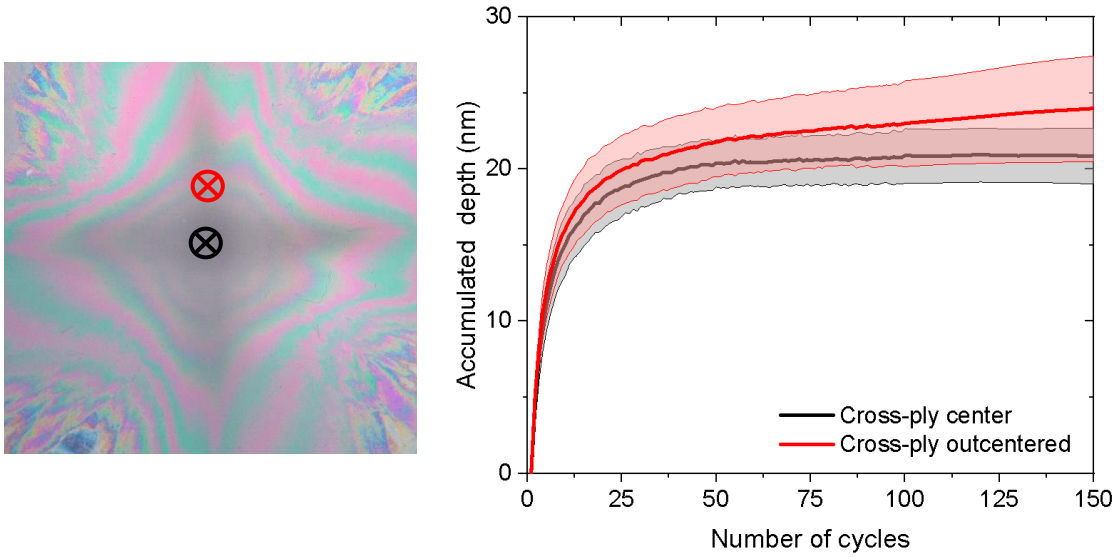

Figure 5.20: (left) Optical image of the tested $(CNF/PVAm)_{80}$ film with cross-ply configuration indicating the approximate location of the centered (black) and out-centered (red) indentations. (right) Accumulated depth vs the number of stress cycles produced on the cross-ply sample.

Finally, the nano-contact fatigue methodology was applied to a film prepared with an internal microstructure composed of a helicoidal arrangement of cellulose nanofibrils. Figure 5.21 shows

the average curve of the accumulated depth of penetration of the indenter as a function of the number of stress cycles measured at the center of the helicoidal sample. For comparison, the average curves obtained for both the random and the unidirectional samples are also shown. It is easy to recognize an enhanced ductility of the helicoidal sample compared to the random film even though the difference in the final penetration depth between both samples was not significant. Moreover, the growth rate of the penetration depth (the slope of the linear region of the curve) seemed to be identical to the one shown by the unidirectional sample, suggesting similar cumulative propagation of the deformation, or seen another way, similar efficiency of absorption of impact energy. The penetration depths of the initial cycles were shallower in the case of the helicoidal sample compared to the unidirectional one, with a less abrupt transition between the initial fast-penetrating regime and the linear-penetrating regime, which might be interpreted as a more gradual propagation of the permanent deformation.

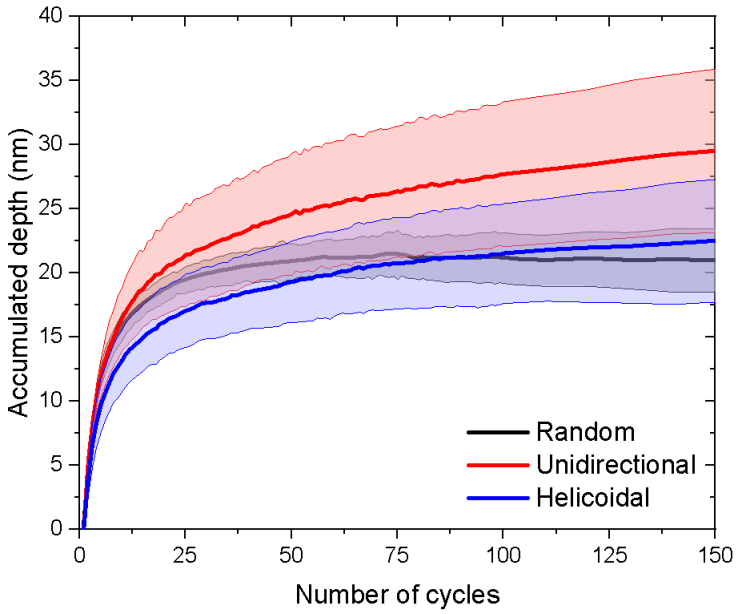

Figure 5.21: Comparison among the normalized accumulated depth vs the number of stress cycles produced on the films with random, unidirectional, and helicoidal (97L1x15°) alignment of the CNFs.

In the absence of more sophisticated methods, the nano-contact fatigue methodology seems to be sensitive and reproducible enough for comparing the ductility behavior of GIS-structured supported thin films. It provides a good starting point to further investigate the toughening

enhancement of thin films with a helicoidal arrangement of the reinforcing cellulose nanofibrils conferred by the combination of LbL and GIS.

Conclusions and perspectives

The aim of the present work was to combine the ability of the grazing incidence spraying (GIS) technique to impart in-plane alignment to anisometric nanoparticles and the sequential assembly approach of the layer-by-layer methodology with the purpose of preparing multilayer films possessing a well-defined arrangement of cellulose nanofibrils (CNF). In particular, we set out to prepare thin films with a bio-inspired twisted ply-wood organization, also referred to as Bouligand structure, in which consecutive layers of parallel aligned nanofibrils are rotated by a constant angle to form a helicoidal microstructure. This organization is at the origin of the enhanced damage tolerance (e.g. impact resistance) of the exoskeletons of some crustaceans, as well as the structural coloration, iridescence, and filtration of circularly polarized light observed in some fruits and scarab beetles.

Through this work, we used statistical methods to find the optimal spraying conditions for preparing highly oriented monolayers and we demonstrated that consecutive nanocellulose layers (CNFs and CNCs) can be effectively aligned in the desired directions, independently of the orientation of the layer below. The unidirectional alignment of cellulose nanofibrils in thick films (~1 µm) was confirmed by polarized microscopy and by Mueller matrix spectroscopic ellipsometry (MMSE). The latter also allowed the quantification of the attained optical birefringence, which was within the range commonly reported for birefringent films prepared by other means with cellulose nanocrystals (CNCs). Moreover, the Mueller matrix data and the modeling of the unidirectional film as an effective medium provided information on the local

orientation of the nanofibrils throughout the sample as well as a simple way to indirectly characterize the volume fraction of the reinforcing phase within the film, provided that the local thickness and the optical constants of the film components are accurately known (this was not the case for the analyzed sample).

Nanocomposite films with the envisioned Bouligand architecture were successfully fabricated, as confirmed by cross-sectional SEM, circular dichroism (CD) spectroscopy, and MMSE. The handedness and pitches of the helicoidal arrangement of the CNFs were varied by the rational selection of the direction of spraying, the angle of in-plane rotation between layer stacks, and the number of layers oriented in the same direction. A characteristic of such structured thin films is the circular Bragg reflection phenomenon in which circularly polarized light having the same handedness that the chiral structure of the film is preferentially reflected while the opposite handedness is transmitted. This behavior was verified by the strong CD peak detected in all helicoidal samples, approximately centered at a wavelength proportional to the average in-plane refractive index of the film and the pitch of the chiral structure, thus providing evidence of the structural nature of the signal.

The spray-assisted preparation of multilayer films with thickness approaching 1 μm showed levels of roughness larger than those observed in similar films prepared by dip-assisted and spin-assisted LbL, which reduced the transparency of the samples (60 – 80 % transmittance in the visible range). However, a couple of samples prepared in a different batch exhibited transparency similar to the one obtained by dipping, thus indicating the feasibility of improvements in this respect. The level of roughness of the thick films augmented with the increasing pH of the PVAm solution, which probably increases the water content and viscoelasticity of the $(CNF/PVAm)_n$ films as suggested by the QCM-D study (although this results cannot be directly extrapolated to the sprayed samples).

The mechanical properties of the CNF-based structured films were investigated by nanoindentation. To properly account for the effect of the underlying substrate on the measured responses we applied a constant stiffness measurement (CSM) methodology and mathematical

models of the composite elastic modulus and hardness. The non-perfect fitting of the elastic model proposed by Bec et al. and the detection of two different values of hardness extracted from Korsunsky's and Bhattacharya's models suggested an internal porous structure of the CNF-based multilayer films. On the other hand, indentations with a Knoop geometry further evidenced the anisotropic behavior of the unidirectionally sprayed samples. Finally, we implemented a nano-contact fatigue methodology to investigate the different mechanical responses of structured cellulose thin films at high strain rates. Both the unidirectional and the helicoidal films showed an increased ductility compared with the random sample, which can be indirectly related to the ability of the structured material to absorb higher impact energies by mechanisms of preferential propagation of damage/deformation.

We also prepared hybrid films with montmorillonite (MTM) clay nanoplatelets inserted into the CNF/PVAm layered structure. This reduced considerably the growth rate of the film thickness, leading to increased preparation time, but it proved to be an effective way to increase the hardness of the resulting composite film as well as reducing greatly the sensitivity of the multilayer system to the humidity.

The present study lays the groundwork for the preparation of nanocomposite films with well-controlled internal structures of the reinforcing fibrillar phase, which can be exploited for conferring enhanced mechanical and optical functionalities to the resulting films. We mostly worked with cellulose nanofibrils, a material with a promising application as an environmentally friendly alternative to petroleum-based raw materials, but the additive manufacturing route of structured thin films presented in this work can be easily extrapolated to other nanofibrillar components such as the rigid cellulose nanocrystals (CNCs), which may improve the birefringence of the uniaxial layers leading to higher efficiency in the filtration of circularly-polarized light. We remark that other fabrications routes are being increasingly exploited for the preparation of chiral CNCs films (e.g. evaporation-induced self-assembly, EISA), which are faster and applicable to larger areas, however, the GIS-LbL methodology represents an alternative highly appealing by its flexibility. For instance, it provides the possibility to incorporate various

sub-structures within the film, e.g. the combination of opposite handedness of the chiral assembly, the alternation with unidirectional segments, or the staking of various pitches. Moreover, the technique offers plenty of room for improvement, optimization, and scale-up possibilities. For instance, it is based on a simple and commercially available technology such as industrial spraying, thus the programming of the spraying sequence in robotic arms can suffice to prepare large-area samples. For speeding up purposes, film components other than polyelectrolytes (e.g. colloidal nanoparticles, latex nanoparticles, etc.) might be investigated.

References

[1] L. F. Nielsen, *Composite Materials: Properties as Influenced by Phase Geometry*, Springer-Verlag Berlin Heidelberg, **2005**.

[2] M. A. Meyers, P.-Y. Y. Chen, A. Y.-M. M. Lin, Y. Seki, *Prog. Mater. Sci.* **2008**, *53*, 1.

[3] W. Barthlott, K. Koch, *Beilstein J. Nanotechnol.* **2011**, *2*, 135.

[4] S. E. Naleway, M. M. Porter, J. McKittrick, M. A. Meyers, *Adv. Mater.* **2015**, *27*, 5455.

[5] L. J. Gibson, *J. R. Soc. Interface* **2012**, *9*, 2749.

[6] A. J. Bidhendi, A. Geitmann, *J. Exp. Bot.* **2016**, *67*, 449.

[7] S. Keten, Z. Xu, B. Ihle, M. J. Buehler, *Nat. Mater.* **2010**, *9*, 359.

[8] S. W. Cranford, A. Tarakanova, N. M. Pugno, M. J. Buehler, *Nature* **2012**, *482*, 72.

[9] C. Fu, Z. Shao, V. Fritz, *Chem. Commun.* **2009**, 6515.

[10] B. L. Thiel, C. Viney, *J. Microsc.* **1997**, *185*, 179.

[11] S. Frische, A. Maunsbach, F. Vollrath, *J. Microsc.* **1998**, *189*, 64.

[12] P. Poza, J. Perez-Rigueiro, M. Elices, J. Llorca, *Eng. Fract. Mech.* **2002**, *69*, 1035.

[13] A. Nova, S. Keten, N. M. Pugno, A. Redaelli, M. J. Buehler, *Nano Lett.* **2010**, *10*, 2626.

[14] T. Giesa, M. Arslan, N. M. Pugno, M. J. Buehler, *Nano Lett.* **2011**, *11*, 5038.

[15] F. Barthelat, Z. Yin, M. J. Buehler, *Nat. Rev. Mater.* **2016**, *1*, 1.

[16] W. Zhang, C. Ye, K. Zheng, J. Zhong, Y. Tang, Y. Fan, M. J. Buehler, S. Ling, D. L. Kaplan, *ACS Nano* **2018**, *12*, 6968.

[17] M. A. Meyers, A. Y. M. Lin, Y. Seki, P. Y. Chen, B. K. Kad, S. Bodde, *JOM* **2006**, *58*, 35.

[18] A. C. Neville, B. M. Luke, *Tissue Cell* **1969**, *1*, 689.

[19] Y. Bouligand, *CR Acad. Sci.(Paris)* **1965**, *261*, 3665.

[20] A. C. Neville, S. Levy, *Planta* **1984**, *162*, 370.

[21] D. Raabe, C. Sachs, P. Romano, *Acta Mater.* **2005**, *53*, 4281.

[22] S. Nikolov, M. Petrov, L. Lymperakis, M. Friák, C. Sachs, H. O. Fabritius, D. Raabe, J. Neugebauer, *Adv. Mater.* **2010**, *22*, 519.

[23] W. Yang, V. R. Sherman, B. Gludovatz, M. Mackey, E. A. Zimmermann, E. H. Chang, E. Schaible, Z. Qin, M. J. Buehler, R. O. Ritchie, M. A. Meyers, *Acta Biomater.* **2014**, *10*, 3599.

[24] P.-Y. Chen, A. Y.-M. Lin, J. McKittrick, M. A. Meyers, *Acta Biomater.* **2008**, *4*, 587.

[25] J. C. Weaver, G. W. Milliron, A. Miserez, K. Evans-Lutterodt, S. Herrera, I. Gallana, W. J. Mershon, B. Swanson, P. Zavattieri, E. DiMasi, D. Kisailus, *Science.* **2012**, *336*, 1275.

[26] E. A. Zimmermann, B. Gludovatz, E. Schaible, N. K. N. Dave, W. Yang, M. A. Meyers, R. O. Ritchie, *Nat. Commun.* **2013**, *4*, 2634.

[27] S. Amini, M. Tadayon, S. Idapalapati, A. Miserez, *Nat. Mater.* **2015**, *14*, 943.

[28] S. N. Patek, W. L. Korff, R. L. Caldwell, *Nature* **2004**, *428*, 819.

[29] S. N. Patek, R. L. Caldwell, *J. Exp. Biol.* **2005**, *208*, 3655.

[30] M. L. Reaka, *J. Morphol.* **1975**, *146*, 55.

[31] S. Amini, A. Masic, L. Bertinetti, J. S. Teguh, J. S. Herrin, X. Zhu, H. Su, A. Miserez, *Nat. Commun.* **2014**, *5*, 3187.

[32] N. A. Yaraghi, N. Guarín-Zapata, L. K. Grunenfelder, E. Hintsala, S. Bhowmick, J. M. Hiller, M. Betts, E. L. Principe, J. Y. Jung, L. Sheppard, R. Wuhrer, J. McKittrick, P. D. Zavattieri, D. Kisailus, *Adv. Mater.* **2016**, *28*, 6769.

[33] J. Ren, Y. Wang, Y. Yao, Y. Wang, X. Fei, P. Qi, S. Lin, D. L. Kaplan, M. J. Buehler, S. Ling, *Chem. Rev.* **2019**, *119*, 12279.

[34] P. Vukusic, J. R. Sambles, *Nature* **2003**, *424*, 852.

[35] J. Sun, B. Bhushan, J. Tong, *RSC Adv.* **2013**, *3*, 14862.

[36] J. P. Vigneron, P. Simonis, *Phys. B Condens. Matter* **2012**, *407*, 4032.

[37] H. P. Meyers, *Introductory Solid State Physics*, CRC Press, **1997**.

[38] S. Vignolini, P. J. Rudall, A. V. Rowland, A. Reed, E. Moyroud, R. B. Faden, J. J. Baumberg, B. J. Glover, U. Steiner, *Proc. Natl. Acad. Sci. U. S. A.* **2012**, *109*, 15712.

[39] S. Vignolini, T. Gregory, M. Kolle, A. Lethbridge, E. Moyroud, U. Steiner, B. J. Glover, P. Vukusic, P. J. Rudall, *J. R. Soc. Interface* **2016**, *13*, 1.

[40] K. S. Gould, D. W. Lee, *Am. J. Bot.* **1996**, *83*, 45.

[41] O. D. Onelli, T. Van De Kamp, J. N. Skepper, J. Powell, T. D. S. Rolo, T. Baumbach, S. Vignolini, *Sci. Rep.* **2017**, *7*, 1.

[42] S. Caveney, *Proc. R. Soc. London. Ser. B. Biol. Sci.* **1971**, *178*, 205.

[43] V. Sharma, M. Crne, J. O. Park, M. Srinivasarao, *Mater. Today Proc.* **2014**, *1*, 161.

[44] A. E. Seago, P. Brady, J. P. Vigneron, T. D. Schultz, *J. R. Soc. Interface* **2009**, *6*, S165.

[45] A. C. Neville, S. Caveney, *Biol. Rev.* **1969**, *45*, 531.

[46] S. Berthier, M. Thomé, P. Simonis, *Mater. Today Proc.* **2014**, *1*, 145.

[47] I. E. Carter, K. Weir, M. W. McCall, A. R. Parker, *J. R. Soc. Interface* **2016**, *13*, 20160015.

[48] L. T. McDonald, E. D. Finlayson, B. D. Wilts, P. Vukusic, *Interface Focus* **2017**, *7*, 1.

[49] C. Joyce, “A Berry So Shiny, It’s Irresistible (And Inedible),” can be found under www.npr.org/2012/09/11/160894364/how-to-get-birds-to-pick-blue-berries-they-can-t-eat?t=1584978922827, **2012**.

[50] L. Roth-Johnson, “Tropical Fruit Inspires Innovative Research,” can be found under www.scienceandfooducla.wordpress.com/?s=margaritaria+nobilis&submit=Search, **2013**.

[51] G. W. Kattawar, *Opt. Photonics News* **1994**, *5*, 42.

[52] T.-H. Chiou, S. Kleinlogel, T. Cronin, R. Caldwell, B. Loeffler, A. Siddiqi, A. Goldizen, J. Marshall, *Curr. Biol.* **2008**, *18*, 429.

[53] D. Klemm, B. Heublein, H. P. Fink, A. Bohn, *Angew. Chemie - Int. Ed.* **2005**, *44*, 3358.

[54] O. J. Rojas, Ed. , *Cellulose Chemistry and Properties: Fibers, Nanocelluloses and Advanced Materials*, Springer, Cham, **2016**.

[55] R. Jonas, L. F. Farah, *Polym. Degrad. Stab.* **1998**, *59*, 101.

[56] E. J. Vandamme, S. De Baets, A. Vanbaelen, K. Joris, P. De Wulf, *Polym. Degrad. Stab.* **1998**, *59*, 93.

[57] D. Klemm, E. D. Cranston, D. Fischer, M. Gama, S. A. Kedzior, D. Kralisch, F. Kramer, T. Kondo, T. Lindström, S. Nietzsche, K. Petzold-Welcke, F. Rauchfuß, *Mater. Today* **2018**, *21*, 720.

[58] *Microfibrillated Cellulose at a Glance - Characteristics and Potential Applications*, Application Leaflet From Borregaard, **2016**.

[59] P. Zugenmaier, *Prog. Polym. Sci.* **2001**, *26*, 1341.

[60] V. Favier, J. Y. Cavaille, G. R. Canova, S. C. Shrivastava, *Polym. Eng. Sci.* **1997**, *37*, 1732.

[61] R. Hashaikeh, P. Krishnamachari, Yarjan Abdul Samad, in *Handb. Polym. Nanocomposites. Process. Perform. Appl. - Vol. C Polym. Nanocomposites Cellul.*

Nanoparticles (Eds.: J.K. Pandey, H. Takagi, A.N. Nakagaito, H.-J. Kim), Springer Materials, **2015**.

[62] S. Beck, J. Bouchard, R. Berry, *Biomacromolecules* **2012**, *13*, 1486.

[63] M. S. Reid, M. Villalobos, E. D. Cranston, *Langmuir* **2017**, *33*, 1583.

[64] F. Cherhal, F. Cousin, I. Capron, *Langmuir* **2015**, *31*, 5596.

[65] Y. Nishiyama, P. Langan, H. Chanzy, *J. Am. Chem. Soc.* **2002**, *124*, 9074.

[66] R. Rusli, S. J. Eichhorn, *Appl. Phys. Lett.* **2008**, *93*, 33111.

[67] A. Šturcová, G. R. Davies, S. J. Eichhorn, *Biomacromolecules* **2005**, *6*, 1055.

[68] K. Tashiro, M. Kobayashi, *Polymer.* **1991**, *32*, 1516.

[69] J. Araki, S. Kuga, *Langmuir* **2001**, *17*, 4493.

[70] J. Araki, M. Wada, S. Kuga, *Langmuir* **2001**, *17*, 21.

[71] M. Roohani, Y. Habibi, N. M. Belgacem, G. Ebrahim, A. N. Karimi, A. Dufresne, *Eur. Polym. J.* **2008**, *44*, 2489.

[72] Y. Habibi, A.-L. Goffin, N. Schiltz, E. Duquesne, P. Dubois, A. Dufresne, *J. Mater. Chem.* **2008**, *18*, 5002.

[73] N. L. G. de Rodriguez, W. Thielemans, A. Dufresne, *Cellulose* **2006**, *13*, 261.

[74] F. Kimura, T. Kimura, M. Tamura, A. Hirai, M. Ikuno, F. Horii, *Langmuir* **2005**, *21*, 2034.

[75] J.-F. Revol, *Carbohydr. Polym.* **1982**, *2*, 123.

[76] S. Beck-Candanedo, M. Roman, D. G. Gray, *Biomacromolecules* **2005**, *6*, 1048.

[77] A. J. Benítez, A. Walther, *J. Mater. Chem. A* **2017**, *5*, 16003.

[78] J.-F. Revol, H. Bradford, J. Giasson, R. H. Marchessault, D. G. Gray, *Int. J. Biol. Macromol.* **1992**, *14*, 170.

[79] J. P. Lagerwall, C. Schütz, M. Salajkova, J. Noh, J. H. Park, G. Scalia, L. Bergström, *NPG*

Asia Mater. **2014**, *6*, 1.

[80] R. Hashaikeh, H. Abushammala, *Carbohydr. Polym.* **2011**, *83*, 1088.

[81] A. F. Turbak, F. W. Snyder, K. R. Sandberg, *Suspensions Containing Microfibrillated Cellulose*, **1983**, U.S. Patent 4,378,381.

[82] M. Henriksson, G. Henriksson, L. A. Berglund, T. Lindström, *Eur. Polym. J.* **2007**, *43*, 3434.

[83] A. Isogai, T. Saito, H. Fukuzumi, *Nanoscale* **2011**, *3*, 71.

[84] A. Boldizar, C. Klason, J. Kubát, P. Näslund, P. Sáha, *Int. J. Polym. Mater. Polym. Biomater.* **1987**, *11*, 229.

[85] M. Pääkkö, M. Ankerfors, H. Kosonen, A. Nykänen, S. Ahola, M. Österberg, J. Ruokolainen, J. Laine, P. T. Larsson, O. Ikkala, T. Lindström, M. Pääkko, M. Ankerfors, H. Kosonen, A. Nykänen, S. Ahola, M. Österberg, J. Ruokolainen, J. Laine, P. T. Larsson, O. Ikkala, T. Lindström, *Biomacromolecules* **2007**, *8*, 1934.

[86] T. Saito, S. Kimura, Y. Nishiyama, A. Isogai, *Biomacromolecules* **2007**, *8*, 2485.

[87] L. Wågberg, G. Decher, M. Norgren, T. Lindström, M. Ankerfors, K. Axnäs, *Langmuir* **2008**, *24*, 784.

[88] C. Goussé, H. Chanzy, G. Excoffier, L. Soubeyrand, E. Fleury, *Polymer.* **2002**, *43*, 2645.

[89] P. Stenstad, M. Andresen, B. S. Tanem, P. Stenius, *Cellulose* **2008**, *15*, 35.

[90] J.-Y. Cavaille, H. Chanzy, E. Fleury, J.-F. Sassi, *Surface-Modified Cellulose Microfibrils, Method for Making the Same, and Use Thereof as a Filler in Composite Materials*, **2000**, U.S. Patent 6,117,545.

[91] M. Andresen, L. S. Johansson, B. S. Tanem, P. Stenius, *Cellulose* **2006**, *13*, 665.

[92] A. Dufresne, *Nanocellulose: From Nature to High Performance Tailored Materials*, Walter De Gruyter, **2012**.

[93] M. Minus, S. Kumar, *JOM* **2005**, *57*, 52.

[94] O. L. Manevitch, G. C. Rutledge, *J. Phys. Chem. B* **2004**, *108*, 1428.

[95] K. Lau, C. Gu, D. Hui, *Compos. Part B Eng.* **2006**, *37*, 425.

[96] S. J. Eichhorn, A. Dufresne, M. Aranguren, N. E. Marcovich, J. R. Capadona, S. J. Rowan, C. Weder, W. Thielemans, M. Roman, S. Renneckar, W. Gindl, S. Veigel, J. Keckes, H. Yano, K. Abe, M. Nogi, A. N. Nakagaito, A. Mangalam, J. Simonsen, A. S. Benight, A. Bismarck, L. A. Berglund, T. Peijs, *J. Mater. Sci.* **2010**, *45*, 1.

[97] H. G. de Oliveira Barud, R. R. da Silva, H. da Silva Barud, A. Tercjak, J. Gutierrez, W. R. Lustri, O. B. de Oliveira, S. J. L. Ribeiro, *Carbohydr. Polym.* **2016**, *153*, 406.

[98] A. J. Brown, *J. Chem. Soc.Trans.* **1886**, *49*, 432.

[99] K. Ariga, Ed. , *Manipulation of Nanoscale Materials: An Introduction to Nanoarchitectonics*, Royal Society Of Chemistry, Cambridge, **2012**.

[100] M. Geissler, Y. Xia, *Adv. Mater.* **2004**, *16*, 1249.

[101] M. J. Madou, *Fundamentals of Microfabrication and Nanotechnology (Volume II): Manufacturing Techniques for Microfabrication and Nanotechnology, 2012*, CRC Press, Boca Raton, FL, USA, **2012**.

[102] D. J. Lipomi, R. V Martinez, G. M. Whitesides, *Angew. Chem. Int. Ed. Engl.* **2011**, *50*, 8566.

[103] S. Li, L. Ren, Z. Yang, Z. Zhang, F. Gao, J. Du, S. Zhang, *Microelectron. Eng.* **2014**, *113*, 143.

[104] M. F. Crommie, C. P. Lutz, D. M. Eigler, *Science.* **1993**, *262*, 218.

[105] S. Y. Chou, P. R. Krauss, W. Zhang, L. Guo, L. Zhuang, *J. Vac. Sci. Technol. B Microelectron. Nanom. Struct. Process. Meas. Phenom.* **1997**, *15*, 2897.

[106] C. J. Brinker, Y. Lu, A. Sellinger, H. Fan, *Adv. Mater.* **1999**, *11*, 579.

[107] G. M. Whitesides, J. K. Kriebel, J. C. Love, *Sci. Prog.* **2005**, *88*, 17.

[108] C. M. Knobler, D. K. Schwartz, *Curr. Opin. Colloid Interface Sci.* **1999**, *4*, 46.

[109] X. Chen, S. Lenhert, M. Hirtz, N. Lu, H. Fuchs, L. Chi, *Acc. Chem. Res.* **2007**, *40*, 393.

[110] Y. Xia, G. M. Whitesides, *Angew. Chemie Int. Ed.* **1998**, *37*, 550.

[111] C. Thibault, V. Le Berre, S. Casimirius, E. Trévisiol, J. François, C. Vieu, *J. Nanobiotechnology* **2005**, *3*, 1.

[112] G. Decher, J. B. Schlenoff, Eds. , *Multilayer Thin Films: Sequential Assembly of Nanocomposite Materials*, *2nd Edition*, Wiley-VCH Verlag, **2012**.

[113] G. Decher, J.-D. Hong, *Makromol. Chemie. Macromol. Symp.* **1991**, *46*, 321.

[114] G. Decher, Y. Lvov, J. Schmitt, *Thin Solid Films* **1994**, *244*, 772.

[115] G. Decher, *Science.* **1997**, *277*, 1232.

[116] E. Hao, T. Lian, *Chem. Mater.* **2000**, *12*, 3392.

[117] Y. Guan, W. Li, Y. Zhang, Z. Shi, J. Tan, F. Wang, Y. Wang, *Compos. Sci. Technol.* **2017**, *144*, 193.

[118] R. S. Pontes, M. Raposo, C. S. Camilo, A. Dhanabalan, M. Ferreira, J. Oliveira ON, *Phys. status solidi* **1999**, *173*, 41.

[119] D. E. Bergbreiter, G. Tao, J. G. Franchina, L. Sussman, *Macromolecules* **2001**, *34*, 3018.

[120] J. Sun, T. Wu, Y. Sun, Z. Wang, X. Zhang, J. Shen, W. Cao, *Chem. Commun.* **1998**, 1853.

[121] P. Kohli, G. J. Blanchard, *Langmuir* **2000**, *16*, 8518.

[122] I. Ichinose, S. Mizuki, S. Ohno, H. Shiraishi, T. Kunitake, *Polym. J.* **1999**, *31*, 1065.

[123] Y. Lvov, K. Ariga, I. Ichinose, T. Kunitake, *J. Chem. Soc. Chem. Commun.* **1995**, *22*, 2313.

[124] T. Cassier, K. Lowack, G. Decher, *Supramol. Sci.* **1998**, *5*, 309.

[125] Y. Shimazaki, R. Nakamura, S. Ito, M. Yamamoto, *Langmuir* **2001**, *17*, 953.

[126] T. Serizawa, H. Yamashita, T. Fujiwara, Y. Kimura, M. Akashi, *Macromolecules* **2001**, *34*, 1996.

[127] C. Picart, P. Lavalle, P. Hubert, F. J. G. Cuisinier, G. Decher, P. Schaaf, J.-C. Voegel, *Langmuir* **2001**, *17*, 7414.

[128] P. Lavalle, C. Gergely, F. J. G. Cuisinier, G. Decher, P. Schaaf, J. C. Voegel, C. Picart, *Macromolecules* **2002**, *35*, 4458.

[129] Z. Tang, N. A. Kotov, S. Magonov, B. Ozturk, *Nat. Mater.* **2003**, *2*, 413.

[130] E. R. Kleinfeld, G. S. Ferguson, *Science.* **1994**, *265*, 370.

[131] T. Sasaki, Y. Ebina, T. Tanaka, M. Harada, M. Watanabe, G. Decher, *Chem. Mater.* **2001**, *13*, 4661.

[132] M. M. Malwitz, S. Lin-Gibson, E. K. Hobbie, P. D. Butler, G. Schmidt, *J. Polym. Sci. Part B Polym. Phys.* **2003**, *41*, 3237.

[133] M. A. Priolo, D. Gamboa, K. M. Holder, J. C. Grunlan, *Nano Lett.* **2010**, *10*, 4970.

[134] J. Peng, C. Huang, C. Cao, E. Saiz, Y. Du, S. Dou, A. P. Tomsia, H. D. Wagner, L. Jiang, Q. Cheng, *Matter* **2020**, *2*, 220.

[135] P. Podsiadlo, M. Michel, J. Lee, E. Verploegen, N. W. S. Kam, V. Ball, J. Lee, Y. Qi, A. J. Hart, P. T. Hammond, N. A. Kotov, *Nano Lett.* **2008**, *8*, 1762.

[136] A. Gilliard, L. C. Winterton, R. V. Andino, J. Lally, *Method for Applying a Coating*, **2004**, US Patent 6,811,805.

[137] J. B. Schlenoff, S. T. Dubas, T. Farhat, *Langmuir* **2000**, *16*, 9968.

[138] J. Cho, K. Char, J. Hong, K. Lee, *Adv. Mater.* **2001**, *13*, 1076.

[139] P. A. Chiarelli, M. S. Johal, J. L. Casson, J. B. Roberts, J. M. Robinson, H. Wang, *Adv. Mater.* **2001**, *13*, 1167.

[140] Y.-C. Li, J. Schulz, S. Mannen, C. Delhom, B. Condon, S. Chang, M. Zammarano, J. C. Grunlan, *ACS Nano* **2010**, *4*, 3325.

[141] J. P. DeRocher, P. Mao, J. Han, M. F. Rubner, R. E. Cohen, *Macromolecules* **2010**, *43*, 2430.

[142] H. Alem, F. Blondeau, K. Glinel, S. Demoustier-Champagne, A. M. Jonas, *Macromolecules* **2007**, *40*, 3366.

[143] G. Schneider, G. Decher, *Nano Lett.* **2004**, *4*, 1833.

[144] J. Yang, H. Li, T. Lan, L. Peng, R. Cui, H. Yang, *Carbohydr. Polym.* **2017**, *178*, 228.

[145] B. Lu, D. Luo, A. Zhao, H. Wang, Y. Zhao, M. F. Maitz, P. Yang, N. Huang, *Prog. Org. Coatings* **2019**, *135*, 240.

[146] J. Huang, Q. Shu, L. Wang, H. Wu, A. Y. Wang, H. Mao, *Biomaterials* **2015**, *39*, 105.

[147] T. He, D. Jańczewski, S. Guo, S. M. Man, S. Jiang, W. S. Tan, *Colloids Surfaces B Biointerfaces* **2018**, *161*, 269.

[148] D. L. Ellis, M. R. Zakin, L. S. Bernstein, M. F. Rubner, *Anal. Chem.* **1996**, *68*, 817.

[149] C. A. Constantine, S. V Mello, A. Dupont, X. Cao, Santos David, Oliveira Osvaldo N., F. T. Strixino, E. C. Pereira, T.-C. Cheng, J. J. Defrank, R. M. Leblanc, *J. Am. Chem. Soc.* **2003**, *125*, 1805.

[150] M. Kwiat, S. Cohen, A. Pevzner, F. Patolsky, *Nano Today* **2013**, *8*, 677.

[151] J.-W. Liu, H.-W. Liang, S.-H. Yu, *Chem. Rev.* **2012**, *112*, 4770.

[152] J.-F. Revol, D. L. Godbout, D. G. Gray, *Solidified Liquid Crystals of Cellulose with Optically Variable Properties*, **1997**, U.S. Patent 5,629,065.

[153] V. Sharma, M. Crne, J. O. Park, M. Srinivasarao, *Science.* **2009**, *325*, 449.

[154] B. R. Harkness, D. G. Gray, *Can. J. Chem.* **1990**, *68*, 1135.

[155] J. Pan, W. Hamad, S. K. Straus, *Macromolecules* **2010**, *43*, 3851.

[156] B. Frka-Petesic, G. Guidetti, G. Kamita, S. Vignolini, *Adv. Mater.* **2017**, *29*, 1.

[157] Y. Habibi, T. Heim, R. Douillard, *J. Polym. Sci. Part B Polym. Phys.* **2008**, *46*, 1430.

[158] S. N. Fernandes, P. L. Almeida, N. Monge, L. E. Aguirre, D. Reis, C. L. P. de Oliveira, A. M. F. Neto, P. Pieranski, M. H. Godinho, *Adv. Mater.* **2017**, *29*, 1.

[159] K. Yao, Q. Meng, V. Bulone, Q. Zhou, *Adv. Mater.* **2017**, *29*, 1.

[160] H. L. Liang, M. M. Bay, R. Vadrucci, C. H. Barty-King, J. Peng, J. J. Baumberg, M. F. L. De Volder, S. Vignolini, *Nat. Commun.* **2018**, *9*, 1.

[161] K. Katagiri, R. Hamasaki, K. Ariga, J. I. Kikuchi, *Langmuir* **2002**, *18*, 6709.

[162] K. Katagiri, R. Hamasaki, K. Ariga, J. ichi Kikuchi, *J. Am. Chem. Soc.* **2002**, *124*, 7892.

[163] Q. Ji, S. B. Yoon, J. P. Hill, A. Vinu, J. S. Yu, K. Ariga, *J. Am. Chem. Soc.* **2009**, *131*, 4220.

[164] A. A. Mamedov, N. A. Kotov, M. Prato, D. M. Guldi, J. P. Wicksted, A. Hirsch, *Nat. Mater.* **2002**, *1*, 190.

[165] E. D. Cranston, D. G. Gray, *Biomacromolecules* **2006**, *7*, 2522.

[166] E. Karabulut, L. Wågberg, *Soft Matter* **2011**, *7*, 3467.

[167] R. Merindol, S. Diabang, O. Felix, T. Roland, C. Gauthier, G. Decher, *ACS Nano* **2015**, *9*, 1127.

[168] R. Blell, X. Lin, T. Lindström, M. Ankerfors, M. Pauly, O. Felix, G. Decher, *ACS Nano* **2017**, *11*, 84.

[169] S. Sekar, V. Lemaire, H. Hu, G. Decher, M. Pauly, *Faraday Discuss.* **2016**, *191*, 373.

[170] H. Hu, M. Pauly, O. Felix, G. Decher, *Nanoscale* **2017**, *9*, 1307.

[171] M. C. Dixon, *J. Biomol. Tech.* **2008**, *19*, 151.

[172] G. Sauerbrey, *Zeitschrift für Phys.* **1959**, *155*, 206.

[173] P. C. Robinson, M. W. Davidson, “Polarized Light Microscopy,” can be found under www.microscopyu.com/techniques/polarized-light/polarized-light-microscopy, **n.d.**

[174] V. Mittal, *Characterization Techniques for Polymer Nanocomposites*, Wiley-VCH Verlag, Weinheim, Germany, **2012**.

[175] R. Rezakhaniha, A. Agianniotis, J. T. C. Schrauwen, A. Griffa, D. Sage, C. V. C. Bouten, F. N. Van De Vosse, M. Unser, N. Stergiopulos, *Biomech. Model. Mechanobiol.* **2012**, *11*, 461.

[176] “Scanning Electron Microscopes (SEM),” can be found under www.jeol.co.jp/en/science/sem.html, **n.d.**

[177] H. Fujiwara, *Spectroscopic Ellipsometry: Principles and Applications*, John Wiley & Sons, Chichester, England, **2007**.

[178] H. Arwin, R. Magnusson, J. Landin, K. Jrrendahl, *Philos. Mag.* **2012**, *92*, 1583.

[179] M. H. Penner, in *Food Anal. Food Sci. Text Ser.* (Ed.: S. Nielsen), Springer, Cham, **2017**.

[180] M. Schäferling, *Chiral Nanophotonics: Chiral Optical Properties of Plasmonic Systems*, Springer International Publishing, **2017**.

[181] A. C. Fischer-Cripps, *Nanoindentation*, Springer New York, **2011**.

[182] J. Hay, *Exp. Tech.* **2009**, *33*, 66.

[183] G. Guillonneau, Nouvelles Techniques de Nano-Indentation Pour Des Conditions Expérimentales Difficiles: Très Faibles Enfoncements, Surfaces Rugueuses, Température, Ecole Centrale de Lyon, **2012**.

[184] W.C. Oliver and G.M. Pharr, *J. Mater. Res.* **1992**, *7*, 1564.

[185] A. C. Fischer-Cripps, *Introduction to Contact Mechanics*, Springer Science And Business Media LLC, New York, USA, **2007**.

[186] W. C. Oliver, J. B. Pethica, *Method for Continuous Determination of the Elastc Stiffness*

of Contact Between Two Bodes, **1989**, US Patent 4,848,141.

[187] L. B. Rockland, *Anal. Chem.* **1960**, *32*, 1375.

[188] J. Hay, P. Agee, E. Herbert, *Exp. Tech.* **2010**, *34*, 86.

[189] J. Nohava, *Dynamic Mechanical Analysis by Nanoindentation. Application Report from Anton Paar GmbH*, **n.d.**

[190] B. D. Beake, S. R. Goodes, J. F. Smith, F. Gao, *J. Mater. Res.* **2004**, *19*, 237.

[191] B. D. Beake, S. R. Goodes, J. F. Smith, A. Zhang, J. E., *Sci. China (Series A)* **2001**, *44 (Supp.)*, 418.

[192] F. Bertrand, M. Maumy-Bertrand, *Maxi Fiches de Statistique Pour Les Scientifiques En 80 Fiches*, Dunod, Paris, **2011**.

[193] J. Antony, *Design of Experiments for Engineers and Scientists*, Elsevier, **2003**.

[194] "How to Analyze Factorial Design," can be found under www.support.minitab.com/en-us/minitab/18/help-and-how-to/modeling-statistics/doe/how-to/factorial/analyze-factorial-design/before-you-start/overview/, **2019**.

[195] A. Rutherford, *Introducing ANOVA and ANCOVA: A GLM Approach*, Sage, London, **2001**.

[196] T. Guo, L. Gu, Y. Zhang, H. Chen, B. Jiang, H. Zhao, Y. Jin, H. Xiao, *J. Mater. Chem. A* **2019**, *7*, 14033.

[197] C. Aulin, E. Karabulut, A. Tran, L. Wågberg, T. Lindström, *ACS Appl. Mater. Interfaces* **2013**, *5*, 7352.

[198] S. Utsel, E. E. Malmström, A. Carlmark, L. Wågberg, *Soft Matter* **2010**, *6*, 342.

[199] C. Martin, B. Jean, *Nord. Pulp Pap. Res. J.* **2014**, *29*, 19.

[200] S. S. Shiratori, M. F. Rubner, *Macromolecules* **2000**, *33*, 4213.

[201] G. Ladam, P. Schaad, J. C. Voegel, P. Schaaf, G. Decher, F. Cuisinier, *Langmuir* **2000**,

16, 1249.

[202] C. Geffroy, M. P. Labeau, K. Wong, B. Cabane, M. A. Cohen Stuart, *Colloids Surfaces A Physicochem. Eng. Asp.* **2000**, *172*, 47.

[203] C. Aulin, I. Varga, P. M. Claesson, L. Wågberg, T. Lindström, *Langmuir* **2008**, *24*, 2509.

[204] R. Merindol, Layer-by-Layer Assembly of Strong Bio-Inspired Nanocomposites, University of Strasbourg, **2014**.

[205] S. Morariu, C. E. Brunchi, M. Bercea, *Ind. Eng. Chem. Res.* **2012**, *51*, 12959.

[206] I. Aggeryd, Å. Olin, *Talanta* **1985**, *32*, 645.

[207] A. Katchalsky, J. Mazur, P. Spitnik, *J. Polym. Sci.* **1957**, *23*, 513.

[208] E. Arinaitwe, M. Pawlik, *Carbohydr. Polym.* **2014**, *99*, 423.

[209] X. Feng, R. Pelton, M. Leduc, S. Champ, *Langmuir* **2007**, *23*, 2970.

[210] T. Crouzier, C. Picart, *Biomacromolecules* **2009**, *10*, 433.

[211] M. Lundin, F. Solaqa, E. Thormann, L. MacAkova, E. Blomberg, *Langmuir* **2011**, *27*, 7537.

[212] V. S. J. Craig, M. Plunkett, *J. Colloid Interface Sci.* **2003**, *262*, 126.

[213] M. McCormick, R. N. Smith, R. Graf, C. J. Barrett, L. Reven, H. W. Spiess, *Macromolecules* **2003**, *36*, 3616.

[214] J. E. Wong, F. Rehfeldt, P. Hänni, M. Tanaka, R. V. Klitzing, *Macromolecules* **2004**, *37*, 7285.

[215] R. Koehler, R. Steitz, R. Von Klitzing, *Adv. Colloid Interface Sci.* **2014**, *207*, 325.

[216] M. Zerball, A. Laschewsky, R. Von Klitzing, *J. Phys. Chem. B* **2015**, *119*, 11879.

[217] N. L. Benbow, J. L. Webber, P. Pawliszak, D. A. Sebben, S. Karpiniec, D. Stringer, M. J. Tobin, J. Vongsvivut, M. Krasowska, D. A. Beattie, *J. Colloid Interface Sci.* **2019**, *553*, 720.

[218] R. A. Ghostine, M. Z. Markarian, J. B. Schlenoff, *J. Am. Chem. Soc.* **2013**, *135*, 7636.

[219] C. N. Wu, T. Saito, S. Fujisawa, H. Fukuzumi, A. Isogai, *Biomacromolecules* **2012**, *13*, 1927.

[220] J. M. Silva, H. S. Barud, A. B. Meneguin, V. R. L. Constantino, S. J. L. Ribeiro, *Appl. Clay Sci.* **2019**, *168*, 428.

[221] J. T. Guzman, Hybrid Nanocellulose / Nanoclay Composites for Food Packaging, Technical University of Denmark, **2016**.

[222] R. Blell, Microfibrillated Cellulose Based Nanomaterials, University of Strasbourg, **2012**.

[223] Z. Wu, N. Bouklas, R. Huang, *Int. J. Solids Struct.* **2013**, *50*, 578.

[224] M. K. Kang, R. Huang, *J. Mech. Phys. Solids* **2010**, *58*, 1582.

[225] V. Trujillo, J. Kim, R. C. Hayward, *Soft Matter* **2008**, *4*, 564.

[226] S. Reculusa, S. Ravaine, *Chem. Mater.* **2003**, *15*, 598.

[227] Y. Guan, S. Yang, Y. Zhang, J. Xu, C. C. Han, N. A. Kotov, *J. Phys. Chem. B* **2006**, *110*, 13484.

[228] R. M. A. Azzam, *J. Opt. Soc. Am.* **1978**, *68*, 1756.

[229] R. Ossikovski, *Opt. Lett.* **2011**, *36*, 2330.

[230] O. Arteaga, B. Kahr, *Opt. Lett.* **2013**, *38*, 1134.

[231] J. Schellman, H. P. Jensen, *Chem. Rev.* **1987**, *87*, 1359.

[232] D. Klemm, B. Philipp, T. Heinze, U. Heinze, W. Wagenknecht, *Comprehensive Cellulose Chemistry. Volume l: Fundamentals and Analytical Methods*, Wiley-VCH Verlag, **1998**.

[233] A. Mendoza-Galván, T. Tejeda-Galán, A. B. Domínguez-Gómez, R. A. Mauricio-Sánchez, K. Järrendahl, H. Arwin, *Nanomaterials* **2019**, *9*, 1.

[234] E. D. Cranston, D. G. Gray, *Colloids Surfaces A Physicochem. Eng. Asp.* **2008**, *325*, 44.

[235] A. Resano-Garcia, Y. Battie, A. En Naciri, S. Akil, N. Chaoui, *J. Chem. Phys.* **2015**, *142*, 1.

[236] T. W. H. Oates, M. Ranjan, S. Facsko, H. Arwin, *Opt. Express* **2011**, *19*, 2014.

[237] H. Wormeester, E. Stefan Kooij, A. Mewe, S. Rekveld, B. Poelsema, *Thin Solid Films* **2004**, *455*, 323.

[238] Y. Battie, I. Izquierdo-Lorenzo, A. Resano-Garcia, A. E. Naciri, S. Akil, P. M. Adam, S. Jradi, *Appl. Surf. Sci.* **2017**, *421*, 301.

[239] S. B. Jones, S. P. Friedman, *Water Resour. Res.* **2000**, *36*, 2821.

[240] M. Sun, H. He, N. Zeng, E. Du, Y. Guo, C. Peng, Y. He, H. Ma, *Appl. Opt.* **2014**, *53*, 2949.

[241] V. Lemaire, Dépôts Alignés de Nanofils d'argent Au Sein de Films Multicouches Pour Des Propriétés Conductrices et Optiques, University of Strasbourg, **2017**.

[242] I. Usov, G. Nyström, J. Adamcik, S. Handschin, C. Schütz, A. Fall, L. Bergström, R. Mezzenga, *Nat. Commun.* **2015**, *6*, 1.

[243] S. K. Kannam, D. P. Oehme, M. S. Doblin, M. J. Gidley, A. Bacic, M. T. Downton, *Carbohydr. Polym.* **2017**, *175*, 433.

[244] R. K. Pinschmidt, *J. Polym. Sci. Part A Polym. Chem.* **2010**, *48*, 2257.

[245] A. Schmalen, Post Polymerization Modification of Poly(Vinyl Amine) with Functional Epoxides: Multifunctional, Antimicrobial, Protein-like Polymers, RWTH Aachen University, **2015**.

[246] G. Wulff, K. Zabrocki, J. Hohn, *Angew. Chemie Int. Ed. English* **1978**, *17*, 535.

[247] G. Wulff, R. Kemmerer, B. Vogt, *J. Am. Chem. Soc.* **1987**, *109*, 7449.

[248] G. Wulff, S. Krieger, *Macromol. Chem. Phys.* **1994**, *195*, 3679.

[249] M. Faryad, A. Lakhtakia, *Adv. Opt. Photonics* **2014**, *6*, 225.

[250] H. P. Jensen, J. A. Schellman, T. Troxell, *Appl. Spectrosc.* **1978**, *32*, 192.

[251] Y. Shindo, M. Nishio, S. Maeda, *Biopolymers* **1990**, *30*, 405.

[252] D. W. Berreman, *J. Opt. Soc. Am.* **1972**, *62*, 502.

[253] D. W. Berreman, *J. Opt. Soc. Am.* **1973**, *63*, 1374.

[254] D. J. Broer, J. Lub, G. N. Mol, *Nature* **1995**, *378*, 467.

[255] T. Kitamura, T. Sumigawa, H. Kitamura, *Fracture Nanomechanics*, Taylor & Francis Group, LLC, Boca Raton, FL, **2016**.

[256] A. Tiwari, S. Natarajan, Eds. , *Applied Nanoindentation in Advanced Materials*, John Wiley & Sons, **2017**.

[257] A. Cameron, *The Principles of Lubrication*, Wiley, **1966**.

[258] J. Menčik, D. Munz, E. Quandt, A. Ludwig, *J. Mater. Res.* **1997**, *12*, 2475.

[259] R. Saha, W. D. Nix, *Acta Mater.* **2002**, *50*, 23.

[260] S. Bec, A. Tonck, J. M. Georges, E. Georges, J. L. Loubet, *Philos. Mag. A Phys. Condens. Matter, Struct. Defects Mech. Prop.* **1996**, *74*, 1061.

[261] A. K. Bhattacharya, W. D. Nix, *Int. J. Solids Struct.* **1988**, *24*, 1287.

[262] A. M. Korsunsky, M. R. McGurk, S. J. Bull, T. F. Page, *Surf. Coatings Technol.* **1998**, *99*, 171.

[263] B. Bhushan, X. Li, *J. Mater. Res.* **1997**, *12*, 54.

[264] W. S. Lee, T. H. Chen, S. L. Chang, in *2009 IEEE 3rd Int. Conf. Nano/Molecular Med. Eng. NANOMED*, **2009**, pp. 164–167.

[265] M. A. Hopcroft, W. D. Nix, T. W. Kenny, *J. Microelectromechanical Syst.* **2010**, *19*, 229.

[266] P. M. Nagy, P. Horváth, G. Pető, E. Kálmán, *Mater. Sci. Forum* **2008**, *604*, 29.

[267] M. Budnitzki, M. Kuna, *J. Mech. Phys. Solids* **2016**, *95*, 64.

[268] Y. Wang, J. Shi, *Mater. Sci. Semicond. Process.* **2019**, *102*, 1.

[269] D. Yoo, S. S. Shiratori, M. F. Rubner, *Macromolecules* **1998**, *31*, 4309.

[270] E. Wassel, M. Es-Souni, M. Dietze, A. Laghrissi, M. Es-Souni, *Prog. Org. Coatings* **2019**, *132*, 108.

[271] D. L. Joslin, W. C. Oliver, *J. Mater. Res.* **1990**, *5*, 123.

[272] Z. Chen, X. Wang, V. Bhakhri, F. Giuliani, A. Atkinson, *Acta Mater.* **2013**, *61*, 5720.

[273] A. S. Michaels, H. J. Bixler, *Ind. Eng. Chem.* **1965**, *57*, 32.

[274] H. H. Hariri, A. M. Lehaf, J. B. Schlenoff, *Macromolecules* **2012**, *45*, 9364.

[275] R. M. Hodge, T. J. Bastow, G. H. Edward, G. P. Simon, A. J. Hill, *Macromolecules* **1996**, *29*, 8137.

[276] M. M. Madani, R. R. Miron, R. D. Granata, *J. Coatings Technol.* **1997**, *69*, 45.

[277] K. De Yao, J. Liu, R. Z. Zhao, W. H. Wang, L. Wei, *Angew. Makromol. Chem.* **1998**, *255*, 71.

[278] K. De Yao, W. G. Liu, J. Liu, *J. Appl. Polym. Sci.* **1999**, *71*, 449.

[279] R. L. de Oliveira, H. da S. Barud, D. T. B. De Salvi, G. F. Perotti, S. J. L. Ribeiro, V. R. L. Constantino, *Ind. Crops Prod.* **2015**, *69*, 415.

[280] F. Knoop, C. G. Peters, W. B. Emerson, *J. Res. Natl. Bur. Stand. (1934).* **1939**, *23*, 39.

[281] S. G. Roberts, P. D. Warren, P. B. Hirsch, *J. Mater. Res.* **1986**, *1*, 162.

[282] P. Mogilevsky, T. A. Parthasarathy, *Mater. Sci. Eng. A* **2007**, *454–455*, 227.

[283] A. S. M. Ang, C. C. Berndt, *Surf. Coatings Technol.* **2014**, *259*, 551.

[284] E. Amitay-Sadovsky, S. Zheng, J. Smith, H. D. Wagner, *Acta Polym.* **1998**, *49*, 588.

[285] Y. C. Kim, M. J. Choi, D. Kwon, J. Y. Kim, *Met. Mater. Int.* **2015**, *21*, 850.

[286] T. Akahori, T. Nagakura, S. Fushimi, A. Yonezu, *Polym. Test.* **2018**, *70*, 378.

[287] L. Riester, T. J. Bell, A. C. Fischer-Cripps, *J. Mater. Res.* **2001**, *16*, 1660.

[288] D. B. Marshall, T. Noma, A. G. Evans, *J. Am. Ceram. Soc.* **1982**, *65*, c175.

[289] N. Moharrami, S. J. Bull, *Thin Solid Films* **2014**, *572*, 189.

[290] B. D. Beake, J. F. Smith, M. J. s. I. García, *Thin Solid Films* **2001**, *398*, 438.

Résumé de thèse en Français

Assemblage couche-par-couche de films composites à base de nanocellulose présentant des superstructures hélicoïdales bio-inspirées

1. Introduction

1.1. Superstructures hélicoïdales naturelles

Au cours de l'évolution, des matériaux nanocomposites complexes ont été développés dans la nature (par exemple la paroi des cellules végétales et l'exosquelette de certains animaux) présentant une structure hiérarchique de l'échelle microscopique à l'échelle macroscopique par assemblage moléculaire. Ces matériaux possèdent souvent des propriétés optiques et/ou mécaniques remarquables en assemblant simplement des éléments durs et moux dont les propriétés individuelles sont en général modestes.[1] Les propriétés remarquables des matériaux composites naturels ont conduit à de nombreuses recherches pour comprendre les relations structure-propriétés de ces matériaux et pour concevoir de nouveaux matériaux avec des performances mécaniques et optiques supérieures. Cependant, il faut noter qu'il n'existe actuellement aucune méthode pour préparer des matériaux composites synthétiques ayant une structure et une composition chimique avec une telle complexité.

Indépendamment de leur composition chimique, les matériaux naturels sont souvent constitués de structures hiérarchiques présentant certaines caractéristiques telles que des nanofibrilles, un empilement multicouche laminaire et des structures mésoporeuses, entre autres.[2] Par exemple,

les nanofibrilles de cellulose sont le composant structural élémentaire de la paroi cellulaire des plantes et des algues vertes, tandis que les nanofibrilles de chitine sont le composant structural primaire de l'exosquelette des arthropodes. Ces nanofibrilles sont regroupées en fibrilles de diamètres de plus en plus grands qui sont ensuite elles-mêmes alignées en structures en couches 2D avant d'être empilées pour former des architectures 3D complexes telles que des hélices, communément appelée "twisted plywood" ou structure Bouligand[3] (Figure R.1).[1,2,4] Cette structure est très répandue dans le règne animal (assemblages à base de chitine) et dans le règne végétal (assemblages à base de cellulose).[5]

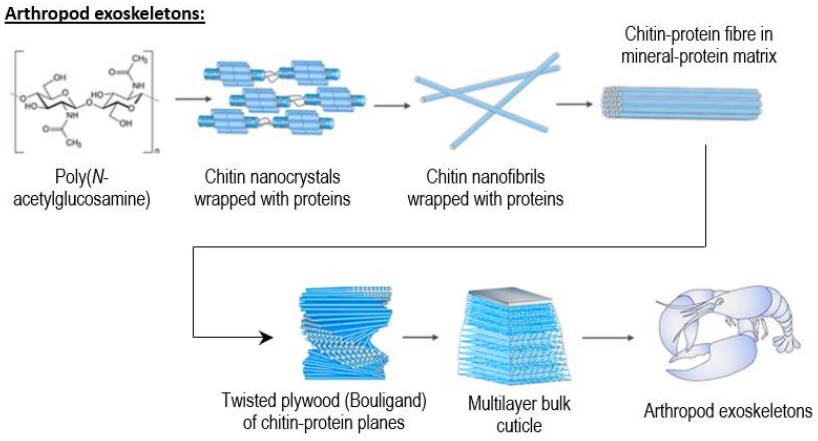

Figure R.1: Schéma de l'organisation hiérarchique de la chitine dans l'exosquelette des arthropodes.[6]

Mécaniquement, la structure Bouligand confère au matériau une ténacité et une isotropie accrues dans différentes directions de l'espace. Un des exemples les plus remarquables et les plus connus de biomatériaux sophistiqués tolérants aux endommagements, dont les propriétés mécaniques exceptionnelles ont été associées à la présence de la structure Bouligand, sont les pattes ravisseuses des crustacés *stomatopodes*, communément appelés crevettes-mantes (*Odontodactylus scyllarus*). Ces pattes comportent deux régions distinctes, une région d'impact externe et une région périodique interne. Cette dernière est constituée d'un réseau hélicoïdal de fibrilles de chitine partiellement minéralisées avec du carbonate de calcium amorphe. Cet arrangement Bouligand fournit plusieurs mécanismes de renforcement qui entravent la propagation catastrophique des fissures dans le matériau. En particulier, il force les fissures à se

propager en suivant un chemin hélicoïdal entre les fibres de chitine, ce qui dissipe une quantité d'énergie plus importante qu'une fissure se propageant en ligne droite.[7]

Ces structures hélicoïdales ne sont pas uniquement associées aux propriétés mécaniques des matériaux naturels mais sont également responsable de phénomènes optiques intéressants, dont les couleurs structurelles de certaines feuilles de plantes, de certains fruits et de l'exosquelette de coléoptères. Dans certains fruits, l'empilement hélicoïdal de microfibrilles de cellulose forme des multicouches dont l'indice de réfraction varie périodiquement dans l'espace. Cet arrangement agit comme un cristal photonique donnant lieu au phénomène de réflexion de Bragg,[8] c'est-à-dire à la fonctionnalité optique du matériau. Lorsque la distance périodique définie par la moitié du pas hélicoïdal (P/2) est comparable à la longueur d'onde de la lumière visible, il se forme une bande photonique qui donne lieu à la réflexion de la lumière dans une plage de longueur d'onde particulière centrée sur un λ_{max} déterminé par la loi de Bragg-Snell :[9]

$$m\lambda_{max} = \bar{n} \cdot P \cdot \sin(\theta) \qquad \text{(Eq. R.2)}$$

où m est l'ordre de diffraction, n est l'indice de réfraction moyen et θ est l'angle de la lumière incidente. En outre, les structures photoniques hélicoïdales présentent une réflexion préférentielle de la lumière polarisée circulairement de même chiralité que celle de la structure hélicoïdale, principalement des hélices gauches dans la nature.[10-14]

1.2. La nanocellulose comme élément constitutif des matériaux nanocomposites

L'intérêt croissant pour le développement de produits fabriqués à partir de ressources renouvelables a fortement encouragé les recherches sur les matériaux à base de cellulose comme une alternative écologique aux matériaux à base de pétrole. La cellulose est le polymère organique le plus abondant sur Terre et une source pratiquement inépuisable de matière première polymèrique durable. De plus, elle combine de nombreuses propriétés intéressantes pour de nombreuses applications techniques, telles que l'hydrophilie, la chiralité, la biodégradabilité, la

non-toxicité, la faible densité, une grande capacité de modification chimique et des propriétés mécanique remarquables.

La structure hiérarchique de la cellulose native peut être décomposée en nanofibres et microfibres semi-cristallines plus petites par des processus de désintégration chimique et mécanique,[15] qui favorisent la fibrillation de la cellulose en un réseau de nanofibrilles de cellulose (CNF) fortement enchevêtrées.[16] Le module d'élasticité spécifique (E/ρ) et la résistance spécifique (σ_b/ρ) de la cellulose ($\rho \approx 1.6$ g/cm^3)[17] surpassent ceux de la plupart des matériaux d'ingénierie. Par conséquent, ses dimensions nanométriques, son rapport d'aspect élevé et sa grande surface font de la cellulose un matériau de choix en tant qu'élément de renfort dans les nanocomposites.

1.3. Fabrication de couches minces nanostructurées : L'approche couche-par-couche

Comme indiqué précédemment, la fabrication synthétique de matériaux fonctionnels présentant des structures complexes telles que celles présentes dans la nature est impossible avec les méthodes actuelles. En ce qui concerne la préparation de matériaux composites nano-organisés multifonctionnels avec un haut niveau de contrôle sur le positionnement spatial de ses constituants, l'assemblage couche-par-couche (LbL),[18-20] introduite par G. Decher dans les années 90, est probablement une des méthodes de nano-fabrication les plus simples et les plus polyvalentes. Les premiers films LbL ont été préparés par trempage, c'est-à-dire par immersion séquentielle d'un substrat chargé dans des solutions de polycation et de polyanion (Figure R.2 A) avec des rinçages intermédiaires. Il s'agit d'une véritable approche "bottom-up" qui permet d'assembler un grand nombre de molécules (polymères, colloïdes, protéines, cellules, …) sur des surfaces de taille, de forme (plane, sphérique) et de nature (or, verre, silicium,…) différentes avec une précision nanométrique en utilisant un processus unique. La technique LbL est basée sur un concept simple (interactions intermoléculaires attractives, principalement électrostatiques) et combine une simplicité expérimentale avec un faible coût de fabrication et un respect de l'environnement (peu polluante). Les propriétés des films peuvent être ajustées en jouant sur un

certain nombre de paramètres tels que la méthode de dépôt, la concentration des molécules, la température, la force ionique, le pH, la nature et la concentration du sel. Cette technique a également été étendue à l'assemblage de composés interagissant par d'autres interactions (liaisons hydrogène, liaisons de coordination, liaisons covalentes).[21-24]

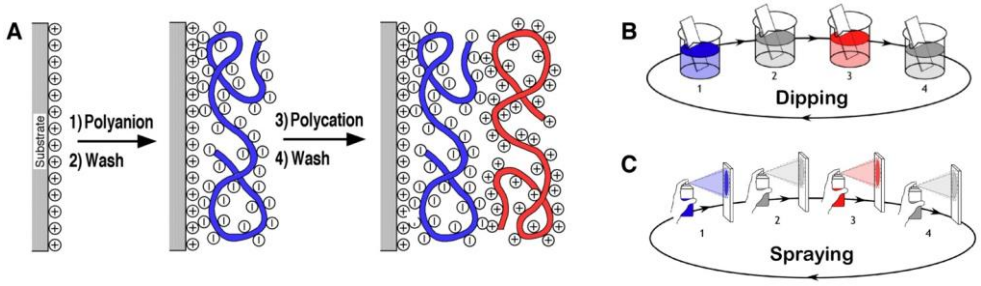

Figure R.2: Schéma du principe de la technique LbL (A) utilisée pour construire par trempage (B) ou par pulvérisation (C) des films multicouches à partir d'un polyanion (bleu) et de polycation (rouge) sur un substrat chargé positivement. Les étapes 2 et 4 représentent des étapes de rinçage.

Pour accélérer le processus de dépôt LbL et augmenter l'attractivité de cette technique pour un développement au niveau industriel, la construction de films multicouches a été réalisée par pulvérisation[25,26] et spin-coating.[27,28] Alors que la séquence des composants dans les films multimatériaux structurés en couches peut être très facilement contrôlée par l'assemblage LbL, le contrôle de l'anisotropie dans le plan n'avait pas encore été réalisé. C'est la raison pour laquelle Blell *et al.* ont introduit récemment une méthode intitulée "pulvérisation à incidence rasante" (GIS) pour l'alignement dans le plan de nanoparticules anisotropes.[29] Alors que la pulvérisation à 90° contre une surface réceptrice produit des films avec une orientation isotrope dans le plan, la pulvérisation à des angles plus faibles (< 20°) provoque un écoulement de liquide directionnel macroscopique sur la surface réceptrice et conduit à des films présentant une anisotropie dans le plan lorsque des nano-objets anisotropes sont utilisés (Figure 1.24). La combinaison du GIS avec l'approche LbL devrait donc permettre de concevoir des films multicouches complexes (par exemple hélicoïdaux) dont la composition et l'orientation peuvent être contrôlées indépendamment dans chaque couche. Ils ont montré que des nanofibrilles de cellulose sont facilement alignés par GIS dans le plan pour produire des films optiquement biréfringents sur de

grandes surfaces. Cette approche a été ensuite étendue à la fabrication de films nanocomposites orientés à base de nanofils d'argent présentant des propriétés optiques hautement anisotropes.[30]

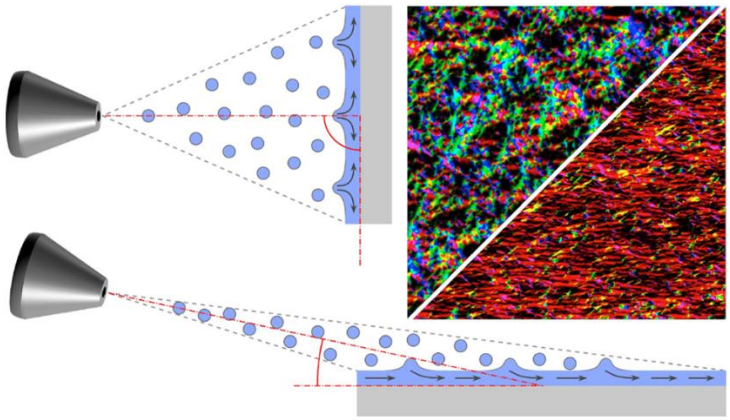

Figure R.3: Schéma de la pulvérisation orthogonale (en haut) et de la pulvérisation à incidence rasante (en bas) et les images correspondantes d'une monocouche de CNFs non-orientés et orientés.[29]

2. Objectif de la thèse

Le développement de matériaux nanocomposites complexes est généralement considéré comme très important mais peu exploré compte tenu de l'absence de techniques appropriées pour leur préparation. L'objectif de ce travail a donc consisté à développer une approche pour préparer des structures hiérarchiques complexes (e.g. hélices) inspirées de la nature a fin d'obtenir des matériaux synthétiques présentant des propriétés mécaniques et optiques similaires ou supérieures à celles des matériaux naturels. Cette approche repose sur la combinaison de la technique LbL et de la pulvérisation à incidence rasante (GIS) pour assembler des films multicouches de structures complexes dans lesquels la direction d'alignement des nanoparticules anisotropes dans le plan peut être contrôlée indépendamment dans chaque couche. Lors de cette étude, nous avons assemblé des nanocelluloses (nanofibrilles (CNF) ou nanocristaux (CNC)), utilisées comme éléments de renforts, et une matrice polymère, la poly(vinylamine) (PVAm), pour assurer la cohésion des couches de cellulose. Nous avons tout d'abord optimisé les conditions de dépôt du GIS pour obtenir un degré d'alignement dans le plan maximum des nanocelluloses puis nous avons validé la possibilité de contrôler l'alignement de ces nano-objets de façon indépendante dans chacune des couches. Cette approche d'assemblage dirigé a finalement été étendue à la construction de films minces $(CNF/polyélectrolyte)_n$ présentant une structure hélicoïdale des

nanofibrilles et leurs propriétés optiques et mécaniques ont été étudiées à l'aide de différentes techniques de caractérisation.

3. Fabrication de nanocomposites à base de cellulose isotropes et anisotropes

Motivés par la nécessité de préparer des films multicouches à base de cellulose d'une épaisseur de l'ordre du micron, prérequis indispensable à la caractérisation mécanique de ces films, la construction de films préparés avec trois polycations différents, à savoir le chitosan (CHI), la poly(vinylamine) (PVAm) et le poly(chlorure de diallyldiméthylammonium) (PDDA), a été suivie par ellipsométrie (Figure R.4). Deux valeurs de pH (8 et 10) ont été utilisées pour les solutions de PVAm et de chitosan, deux polyélectrolytes faibles, pour étudier la croissance de ces films. Le régime de croissance le plus rapide a été observé pour les films fabriqués avec de la PVAm (croissance linéaire) et le plus faible, pour les films assemblés avec du chitosan (croissance superlinéaire). Par ailleurs, des films deux à trois fois plus épais ont été obtenus avec une solution de PVAm à pH = 10. La PVAm a donc été sélectionnée pour la fabrication de films épais à base de cellulose.

Comme la préparation de films avec une structure hélicoïdale repose sur le fait de pouvoir aligner indépendamment les nanofibrilles de cellulose dans chaque couche, nous avons d'abord fait varier les paramètres de pulvérisation et étudier leurs interdépendances via des méthodes statistiques dans le but d'identifier les conditions de pulvérisation optimales pour atteindre le degré d'alignement le plus élevé possible dans une monocouche de CNFs. Ce dernier a été obtenu en utilisant une longue durée de pulvérisation, une suspension de CNFs diluée, le débit de liquide le plus faible et le débit d'air le plus élevé. Cette combinaison optimale des paramètres a produit un alignement dans le plan des nanofibrilles parallèle à la direction de pulvérisation d'environ 85 %.

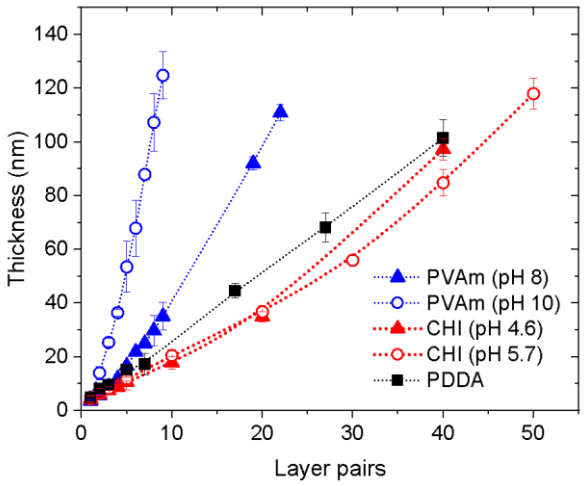

Figure R.4: Variation de l'épaisseur de films à base de CNFs préparés avec différentes polycations en fonction du nombre de paires de couches. Les lignes en pointillés sont simplement un guide pour les yeux.

Suite à ce résultat, nous avons étudié l'influence de l'orientation de la couche déposée sur l'orientation de la couche suivante. La Figure R.5 montre la superposition des images AFM prises sur les première et deuxième couches de CNFs d'un échantillon croisé. Dans ces images, l'orientation perpendiculaire des nanofibrilles dans les deux couches est clairement visible, ce qui démontre que les CNFs peuvent être efficacement orientés par GIS indépendamment de la direction d'orientation des nanofibrilles présentes dans la couche inférieure.

L'étape suivante a consisté à préparer des films orientés d'une épaisseur de l'ordre du micron. Ainsi, des films avec 100 paires de couches, $(CNF/PVAm)_{100}$, ont été préparés en pulvérisant toutes les couches de CNFs dans la même direction en utilisant les conditions de pulvérisation optimales précédemment identifiées. Une solution de PVAm à un pH = 10 a été utilisée pour une croissance plus rapide du film. Un motif concentrique de couleurs d'interférence s'est développé au fur et à mesure de la construction des films (Figure R.6). Les franges de couleur observées ont été attribuées à différentes épaisseurs du film résultant de la pulvérisation. Cela a été vérifié en mesurant l'épaisseur du film par ellipsométrie à des distances croissantes le long de l'axe central de l'échantillon. Pour limiter la formation de ces motifs concentriques, une pulvérisation alternée à 180° a été utilisée pour la préparation des films épais unidirectionnels. Cependant, ces films deviennent opaques (rugueux) à partir d'une certaine épaisseur et de ce fait, il n'est plus possible de suivre la croissance des films épais par ellipsométrie.

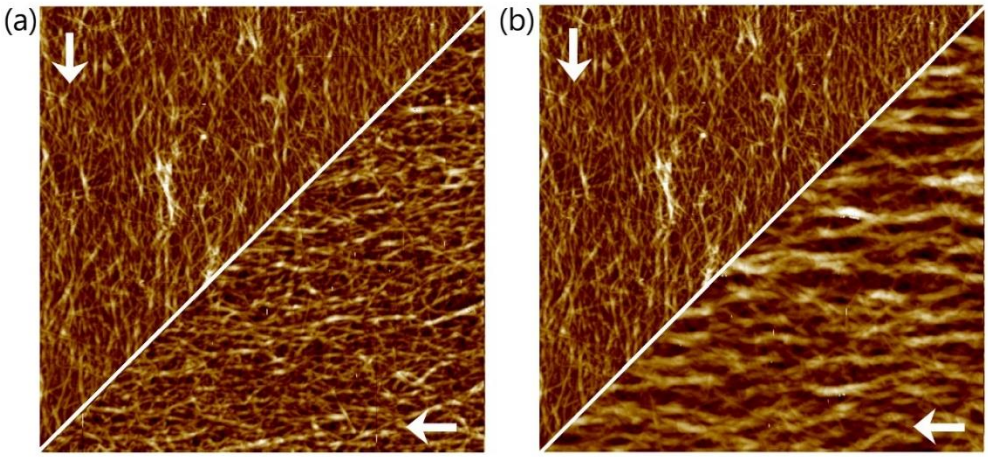

Figure R.5: Superposition d'images AFM représentatives de la première et de la deuxième couche de CNFs pulvérisées dans des directions perpendiculaires en utilisant (a) du PVAm à pH 8 et (b) du PVAm à pH 10. Les flèches verticales indiquent la direction de la pulvérisation de la première couche et les flèches horizontales, la direction de la pulvérisation de la deuxième couche. La taille des images est de 2x2 μm^2.

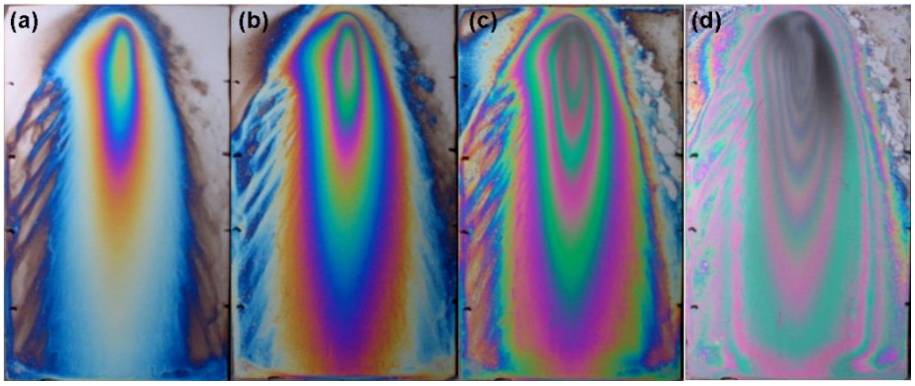

Figure R.6: Images optiques des motifs colorés observés pour des échantillons unidirectionnels préparés GIS avec un nombre croissant de paires de couches (LP) : 20 LP, 30 LP, 50 LP et 100 LP (de (a) à (d)).

Par conséquent, le centre de ces films épais a été observé par microscopie optique avec des polariseurs croisés pour vérifier l'alignement unidirectionnel des CNFs (Figure R.7). Comme prévu pour un échantillon anisotrope, une extinction totale de la lumière est observée lorsque la direction de pulvérisation (et donc l'orientation des fibrilles) était parallèle à l'un ou l'autre des polariseurs, alors que la luminosité relative de l'échantillon était maximale pour chaque rotation de 45° par rapport aux deux polariseurs. L'anisotropie optique détectée dans les échantillons orientés de façon unidirectionnelle est donc une conséquence directe de l'anisotropie structurelle

des films, ce qui confirme que l'alignement dans le plan des couches de CNFs a été maintenu lors de la construction malgré la rugosité croissante des films.

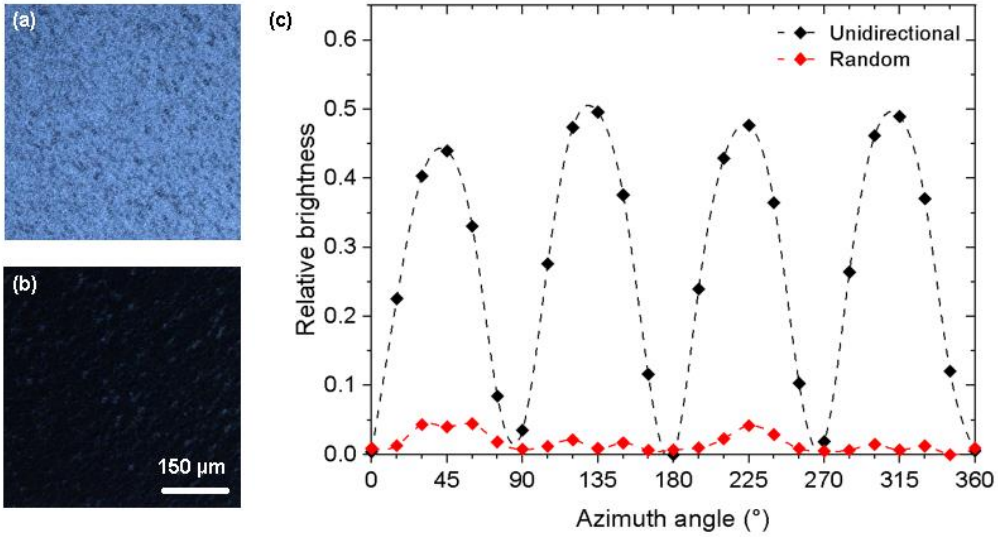

Figure R.7: Micrographies optiques prises entre des polariseurs croisés au centre d'un film unidirectionnel $(CNF/PVAm)_{100}$ lorsque l'angle entre la direction de pulvérisation et le polariseur était (a) de 45° et (b) de 0°. (c) Variation angulaire de la luminosité relative pour des films avec une orientation aléatoire et unidirectionnelle.

Par ailleurs, nous avons préparé un échantillon avec un alignement croisé des couches de CNF, c'est-à-dire un échantillon dans lequel l'orientation de chaque couche de cellulose a été tournée de 90° par rapport aux couches adjacentes. Dans ce cas, le motif en franges colorées a pris la forme d'une croix (Figure R.8). Les micrographies optiques prises au centre de l'échantillon entre des polariseurs croisés à différents angles d'azimut ont montré un comportement optique isotrope, comparable à celui de l'échantillon aléatoire (Figure R.7). Lorsque les micrographies ont été prises en dehors du centre de l'échantillon (à 4 mm et 8 mm de distance le long des axes de pulvérisation), une réponse anisotrope a été détectée, caractérisée par une luminosité relative maximale et une extinction totale de la lumière alternant tous les 45° dans le plan. Ces résultats démontrent que les couches respectives de l'échantillon étaient effectivement orientées de façon unidirectionnelle dans les deux directions de pulvérisation.

Enfin, nous avons assemblé des films $(CNF/PVAm)_n$ ayant une structure hélicoïdale en faisant tourner l'échantillon d'un angle constant après le dépôt d'un nombre défini de couches. L'angle

de rotation a été choisi soit dans le sens des aiguilles d'une montre, soit dans le sens inverse, pour fabriquer délibérément des films avec une hélicité droite ou gauche. De plus, le pas de l'hélice a été adapté en ajustant soit l'angle de rotation dans le plan entre les piles de couches, soit le nombre de couches mono-orientées empilées entre les rotations, ou les deux. Lors de la construction des films hélicoïdaux, nous avons observé la formation de cercles concentriques de couleur caractérisant un gradient d'épaisseur (Figure R.9). Comme pour l'échantillon croisé, la luminosité relative détectée en dehors du centre démontre que les couches de CNF sont alignées (Figure R.9).

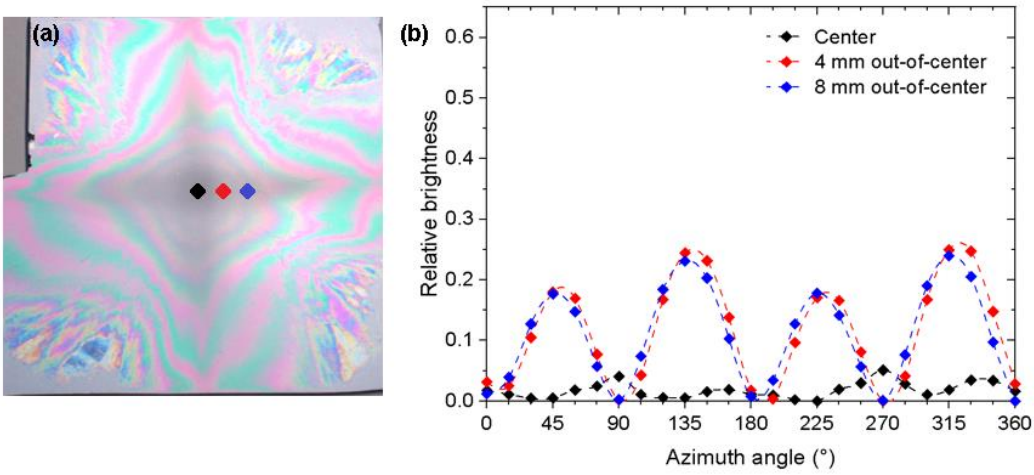

Figure R.8: (a) Micrographies optiques d'un film $(PVAm/CNF)_{80}$ avec une structure en couches croisées. (b) Variation angulaire de la luminosité relative mesurée au centre et à 4 mm et 8 mm de distance le long des axes de pulvérisation par rapport au centre du film indiqué en (a).

Pour vérifier l'alignement hélicoïdal des CNFs dans ces films, des images MEB en coupe transversale ont été réalisées dans le but d'observer l'agencement des nanofibrilles. Une image MEB représentative de la section transversale d'un film constitué d'une hélice à deux tours avec un pas théorique de 500 nm est présentée dans la Figure R.10(b). Le faible diamètre des nanofibrilles (1 - 2 nm) et éventuellement le niveau élevé d'hydratation du film ont empêché l'observation directe de l'agencement des CNFs. Néanmoins, une ultrastructure composée de 4 couches distinctes a été imagée. Le nombre et les dimensions correspondent à un demi-pas de l'hélicoïde, comme le montre schématiquement la figure R.10(a). Cette stratification a été interprétée comme étant causée par la différence du comportement de rupture des couches

périodiques alignées parallèlement au plan de fracture par rapport à celles alignées dans toutes les autres directions, et elle constitue donc une preuve indirecte de l'agencement hélicoïdal des CNFs.

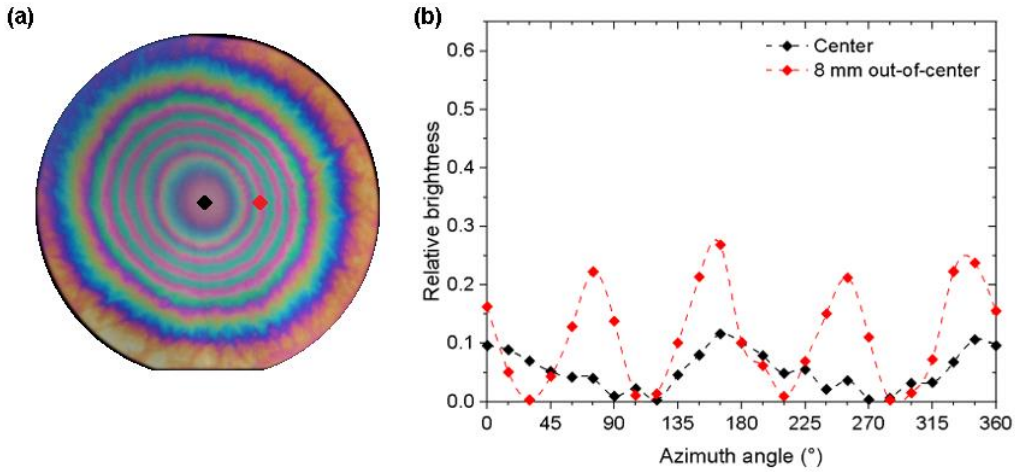

Figure R.9: (a) Photographie optique montrant les couleurs d'interférence concentriques observées pour un film hélicoïdal avec une hélicité droite composé de 144 paires de couches et de 2 tours. (b) Variation angulaire de la luminosité relative mesurée au centre et à 8 mm du centre du film indiqué en (a).

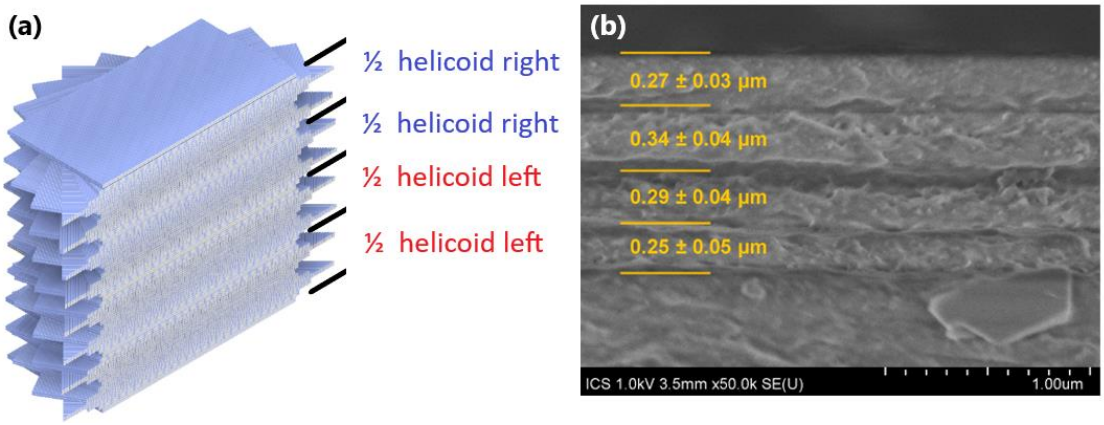

Figure R.10: (a) Schéma 3D de la coupe transversale d'un film hélicoïdal alternant un tour à gauche et un tour à droite. (b) Image MEB d'une coupe transversale d'un échantillon hélicoïdal présentant une ultrastructure à 4 couches correspondant à quatre demi-pas des hélicoïdes.

4. Caractérisation optique des films à base de CNF structurés par GIS

Nous nous sommes ensuite appuyés sur différentes techniques de caractérisation optique pour (i) vérifier la structure hélicoïdale des films à base de cellulose et (ii) étudier leur comportement optique. En particulier, nous avons utilisé l'ellipsométrie spectroscopique à matrice de Mueller (MMSE) pour étudier les propriétés de polarisation d'un film multicouche $(CNF/PVAm)_{97}$ avec

un alignement unidirectionnel des nanofibrilles. Toutes les mesures MMSE ont été effectuées par Yann Battie de l'Université de Lorraine. Il a montré que les propriétés de polarisation de l'échantillon unidirectionnel étaient dominées par de la biréfringence linéaire (LB) qui était au moins un ordre de grandeur plus élevée que le dichroïsme linéaire, LD (Figure R.11). Par conséquent, l'échantillon présentait une anisotropie d'indice de réfraction. Au contraire, l'échantillon aléatoire était isotrope. Nous avons calculé que la biréfringence effective de l'échantillon unidirectionnel était de Δn = 0,029 ± 0,003. Cette valeur correspond à peu de chose prêt à la moitié des valeurs rapportées pour la biréfringence de la cellulose, qui varient de 0,045 à 0,062 selon la source,[31] mais elle se situe entre les valeurs rapportées pour des films biréfringents à base de nanocristaux de cellulose préparés par trempage[32] et spin-coating.[33]

Les propriétés chirales de films multicouches $(PVAm/CNF)_n$ possédant différentes structures hélicoïdales ont été étudiées par dichroïsme circulaire (CD). Tout d'abord, nous avons comparé deux films dont la seule différence structurale était le sens de rotation (droite ou gauche) entre les couches de CNFs. Les spectres de dichroïsme circulaire obtenus pour ces deux échantillons sont présentés à la Figure R.12. Ces spectres sont à comparer avec ceux obtenus pour un échantillon aléatoire préparé par trempage, la suspension de CNFs pur (1 mg/mL) et la solution de PVAm (10 mg/mL) qui montrent une chiralité relativement faible. La conclusion la plus intéressante de ces spectres CD est la réponse symétrique des films hélicoïdaux préparés avec une hélicité opposée, ce qui a permis de confirmer l'assemblage hélicoïdal droite et gauche des CNFs dans ces films et leur chiralité opposée. Les spectres CD de ces films présentent des pics positifs et négatifs à différentes longueurs d'onde et un changement de signe autour de 230 nm.

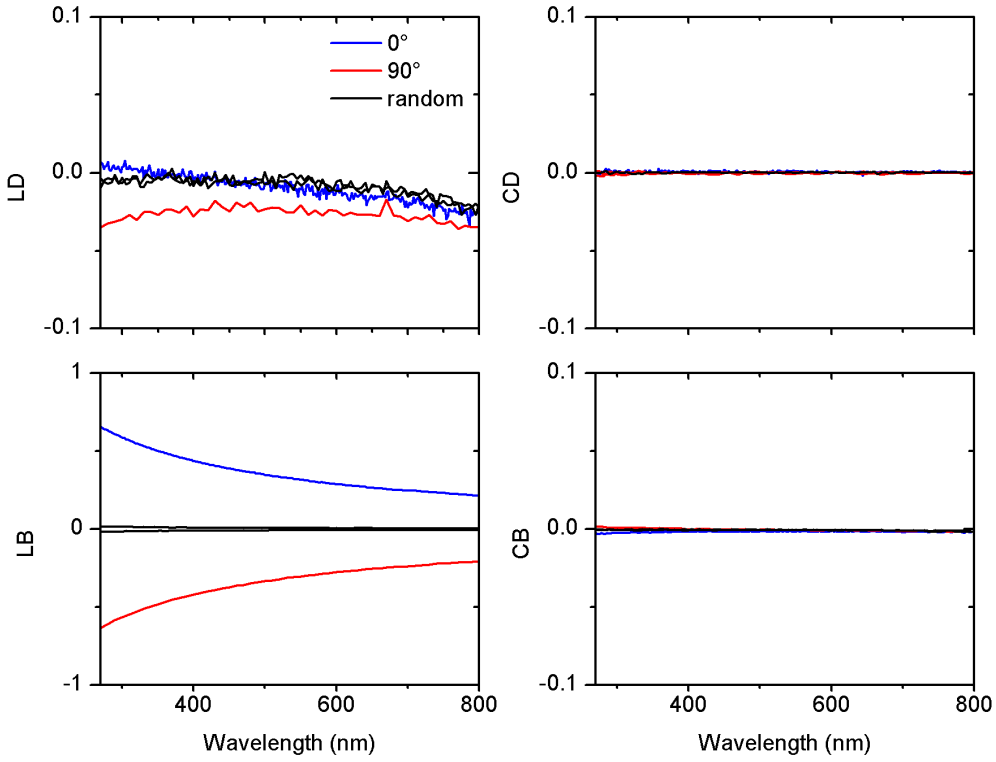

Figure R.11: Spectres *LD*, *LB*, *CD* et *CB* extraits de la matrice de Mueller pour des échantillons unidirectionnels et aléatoires aux angles d'azimut 0° et 90°. Par souci de simplicité, les données des deux angles de l'échantillon aléatoire ont été tracées dans la même couleur (noir).

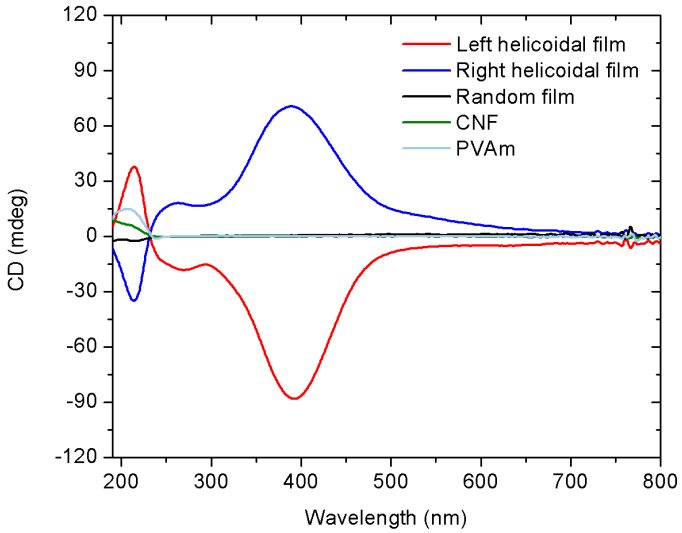

Figure R.12: Spectres CD de films hélicoïdaux droite et gauche, d'une solution de PVAm, d'une suspension de CNFs et d'un film aléatoire préparé par trempage.

Nous nous sommes concentrés sur l'analyse du pic large et intense situé autour de 390 nm, qui a été attribué à l'assemblage structurel en hélice des CNFs (abscence de réponse CD pour les CNFs et la PVAm en solution dans cette région). Le pic positif du film hélicoïdal d'hélicité droite

indique que la lumière polarisée circulairement gauche est transmise de préférence, comme cela est observé pour le phénomène de Bragg circulaire.[34] La même observation s'applique au signal CD négatif mesuré pour l'échantillon d'hélicité gauche. Nous avons estimé que la longueur d'onde pour la réflexion sélective de Bragg est vers 371 nm (±10% de l'incertitude supposée pour l'épaisseur), ce qui est en accord avec le pic structurel du CD (390 nm). En complément des mesures de CD, nous avons également confirmé l'assemblage hélicoïdal des CNFs (droite et gauche) dans les films par ellipsométrie spectroscopique à matrice de Mueller.

Nous avons ensuite comparé le dichroïsme circulaire de trois films hélicoïdaux ayant des valeurs différentes pour le pas (80 nm, 240 nm et 475 nm, respectivement). Nous avons observé des différences significatives dans la position des pics structurels en CD (Figure R.13), ce qui ne laisse aucun doute sur l'influence du pas de l'hélice sur ce paramètre. La position du pic principal augmente linéairement vers le rouge avec l'augmentation du pas de l'hélice, comme le prévoit la loi de Bragg.

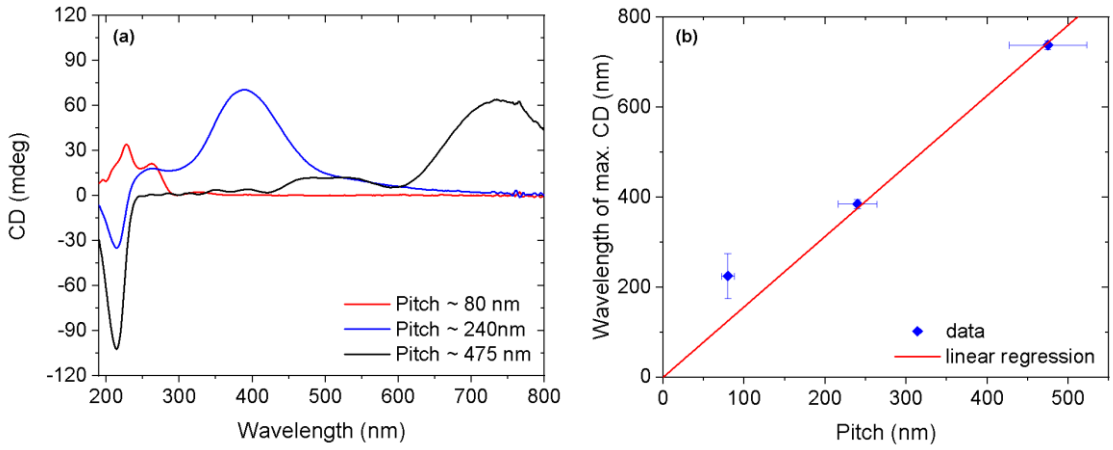

Figure R.13 : (a) Spectres CD de trois films hélicoïdaux avec différents pas. (b) Relation linéaire entre la position du pic du CD (λ max) et le pas de l'hélice.

Les arrangements unidirectionnels et hélicoïdaux des CNFs étudiés jusqu'à présent représentent les structures les plus élémentaires qui peuvent être fabriquées en combinant LbL et GIS. Des architectures plus complexes pourraient cependant être réalisées en alternant des hélices droite et gauche ou des couches unidirectionnelles et des hélices pour la réflexion simultanée de la lumière

polarisée circulairement droite et gauche, l'empilement de gradients de pas d'hélice pour la filtration large bande,[35] ou une combinaison de tous ces éléments.

5. Caractérisation mécanique des films multicouches à base de CNF

La caractérisation mécanique des films supportés d'une épaisseur d'environ 1 µm, fabriqués à partir de CNF et de PVAm, a été réalisée au moyen de trois méthodes de nanoindentation. Premièrement, nous avons étudié le module élastique et la dureté des films minces supportés en appliquant une mesure continue de la rigidité (CSM),[36,37] qui est basée sur la superposition d'une petite oscillation harmonique à la charge monotone appliqué à un indenteur. Cette méthodologie a permis d'étudier l'évolution de ces deux grandeurs en fonction de la profondeur de pénétration de l'indenteur dans l'échantillon. Nous avons utilisé le modèle analytique proposé par Bec et al.[38] pour extraire et rapporter le module réel du film, E_f, à partir des mesures globales, ainsi que les modèles de Bhattacharya[39] et de Korsunsky[40] pour extraire la dureté du film mince, Hf. L'ajustement numérique de ces modèles aux courbes expérimentales nous a permis de déterminer le module élastique intrinsèque et la dureté des films multicouches préparés tout au long de cette thèse ; ces valeurs sont discutées et comparées en fonction des différents paramètres de préparation des films et des conditions de mesure.

L'ajustement relatif du modèle élastique proposé par Bec et al. a permis de mieux comprendre les caractéristiques internes des films multicouches à base de CNFs, car il suggère que les propriétés mécaniques de ces films n'étaient pas homogènes. Cette observation a été confirmée par les deux valeurs de dureté différentes extraites des modèles de Korsunsky et de Bhattacharya. Nous avons proposé que la structure poreuse interne des films multicouches est responsable du gradient des propriétés mécaniques. L'incorporation d'argile dans les films a légèrement amélioré leurs propriétés mécaniques, en particulier en présence d'humidité. De plus, l'alignement parallèle des nanofibres dans les films semble également augmenter leurs propriétés, bien que la question demeure de savoir si ce résultat reflète les propriétés intrinsèques du film ou s'il est biaisé par l'utilisation d'un indenteur Berkovich non axisymétrique.

Nous avons alors exploité la sensibilité d'un indenteur Knoop à l'anisotropie des matériaux pour démontrer les caractéristiques anisotropes des films épais unidirectionnels $(CNF/PVAm)_n$. Pour ce faire, nous avons mesuré le module élastique et la dureté à trois angles azimutaux entre la direction théorique d'alignement des nanofibrilles et la diagonale la plus longue de la pointe Knoop. Nous avons comparé les résultats obtenus sur des films unidirectionnels préparés par GIS à ceux obtenus sur un échantillon témoin, idéalement aléatoire, préparé par pulvérisation orthogonale. La réponse anisotrope des deux grandeurs mécaniques sur le film unidirectionnel résulte de l'alignement parallèle de la direction ayant la plus forte concentration de contraintes (celle de la longue diagonale de l'indenteur) avec la direction plus faible de l'échantillon, c'est-à-dire celle dans laquelle les déformations élastiques et plastiques se produisent par la séparation des fibrilles alignées et liées entre elles par de faibles interactions non covalentes (liaisons hydrogène et électrostatiques avec le PVAm). Au contraire, lorsque la direction de la concentration maximale des contraintes est perpendiculaire à l'orientation des nanofibrilles, la déformation nécessite le déplacement collectif de quantités comparativement plus importantes de nanofibrilles et la rupture de liaisons covalentes, ce qui entraîne une plus grande résistance à la déformation élastique et plastique. Cette situation est représentée schématiquement dans la figure R.14.

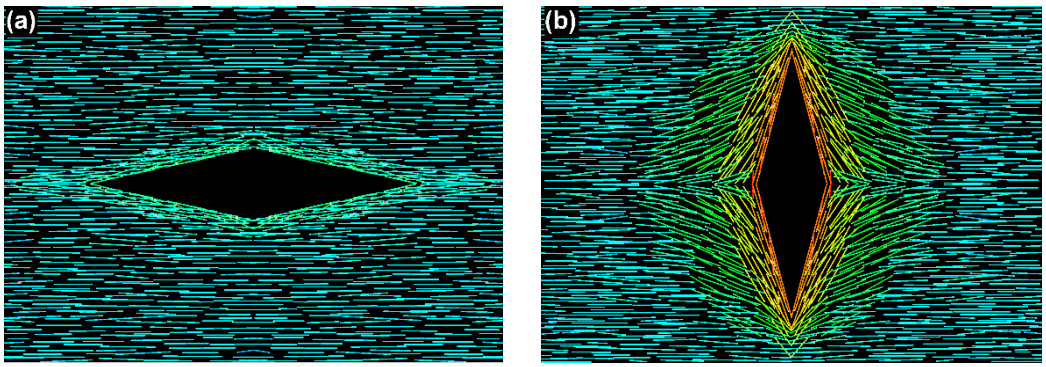

Figure R.14: Représentation schématique de la déformation atteinte lorsque l'axe long de l'indenteur est (a) parallèle ou (b) perpendiculaire à la direction principale d'alignement des CNFs. Les lignes représentent l'alignement parallèle des nanofibrilles de cellulose. Elles se déforment sous l'application de la charge d'indentation mais le nombre de nanofibrilles déformées dépend de l'orientation de l'indenteur Knoop. Les différents angles d'alignement sont colorés différemment par le plug-in OrientationJ d'ImageJ.

Comme prévu, la caractérisation de l'échantillon hélicoïdal avec un indenteur Knoop n'a pas permis de constater de différence significative pour le module élastique ou la dureté mesuré à différents angles azimutaux, de sorte que l'échantillon peut être considéré comme un matériau quasi-isotrope dans le plan.

Les propriétés mécaniques anisotropes des films à alignement unidirectionnel impliquent une direction préférentielle de propagation de la déformation (ou de l'endommagement, par exemple la fissuration), favorisée par la séparation des nanofibrilles (ou des faisceaux de nanofibrilles) qui demande peu d'énergie, comme nous l'avons vu précédemment. Cette directionnalité est à l'origine de la ténacité accrue observée dans les matériaux naturels possédant des arrangements hélicoïdaux dans la phase de renforcement fibrillaire, puisqu'elle favorise la déviation des fissures/déformations suivant des chemins plus longs et tortueux qui dissipent une plus grande quantité d'énergie. Nous avons tenté de démontrer le comportement mécanique amélioré des films multicouches à structure hélicoïdale à base de CNFs, lorsqu'ils sont soumis à des sollicitations avec des taux de déformation élevés, en employant une technique d'essai de fatigue répétitive à l'échelle nanométrique[41]. Cette technique est basée sur un cycle de sollicitation répétitif ("impact") de la sonde de test tout en suivant via la pénétration l'évolution des dommages générés dans le film avec le temps.

La figure R.15(a) compare l'évolution moyenne de la profondeur cumulée mesurée sur les films aléatoire et unidirectionnel. La principale information extraite de ces expériences est la forme de la courbe, car c'est le paramètre qui met en évidence les différences de ductilité (ou d'endommagement) entre les deux matériaux. La déformation permanente à l'intérieur du film nécessite moins d'énergie en séparant les nanofibrilles liées par les chaines faibles de polymère qu'en cassant les nanofibrilles de cellulose résistantes. Par conséquent, lorsque toutes les couches de cellulose sont alignées dans une direction préférentielle, l'énergie donnée au film par chaque impact de l'indenteur est suffisante pour étendre les fissures précédemment formées dans la direction principale d'alignement ou pour séparer les nanofibrilles d'une couche inférieure, ce qui

entraîne l'augmentation continue de la profondeur de pénétration observée pour l'échantillon unidirectionnel. Au contraire, l'échantillon aléatoire n'a pas de direction préférentielle pour la séparation des fibrilles, par conséquent, après un certain nombre d'impacts, aucun dommage supplémentaire n'est observé avec le niveau d'énergie fourni au matériau ; une pénétration supplémentaire ne se produirait que pour un niveau de charge accru. L'ampleur de la déformation cyclique induite est une mesure de la ductilité du film, associée à une déformation plastique importante avant la rupture, alors que les défaillances fragiles impliquent généralement une faible déformation plastique[42]. Le fait que le film avec l'alignement unidirectionnel des CNFs soit plus enclin à se déformer de manière permanente sous des sollicitations de fortes contraintes que le film sans structure suggère que l'alignement parallèle des nanofibrilles fournit au film multicouche un mécanisme de dissipation de l'énergie d'impact qui n'est pas présent dans l'échantillon avec une orientation aléatoire.

Enfin, cette méthodologie de fatigue par nano-contact a été appliquée à un film préparé avec une microstructure interne composée d'un arrangement hélicoïdal des nanofibrilles de cellulose (figure R.15(b)). Il a été observé une ductilité accrue de l'échantillon hélicoïdal par

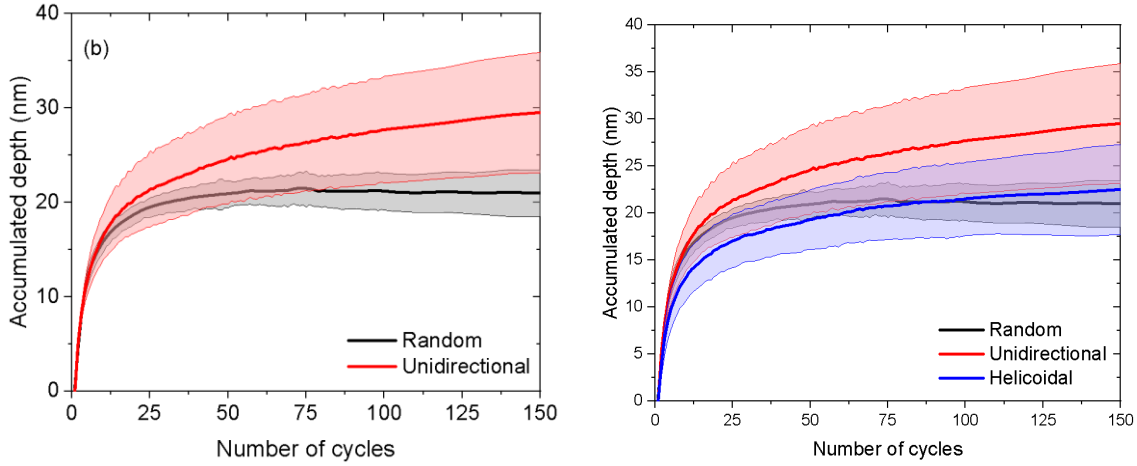

Figure R.15: (a) Comparaison des courbes de profondeur moyennes cumulées pour les échantillons aléatoires et unidirectionnels. Les zones ombragées correspondent à l'écart type de toutes les courbes mesurées. (b) Comparaison entre la profondeur cumulée normalisée et le nombre de cycles de contrainte produits sur les films avec un alignement aléatoire, unidirectionnel et hélicoïdal des CNFs.

rapport au film aléatoire, même si la différence de profondeur de pénétration finale entre les deux échantillons n'est pas significative. De plus, le taux de croissance de la profondeur de pénétration (c'est-à-dire la pente de la région linéaire de la courbe) semblait être identique à celui de l'échantillon unidirectionnel, ce qui suggère une propagation cumulative similaire de la déformation, ou vu d'une autre manière, une efficacité similaire de l'absorption de l'énergie d'impact.

6. Conclusions

Lors de ce travail, nous avons utilisé des méthodes statistiques pour identifier les conditions de pulvérisation optimales pour déposer par GIS une monocouche de CNFs avec un degré d'alignement maximum et nous avons vérifié que des couches consécutives de nanocellulose peuvent être alignées dans les directions souhaitées, indépendamment de l'orientation de la couche inférieure. L'alignement unidirectionnel des nanofibrilles de cellulose en couches épaisses (~1 µm) a été démontré par microscopie optique avec des polariseurs croisés et ellipsométrie spectroscopique à matrice de Mueller (MMSE). Cette dernière a également permis de quantifier la biréfringence optique de ces films anisotropes, qui se situait dans la gamme de valeurs rapportées pour des films biréfringents préparés par d'autres méthodes avec des nanocristaux de cellulose. En outre, les données extraites de la matrice de Mueller ont fourni des informations sur l'orientation locale des nanofibrilles dans l'ensemble de l'échantillon ainsi qu'un moyen simple de caractériser indirectement la fraction volumique de la phase de renforcement à l'intérieur du film, à condition que l'épaisseur locale et les constantes optiques des composants du film soient connues avec précision (ce qui n'était pas le cas pour l'échantillon analysé).

Des films nanocomposites avec une structure Bouligand ont été fabriqués avec succès, comme le prouvent les images de MEB en coupe transversale, le dichroïsme circulaire (CD) et le MMSE. L'hélicité et le pas de la structure hélicoïdale des CNFs ont été variés par le contrôle de la direction de pulvérisation et du nombre de couches orientées dans la même direction. Ces films minces nanostructurés se caractérisent par le phénomène de réflexion circulaire de Bragg dans lequel la lumière polarisée circulairement ayant la même hélicité que la structure chirale du film est

réfléchie de préférence tandis que l'hélicité opposée est transmise. Ce comportement a été vérifié par le fort pic de CD détecté dans tous les échantillons hélicoïdaux, approximativement centré à une longueur d'onde proportionnelle à l'indice de réfraction moyen dans le plan du film et au pas de la structure hélicoïdale, fournissant ainsi la preuve de la nature structurelle du signal.

Les propriétés mécaniques des films structurés à base de CNFs ont été étudiées par nanoindentation. L'ajustement relatif du modèle élastique proposé par Bec et al. et les deux valeurs de dureté différentes extraites des modèles de Korsunsky et de Bhattacharya ont suggéré une structure poreuse interne de ces films multicouches induisant un gradient de propriété dans l'épaisseurs. D'autre part, des tests de nanoindentation avec un indenteur disymétrique Knoop ont mis en évidence le comportement anisotrope des échantillons unidirectionnels. Enfin, nous avons mis en œuvre une méthodologie de fatigue par nano-contact pour étudier les différentes réponses mécaniques des films minces de cellulose structurés à des taux de déformation élevés. Les films unidirectionnels et hélicoïdaux ont montré une ductilité accrue par rapport à l'échantillon aléatoire, ce qui peut être lié à la capacité du matériau structuré à absorber des énergies d'impact plus élevées par des mécanismes de propagation préférentielle d'endommagements/déformations.

La présente étude pose les bases de la préparation de films nanocomposites bio-inspirés complexes avec des structures internes bien contrôlées combinant par exemple des propriétés physiques anisotropes (mécanique et optique), la biodégradabilité ou la durabilité pour de nouvelles applications dans différents domaines tels que les capteurs, les emballages, l'électronique et l'optique.

7. References

[1] M. A. Meyers, P.-Y. Y. Chen, A. Y.-M. M. Lin, Y. Seki, Prog. Mater. Sci. **2008**, 53, 1.

[2] S. E. Naleway, M. M. Porter, J. McKittrick, M. A. Meyers, Adv. Mater. **2015**, 27, 5455.

[3] M. A. Meyers, A. Y. M. Lin, Y. Seki, P. Y. Chen, B. K. Kad, S. Bodde, Jom **2006**, 58, 35.

[4] A. C. Neville, B. M. Luke, Tissue Cell **1969**, 1, 689.

[5] A. C. Neville, S. Levy, Planta **1984**, 162, 370.

[6] J. Ren, Y. Wang, Y. Yao, Y. Wang, X. Fei, P. Qi, S. Lin, D. L. Kaplan, M. J. Buehler, S. Ling, Chem. Rev. **2019**, 119, 12279.

[7] J. C. Weaver, G. W. Milliron, A. Miserez, K. Evans-Lutterodt, S. Herrera, I. Gallana, W. J. Mershon, B. Swanson, P. Zavattieri, E. DiMasi, D. Kisailus, Science. **2012**, 336, 1275.

[8] J. P. Vigneron, P. Simonis, Phys. B Condens. Matter **2012**, 407, 4032.

[9] H. P. Meyers, Introductory Solid State Physics, CRC Press, **1997**.

[10] A. C. Neville, S. Caveney, Biol. Rev. **1969**, 45, 531.

[11] V. Sharma, M. Crne, J. O. Park, M. Srinivasarao, Mater. Today Proc. **2014**, 1, 161.

[12] S. Berthier, M. Thomé, P. Simonis, Mater. Today Proc. **2014**, 1, 145.

[13] I. E. Carter, K. Weir, M. W. McCall, A. R. Parker, J. R. Soc. Interface **2016**, 13.

[14] L. T. McDonald, E. D. Finlayson, B. D. Wilts, P. Vukusic, Interface Focus **2017**, 7, 1.

[15] R. Hashaikeh, P. Krishnamachari, Yarjan Abdul Samad, in Handb. Polym. Nanocomposites. Process. Perform. Appl. - Vol. C Polym. Nanocomposites Cellul. Nanoparticles (Eds.: J.K. Pandey, H. Takagi, A.N. Nakagaito, H.-J. Kim), Springer Materials, **2015**.

[16] A. F. Turbak, F. W. Snyder, K. R. Sandberg, Suspensions Containing Microfibrillated Cellulose, **1983**, U.S. Patent 4,378,381.

[17] Y. Nishiyama, P. Langan, H. Chanzy, J. Am. Chem. Soc. **2002**, 124, 9074.

[18] G. Decher, J. D. Hong, Ber Bunsen-Ges Phys Chem **1991**, 95, 1430.

[19] G. Decher, Y. Lvov, J. Schmitt, Thin Solid Films **1994**, 244, 772.

[20] G. Decher, Science. **1997**, 277, 1232.

[21] E. Hao, T. Lian, Chem. Mater. **2000**, 12, 3392.

[22] Y. Guan, W. Li, Y. Zhang, Z. Shi, J. Tan, F. Wang, Y. Wang, Compos. Sci. Technol. **2017**, 144, 193.

[23] R. S. Pontes, M. Raposo, C. S. Camilo, A. Dhanabalan, M. Ferreira, J. Oliveira ON, Phys. status solidi **1999**, 173, 41.

[24] D. E. Bergbreiter, G. Tao, J. G. Franchina, L. Sussman, Macromolecules **2001**, 34, 3018.

[25] A. Gilliard, L. C. Winterton, R. V. Andino, J. Lally, Method for Applying a Coating, **2004**, US Patent 6,811,805.

[26] J. B. Schlenoff, S. T. Dubas, T. Farhat, Langmuir **2000**, 16, 9968.

[27] J. Cho, K. Char, J. Hong, K. Lee, Adv. Mater. **2001**, 13, 1076.

[28] P. A. Chiarelli, M. S. Johal, J. L. Casson, J. B. Roberts, J. M. Robinson, H. Wang, Adv. Mater. **2001**, 13, 1167.

[29] R. Blell, X. Lin, T. Lindström, M. Ankerfors, M. Pauly, O. Felix, G. Decher, ACS Nano **2017**, 11, 84.

[30] H. Hu, M. Pauly, O. Felix, G. Decher, Nanoscale **2017**, 9, 1307.

[31] D. Klemm, B. Philipp, T. Heinze, U. Heinze, W. Wagenknecht, Comprehensive Cellulose Chemistry. Volume l: Fundamentals and Analytical Methods, Wiley-VCH Verlag, **1998**.

[32] A. Mendoza-Galván, T. Tejeda-Galán, A. B. Domínguez-Gómez, R. A. Mauricio-Sánchez, K. Järrendahl, H. Arwin, Nanomaterials **2019**, 9, 1.

[33] E. D. Cranston, D. G. Gray, Colloids Surfaces A Physicochem. Eng. Asp. **2008**, 325, 44.

[34] M. Faryad, A. Lakhtakia, Adv. Opt. Photonics **2014**, 6, 225.

[35] D. J. Broer, J. Lub, G. N. Mol, Nature **1995**, 378, 467.

[36] W. C. Oliver, J. B. Pethica, Method for Continuous Determination of the Elastc Stiffness of Contact Between Two Bodes, **1989**, US Patent 4,848,141.

[37] W.C. Oliver and G.M. Pharr, J. Mater. Res. **1992**, 7, 1564.

[38] S. Bec, A. Tonck, J. M. Georges, E. Georges, J. L. Loubet, Philos. Mag. A Phys. Condens. Matter, Struct. Defects Mech. Prop. **1996**, 74, 1061.

[39] A. K. Bhattacharya, W. D. Nix, Int. J. Solids Struct. **1988**, 24, 1287.

[40] A. M. Korsunsky, M. R. McGurk, S. J. Bull, T. F. Page, Surf. Coatings Technol. **1998**, 99, 171.

[41] B. D. Beake, J. F. Smith, M. J. s. I. García, Thin Solid Films **2001**, 398–399, 438.

[42] B. D. Beake, S. R. Goodes, J. F. Smith, F. Gao, J. Mater. Res. **2004**, 19, 237.

Université de Strasbourg

Randy MUJICA

Institut Charles SADRON CNRS - ULP - STRASBOURG

Layer-by-Layer assembly of nanocellulose composite films with bio-inspired helicoidal superstructures

Résumé

Les propriétés optiques et mécaniques remarquables des matériaux naturels sont souvent associées à la complexité de leurs structures hiérarchiques. L'une des plus complexes est la structure hélicoïdale, constituée de plusieurs couches de fibres alignées dont l'orientation tourne entre les couches voisines. Cette microstructure, dite de Bouligand, est associée à la résistance aux chocs accrue de la carapace de certains crustacés ainsi qu'à la réflexion préférentielle de la lumière polarisée circulaire de certains fruits et insectes. Dans ce travail, nous avons fabriqué des films minces bio-inspirés complexes composés de nanofibrilles de cellulose et de poly(vinylamine) en utilisant l'approche couche-par-couche (LbL) et la pulvérisation à incidence rasante (GIS), une méthode permettant de contrôler l'alignement dans le plan de nano-objets anisotropes comme les nanofibrilles de cellulose. Nous avons démontré la possibilité de contrôler de façon indépendante la direction de l'alignement de chaque couche de cellulose. Ainsi, nous avons pu préparer des films minces avec une orientation unidirectionnelle, croisée ou hélicoïdale des nanofibrilles de cellulose, ce qu'il n'est pas possible de faire avec d'autres procédés de fabrication. Les propriétés optiques de ces films ont été caractérisées par dichroïsme circulaire et ellipsométrie spectroscopique à matrice de Mueller. Nous avons observé que la réponse chirale des films hélicoïdaux est contrôlée par le sens de rotation, le pas de l'hélice et le nombre de couches avant rotation. Les propriétés mécaniques de ces films ont été étudiées par différentes méthodes de nanoindentation. La méthodologie de fatigue par nano-contact a montré une ductilité accrue des films unidirectionnels et hélicoïdaux, qui peut être indirectement liée à une absorption accrue de l'énergie de ce matériau lors des sollicitations en raison de sa structure interne.

Mots clés : Nanocellulose, assemblage couche-par-couche, alignement par pulvérisation, films nanostructurés hélicoïdaux, matériaux bio-inspirés complexes, propriétés optiques et mécaniques anisotropes

Résumé en anglais

The remarkable optical and mechanical properties of natural materials are often associated with the complexity of their hierarchical structures. One of the most complexes is the helical structure which consists of several layers of unidirectionally aligned fibers whose orientation rotates with respect to their neighboring layers. This so-called Bouligand microstructure is responsible for the enhanced impact resistance of the shell of some crustaceans as well as the preferential reflection of circularly polarized light of certain fruits and insects. Here, we fabricated complex bio-inspired thin films made of cellulose nanofibrils and poly(vinylamine) using the layer-by-layer (LbL) approach and grazing incidence spraying (GIS), a method allowing to control the in-plane alignment of anisotropic nano-objects like cellulose nanofibrils. We demonstrated the independent direction of alignment of each cellulose layer, which allowed the preparation of thin films with well-defined internal structures, namely, unidirectional, cross-ply or helical arrangement of the reinforcing nanofibrils, which is impossible to achieve by any other fabrication process. The optical properties of these films were characterized by circular dichroism (CD) and by Mueller matrix ellipsometry. The chirality observed for helicoidal films is controlled by the rotation direction, the pitch, and the number of layers. The mechanical properties of these cellulose-based films were studied by various nanoindentation methods. A nano-contact fatigue methodology showed an increased ductility of the unidirectional and helicoidal films, which can be indirectly related to enhanced absorption of energy of this material owing to their internal structure.

Keywords: Nanocellulose, layer-by-layer assembly, spray-assisted alignment, helicoidal nanostructured films, complex bio-inspired materials, anisotropic optical and mechanical properties